

グループ2

神経細胞の酸化ストレスによる機能障害と細胞死メカニズムの解明

24S-ヒドロキシコレステロール誘導性神経細胞死のメカニズムと抑制ストラテジー

同志社大学大学院生命医科学研究科	野口範子
同志社大学生命医科学部	斉藤芳郎
同志社大学生命医科学部	浦野泰臣
東京女子医科大学病理	柴田亮行

1. はじめに

アルツハイマー病やパーキンソン病など神経変性疾患は、神経細胞死が主な原因となって発症する。神経変性疾患の発症に酸化ストレスや脂質代謝が関連することが注目されているが、まだその詳細は明らかにされていない。われわれは脳に特異的な代謝様式があることが知られているコレステロールに着目し、その酸化生成物と細胞死の関係について研究を行ってきた。神経細胞内で産生されるコレステロール酸化生成物は、神経細胞にプログラムされたネクロシス(ネクロトーシス)を誘導することを見いだした。本研究は、その細胞死の詳細なメカニズムを明らかにし、これに対する抑制方法を開発することにより、神経変性疾患の治療、予防方法を提案することを目標としておこなった。

2. 研究の背景

脳のコレステロール代謝

脳のコレステロール代謝は、他の臓器とは異なる特殊な環境に適応したメカニズムによって制御されている。脳以外の組織では、コレステロールは細胞内の生合成と食餌由来の両方から供給される。食餌性コレステロールはリポタンパク質に組込まれて各臓器・組織に運ばれ、逆に細胞内の過剰なコレステロールはリポタンパク質に引き抜かれて循環系に戻る。しかし、リポタンパク質やコレステロールは血液脳関門を通ることができないため、脳は食餌性コレステロールの供給を受けることはできない。そこで、脳の細胞はもっぱらコレステロール生合成を行うことによりコレステロールレベルを維持しているが、濃度が過剰になった場合に、血液脳関門を通過できないため循環系に戻すことができない。そこで生体は、脳の細胞だけにコレステロール 24S ヒドロキシラーゼ(CYP46A1)という酸化酵素を発現して、血液脳関門を通過できる 24S-ヒドロキシコレステロール(24S-OHC)を産生するしくみを備えており (図 1)、脳で過剰になったコレステロールは 24S-OHC に変換されて循環系に排出される。24S-OHC はまた、核

内受容体の LXR (Liver X Receptor) のリガンドや SREBP2 (Sterol Regulatory Element-Binding Protein 2) の活性化抑制因子として働くことにより、細胞の脂質代謝制御に関わっていることが知られている。

その一方で、老人斑周辺の CYP46A1 の高発現や、AD 患者の血漿や脳脊髄液中の 24S-OHC の濃度が健常人より高いなど、24S-OHC と AD 発症との関連が報告されている。また、24S-OHC は神経細胞毒性を示すことも報告されていたが、その詳細なメカニズムは不明であった。われわれは、24S-OHC が神経細胞 (neuroblastoma, SH-SY5Y) に RIPK1 (Receptor Interacting protein Kinase 1) 依存性のネクローシスを誘導することを見いだした (Yamanaka et al. *J. Biol. Chem.* 286, 24666-24673, 2011)。

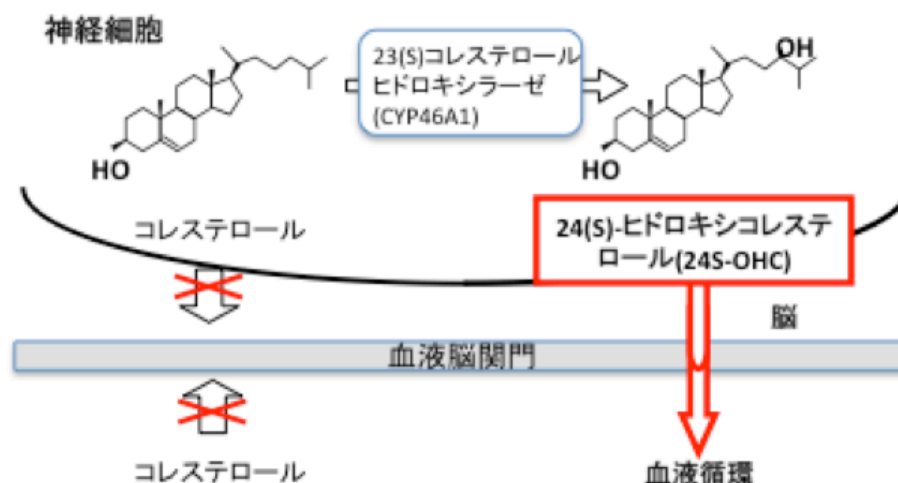


図1 脳のコレステロール恒常性維持のしくみ

3. 研究成果

(1) 24S-OHC 処理細胞内の脂肪滴様構造の形成および細胞死と ACAT 阻害剤の効果

24S-OHC 処理後の SH-SY5Y 細胞を、中性脂質と反応して蛍光を発する色素 Nile red を用いて染色を行うと、脂肪滴様の構造体が蓄積していることがわかった (図 2 A, B)。通常、細胞内の過剰なコレステロールは、小胞体に存在する acyl-CoA:cholesterol acyltransferase (ACAT) の作用により脂肪酸がエステル結合したエステル体としてリン脂質膜に囲まれた状態 (脂肪滴) で蓄積することが知られている。ACAT には ACAT1 と ACAT2 の二つのアイソフォームが存在するが、脳では ACAT1 のみが発現している。24S-OHC で処理した細胞内に蓄積している脂肪滴様の構造体が、ACAT の作用によってできたものであるかどうか確認するため、ACAT の阻害剤 F12511 と ACAT1 特異的阻害剤 K-604 の添加効果を調べた。F12511、K-604 の添加により、24S-OHC が誘導

する脂肪滴様の構造体は観察されなくなった (図 2 A, B)。

次に 24S-OHC が誘導する細胞死に対する F12511 および K-604 の添加効果を調べたところ、細胞死はこれら阻害剤によりほぼ完全に抑制されることが明らかになった (図 2 C,D)。ACAT1 をノックダウンした神経細胞に 24S-OHC を添加した場合も、ACAT の阻害剤処理と同様に、脂肪滴様の構造体は観察されず、細胞死はほぼ完全に抑制された(data not shown)。以上の結果から、24S-OHC を添加した神経細胞内では、ACAT1 の作用により脂肪滴様の構造体が形成され、これが 24S-OHC が誘導する神経細胞死に重要な役割を担っていることが示唆された(Yamanaka et al. *Cell Death Dis.*, 5: e990, 2014)。

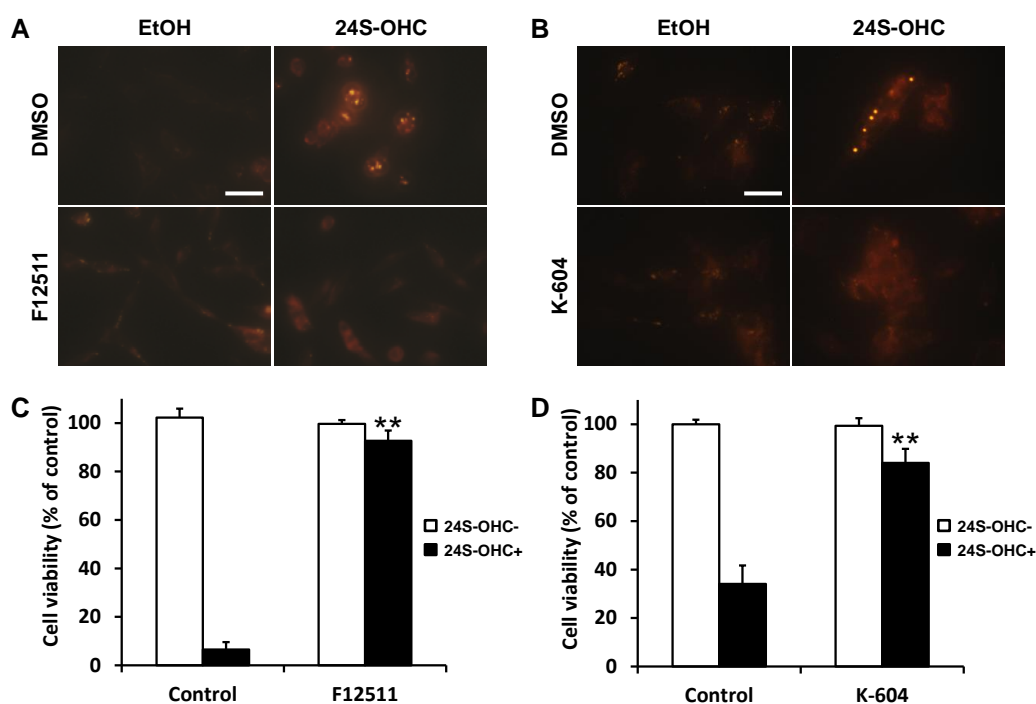


図 2 24S-OHC による細胞内脂肪滴様構造形成と細胞死に対する ACAT の関与

SH-SY5Y 細胞を ACAT 阻害剤 F12511 もしくは ACAT1 特異的阻害剤 K-604 で処理し、24S-OHC を添加した. A, B) 脂肪滴様構造は Nile red 染色により確認した. C, D) 細胞生存率は WST-8 法により測定した. ** $p < 0.01$ vs control, mean \pm SD (n=3)

(2) 24S-OHC 処理によって細胞に蓄積する 24S-OHC エステル体の解析

ACAT の働きを抑えることによって脂肪滴様の構造が消失することから、24S-OHC 処理によって細胞内にはコレステロールや 24S-OHC のエステル体が蓄積していることが推測された。そこで、高速液体クロマトグラフィー(HPLC)を用いて分析をおこな

った。評品によりコレステロールのピーク位置を確認した。未処理の細胞のクロマトグラフィーと 24S-OHC 処理した細胞のクロマトグラフィーを比較すると、24S-OHC 処理により 4 つの新たなピーク (# 1 ~ # 4) が検出された (図 3 A,B)。また、ACAT 阻害剤によりこれらのピークは消失することがわかった (図 3 C)。次に、24S-OHC 処理細胞の分析クロマトグラフィーにみられたコレステロールおよび 4 ピーク (# 1 ~ # 4) を分取し、ケン化処理前後の試料について、ガスクロマトグラフィー質量分析計 (GC-MS) を用いて 24S-OHC (図 3 D) とコレステロール (図 3 E) を測定した。その結果、# 1、# 2、# 3 そして # 4 にはそれぞれオレイン酸、リノール酸、アラキドン酸、そしてドコサヘキサエン酸という不飽和脂肪酸がエステル結合していることがわかった。コレステロールはエステル化されていないこともわかった。さらに、これら 4 種類の 24S-OHC エステル体の合成に成功し、同定に寄与した (Takabe et al. *J. Lipid Res.* 57:2005-2014, 2016, Shibuya et al. *Bioorgan. Med. Chem.*, 24:2559-2566, 2016)。

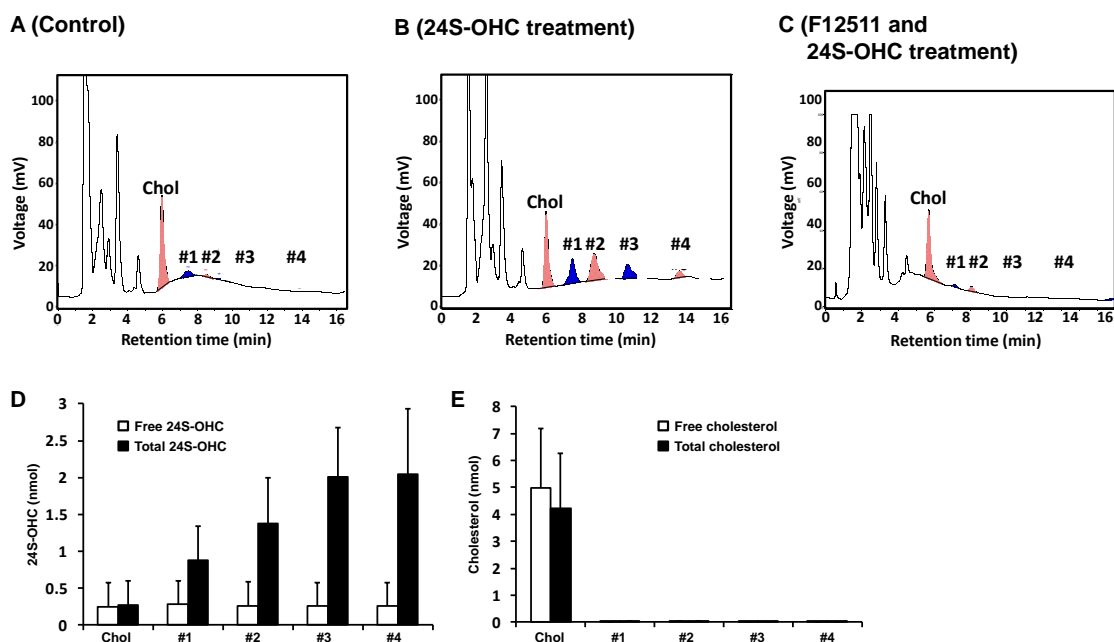


図 3 細胞内コレステロール類とエステル体の分析

(3) 酸化ストレス非依存的な 24S-OHC 誘導性神経細胞死とビタミン E による抑制

24S-OHC によって神経細胞に誘導されるネクロトーシスに活性酸素種が関与しているかどうか、活性酸素種を検出する蛍光プローブを用いて調べた。細胞内の活性酸素種の検出に一般的によく用いられる DCFH-DA (2',7'-dichlorodihydrofluorescein diacetate) で処理した SH-SY5Y 細胞に、24S-OHC もしくは Cumene ヒドロペルオキ

シド (Cumene-OOH)を添加し、フローサイトメーターを用いて蛍光を測定したところ、Cumene-OOH を添加した細胞では蛍光が増加するのに対して、24S-OHC 添加では蛍光は全く増加しなかった(図 4 A)。また、脂質ヒドロペルオキシドを特異的に検出する蛍光プローブ Liperfluo を用いて検出を試みた。Cumene-OOH を添加した細胞では蛍光の著しい増加が見られたのに対して、24S-OHC では全く蛍光増加はみられなかった(図 4 B)。これらの結果は、24S-OHC が誘導するネクロトーシスには活性酸素種は関与しないことを示している(Yamanaka et al. *RSC Advances*. 2:7894-7900, 2012, Noguchi et al. *Free Rad. Biol. Med.* 87:366-372, 2015)。

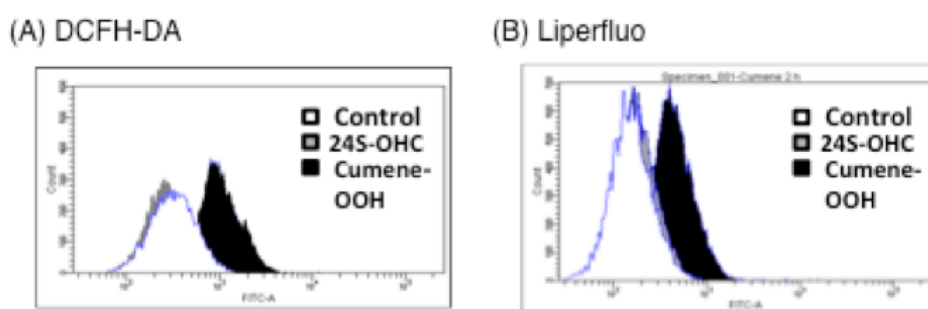
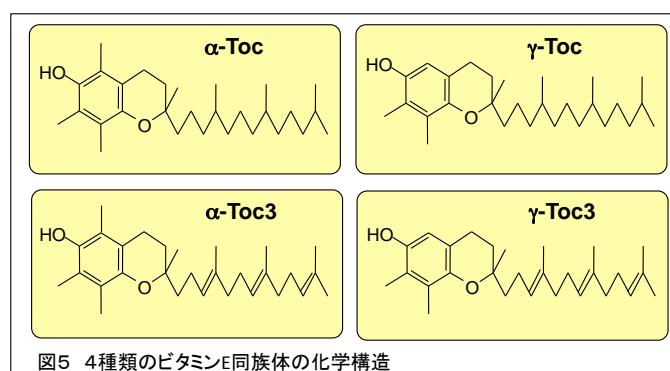


図 4 蛍光プローブを用いた細胞内活性酸素種と脂質ヒドロペルオキシドの検出

ラジカル補足型抗酸化物として知られるビタミン E の AD 発症予防効果は 20 年前から注目をされており、介入試験や疫学調査が行われてきている。そこで、われわれは 8 種類のビタミン E 同族体のうち、 α -tocopherol (α -Toc)、 γ -Toc、 α -tocotrienol (α -Toc 3)、 γ -Toc 3 の 4 種類について、24S-OHC が誘導する神経細胞死に対する抑制効果を調べた(図 5)。その結果、側鎖に二重結合がない Toc は細胞死を抑制するが、二重結合がある Toc 3 は抑制しないことが明らかとなった(図 6)。二重結合の有無は膜の流動性に対する効果が異なることが知られており、膜の流動性を低下させる Toc は細胞死を抑制することが示唆された(Nakazawa et al. *J. Steroid Biochem. Mol. Biol.* 169:69-76, 2017)。



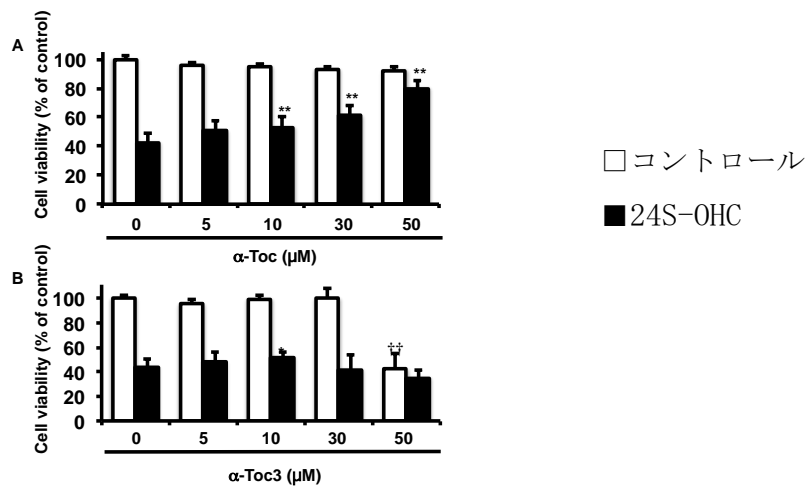


図6 ビタミンE同族体の種類による細胞死抑制効果のちがい

24S-OHCによって誘導された神経細胞死に対してTocは抑制効果を示すが、Toc3は抑制しない。

Mean ± S. D., ** $p < 0.01$, v. s. 24S-OHC only, $n=3$, Tukey, ANOVA.

(4) CaMKII阻害剤による24S-OHC誘導性神経細胞死の抑制

24S-OHC誘導神経細胞死はRIPK1依存性であるが、TNF α 誘導性ネクロトーシスにおいてRIPK1の基質となるRIPK3を必要としないことがわかった(Ho-Vo et al. *Steroids*, 99:230-237, 2015)。24S-OHCによるRIPK1の活性化に対するcalmodulin-dependent protein kinase II (CaMKII)の関与について調べたところ、この二つのkinaseは相互にリン酸化し合うことがわかった。さらに、CaMKIIの阻害ペプチド(M6とmM3)によって、24S-OHCが誘導するCaMKIIのリン酸化が抑制されると同時に細胞死が抑制された(data not shown)。

(5) 24S-OHCによるERストレスの誘導

中性脂質染色により観察された24S-OHC処理細胞内の脂肪滴様構造について、電子顕微鏡標本を作成してより詳細な形態を調べたところ、図6に示すように小胞体(ER)膜に接して脂肪滴様構造が存在し、ER腔が拡張している様子が確認された(図7A, B)。このようなERの顕著な形態変化から、ERストレスシグナルの活性化が推定された。

め (図7 C)、3つの ER ストレスシグナルタンパク質(PERK, ATF6, IRE1 α)の活性化を調べた。その結果すべてのタンパク質の活性化が確認された(data not shown)。

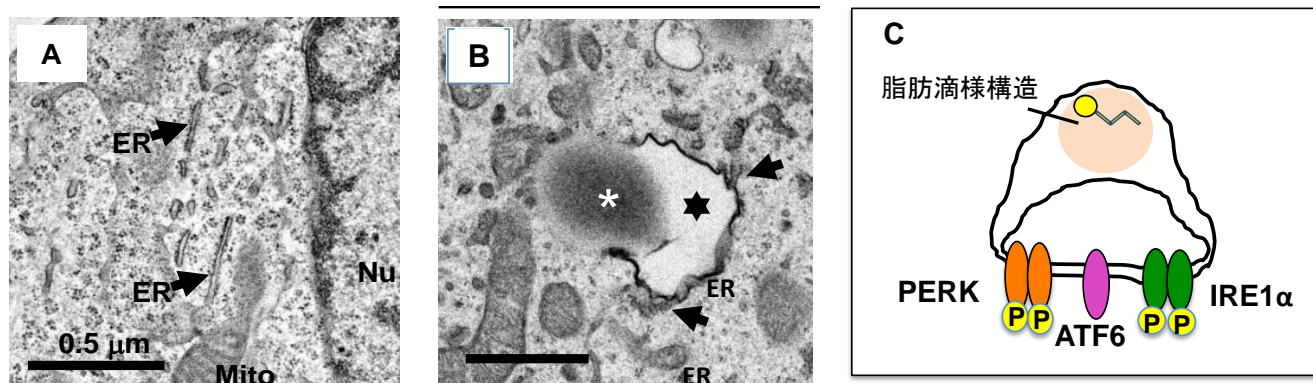


図7 24S-OHC で処理された細胞内に観察された小胞体の形態変化と脂肪滴様構造の形成と ER ストレスモデル図

4. 今後の展望

本研究によって、24S-OHCによる神経細胞死のメカニズムについて多くの知見を得、様々な作用点をもつ化合物について細胞死抑制効果を評価した。その中でもっとも優れた抑制効果を示したのは ACAT1 の阻害剤であった。ACAT1 の阻害剤を用いると、エステル体と脂肪滴様構造が消失し、細胞死はほぼ完全に抑制された。しかしながら、ACAT1 阻害剤は血液脳関門の透過性が低いため、脳に到達させることができないという問題がある。そこで、ACAT1 阻害剤をマウスに経鼻投与したところ、脳内の 24S-OHC が増加したことから、経鼻投与による ACAT1 阻害剤の脳への移行可能性が示された。今後は ACAT1 阻害剤をより効率よく脳へ移行させる方法を確認するとともに、AD モデル動物を用いて高次機能の改善効果を評価する必要がある。

業績リスト

原著論文

- 1) Lai Teng Ling, Yoshiro Saito, Uma Devi Palanisamy, Hwee Ming Cheng, and Noriko Noguchi
Cytoprotective effects of geraniin against peroxynitrite- and peroxy radical-induced cell death via free radical scavenging activity. *Food Chemistry*, 132, 1899-1907. 2012
- 2) Kazunori Yamanaka, Yoshiro Saito, Junji Sakiyama, Yuya Ohuchi, Fumio Oseto, and Noriko Noguchi, A novel fluorescent probe with high sensitivity and selective detection of lipid hydroperoxides in cells, *RSC Advances*, *RSC Adv.*, 2 (20), 7894 - 7900, 2012
- 3) H. Sawada, Y. Saito, N. Noguchi, Enhanced CD36 expression changes the role of Nrf2 activation from anti-atherogenic to pro-atherogenic in apoE-deficient mice, *Atherosclerosis*, 225, 83-90, 2012
- 4) Nobuhiko Harada, Koichi Ito, Tomonori Hosoya, Junsei Mimura, Atsushi Maruyama, Noriko Noguchi, Kenichi Yagami, Naoki Morito, Satoru Takahashi, Jon M. Maher, Masayuki Yamamoto, and Ken Itoh, Nrf2 in bone marrow-derived cells positively contributes to the advanced stage of atherosclerotic plaque formation. *Free Radical Biology and Medicine*, 53, 2256-2262, 2012
- 5) Takashi Hamajima, Yuichi Mushimoto, Hironori Kobayashi, Yoshiro Saito, and Kazumichi Onigata , Novel compound heterozygous mutations in the SBP2 gene: characteristic clinical manifestations and the implications of GH and triiodothyronine in longitudinal bone growth and maturation. *European Journal of Endocrinology*, 166, 757-764, 2012.
- 6) Hirofumi Misu, Kazuhide Ishikura, Seiichiro Kurita, Yumie Takeshita, Tsuguhito Ota, Yoshiro Saito, Kazuhiko Takahashi, Shuichi Kaneko, and Toshinari Takamura, Inverse Correlation between Serum Levels of Selenoprotein P and Adiponectin in Patients with Type 2 Diabetes. *PLoS ONE*, 7, e34952, 2012.
- 7) Hayashi I., Takatori S., Urano Y., Miyake Y., Takagi J., Sakata-Yanagimoto M., Iwanari H., Osawa S., Morohashi Y., Li T., Wong P.C., Chiba S., Kodama T., Hamakubo T., Tomita T., Iwatsubo T.
Neutralization of the γ -secretase activity by monoclonal antibody against extracellular domain of nicastrin. *Oncogene* 31, 787-798, 2012
- 8) Izumi Kato, Hiroshi Maita, Kazuko Takahashi-Niki,, Yoshiro Saito, Noriko Noguchi, Sanae M.M.Iguchi-Ariga, Hiroyoshi Ariga, Oxidized DJ-1 inhibits p53 by sequestering p53 from promoters in a DNA-binding affinity-dependent manner, *Mol. Cell Biol.*, 33, 340-359, 2013
- 9) Urano Y., Ochiai S., Noguchi N. Suppression of amyloid- β production by 24S-hydroxycholesterol via inhibition of intracellular amyloid precursor protein trafficking. *FASEB J.*, 27, 4305-4315, 2013

- 10) Harada H., Warabi E., Matsuki T., Yanagawa T., Okada K., Uwayama J., Ikeda A., Nakaso K., Kirii K., Noguchi N., Bukawa H., Siow R., Mann G., Shoda J., Ishii T., Sakurai T. Deficiency of p62/Sequestosome 1 causes hyperphagia due to leptin resistance in the brain. *J. Neurosci.* 33, 14767-14777, 2013
- 11) Yamanaka K., Urano Y., Takabe W., Saito Y., Noguchi N. Induction of apoptosis and necroptosis by 24(S)-hydroxycholesterol is dependent on activity of acyl-CoA:cholesterol acyltransferase 1. *Cell Death Dis.* 5, e990, 2014
- 12) Okabe A., Urano Y., Itoh S., Suda N., Kotani R., Nishimura Y., Saito Y., Noguchi N. Adaptive responses induced by 24S-hydroxycholesterol through liver X receptor pathway reduce 7-ketocholesterol-caused neuronal cell death. *Redox Biol.*, 2, 28-35, 2014
- 13) Y. Saito, N. Noguchi, 7-Hydroxycholesterol as a possible biomarker of cellular lipid peroxidation: Difference between cellular and plasma lipid peroxidation, A special issue on Oxysterols, *Biochem. Biophys. Res. Commun.* 446, 741-744, 2014.
- 14) N. Noguchi, Y. Saito, Y. Urano, Diverse functions of 24(S)-hydroxycholesterol in the brain. A special issue on Oxysterols, *Biochem. Biophys. Res. Commun.* 446, 692-696, 2014
- 15) K. Ishikura, H. Misu, M. Kumazaki, H. Takayama, N. Matsuzawa-Nagata, N. Tajima, K. Chikamoto, F. Lan, H. Ando, T. Ota, M. Sakurai, Y. Takeshita, K. Kato, A. Fujimura, K. Miyamoto, Y. Saito, S. Kameo, Y. Okamoto, Y. Takuwa, K. Takahashi, H. Kidoya, N. Takakura, S. Kaneko, and T. Takamura, Selenoprotein P as a diabetes-associated hepatokine that impairs angiogenesis by inducing VEGF resistance in vascular endothelial cells. *Diabetologia*, 57, 1968-1976, 2014.
- 16) Y. Saito, T. Miyasaka, H. Hatsuta, K. Takahashi-Niki, K. Hayashi, Y. Mita, O. Kusano-Arai, H. Iwanari, H. Ariga, T. Hamakubo, Y. Yoshida, E. Niki, S. Murayama, Y. Ihara, and N. Noguchi, Immunostaining of oxidized DJ-1 in human and mouse brain, *J. Neuropathol. Exp. Neurol.*, 73, 714-728, 2014.
- 17) I. Ogawa, Y. Saito, K. Saigoh, Y. Hosoi, Y. Mitsui, N. Noguchi, and S. Kusunoki, The significance of oxidized DJ-1 protein (oxDJ-1) as a biomarker for Parkinson's disease, *Brain Nerve*, 66, 471-477, 2014.
- 18) K. Yamanaka, Y. Urano, W. Takabe, Y. Saito, and N. Noguchi, Induction of apoptosis and necroptosis by 24(S)-hydroxycholesterol is dependent on activity of acyl-CoA:cholesterol acyltransferase, 1, *Cell Death Dis.*, 5, e990, 2014.
- 19) H. Takayama, H. Misu, H. Iwama, K. Chikamoto, Y. Saito, K. Murao, A. Teraguchi, F. Lan, A. Kikuchi, R. Saito, N. Tajima, T. Shirasaki, S. Matsugo, K. Miyamoto, S. Kaneko, and T. Takamura, Metformin Suppresses Expression of the Selenoprotein P gene via an AMPK-FoxO3a Pathway in H4IIEC3

- Hepatocytes. *J. Biol. Chem.*, 289, 335-45, 2014.
- 20) D.-K. Ho Vo, Y. Urano, W. Takabe, Y. Saito, N. Noguchi, 24(S)-Hydroxycholesterol induces RIPK1-dependent but MLKL-independent cell death in the absence of caspase-8, *Steroids*, 99, 230-237, 2015.
 - 21) K. Takagane, J. Nojima, H. Mitsuhashi, S. Suo, D. Yanagihara, F. Takaiwa, Y. Urano, N. Noguchi, S. Ishiura, A β induces oxidative stress in senescence-accelerated (SAMP8) mice, *Biosci. Biotech. Biochem.*, 23, 1-7, 2015.
 - 22) Shioji Ishiwatari, Minako Takahashi, Chie Yasuda, Maho Nakagawa, Tatsuya Kon, Yoshiro Saito, Noriko Noguchi, and Shoko Matsukuma, The protective role of DJ-1 in ultraviolet-induced damage of human skin: DJ-1 levels in the stratum corneum as an indicator of antioxidative defense. *Arch. Dermatol. Res.* 307, 925-935, 2015.
 - 23) Noriko Noguchi, Yasuomi Urano, Wakako Takabe, and Yoshiro Saito, New aspects of 24S-hydroxycholesterol in modulating neuronal cell death, *Free Radic. Biol. Med.*, 87, 366-372, 2015
 - 24) Yoshiro Saito, Mototada Shichiri, Takashi Hamajima, Noriko Ishida, Yuichiro Mita, Shohei Nakao, Yoshihisa Hagihara, Yasukazu Yoshida, Kazuhiko Takahashi, Etsuo Niki, and Noriko Noguchi, Enhancement of lipid peroxidation and its amelioration by vitamin E in a subject with mutations in the SBP2 gene, *J. Lipid Res.*, 562172-82, 2015
 - 25) Mayuko Morita, Azusa Sekine, Yasuomi Urano, Taki Nishimura, Wakako Takabe, Hiroyuki Arai, Takao Hamakubo, Tatsuhiko Kodama, and Noriko Noguchi, Lysophosphatidylcholine promotes SREBP-2 activation via rapid cholesterol efflux and SREBP-2-independent cytokine release in human endothelial cells, *J. Biochem*, 158, 331-338, 2015
 - 26) Takeshi Kumagai, Hiroko Usami, Nao Matsukawa, Fumie Nakashima, Miho Chikazawa, Takahiro Shibata, Noriko Noguchi, and Koji Uchida, Functional interaction between cyclooxygenase-2 and p53 in response to an endogenous electrophile, *Redox Biol.*, 4, 74-86, 2015
 - 27) Kimiyuki Shibuya, Toshiaki Watanabe, Yasuomi Urano, Wakako Takabe, Noriko Noguchi, Hiroaki Kitagishi, Synthesis of 24(S)-hydroxycholesterol esters responsible for the induction of neuronal cell death. *Bioorgan. Med. Chem.*, 24, 2559-2566, 2016.
 - 28) Noriko Noguchi, Ebselen, a useful tool for understanding cellular redox biology and a promising drug candidate for use in human diseases. *Arch. Biochem. Biophys.*, 595, 109-112, 2016.

- 29) Mutsumi Tanaka, Yoshiro Saito, Hirofumi Misu, Seiji Kato, Yuki Kita, Yumie Takeshita, Takehiro Kanamori, Toru Nagano, Masatoshi Nakagen, Takeshi Urabe, Toshinari Takamura, Shuichi Kaneko, Kazuhiko Takahashi, and Naoto Matsuyama, Development of a sol particle homogeneous immunoassay for measuring full-length selenoprotein P in human serum, *J. Clin. Lab. Anal.*, 30, 114-122, 2016
- 30) Rina Kotani, Yasuomi Urano, Hachiro Sugimoto, Noriko Noguchi, Decrease of amyloid- β levels by curcumin derivative via modulation of amyloid- β protein precursor trafficking. *J. Alzheimer's Disease*, 56, 529-542, 2016.
- 31) Wakako Takabe, Yasuomi Urano, Diep-Khanh Ho Vo, Kimiyuki Shibuya, Tanno M., Hiroaki Kitagishi, Toyoshi Fujimoto, Noriko Noguchi, Esterification of 24(S)-hydroxycholesterol induces formation of atypical lipid droplet-like structure leading to neuronal cell death. *J. Lipid Res.* 57, 2005-2014, 2016
- 32) Yoshiro Saito, Noriko Noguchi. Oxidized Lipoprotein as a Major Vessel Cell Proliferator in Oxidized Human Serum. *PLoS One*. 11:e0160530, 2016
- 33) Saito Y, Akazawa-Ogawa Y, Matsumura A, Saigoh K, Itoh S, Sutou K, Kobayashi M, Mita Y, Shichiri M, Hisahara S, Hara Y, Fujimura H, Takamatsu H, Hagihara Y, Yoshida Y, Hamakubo T, Kusunoki S, Shimohama S, Noguchi N. Oxidation and interaction of DJ-1 with 20S proteasome in the erythrocytes of early stage Parkinson's disease patients. *Sci Rep*. Jul 29;6:30793, 2016
- 34) Bharatwaj Sowrirajan, Yoshiro Saito, Deepak Poudyal, Qian Chen, Hongyan Sui, Suk See DeRavin, Hiromi Imamichi, Toyotaka Sato, Douglas B. Kuhns, Noriko Noguchi, Harry L. Malech, H. Clifford Lane and Tomozumi Imamichi, Interleukin-27 Enhances the Potential of Reactive Oxygen Species Generation from Monocyte-derived Macrophages and Dendritic cells by Induction of p47phox. *Sci. Rep.*, 7:43441, 2017
- 35) Hirofumi Misu, Hiroaki Takayama, Yoshiro Saito, Yuichiro Mita, Akihiro Kikuchi, Kiyo-aki Ishii, Keita Chikamoto, Takehiro Kanamori, Natsumi Tajima, Fei LanLan, Yumie Takeshita, Masao Honda, Mutsumi Tanaka, Seiji Kato, Naoto Matsuyama, Yuya Yoshioka, Kaito Iwayama, Kumpei Tokuyama, Nobuhiko Akazawa, Seiji Maeda, Kazuhiro Takekoshi, Seiichi Matsugo, Noriko Noguchi, Shuichi Kaneko, and Toshinari Takamura, Deficiency of the hepatokine selenoprotein P increases responsiveness to exercise in mice through upregulation of ROS and AMPK in muscle. *Nature Med.*, in press, 2017
- 36) Takaya Nakazawa, Yuta Miyonoki, Yasuomi Urano, Madoka Uehara, Yoshiro Saito, Noriko Noguchi, Effect of vitamin E on 24(S)-hydroxycholesterol-induced necroptosis-like cell death and apoptosis. *J. Steroid Biochem. Mol. Biol.*, 169:69-76, 2017.

- 37) Yamamoto T, Kato Y, Hiroi A, Shibata N, Osawa M, Kobayashi M, Post-transcriptional regulation of fukutin in an astrocytic cell line. *Int. J. Exp. Pathol.*, 93:46-55, 2012.
- 38) Kawaguchi-Niida M, Yamamoto T, Kato Y, Inose Y, Shibata N, MCP-1/CCR2 signaling-mediated astrocytosis is accelerated in a transgenic mouse model of SOD1-mutated familial ALS. *Acta Neuropathol. Commun.*, 1: 21, 2013.
- 39) Ishisaka A, Mukai R, Terao J, Shibata N, Kawai Y: Specific localization of quercetin-3-O-glucuronide in human brain. *Archiv. Biochem. Biophys.*, 558:11-17, 2014.
- 40) Inose Y, Kato Y, Kitagawa K, Uchiyama S, Shibata N: Activated microglia in ischemic stroke penumbra upregulate MCP-1 and CCR2 expression in response to lysophosphatidylcholine derived from adjacent neurons and astrocytes. *Neuropathology*, 35:209-223, 2014.
- 41) Umahara T, Uchihara T, Shibata N, Nakamura A, Hanyu H. 14-3-3 eta isoform colocalizes TDP-43 on the coarse granules in the anterior horn cells of patients with sporadic amyotrophic lateral sclerosis. *Brain Res.*, 1646:132-138, 2016.

著書

- 1) 野口範子、Necroptosis、医学のあゆみ別冊pp. 142-144, 2012, 日本医学出版、東京
- 2) 西尾敬子、石田規子、斎藤芳郎、赤澤陽子、七里基督、吉田康一、萩原義久、野口範子、John Chirico、Jefferey Atkinson、二木鋭雄、 α -トコフェロールリン酸の細胞および生体への取り込みと抗酸化作用、ビタミンEの進歩 XV, pp. 15-19, 2012ビタミンE研究会、東京
- 3) 山中一哲、斎藤芳郎、山盛徹、浦野泰臣、野口範子、24S-0HC誘導性細胞死に対するビタミンE類の添加効果、ビタミンEの進歩 XV, pp. 20-25, 2012, ビタミンE研究会、東京
- 4) 斎藤芳郎、野口範子「パーキンソン病と酸化ストレス」酸化ストレスの医学, 第2版, 264-271, 2014
- 5) 斎藤芳郎、野口範子、神経変性とレドックスパーキンソン病関連分子DJ-1のレドックス制御機能、レドックスUPDATE, 4, 224-228, 2015, 医歯薬出版、東京
- 6) 野口範子、「酸化ストレスと疾患」、ストレスシグナルと疾患、医学のあゆみ, 254, 347-352, 2015, 医歯薬出版、東京
- 7) 野口範子、脳のコレステロール代謝と神経変性疾患、生物の科学遺伝, 70, 225-229, 2016, エヌティーエス、東京
- 8) 斎藤芳郎、セレンの生物学-セレノプロテインの機能と疾患、細胞工学, 35, 240-246, 2016, 秀潤社、東京

総説

- 1) 山中一哲、野口範子、新しい細胞死ネクローシス～プログラムされたネクローシス～、DOJINDO NEWS、145, 1-6, 2012
- 2) Saito Y., Noguchi N. 7-Hydroxycholesterol as a possible biomarker of cellular lipid peroxidation: Difference between cellular and plasma lipid peroxidation. *Biochem. Biophys. Res. Commun.* 446, 741-744, 2014
- 3) Noguchi N., Saito Y., Urano Y. Diverse functions of 24(S)-hydroxycholesterol in the brain. *Biochem. Biophys. Res. Commun.* 446, 692-696, 2014
- 4) 斎藤芳郎 パーキンソン病におけるバイオマーカーの現状-マイケルJフォックス財団の取り組み ファルマシア **49**, 870-872, 2014
- 5) Masui K, Shibata N, Cavenee WK, Mischel PS. mTORC2 activity in brain cancer: extracellular nutrients are required to maintain oncogenic signaling. *Bioessays.* 38, 839-844, 2016.

招待講演

- 1) 野口範子 生体の酸化ストレス防御能を評価する 京都フォーラム
- 2) 野口範子 細胞死の種類と抗酸化作用 第12回A0B研究会
- 3) 野口範子 新しい細胞死形態ネクローシスとレドックス制御 日本学術振興会170委員会
- 4) 野口範子 抗酸化物質による遺伝子発現制御と疾患 未来へのバイオ技術勉強会
- 5) 野口範子 Dual Functions of 24S-Hydroxycholesterol in Neurodegenerative Diseases Induced by Oxidative Stress 日本神経科学会
- 6) 野口範子 コレステロール代謝と酸化ストレス 臨床ストレス応答学会
- 7) 野口範子 「神経細胞のDJ-1分泌に対するA0Bの効果」第10回A0B研究会, Tokyo, 12 July, 2013
- 8) 斎藤芳郎, 七里元督, 濱島 崇, 萩原義久, 吉田康一, 野口範子 「SBP2遺伝子異常に伴う酸化ストレスに対するビタミンEの効果- コレステロール酸化物による脂質酸化の評価」第16回 Vitamin E Update Forum, Tokyo, 19 August, 2013
- 9) 斎藤芳郎, 山中一哲, 浦野泰臣, 野口範子 「脳特異的24(S)-ヒドロキシコレステロールにより誘導されるプログラムネクローシスおよび細胞保護作用の分子メカニズム」第55回日本脂質生化学会, Matsushima, 6 September, 2013
- 10) Noguchi N., Yamanaka K., Takabe W., Urano Y., Saito Y. 「Novel insights of brain-specific produced oxysterol in neurodegenerative diseases.」第86回日本生化学会, Yokohama, 13 September, 2013

- 11) Saito Y., Noguchi N. 「7-hydroxycholesterol as a possible biomarker of cellular lipid peroxidation-difference between cellular and plasma lipid peroxidation.」 3rd ENOR Symposium Oxysterols: Markers and Pathways, Swansea, UK, 20 September, 2013
- 12) Noriko Noguchi, Yoshiro Saito, Yasuomi Urano, 「Diverse functions of 24(S)-hydroxycholesterol in the brain.」 3rd ENOR Symposium Oxysterols: Markers and Pathways, Swansea, UK, 20 September, 2013
- 13) 野口範子, 斎藤芳郎, 浦野泰臣, 山中一哲, 高部稚子, Diep K. 「脳で産生されるオキシステロールの功罪」 京大生命医学研究科セミナー, Shiga, 31 Oct, 201
- 14) 野口範子 「脳特異的コレステロール酸化物による神経細胞死のメカニズムとその抑制戦略」 京大再生医科学セミナー, Kyoto, 30 November, 2013
- 15) Noriko Noguchi. New aspects of 24S-hydroxycholesterol in modulating neuronal cell death. 17th Biennial Meeting of Society for Free Radical Research International, Kyoto, 26 March, 2014
- 16) 高部稚子, 山中一哲, 浦野泰臣, 斎藤芳郎, 野口範子 「酸化コレステロール24S-OHC により誘導されるNecroptosis のメカニズム」 第67回日本酸化ストレス学会学術集会, Kyoto, 4 September, 2014
- 17) Noriko Noguchi, Wakako Takabe, Yasuomi Urano, Yoshiro Saito. Mechanisms of neuronal cell death induced by 24(S)-hydroxycholesterol. 4th ENOR Symposium, Translational Research on Oxysterols, Coimbra, Portugal, 18-19 September, 2014
- 18) Noriko Noguchi, Khanh Vo-Diep, Wakako Takabe, Yasuomi Urano, Yoshiro Saito, Two different ways for neuronal cell death induced by 24(S)-hydroxycholesterol, 5th ENOR Symposium, Translational Research on Oxysterols, Coimbra, Portugal, 24-25 September, 2015
- 19) 世界脳週間講演会 脳はコレステロールが好きーしかし、時として闘いもある, 堀川高校 18 June, 2016
- 20) 日本美容皮膚学会角層バイオマーカーの開発と応用 酸化ストレスと老化・寿命と闘う抗酸化タンパク質DJ-1 東京京王プラザホテル, 06 Aug, 2016
- 21) 柴田亮行. 「TDP-43プロテノパチーの疾患スペクトラム」 第105回日本病理学会総会 診療領域別講習特別プログラム・研究講習会19シンポジウムSY-19-3: 神経変性疾患・病理専門医に求められる神経病理Up to Date: 非腫瘍性疾患を中心として, 仙台 2016年5月14日.
- 22) 柴田亮行. 「Neuroinflammation」 メマリー神経学エキスパートミーティング(特別講演) 函館, 2013年8月2日.
- 23) 柴田亮行. 「筋萎縮性側索硬化症の最上流イベントは何か? 酸化ストレスと神経炎症」 第5回Kyoto Neuropathology Conference (特別講演) 京都 2012年4月5日.

学会発表

- 1) 西郷和真, 池上郁子, 細井幸子, 高田和男, 宮本勝一, 三井 良之, 斎藤芳郎、野口範子、楠進「パーキンソン病における酸化型DJ-1測定とMIBG心筋シンチグラフィの関連について」第53回日本神経学会学術大会 P(1)-102、2012年5月24日（東京）
- 2) 御簾博文、斎藤芳郎、松郷誠一、高橋和彦、金子周一、篁俊成「抗酸化へパトカインセレノプロテインPは活性酸素/AMPK/PGC1 α 経路の抑制を介して運動療法抵抗性の原因となる」酸化ストレス学会 2012年6月6日（徳島）
- 3) 崎山順次, 山中一哲, 斎藤芳郎, 野口範子「新規蛍光プローブ Liperfluo を用いた細胞内過酸化脂質の特異的検出」酸化ストレス学会 2012年6月6日（徳島）
- 4) 浦野泰臣, 野口範子「アミロイド前駆体タンパク質細胞内輸送へのオキシステロールの関与機構の解明」第54回日本脂質生化学会、2012年6月7日（福岡）
- 5) 岡部旭史、浦野泰臣、斎藤芳郎、野口範子「7-Ketocholesterol誘導性神経細胞死に対する24S-hydroxycholesterolの適応反応誘導による抑制のメカニズムの解明」第35回日本分子生物学会2012年12月12日、福岡
- 6) 山中 一哲、浦野 泰臣、斎藤 芳郎、野口 範子「24S-hydroxycholesterol誘導性細胞死“Necroptosis” における脂質代謝異常」第85回日本生化学会、2012年12月13日（福岡）
- 7) 澤田浩隆、斎藤芳郎、野口範子「ApoE欠損マウスの動脈硬化発症に対するラジカル捕捉とNrf2活性化の作用効果に関する研究」第85回日本生化学会、2012年12月16日（福岡）
- 8) 斎藤芳郎、宮坂知宏、浜窪隆雄、二木鋭雄、井原康夫、野口範子「パーキンソン病患者の脳内および赤血球中における酸化DJ-1の生成」第85回日本生化学会、2012年12月16日（福岡）
- 9) Y Saito, K Hayashi, T Hamakubo, N Noguchi , 「Oxidation of DJ-1 induced by 6-hydroxydopamine decreasing intracellular glutathione.」 Neuroscience, 2012年10月15日, (New Oriens)
- 10) 斎藤芳郎、七里元督、濱島崇、萩原義久、吉田康一、野口範子「SBP2 遺伝子異常に伴う酸化ストレスに対するビタミンE の効果」ビタミンE研究会（東京）2013年1月12日（東京）
- 11) Yoshiro Saito, Tomohiro Miyasaka, Takao Hamakubo³, Etsuo Niki, Yasuo Ihara, Noriko Noguchi¹ 「Oxidized DJ-1 in the brain and erythrocytes of Parkinson disease patients and model animals」ADPD 2013年3月9日（Florence）
- 12) 斎藤芳郎、七里元督、濱島 崇、萩原義久、吉田康一、野口範子「セレン欠乏に伴う酸化ストレス障害に対するビタミン E の効果-SBP2 遺伝子異常に対する治療への応用」第 65 回ビタミン学会, Tokyo, 17 May, 2013

- 13) Noguchi N., Yamanaka K., Urano Y., Saito Y. 「24(S)-Hydroxycholesterol induces either apoptosis or necroptosis, using caspase-8 dependent switching machinery of cells.」Cold Spring Harbor Asia, Sezu, China, 17 April, 2013
- 14) 斎藤芳郎, 羽田恵美, 村石彩沙美, 人見穰, 佐野護, 野口範子 「ラット副腎髄質由来褐色細胞腫 PC12D細胞から分泌される過酸化水素消去因子に関する研究」第66回日本酸化ストレス学会, Nagoya, 13 June, 2013
- 15) 小林茉佑香, 村松香奈, 斎藤芳郎, 野口範子 「パーキンソン病関連分子DJ-1の酸化に伴う高分子化およびシステインの役割に関する研究」第66回日本酸化ストレス学会, Nagoya, 13 June, 2013
- 16) Saito Y., Miyasaka T., Hamakubo T., Niki E., Noguchi N. 「Oxidation of DJ-1 in the brain of Parkinson disease patients-possible biomarker for diagnosis of Parkinson disease at early stage.」Neuro2013, Kyoto, 20 June, 2013
- 17) 高金くらら, 野嶋 純, 柳原 大, 浦野泰臣, 野口範子, 高岩文雄, 石浦章一 「食物ワクチンによる孤発性アルツハイマー病モデルの治療」第86回日本生化学会, Yokohama, 11 September, 2013
- 18) 吉岡 佑弥, 西藤 有希奈, 三田雄一郎, 高橋 和彦, 野口 範子, 斎藤 芳郎 「⁷⁵Seおよび免疫学的手法を用いたセレノプロテインPのセレン運搬機構の解析」第86回日本生化学会, Yokohama, 12 September, 2013
- 19) Saito Y., Tanaka M., Misu H., Takamura T., Takahashi K., Noguchi N. 「Development of human selenoprotein P measurement system as a possible biomarker of insulin resistance in type 2 diabetes.」10th International Symposium on Selenium in Biology and Medicine, Berlin, Germany, 15 September, 2013
- 20) Saito Y., Yoshioka Y., Mita Y., Nakayama K., Nishito Y., Takahashi K., Noguchi N. 「Study of selenium supply mechanism of selenoprotein P using ⁷⁵Se and immunological methods.」10th International Symposium on Selenium in Biology and Medicine, Berlin, Germany, 16 September, 2013
- 21) 野口範子, 斎藤芳郎, 浦野泰臣, 山中一哲, 高部稚子, Diep K. 「脳で産生される酸化コレステロール24S-hydroxycholesterol による細胞死メカニズム」第1回高次神経機能障害シンポジウム, Kyoto, 5 October, 2013
- 22) 小谷理奈, 浦野泰臣, 杉本八郎, 野口範子 「Amyloid β産生を抑制するクルクミン誘導体の同定とそのメカニズムの解明」第36回日本分子生物学会, Kobe, 3 December, 2013
- 23) 林 宏次朗, 斎藤 芳郎, 宮坂 知宏, 仁木 加寿子, 有賀 寛芳, 野口 範子 「細胞内および脳内における酸化DJ-1の分布に関する研究」第36回日本分子生物学会, Kobe, 4 December, 2013

- 24) 山本貴之, 浦野泰臣, 斎藤芳郎, 野口範子 「パーキンソン病関連分子DJ-1の細胞外分泌メカニズムの解析」 第36回日本分子生物学会, Kobe, 4 December, 2013
- 25) 四方彩香, 浦野泰臣, 斎藤芳郎, 野口範子 「細胞内コレステロール局在に対するLysophosphatidylcholineの影響」 第36回日本分子生物学会, Kobe, 5 December, 2013
- 26) 斎藤芳郎 「グルタミン酸による神経細胞死抑制物質の探索およびその抑制メカニズムの解析」 第51回同志社大学理工学研究所研究発表会, Kyoto, 14 December, 2013
- 27) 斎藤芳郎 「24S-ヒドロキシコレステロールによる神経細胞死のメカニズム解析」 第51回同志社大学理工学研究所研究発表会, Kyoto, 14 December, 2013
- 28) 野口範子, 斎藤芳郎, 浦野泰臣 「コレステロール酸化物が誘導する細胞死における活性酸素種の関与」 第51回同志社大学理工学研究所研究発表会, Kyoto, 14 December, 2013
- 29) 斎藤芳郎, 山本貴之, 浦野泰臣, 野口範子 「パーキンソン病関連分子DJ-1の細胞外分泌に及ぼすビタミンEの効果」 第25回ビタミンE研究会, Yonago, 25 January, 2014
- 30) 野木秀哉, 川崎亮, 岩出尚, 田嶋邦彦, 野口範子, 植月啓太, 富田直秀 「電子線照射 *dl*- α -Tocopherol 混合超高分子量ポリエチレン内におけるラジカル反応制御」 第25回ビタミンE研究会, Yonago, 25 January, 2014
- 31) Vo DK, Yamanaka K., Urano Y., Takabe W., Saito Y., Noguchi N. 「Lipid droplet formation, the major initial event of 24(S)-hydroxycholesterol-induced cell death through necroptosis and apoptosis.」 17th Biennial Meeting of Society for Free Radical Research International, Kyoto, 26 March, 2014
- 32) 中山華穂, 三田雄一郎, 吉岡佑弥, 西藤有希奈, 高橋和彦, 野口範子, 斎藤芳郎 「インスリン抵抗性バイオマーカー“セレノプロテインP”の中和抗体の探索およびin vivoでの評価—新規2型糖尿病の治療薬創成を目指して」 日本薬学会第134年会, Kumamoto, 30 March, 2014
- 33) 斎藤芳郎, 吉岡佑弥, 三田雄一郎, 御簾博文, 田中睦, 篁俊成, 野口範子 「血漿セレノプロテインPによるセレン代謝制御と2型糖尿病」 第25回日本微量元素学会, Okayama, 3 July 2014
- 34) 浦野泰臣, 山中一哲, 高部稚子, 斎藤芳郎, 野口範子 「脳特異的オキシステロール 24S-hydroxycholesterolによる細胞死メカニズムの解析」 第23回日本Cell Death学会学術集会, Tokyo, 18 July, 2014
- 35) 斎藤芳郎, 七里元督, 濱島崇, 萩原義之, 吉田康一, 野口範子 「SBP2変異によるセレン含有蛋白質に対するビタミンEの効果—投与および投与中止に伴う脂質酸化物の変化」 第17回Vitamin E Update Forum, Tokyo, 6 August, 2014
- 36) 樞拓磨, 斎藤芳郎, 林宏次朗, 三田雄一郎, 片岡佑斗, 野口範子 「パーキンソン病モデルマウス脳内におけるDJ-1の酸化」 第67回日本酸化ストレス学会, Kyoto, 3, September, 2014
- 37) 西村祐貴, 浦野泰臣, 高部稚子, 野口範子 「アストロサイトに対する24S-hydroxycholesterolの細胞死誘導機序の解明」 第67回日本酸化ストレス学会, Kyoto, 4 September, 2014

- 38) 小林茉佑香, 斎藤 芳郎, 菊池 愛, 村松香奈, 野口範子「パーキンソン病関連タンパク質DJ-1の酸化による高分子化に関する研究」第67回日本酸化ストレス学会, Kyoto, 4 September
- 39) 西郷和真, 斎藤芳郎, 小川郁子, 細井幸恵, 三井良之, 花田一志, 上田昌美, 石井一成, 野口範子, 楠進「血中の酸化型 DJ-1 異常高値の臨床的意義」第 67 回日本酸化ストレス学会, Kyoto, 4 September 2014
- 40) 三田雄一郎, 斎藤芳郎, 野口範子「糖尿病関連タンパク質Selenoprotein Pの発現制御機構の解析」第 6 7 回日本酸化ストレス学会, Kyoto, 4 September, 2014
- 41) 斎藤芳郎, 宮坂知宏, 初田裕幸, 仁木加寿子, 有賀寛芳, 村山繁雄, 井原康夫, 野口範子「酸化DJ-1特異的抗体を用いたマウスおよびヒト脳切片の免疫染色」第37回日本神経科学会 Neuroscience 2014, Yokohama, 12 September 2014
- 42) 斎藤芳郎「新規糖尿病バイオマーカーを標的とする 2 型糖尿病治療薬」第1回A-STEP発 新技術説明会, Tokyo, 28 October 2014
- 43) Yoshiro SAITO, Tomohiro MIYASAKA, Hiroyuki HATSUTA, Kazuko TAKAHASHI-NIKI, Hiroyoshi ARIGA, Shigeo MURAYAMA, Yasuo IHARA, Noriko NOGUCHI. Immunostaining of oxidized DJ-1 in human and mouse brain. Neuroscience 2014, Washington DC, USA, 17 November 2014.
- 44) 吉岡佑弥, 三田雄一郎, 西藤有希奈, 野口範子, 斎藤 芳郎「セレノプロテインPは分解経路・非分解経路を介して細胞内へセレンを供給する」第87回日本生化学会, Kyoto, 18 November, 2014
- 45) Yoshiro Saito, Mototada Shichiri, Takashi Hamajima, and Noriko Noguchi. Enhancement of Oxidative Stress and Its Amelioration by Vitamin E in a Subject with Mutations in the Selenocysteine Insertion Sequence-Binding Protein 2 (SBP2) Gene. SFRBM's 21th Annual Meeting, Seattle USA, 21 November 2014.
- 46) 藤 綾乃, 浦野 泰臣, 矢白木 翔平, 里見 ちひろ, 斎藤 芳郎, 野口 範子「パーキンソン病関連分子DJ-1のオートファジーを介した細胞外分泌」第37回日本分子生物学会, Yokohama, 25 November, 2014
- 47) 小谷 理奈, 浦野 泰臣, 杉本 八郎, 野口 範子「Amyloid β 産生抑制効果を有するクルクミン誘導体の作用機序の解明」第37回日本分子生物学会, Yokohama, 27 November, 2014
- 48) 西郷和真, 斎藤芳郎, 小川郁子, 細井幸恵, 三井良之, 花田一志, 上田昌美, 石井一成, 野口範子, 楠進「PD の診断マーカーである血中 oxDJ-1 の異常高値を示した DLB の 4 例」第 33 回日本認知症学会, Yokohama, 1 December, 2014
- 49) 山田幸子, 浦野泰臣, 野口範子「Amyloid β peptide 産生に対するビタミン E の影響」第 26 回ビタミン E 研究会, Tokyo, 9 January, 2015

- 50) 三田雄一郎, 斎藤芳郎, 野口範子 「セレノプロテイン P の発現・分泌に与える過酸化水素および抗酸化物質の影響」 第 26 回ビタミン E 研究会、Tokyo、9 January 2015
- 51) 斎藤芳郎, 七里元督, 濱島崇, 萩原義之, 吉田康一, 野口範子 「セレン含有タンパク質が低下したSBP2変異患者におけるビタミンEの投与および投与中止に伴う変化」第26回ビタミン E 研究会,Tokyo,10 January, 2015
- 52) 稲荷尚吾, 高部稚子, 三田雄一郎, 御簾博文, 篁 俊成, 野口範子, 斎藤芳郎 血漿セレン含有タンパク質 Selenoprotein P による膵臓 β 細胞障害のメカニズム解析 第 62 回日本生化学会近畿支部例会, 16 May 2015
- 53) 斎藤芳郎, 七里元督, 濱島 崇, 萩原義久, 吉田康一, 野口範子 SBP2 変異によるセレン含有タンパク質欠乏患者におけるコレステロールの酸化—細胞膜と血漿リポタンパク質の酸化反応の違い 第 57 回日本脂質生化学会, 28 May 2015
- 54) 三田雄一郎, 岩崎安紗, 樫 拓磨, 片岡佑斗, 斎藤芳郎, 野口範子 各臓器における酸化 DJ-1 の分布と加齢に伴う変化 第 68 回日本酸化ストレス学会, 11 June, 2015
- 55) 斎藤芳郎「パーキンソン病関連分子DJ-1のシステイン酸化体の検出法開発から早期診断への応用展開」第15回日本蛋白質科学会,Tokushima, 14 June, 2015
- 56) 斎藤芳郎「血漿セレン含有タンパク質セレノプロテインPのレドックス制御機能—2型糖尿病の治療標的として」第10回レドックス170委員会, Tsuruoka, 20 August, 2015
- 57) 野口範子, 細胞死と抗酸化—ビタミンEの役割は—, Vitamin E update forum, Aug. 28, 2015
- 58) 野口範子, 新井洋由, 神経細胞死メカニズムの違いとビタミンEの作用特異性について, 脂溶性ビタミン総合研究委員会, Sep. 18, 2015.
- 59) Noriko Noguchi, Khanh Vo-Diep, Wakako Takabe, Yasuomi Urano, Yoshiro Saito, Two different ways for neuronal cell death induced by 24(S)-hydroxycholesterol. European Network Oxysterol Res., Sep 25, 2015.
- 60) Yoshiro Saito, Yuichiro Mita, Kojiro Hayashi, Takuma Kashi, Yuto Kataoka, Asa Iwasaki, and Noriko Noguchi Distribution of oxidized DJ-1 in human and mouse brain- Effects of aging process SFRBM's 22th Annual Meeting, Boston USA, 20 November 2015.
- 61) Vo DK, Urano Y., Takabe W., Saito Y., Noguchi N. 24(S)-Hydroxycholesterol Induces RIPK1-Dependent But MLKL-Independent Cell Death in the Absence of Caspase-8. SFRBM2015, Nov. 20, 2015
- 62) 樫 拓磨, 片岡佑斗, 林 宏次郎, 三田雄一郎, 斎藤芳郎, 野口範子 パーキンソン病モデルマウス脳内における酸化 DJ-1 の分布 第 88 回日本生化学会・第 38 回日本分子生物学会年会 合同年会 (BMB2015) , Kobe, 1 December 2015

- 63) 三田雄一郎, 岩崎安紗, 樫 拓磨, 片岡佑斗, 斎藤芳郎, 野口範子 パーキンソン病関連分子 DJ-1 の酸化レベルは加齢に伴い変化する 第 88 回日本生化学会・第 38 回日本分子生物学会年会 合同年会 (BMB2015) , Kobe, 1 December 2015
- 64) 東浦涼, 浦野泰臣, 野口範子, 杉本八郎, Amyloid β 産生抑制効果を有するクルクミン誘導体の作用機序の解明、BMB2015、Dec. 1, 2015
- 65) 中澤孝哉, 浦野泰臣, 西川喜代孝, 野口範子, 24S-hydroxycholesterol 誘導性神経細胞死への CaMKII の関与, BMB2015, Dec. 2, 2015
- 66) 今野敬斗, 浦野泰臣, 藤綾乃, 斎藤芳郎, 野口範子, パーキンソン病関連タンパク質 DJ-1 の細胞外分泌メカニズムの解析, BMB2015, Dec. 2, 2015
- 67) 宮軒勇太, 浦野泰臣, 野口範子, 24S-Hydroxycholesterol により誘導される necroptosis 様細胞死機構の解析、BMB2015、Dec. 3, 2015
- 68) 稲荷尚吾, 高部稚子, 三田雄一郎, 御簾博文, 篁 俊成, 野口範子, 斎藤芳郎 膝 β 細胞モデル MIN6 は過剰な Selenoprotein P により障害を受ける 第 88 回日本生化学会・第 38 回日本分子生物学会年会 合同年会 (BMB2015) , Kobe, 3 December 2015
- 69) 斎藤芳郎, 稲荷尚吾, 三田雄一郎, 高部稚子, 御簾博文, 篁俊成, 野口範子 セレノプロテイン P による膝 β 細胞死に対するビタミン E の効果 第 27 回ビタミン E 研究会, Takamatsu, 9 January 2016
- 70) 宮軒勇太, 中澤孝哉, 上原まどか, 浦野泰臣, 斎藤芳郎, 野口範子 24S-Hydroxycholesterol 誘導性神経細胞死に対するビタミン E の抑制効果 第 27 回ビタミン E 研究会, Takamatsu, 8 January 2016
- 71) Shibata N, Niida-Kawaguchi M, Inose Y, Muramatsu F, Kato Y, Yamamoto T, Sawada T: Glutamate stimulates motor neurons to form intracellular p-TDP-43 aggregates. /In: The 25th International Symposium on ALS/MND/ (シンポジウム C13; 2014 年 12 月 5 日; Brussels, Belgium).
- 72) Shibata N, Inose Y, Niida-Kawaguchi M, Toi S, Kakita A, Takahashi H: Upregulation of xCT in spinal cords from sporadic ALS patients. /In: The 18th International Congress of Neuropathology/ (示説 P154-03; 2014 年 9 月 15 日, Rio de Janeiro, Brazil).
- 73) 柴田亮行, 佐久間美帆, 増井憲太, 猪瀬悠理, 新井田素子, 加藤陽一郎, 柿田明美, 野口範子. ミクログリアは可溶鉄刺激によりグルタミン酸を放出する. 第 57 回日本神経病理学会総会学術研究会, 弘前, 2016 年 6 月 3 日.
- 74) 柴田亮行, 新井田素子, 猪瀬悠理, 廣井敦子, 山本智子, 加藤陽一郎, 山本智子. ALS 脊髄における細胞外グルタミン酸濃度の p-TDP-43 凝集体形成との関連. 第 56 回日本神経病理学会総会学術研究会, 福岡 2015 年 6 月 4 日.

特許出願：

- 1) 田中睦、斎藤芳郎「被測定物質の分別測定方法」 特願2012-198464、2012/09/10
- 2) 浦野泰臣、野口範子、斎藤芳郎、山中一哲「細胞死抑制剤」特願2012-242950、2012/11/02
- 3) 斎藤芳郎、吉岡佑弥、中山華穂、西藤有希奈、三田雄一郎、野口範子「2型糖尿病の治療及び予防薬」 特願2013-175612、2013/08/27、優先権主張出願：特願2014-165695、2014/08/18
- 4) 御簾博文、金子周一、竹下有美枝、篁俊成、田中睦、斎藤芳郎「2型糖尿病患者の治療薬選択の補助方法、治療薬の効果予測方法及び検査方法」 特願2014-184499、2014/9/10、特許第5885158号、2016/02/19
- 5) 斎藤芳郎、野口範子、浜窪隆雄、岩成宏子、二木鋭雄、吉田康一、新井修一「含硫アミノ酸を含むポリペプチドに対する抗体」 特願2012-028138、2012/02/13
- 6) 浦野泰臣、野口範子、北岸宏亮、高部稚子、丹野将貴、渋谷公幸、三宅祥元、「ヒドロキシコレステロール脂肪酸エステルの検出方法」特願2015-186371、2015/9/24

受賞

- 1) 中山華穂、日本薬学会第134年会、Kumamoto, 30 March, 2014「優秀発表賞」
- 2) Diep-Khanh Ho Vo, 17th Biennial Meeting of Society for Free Radical Research International, 「Young Investigator Award」
- 3) 小林 茉佑香、斎藤 芳郎、菊池 愛、村松 香奈、野口範子 「パーキンソン病関連タンパク質DJ-1の酸化による高分子化に関する研究」第67回日本酸化ストレス学会、Kyoto, 4 September, 「優秀演題賞」
- 4) 稲荷尚吾 優秀発表賞 第62回日本生化学会近畿支部例会 (16 May, 2015)
- 5) 稲荷尚吾 若手優秀発表賞 第38回日本分子生物学会・第88回日本生化学会合同学会 BMB2015 (3 December, 2015)
- 6) Diep-Khanh Ho Vo, Yasuomi Urano, Wakako Takabe, and Noriko Noguchi, Young investigator award, The Society for Redox Biology and Medicine's 22nd Annual Meeting, SFRBM 2015 (21 Nov, 2015)
- 7) Shogo Inari, Yuichiro Mita, Wakako Takabe, Noriko Noguchi, Yoshiro Saito, Young investigator award, The Society for Redox Biology and Medicine's 23rd Annual Meeting, SFRBM 2016 (20 Nov, 2016)
- 8) 猪瀬悠理 2015年度日本脳卒中学会賞

Induction of apoptosis and necroptosis by 24(S)-hydroxycholesterol is dependent on activity of acyl-CoA:cholesterol acyltransferase 1

K Yamanaka¹, Y Urano^{*1}, W Takabe¹, Y Saito¹ and N Noguchi^{*1}

24(S)-hydroxycholesterol (24S-OHC), which is enzymatically produced in the brain, has an important role in maintaining brain cholesterol homeostasis. We have previously reported that 24S-OHC induces necroptosis in human neuroblastoma SH-SY5Y cells. In the present study, we investigated the mechanisms by which 24S-OHC-induced cell death occurs. We found that lipid droplets formed at the early stages in the treatment of SH-SY5Y cells with 24S-OHC. These lipid droplets could be almost completely eliminated by treatment with a specific inhibitor or by siRNA knockdown of acyl-CoA:cholesterol acyltransferase 1 (ACAT1). In association with disappearance of lipid droplets, cell viability was recovered by treatment with the inhibitor or siRNA for ACAT1. Using gas chromatography–mass spectrometry, we confirmed that 24S-OHC-treated cells exhibited accumulation of 24S-OHC esters but not of cholesteryl esters and confirmed that accumulation of 24S-OHC esters was reduced when ACAT1 was inhibited. 24S-OHC induced apoptosis in T-lymphoma Jurkat cells, which endogenously expressed caspase-8, but did not induce apoptosis in SH-SY5Y cells, which expressed no caspase-8. In Jurkat cells treated with the pan-caspase inhibitor ZVAD and in caspase-8-deficient Jurkat cells, 24S-OHC was found to induce caspase-independent cell death, and this was partially but significantly inhibited by Necrostatin-1. Similarly, knockdown of receptor-interacting protein kinase 3, which is one of the essential kinases for necroptosis, significantly suppressed 24S-OHC-induced cell death in Jurkat cells treated with ZVAD. These results suggest that 24S-OHC can induce apoptosis or necroptosis, which of the two is induced being determined by caspase activity. Regardless of the presence or absence of ZVAD, 24S-OHC treatment induced the formation of lipid droplets and cell death in Jurkat cells, and this was suppressed by treatment with ACAT1 inhibitor. Collectively, these results suggest that it is ACAT1-catalyzed 24S-OHC esterification and the resulting lipid droplet formation that is the initial key event which is responsible for 24S-OHC-induced cell death.

Cell Death and Disease (2014) 5, e990; doi:10.1038/cddis.2013.524; published online 9 January 2014

Subject Category: Neuroscience

Cell death has traditionally been classified as being either apoptosis or necrosis, description in textbooks implying that these involve opposed mechanisms. Although necrosis has generally been considered to be cell death that is accidental and passive, there is growing evidence that some necrosis is in fact programmed cell death,^{1,2} the term 'necroptosis'.³ Necroptosis is involved in many physiological and pathological processes, such as viral infection,⁴ neuronal excitotoxicity,⁵ and ischemic injury.^{3,6} Necroptosis is defined as cell death that is necrosis-like, caspase-independent, and mediated through a pathway depending on the receptor-interacting protein kinase 1 (RIPK1)–RIPK3 complex. Necroptosis is further defined as being inhibited by Necrostatin-1 (Nec-1), a specific inhibitor of RIPK1 kinase activity.³ Interestingly, necroptosis can be induced by apoptosis-inducing ligands such as Fas ligand or tumor necrosis factor α (TNF α). These ligands usually bind with so-called death receptors

(such as Fas or TNF receptor), resulting in activation of apoptotic machineries. Conversely, it has been found that in some cell lines the presence of caspase inhibitor blocks apoptosis and unveils caspase-independent necroptosis.^{7,8} Activation of death receptor can therefore result in either apoptosis or necroptosis, caspase-8 being known to act in a key role for determining which form of cell death will occur.⁹

We have previously reported that high concentrations of 24(S)-hydroxycholesterol (24S-OHC) induce necroptosis in neuronal cells.¹⁰ As the blood–brain barrier prevents cholesterol translocation between the brain and the circulation, brain cholesterol is locally synthesized, and its levels are not affected by dietary cholesterol.¹¹ To maintain a steady-state level of cholesterol in the brain, the neuronal enzyme cholesterol 24-hydroxylase (CYP46A1) converts excess amounts of cholesterol into 24S-OHC, which readily crosses

¹Department of Medical Life Systems, Faculty of Life and Medical Sciences, Doshisha University, Kyoto, Japan

*Corresponding authors: Y Urano or N Noguchi, Department of Medical Life Systems, Faculty of Life and Medical Sciences, Doshisha University, 1-3 Miyakodani, Tatara, Kyotanabe, Kyoto 610-0394, Japan. Tel: +81 774 65-6260; Fax: +81 774 65 6262; E-mail: yurano@mail.doshisha.ac.jp or nnoguchi@mail.doshisha.ac.jp

Keywords: 24S-hydroxycholesterol; apoptosis; necroptosis; acyl-CoA:cholesterol acyltransferase; lipid droplets

Abbreviations: ACAT, acyl-CoA:cholesterol acyltransferase; AD, Alzheimer's disease; CHX, cycloheximide; CYP46A1, cholesterol 24-hydroxylase; GC–MS, gas chromatography–mass spectrometry; HPLC, high-performance liquid chromatography; LDH, lactate dehydrogenase; Nec-1, Necrostatin-1; RIPK, receptor-interacting protein kinase; TNF α , tumor necrosis factor α ; ZVAD, ZVAD-fmk; 24S-OHC, 24(S)-hydroxycholesterol

Received 19.8.13; revised 18.11.13; accepted 25.11.13; Edited by E Baehrecke

the blood–brain barrier.¹² It has been reported that free 24S-OHC is present at concentrations of up to 30 μ M in the human brain.¹³ Several lines of evidence suggest that 24S-OHC is linked to the development of Alzheimer's disease (AD).^{14,15} Higher concentrations of 24S-OHC have been detected in plasma and cerebrospinal fluid of patients with AD or mild cognitive impairment than is present in healthy subjects.^{16,17} Selective expression of CYP46A1 around neuritic plaques has also been reported.¹⁸ Furthermore, as 24S-OHC has been shown to possess potent neurotoxicity, it is presumed to be involved in the etiology of neurodegenerative disease.¹⁹ We have shown that 24S-OHC induces cell death in human neuroblastoma SH-SY5Y cells and rat primary cortical neuronal cells without any of the features typical of apoptosis.¹⁰ Instead, we found that Nec-1 or siRNA knockdown of RIPK1 significantly suppressed 24S-OHC-induced cell death, demonstrating that necroptosis may account for 24S-OHC-induced neuronal cell death. We further showed in our previous study that the neuronal cells used in that study did not express caspase-8, suggesting that 24S-OHC induces necroptosis specifically in neuronal cells because of the absence of caspase-8; however, the molecular mechanisms responsible for induction of cell death still remained unclear.

In the present study, we used not only SH-SY5Y cells but also human T lymphoma Jurkat cells to further investigate the mechanisms responsible for 24S-OHC-induced cell death. We found that cytosolic lipid droplets formed in the early stages in cells treated with 24S-OHC. Lipid droplets are unique intracellular organelles that store neutral lipids for membrane synthesis and energy supply.²⁰ As accumulation of free cholesterol can be toxic to cells, free cholesterol is converted to cholesteryl esters, which mainly exist as lipid droplets.²¹ Acyl-CoA:cholesterol acyltransferase (ACAT) catalyzes the esterification of free cholesterol to cholesteryl esters in the endoplasmic reticulum.²² Two ACAT isoenzymes, ACAT1 and ACAT2 have been identified. ACAT1 is the main isoenzyme in the brain.^{22,23} Here, we demonstrate that the esterified form of 24S-OHC is accumulated in 24S-OHC-treated cells. We also found that 24S-OHC induced either apoptosis or necroptosis, which of the two was induced being determined by caspase activity. We conclude that ACAT1-mediated esterification of 24S-OHC and formation of lipid droplets have important roles in 24S-OHC-induced apoptosis and necroptosis.

Results

Lipid droplet formation mediated by ACAT activity was involved in 24S-OHC-induced cell death in SH-SY5Y cells. Following exposure of SH-SY5Y cells to 24S-OHC for about 6 h, it was noted during monitoring of cell morphology that lipid droplet-like structures had formed. We therefore used the fluorescent probe Nile red²⁴ to examine whether these structures were neutral lipid-enriched droplets. Cells treated with 24S-OHC for 6 h had cytoplasmic structures that stained positive with Nile red, suggesting that 24S-OHC treatment had induced formation of droplets enriched with neutral lipids (Figure 1a upper panel). Pretreatment of cells with F12511, an inhibitor of both ACAT1 and ACAT2,²⁵

suppressed 24S-OHC-induced lipid droplet formation (Figure 1a lower panel). To evaluate whether 24S-OHC-induced lipid droplet formation was correlated with cell death, we examined the effect of F12511 on 24S-OHC-induced cell death by lactate dehydrogenase (LDH) activity assay. The results showed that F12511 almost completely suppressed 24S-OHC-induced cell death (Figure 1b).

Selective inhibitor or siRNA knockdown of ACAT1 suppressed 24S-OHC-induced cell death in SH-SY5Y cells.

As it has been reported that ACAT1 is the main isoenzyme in the brain, and real-time PCR analysis revealed that *ACAT1* mRNA but not *ACAT2* mRNA was expressed in SH-SY5Y cells (Supplementary Figure S1), we tested the effects of the selective ACAT1 inhibitor K-604²⁶ on 24S-OHC-induced lipid droplet formation and cell death. Nile red staining showed that, as was the case with F12511, K-604 suppressed formation of lipid droplets in cells treated with 24S-OHC for 6 h (Figure 1c). K-604 also suppressed 24S-OHC-induced cell death (Figure 1d). Furthermore, we performed siRNA knockdown of ACAT1 in SH-SY5Y cells and confirmed a marked decline in constitutive ACAT1 protein levels (Figures 2a and b). Under these conditions, 24S-OHC-induced lipid droplet formation was suppressed (Figure 2c) and 24S-OHC-induced cell death was significantly inhibited, similar to that which was observed with F12511 treatment (Figure 2d). Taken together, these results suggest that ACAT1 is involved in neuronal cell death induced by 24S-OHC.

The esterified form of 24S-OHC accumulated in 24S-OHC-treated SH-SY5Y cells.

As lipid droplet formation was involved in 24S-OHC-induced cell death, we analyzed lipid components by using gas chromatography–mass spectrometry (GC–MS) in SH-SY5Y cells treated with 24S-OHC for 6 h. A saponification step was used to remove fatty acids from sterol esters and derivatize sterol molecules for detection by GC–MS. Free cholesterol (before saponification) and total cholesterol (after saponification) were both measured, the difference between these values being taken to be the amount of cholesteryl esters. The same measurement was performed for 24S-OHC and for 24S-OHC esters. The results showed that neither cholesterol content nor cholesteryl ester content was affected by 24S-OHC treatment (Figure 3a). 24S-OHC was not detected in control cells, and accumulation of 24S-OHC and 24S-OHC esters was observed in 24S-OHC-treated cells (Figure 3b), it being possible to prevent this accumulation of 24S-OHC esters by treatment with F12511 (Figure 3b). In SH-SY5Y cells transfected with ACAT1 siRNA, cholesterol levels remained unaffected (Supplementary Figure S2A), but the production of 24S-OHC esters was inhibited (Supplementary Figure S2B). Together, these data indicate that ACAT1 esterified 24S-OHC but not cholesterol and that this caused formation of lipid droplets in 24S-OHC-treated SH-SY5Y cells.

To further confirm the production of the esterified form of 24S-OHC, cell samples without saponification were analyzed by reverse-phase high-performance liquid chromatography (HPLC). As compared with the vehicle control condition (Figure 4a), significant increase was observed at four peaks

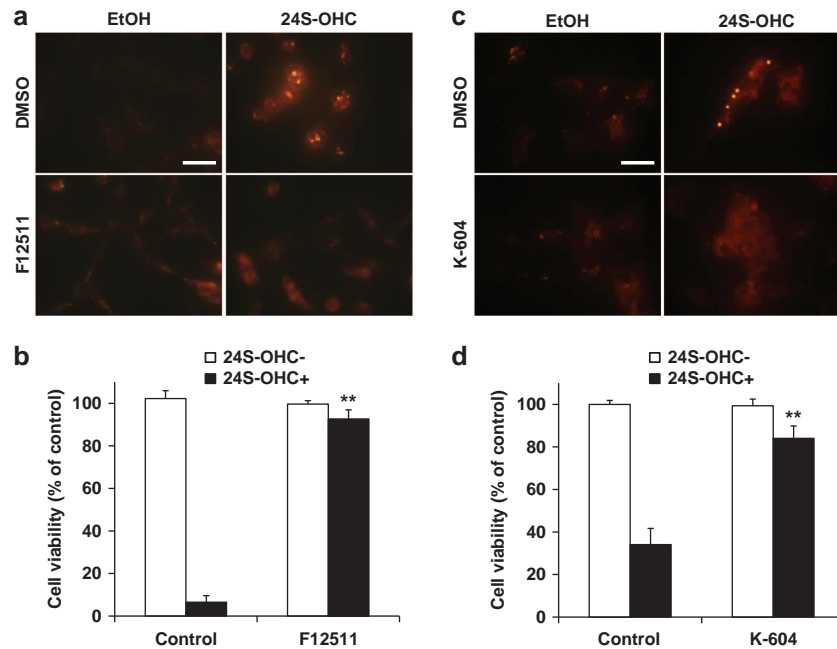


Figure 1 Lipid droplet formation by ACAT1 is involved in SH-SY5Y cell death induced by 24S-OHC. (a and b) SH-SY5Y cells were pretreated with or without 5 μ M F12511 for 15 min and were then treated with 50 μ M 24S-OHC for 6 h (a) or 24 h (b). (a) Cells were subjected to Nile red staining. Representative images are shown. Bar, 20 μ m. (b) Cell viability was measured by LDH activity assay. (c and d) SH-SY5Y cells were pretreated with or without 2 μ M K-604 for 15 min and were then treated with 50 μ M 24S-OHC for 6 h (c) or 24 h (d). (c) Cells were stained with Nile red. Representative images are shown. Bar, 20 μ m. (d) Cell viability was measured by LDH activity assay. ** $P < 0.01$, when compared with cells treated with 24S-OHC alone

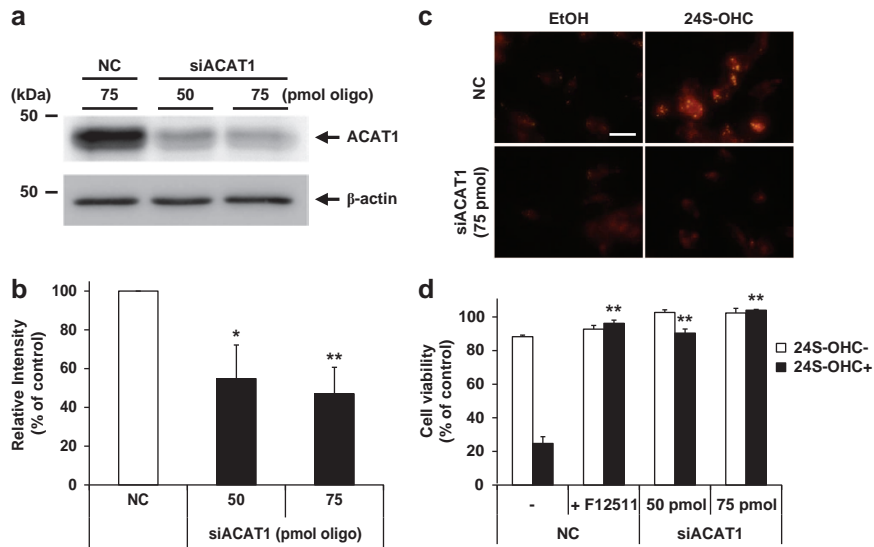


Figure 2 Knockdown of ACAT1 suppressed 24S-OHC-induced cell death in SH-SY5Y cells. (a and b) SH-SY5Y cells were transfected with ACAT1 (siACAT1) or negative control (NC) siRNA oligo for 48 h. (a) Whole cell lysates were immunoblotted with appropriate antibodies as indicated. (b) Relative expression levels of ACAT1 are shown. * $P < 0.05$, ** $P < 0.01$ versus NC siRNA. (c and d) The cells were challenged with 50 μ M 24S-OHC for 6 h (c) or 24 h (d). (c) Cells were stained with Nile red. Representative images are shown. Bar, 20 μ m. (d) Cell viability was measured by LDH activity assay. ** $P < 0.01$, when compared with NC siRNA + 24S-OHC

for 24S-OHC-treated cells (Figure 4b). These four peaks disappeared when cells were co-treated with 24S-OHC and F12511 (Figure 4c). During this HPLC analysis, free 24S-OHC and free cholesterol were detected at 2.5 and 4 min, respectively, and cholesteryl esters were detected at retention times > 45 min (data not shown). We then collected these four

unidentified peaks as four fractions and analyzed by GC-MS with or without saponification. The results show that all four fractions contained the esterified form of 24S-OHC (Figure 4d) but not cholesterol (Figure 4e). Collectively, these results suggest that 24S-OHC treatment induced accumulation of various kinds of 24S-OHC esters but not of cholesteryl esters.

24S-OHC induced necroptosis in caspase-inhibited Jurkat cells. To investigate the effects of caspase-8 expression on induction of cell death by 24S-OHC, we used

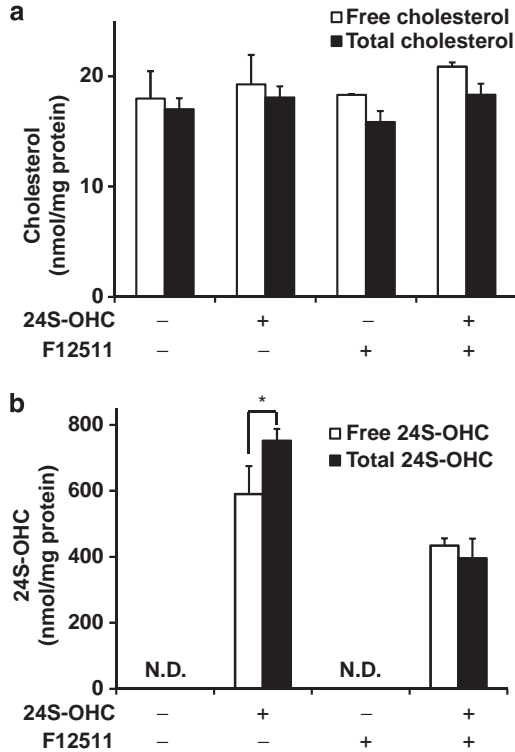


Figure 3 24S-OHC treatment induced formation of esterified 24S-OHC but not of cholesterol. (a and b) SH-SY5Y cells were pretreated with and without 5 μ M F12511 for 15 min and were then treated with 50 μ M 24S-OHC for 6 h. The cells were subjected to lipid extraction and measurement of cholesterol (a) and 24S-OHC (b) by using GC-MS. N.D., not detected. * $P < 0.05$

human T lymphoma Jurkat cells that endogenously expressed caspase-8. We first examined the effect of the pan-caspase inhibitor ZVAD-fmk (ZVAD) on 24S-OHC-induced cell death in Jurkat cells. Jurkat cells were treated with 24S-OHC in the presence or absence of ZVAD for 24 h. Cell viability was measured by WST-8 assay. 24S-OHC treatment significantly decreased cell viability regardless of whether ZVAD was present (Figure 5a). We also used immunoblotting to evaluate the activation of caspase-8 and caspase-3 in cells treated with 24S-OHC for 6 h. The results show that cleaved forms of caspase-8 and caspase-3 were observed in cells treated with 24S-OHC alone (Figure 5b), indicating that 24S-OHC induced apoptosis in Jurkat cells. Interestingly, activation of caspase-8 and caspase-3 was inhibited by ZVAD (Figure 5b), but ZVAD treatment did not exhibit any protective effect on 24S-OHC-induced cell death (Figure 5a). In control experiments, TNF α and cycloheximide (CHX) induced activation of caspase-8 and caspase-3 in Jurkat cells (data not shown), and activation of each was inhibited by ZVAD (Figure 5b). As active caspase-8 has been demonstrated to cleave and inactivate RIPK1, thereby regulating initiation of necroptosis,² we examined the expression level of RIPK1. As expected, 24S-OHC treatment reduced RIPK1 protein levels, this reduction being suppressed by co-treatment with ZVAD (Figure 5b). These results suggest that in the presence of ZVAD 24S-OHC induces caspase-independent cell death in Jurkat cells. To evaluate whether necroptosis accounts for the caspase-independent cell death induced by 24S-OHC, we examined the effect of the specific necroptosis inhibitor Nec-1 on cell death induced by 24S-OHC in the presence of ZVAD. The results showed that Nec-1 significantly suppressed cell death induced by 24S-OHC in the presence of ZVAD (Figure 5c). We further examined the role of caspase-8 in 24S-OHC-induced cell death using caspase-8-deficient Jurkat cells. 24S-OHC treatment significantly decreased cell viability

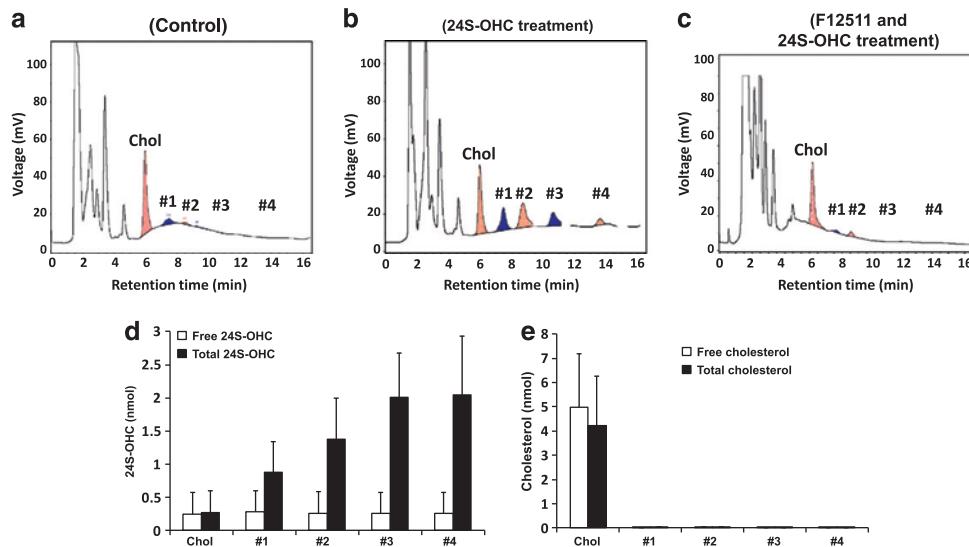


Figure 4 Various kinds of 24S-OHC esters accumulated in 24S-OHC-treated SH-SY5Y cells. SH-SY5Y cells were treated with (a) vehicle or (b, d and e) 50 μ M 24S-OHC or (c) 50 μ M 24S-OHC + 5 μ M F12511 for 6 h as in Figure 1. (a-c) Lipid extracts were subjected to HPLC analysis. (d and e) The fractions collected by HPLC from panel (b) were further subjected to GC-MS analysis with or without saponification to measure 24S-OHC (d) or cholesterol (e) content

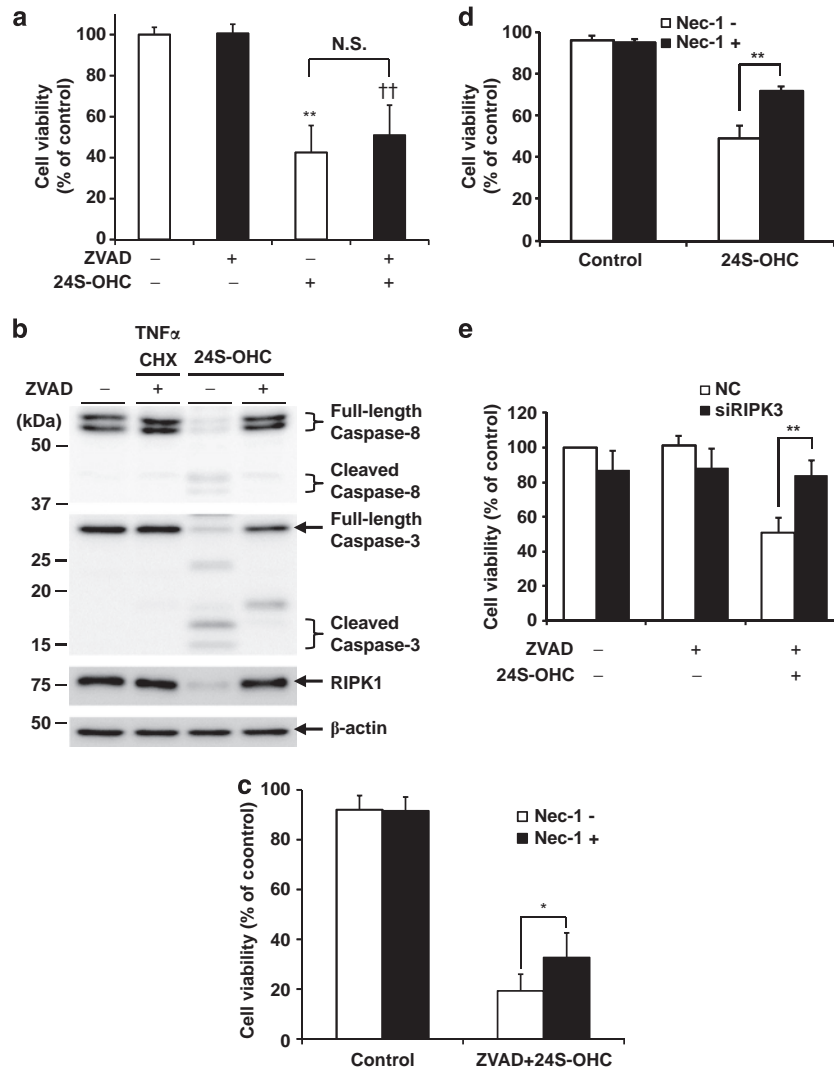


Figure 5 24S-OHC induced apoptosis and necroptosis in Jurkat cells. (a) Jurkat cells were pretreated with 20 μ M ZVAD for 1 h and were then treated with 50 μ M 24S-OHC for 24 h. Cell viability was measured by WST-8 assay. N.S., not significant. $**P < 0.01$, when compared with cells without ZVAD and 24S-OHC; $††P < 0.01$, when compared with ZVAD-treated cells. (b) Jurkat cells were pretreated with 20 μ M ZVAD for 1 h and were then incubated with 50 μ M 24S-OHC for 6 h. As a control, cells were treated with 100 ng/ml CHX and 100 μ g/ml TNF α . Whole cell lysates were immunoblotted with appropriate antibodies as indicated. (c) Jurkat cells were pretreated with 20 μ M ZVAD and 100 μ M Nec-1 for 1 h and were then treated with 50 μ M 24S-OHC for 16 h. Cell viability was measured by flow cytometry using propidium iodide. $*P < 0.05$. (d) Caspase-8-deficient Jurkat cells were pretreated with 100 μ M Nec-1 for 1 h and were then treated with 50 μ M 24S-OHC for 16 h. Cell viability was measured by flow cytometry using propidium iodide. $**P < 0.01$. (e) Jurkat cells were transfected with RIPK3 (siRIPK3) or negative control (NC) siRNA oligo for 72 h. The cells were pretreated with 20 μ M ZVAD for 1 h and were then treated with 50 μ M 24S-OHC for 24 h. Cell viability was measured by WST-8 assay. $**P < 0.01$ when compared with NC siRNA + 24S-OHC + ZVAD

(Figure 5d), and this decrease in viability was significantly suppressed by Nec-1, suggesting that 24S-OHC induced necroptosis in caspase-8-deficient Jurkat cells. To further confirm the involvement of necroptosis in 24S-OHC-induced cell death, we evaluated the effect of RIPK3 knockdown in Jurkat cells. In the presence of ZVAD, RIPK3 siRNA significantly suppressed cell death induced by 24S-OHC (Figure 5e). Together, these results indicate that 24S-OHC induces either apoptosis or necroptosis in Jurkat cells, which of the two forms of cell death is induced being dependent on caspase activities, especially caspase-8 activity.

Lipid droplet formation mediated by ACAT1 activity was involved in 24S-OHC-induced apoptosis and necroptosis in Jurkat cells. To investigate whether ACAT1 is involved in

24S-OHC-induced apoptosis and necroptosis, we carried out a series of experiments on Jurkat cells in the presence and absence of ZVAD. Real-time PCR analysis revealed that *ACAT1* mRNA but not *ACAT2* mRNA was expressed in Jurkat cells as well as in SH-SY5Y cells (Supplementary Figure S1), suggesting that ACAT1 is the main isoenzyme in Jurkat cells. Nile red staining showed that in the absence of ZVAD 24S-OHC treatment induced the formation of lipid droplets (Figure 6a). It was further observed that formation of these Nile red-positive lipid droplets could be reduced by treatment with K-604 (Figure 6a) or F12511 (Supplementary Figure S3A). We next evaluated whether 24S-OHC-induced lipid droplet formation was observed under necroptosis-inducing condition (ZVAD+). The results showed that 24S-OHC treatment induced lipid droplet formation and that

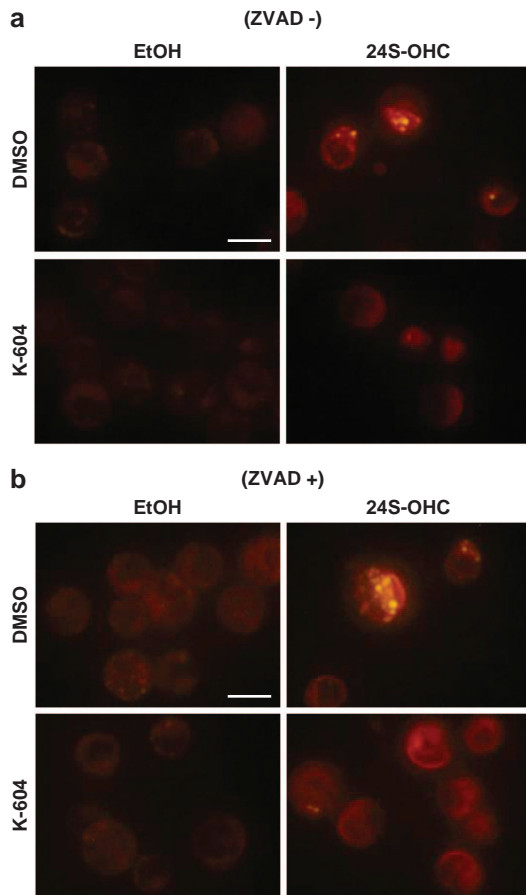


Figure 6 24S-OHC induced lipid droplet formation in Jurkat cells treated with or without ZVAD. (a and b) Jurkat cells were pretreated with or without 2 μ M K-604 for 15 min and were then treated with 50 μ M 24S-OHC for 6 h in the absence (a) or presence (b) of ZVAD. Cells were stained with Nile red. Representative images are shown. Bar, 20 μ m

this could be suppressed by inhibition of ACAT1 activity (Figure 6b and Supplementary Figure S3B). These results revealed that, regardless of the presence or absence of ZVAD, 24S-OHC treatment induces ACAT1-mediated esterification of sterols and lipid droplet formation in Jurkat cells.

We then evaluated the effect of ACAT inhibitor on 24S-OHC-induced cell death in Jurkat cells. Under both apoptosis-inducing condition (ZVAD $-$) and necroptosis-inducing condition (ZVAD $+$), F12511 inhibited 24S-OHC-induced cell death (Figure 7a). The selective ACAT1 inhibitor K-604 also suppressed both types of cell death (Figure 7b). These results suggest that ACAT1-mediated lipid droplet formation is a common early-stage event that occurs in 24S-OHC-induced cell death regardless of whether that cell death is caspase dependent or caspase independent.

Discussion

Lipid droplets have significant biological roles in many cell types.²⁰ Their hydrophobic cores store neutral lipids such as triglyceride and cholesteryl esters for supplying metabolic energy and membrane components. Lipid droplets also serve

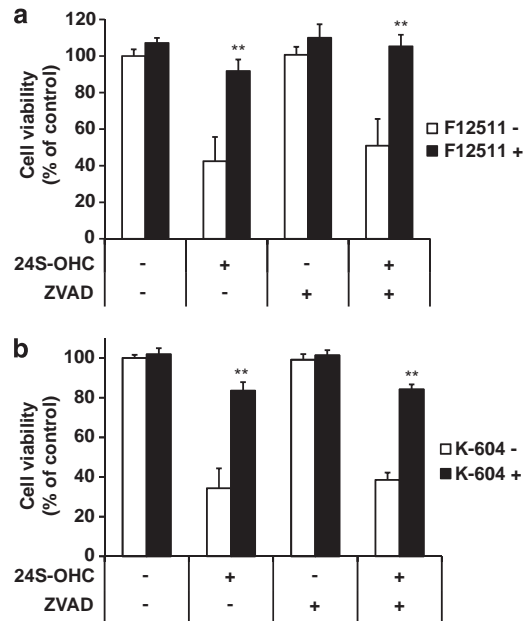


Figure 7 ACAT inhibitor suppressed 24S-OHC-induced cell death in Jurkat cells treated with or without ZVAD. (a and b) Jurkat cells were pretreated with or without 5 μ M F12511 (a) or 2 μ M K-604 (b) for 15 min and were then treated with 50 μ M 24S-OHC for 24 h in the absence or presence of ZVAD. Cell viability was measured by WST-8 assay. ** $P < 0.01$, when compared with the cells treated with 24S-OHC in the absence of ACAT inhibitor

in protein storage and degradation. It had generally been thought that ACAT-mediated esterification of cholesterol with fatty acid results in the formation of cholesteryl ester-enriched lipid droplets, which serve in a protective role by preventing cytotoxic accumulation of free cholesterol.²¹ It has been reported that an unsaturated fatty acid, oleic acid, promotes the formation of triglyceride-enriched lipid droplets while barely inducing apoptosis; and that a saturated fatty acid, palmitic acid, poorly forms lipid droplets while significantly inducing apoptosis.²⁷ Contrary to such conventional findings, our present data showed that formation of lipid droplets upon 24S-OHC treatment correlates with induction of cell death. Although it was not clear in the present study whether the esterified form of 24S-OHC itself was cytotoxic or whether it was the formation of lipid droplets that triggered cell death signaling, we showed that esterification of 24S-OHC by action of ACAT1 was definitely responsible for initiating cell death signaling. It is possible to hypothesize that certain proteins which suppress cell death, for example, cellular FLICE inhibitory protein²⁸ or cellular inhibitor of apoptosis,²⁹ might collect within lipid droplets. It is also possible that lipid droplets may provide an intracellular platform permitting association of certain proteins that promote cell death signaling.

Interestingly, employment of inhibitor or siRNA knockdown of ACAT1 almost completely inhibited the cytotoxic effects of 24S-OHC in both SH-SY5Y and Jurkat cells. ACAT1 esterifies various oxysterols such as 7-ketocholesterol and 25-OHC.^{30,31} It is therefore plausible that 24S-OHC might also be available as a substrate for ACAT1. Indeed, GC-MS analysis revealed that there was accumulation of 24S-OHC esters but not cholesteryl esters in 24S-OHC-treated cells.

In macrophages, ACAT promotes 7-ketocholesterol-induced caspase-3-dependent apoptosis via accumulation of 7-ketocholesterol esters.³² In mast cells, ACAT is implicated in 24(S),25-epoxycholesterol-induced apoptosis.³³ In contrast, a plant sitosterol, which was poorly esterified by ACAT, was found to trigger caspase-independent necroptosis in macrophages.³⁴ We have previously shown that 7-ketocholesterol, 7 α -OHC, 7 β -OHC, and 22R-OHC induce SH-SY5Y cell death and that this was not prevented by Nec-1.¹⁰ In the present study, we further examined whether ACAT1 was involved in cell death induced by these oxysterols, as a result of which we found that Nile red staining showed that these oxysterols did not induce lipid droplet formation (Supplementary Figure S4A), and we found that ACAT inhibitor did not suppress cell death induced by these oxysterols (Supplementary Figure S4B). Together, the current data suggest that differences in the structures of oxysterols and their esterified forms are important factors for determining the pathway by which cell death occurs. As HPLC analysis showed that at least four kinds of 24S-OHC esters accumulated in 24S-OHC-treated cells, studies to identify which 24S-OHC esters are responsible for the induction of cell death may provide further insight. Because standards for each 24S-OHC ester are not commercially available, further experiments will be required to characterize and quantify the individual 24S-OHC esters. It should be noted that the amount of free 24S-OHC in cells co-treated with 24S-OHC and F12511 was lower than that in cells treated with 24S-OHC alone (Figure 3b). There is a possibility that F12511 may affect influx and/or efflux of 24S-OHC. However, ACAT1 inhibition almost completely inhibited esterification of 24S-OHC, and this was accompanied by a corresponding suppression of 24S-OHC-induced cell death. We therefore concluded that it is the esterification of 24S-OHC by ACAT1 and the resulting lipid droplet formation that triggers cell death signaling. It has been reported that ACAT1 gene ablation or ACAT inhibitor ameliorates amyloid pathology in AD mice.²³ In the light of our present results, it is thought that ACAT1 inhibitors may hold promise for treating neurodegenerative diseases due also to their presumed role in cell death inhibition.

Our results show that in Jurkat cells ACAT inhibition suppressed both 24S-OHC-induced formation of lipid droplets and cell death regardless of whether or not caspase inhibitor was present (Figure 6 and Figure 7). These results suggest that esterification of 24S-OHC is an early-stage event in the cell death machinery and more particularly that it occurs upstream of the switching point for apoptosis and necroptosis. As ACAT1 inhibition also suppresses 24S-OHC-induced lipid droplet formation and cell death in SH-SY5Y cells, we propose that esterification of 24S-OHC by ACAT1 is the common mechanism responsible for 24S-OHC-induced cell death in different cell types. It has been reported that there are two key pathways for apoptosis signaling, one being the extrinsic pathway which is initiated through cell surface death receptors and which results in caspase-8 activation, and the other being the intrinsic pathway which is initiated through a mitochondrion-centered control mechanism.³⁵ Drug-induced caspase-8 activation in death receptor-independent apoptosis has been reported in several types of cells.^{36,37} Our results in Jurkat cells showed that 24S-OHC induced activation of

caspase-8, resulting in activation of apoptotic machineries. The possibility that certain death receptor was involved in 24S-OHC-induced cell death should be addressed in the near future. It has been known that autocrine secretion of death ligands such as TNF α upon stimulation with a cytotoxic compound induces apoptosis.³⁸ We therefore evaluated TNF α secretion from 24S-OHC-treated SH-SY5Y cells and found no secretion of TNF α into the culture medium after 6 and 12 h treatment (data not shown). Further experiments will be required to address whether other ligands might be secreted to stimulate cell death receptors. In the cells treated with caspase inhibitor or in caspase-8-deficient cells, 24S-OHC still caused cell death, and this was partially but significantly inhibited by Nec-1. Furthermore, siRNA for RIPK3 strongly suppressed 24S-OHC-induced cell death. These results suggest that it is mainly necroptosis that is responsible for 24S-OHC-induced cell death in the absence of caspase-8 activity.

Here we have presented a novel mechanism of cell death that includes both apoptosis and necroptosis induced by an oxidation product of cholesterol. The esterification of oxysterol by ACAT1 is a common initial event in both of these cell death modalities. From the clinical viewpoint, it is noteworthy that 24S-OHC is predominantly produced in the brain and may be responsible for neuronal cell death in neurodegenerative diseases. We have therefore provided the basis for potential therapeutic strategies in which ACAT1 inhibitors are used to treat neurodegenerative diseases.

Materials and Methods

Materials. ACAT inhibitor F12511 and anti-ACAT1 antibody (DM102) were the generous gifts of Dr. Ta-Yuan Chang (Dartmouth Medical School, Hanover, NH, USA). ACAT1 inhibitor K-604 was kindly provided by Kowa Company, Ltd (Tokyo, Japan). Dulbecco's modified Eagle's medium/nutrient mixture Ham's F-12 (DMEM/F-12) was obtained from Invitrogen (Carlsbad, CA, USA). RPMI-1640 was obtained from Sigma-Aldrich (St. Louis, MO, USA). Fetal bovine serum was from Hyclone (Thermo Scientific, Logan, UT, USA). 24S-OHC was from Biomol International (Plymouth Meeting, PA, USA), this having been dissolved in ethanol and stored at -20°C . Pan-caspase inhibitor ZVAD was from Medical and Biological Laboratories (Nagoya, Japan). TNF α , CHX, and N,O-bis(trimethylsilyl)-trifluoroacetamide were purchased from Wako (Osaka, Japan). Nec-1 and Nile red were from Sigma-Aldrich, these, respectively, being dissolved in DMSO and stored at -20°C under light-shielded conditions. The following antibodies were from commercial sources: caspase-8 (No. M058-3), Medical and Biological Laboratories; caspase-3 (No. 9662), Cell Signaling (Beverly, MA, USA); RIPK1 (No. 551041), BD Biosciences (San Jose, CA, USA); and β -actin (No. A5441), Sigma. All other chemicals, of analytical grade, were obtained from Sigma-Aldrich or Wako.

Cell lines and cell culture. SH-SY5Y human neuroblastoma cells, Jurkat human T cell leukemia cells, and caspase-8-deficient Jurkat cells (clone I 9.2) were purchased from American Type Culture Collection (Manassas, VA, USA). Cells were routinely maintained in DMEM/F-12 (SH-SY5Y) or RPMI-1640 (Jurkat) medium containing 10% heat-inactivated fetal bovine serum and antibiotics (100 U/ml penicillin, 100 $\mu\text{g}/\text{ml}$ streptomycin; Invitrogen). For treatment, SH-SY5Y cells and Jurkat cells were seeded at a density of 3.0×10^5 cells/ml. Cells were grown at 37°C under an atmosphere of 95% air and 5% CO_2 .

Cell treatment. To examine the toxicity of 24S-OHC in SH-SY5Y cells and Jurkat cells, cells were treated with 50 μM 24S-OHC for the indicated periods. To evaluate the effects of ZVAD or ACAT inhibitor, the cells were pretreated with 20 μM ZVAD for 1 h or with 5 μM F12511 or 2 μM K-604 for 15 min before further treatments.

Determination of cell viability. For determination of cell viability in Jurkat cells, WST-8 assay was performed using Cell Counting Kit-8 according to the

manufacturer's instructions (Dojindo, Kumamoto, Japan). Flow cytometry using propidium iodide staining was conducted as described previously.¹⁰ Briefly, control and treated cells were stained with propidium iodide, followed by analysis using a BD FACSAria™ II cell sorter (Becton, Dickinson and Company, Franklin Lakes, NJ USA) with a 488 nm argon laser. For determination of cell viability in SH-SY5Y cells, LDH activity assay was performed as described previously.³⁹ Data are expressed as percentage of total LDH activity, after subtraction of background determined from the serum medium alone.

Immunoblotting. Whole cell lysates were prepared in lysis buffer (50 mM Tris-HCl, pH 7.4, 150 mM NaCl, 1% Nonidet P-40, 2 mM EDTA) to which protease inhibitor cocktail (nacalai tesque, Kyoto, Japan) had been added. Nuclei and unlysed cellular debris were removed by centrifugation at $16000 \times g$ for 10 min. The protein samples were subjected to SDS-PAGE and immunoblotting by using appropriate antibodies.

Nile red staining. To confirm the presence of lipid droplets in 24S-OHC-treated cells, cells were fixed by 4% paraformaldehyde phosphate buffer solution at room temperature for 30 min. After washing out fixing solution, the cells were incubated with PBS, including 50 ng/ml Nile red for 5 min in the dark. Fluorescence images of Nile red staining were obtained using a fluorescence microscope (OLYMPUS IX71, Tokyo, Japan).

Knockdown of ACAT1 and RIPK3 by small interfering RNA. Stealth siRNA targeting human ACAT1 (5'-UAGAACUCCAAUCUGGAAGAU CAUG-3') and Stealth RNAi negative control (NC) were obtained from Invitrogen. The siRNA targeting human RIPK3⁴ was obtained from Hokkaido System Science (Sapporo, Japan). SH-SY5Y cells grown in six-well plates were transfected with siRNA, at a concentration of 50 or 75 pmol/well by Lipofectamine RNAiMAX (Invitrogen) for 48 h (ACAT1) or by 60 pmol/well by HiPerFect (Qiagen, Hilden, Germany) for 72 h (RIPK3) before further experiments. To confirm knockdown efficiency for ACAT1, whole cell lysates were analyzed by immunoblotting using DM102 antibody.

Cholesterol and 24S-OHC measurement by GC-MS. The levels of cholesterol and 24S-OHC were measured by GC-MS using a previously reported method.⁴⁰ Briefly, the cells in 1 ml PBS were divided equally into two portions, one for total sterol (with saponification) and the other for free sterol (without saponification). Each cell suspension was added to 500 μ l of 100 nM internal standards and 100 μ M butylated hydroxytoluene in methanol. Saponification was carried out by adding 500 μ l of 1 M KOH in methanol followed by incubation on a shaker at 40 °C for 30 min. Lipids were extracted by adding 2 ml of 10% acetic acid in water and 5 ml of chloroform/ethyl acetate (4:1, v/v), followed by vortexing for 1 min and centrifugation at $3000 \times g$ for 10 min at 4 °C. After removal of the water layer, the chloroform/ethyl acetate layer was evaporated to dryness under nitrogen. As silylating agent, 30 μ l of N,O-bis(trimethylsilyl)-trifluoroacetamide was added to the dried residue. The solution was mixed vigorously by vortexing and was incubated for 60 min at 60 °C to obtain trimethylsilyl esters and ethers. After mixing with 50 μ l of acetone, an aliquot of this sample was injected into a gas chromatograph (GC 6890 N; Agilent Technologies, Palo Alto, CA, USA) that was equipped with a quadrupole mass spectrometer (5973 Network; Agilent Technologies). A fused silica capillary column (HP-5MS, 5% phenylmethyl siloxane, 30 \times 0.25 mm²; Agilent Technologies) was used. Helium was used as carrier gas at a flow rate of 1.2 ml/min. Temperature programming was carried out to bring the temperature from 60 °C to 280 °C at 10 °C/min. The injector temperature was set to 250 °C, and the temperatures of the transfer lines to the mass detector and ion source were 250 °C and 230 °C, respectively. Electron energy was set to 70 eV. Cholesterol and 24S-OHC were identified based on their retention times and mass patterns; ions having m/z 458 for cholesterol and 413 for 24S-OHC were selected for the quantification. Cholesterol and 24S-OHC were identified quantitatively using cholesterol-d7 and 27-OHC-d6 (Avanti Polar Lipids, Alabaster, AL, USA) as internal standards, respectively.

Lipid fractionation by HPLC. Cells were lysed in 1 ml of 0.2 M NaOH and were neutralized by 64 μ l of 3 M HCl and 45 μ l of 1 M KH₂PO₄.⁴¹ Lysate was transferred to glass tubes and to the lysate in each tube three times its volume of Folch solvent (chloroform/methanol, 2:1, v/v) and 1 ml H₂O were then added. After centrifugation at 3500 r.p.m. ($2330 \times g$) for 10 min, the chloroform phase was transferred into fresh tubes. The extracts were evaporated under a stream of N₂,

the dry residue was then dissolved in 100 μ l eluent without water, and this was injected to HPLC. HPLC was carried out on an Inertsil ODS-3 column (5 μ m, 4.6 \times 250 mm; GL Science, Tokyo, Japan) as described previously.⁴² The HPLC apparatus consisted of a pump (PU-980 Intelligent HPLC Pump; Nihon Bunko, Tokyo, Japan), a detector (UV-970 Intelligent UV/VIS Detector, Nihon Bunko), and a calculator (EPC-500; Eicom, Kyoto, Japan). The flow rate of eluent (acetonitrile/2-propanol/H₂O, 43/53/4) was 1.0 ml/min.

RNA isolation and real-time PCR. Total RNA isolation and real-time PCR were conducted as described previously.¹⁵ The following primers were used: human ACAT1 forward, 5'-GCAAGGCGCTCTCTTAGATG-3'; reverse, 5'-AGGAGGGCAATAACATGTGATATATT-3'; and human ACAT2 forward, 5'-TGGCTCAACGCCTTTGC-3'; reverse, 5'-CCAGTCCCGGTAGAACATCCT-3'.

Statistical analysis. Data are reported as mean \pm S.D. of at least three independent experiments unless otherwise indicated. The statistical significance of the difference between the determinations was calculated by an analysis of variance using Tukey's test for multiple comparisons. The difference was considered significant when the *P* value was <0.05.

Conflict of Interest

The authors declare no conflict of interest.

Acknowledgements. We thank Dr. Yoko Ogawa Akazawa (National Institute of Advanced Industrial Science and Technology, Osaka, Japan) for supporting GC-MS analysis. We thank Dr. Paul Huang in Dr. Ta-Yuan Chang's lab (Dartmouth Medical School) for providing the ACAT1 siRNA sequence used in this study. We also thank Dr. Ta-Yuan Chang and Kowa Co. Ltd (Tokyo, Japan) for providing valuable reagents. This work was supported in part by the KAKENHI Grant-in-Aid for Young Scientists (B) 23700428, 25830041 to YU and for JSPS fellows 243567 to KY from JSPS and the MEXT-Supported Program for the Strategic Research Foundation at Private Universities in Japan for the years 2012–2016.

- Christofferson DE, Yuan J. Necroptosis as an alternative form of programmed cell death. *Curr Opin Cell Biol* 2010; **22**: 263–268.
- Vandenabeele P, Galluzzi L, Vanden Berghie T, Kroemer G. Molecular mechanisms of necroptosis: an ordered cellular explosion. *Nat Rev Mol Cell Biol* 2010; **11**: 700–714.
- Degterev A, Huang Z, Boyce M, Li Y, Jagtap P, Mizushima N *et al*. Chemical inhibitor of nonapoptotic cell death with therapeutic potential for ischemic brain injury. *Nat Chem Biol* 2005; **1**: 112–119.
- Cho YS, Challa S, Moqin D, Genga R, Ray TD, Guildford M *et al*. Phosphorylation-driven assembly of the RIP1-RIP3 complex regulates programmed necrosis and virus-induced inflammation. *Cell* 2009; **137**: 1112–1123.
- Xu X, Chua CC, Kong J, Kostrzewa RM, Kumaraguru U, Hamdy RC *et al*. Necrostatin-1 protects against glutamate-induced glutathione depletion and caspase-independent cell death in HT-22 cells. *J Neurochem* 2007; **103**: 2004–2014.
- Rosenbaum DM, Degterev A, David J, Rosenbaum PS, Roth S, Grotta JC *et al*. Necroptosis, a novel form of caspase-independent cell death, contributes to neuronal damage in a retinal ischemia-reperfusion injury model. *J Neurosci Res* 2010; **88**: 1569–1576.
- Vercammen D, Vandenabeele P, Beyaert R, Declercq W, Fiers W. Tumour necrosis factor-induced necrosis versus anti-Fas-induced apoptosis in L929 cells. *Cytokine* 1997; **9**: 801–808.
- He S, Wang L, Miao L, Wang T, Du F, Zhao L *et al*. Receptor interacting protein kinase-3 determines cellular necrotic response to TNF- α . *Cell* 2009; **137**: 1100–1111.
- Wilson NS, Dixit V, Ashkenazi A. Death receptor signal transducers: nodes of coordination in immune signaling networks. *Nat Immunol* 2009; **10**: 348–355.
- Yamanaka K, Saito Y, Yamamori T, Urano Y, Noguchi N. 24(S)-hydroxycholesterol induces neuronal cell death through necroptosis, a form of programmed necrosis. *J Biol Chem* 2011; **286**: 24666–24673.
- Dietschy JM, Turley SD. Thematic review series: brain lipids. Cholesterol metabolism in the central nervous system during early development and in the mature animal. *J Lipid Res* 2004; **45**: 1375–1397.
- Russell DW, Halford RW, Ramirez DM, Shah R, Kotti T. Cholesterol 24-hydroxylase: an enzyme of cholesterol turnover in the brain. *Annu Rev Biochem* 2009; **78**: 1017–1040.
- Björkhem I, Lütjohann D, Diczfalussy U, Stähle L, Ahlborg G, Wahren J. Cholesterol homeostasis in human brain: turnover of 24S-hydroxycholesterol and evidence for a cerebral origin of most of this oxysterol in the circulation. *J Lipid Res* 1998; **39**: 1594–1600.
- Jeitner TM, Voloshyna I, Reiss AB. Oxysterol derivatives of cholesterol in neurodegenerative disorders. *Curr Med Chem* 2010; **18**: 1515–1525.

15. Urano Y, Ochiai S, Noguchi N. Suppression of amyloid-beta production by 24S-hydroxycholesterol via inhibition of intracellular amyloid precursor protein trafficking. *FASEB J* 2013; **27**: 4305–4315.
16. Shafaati M, Solomon A, Kivipelto M, Björkhem I, Leoni V. Levels of ApoE in cerebrospinal fluid are correlated with Tau and 24S-hydroxycholesterol in patients with cognitive disorders. *Neurosci Lett* 2007; **425**: 78–82.
17. Lütjohann D, Papassotiropoulos A, Björkhem I, Locatelli S, Bagli M, Oehring RD *et al*. Plasma 24S-hydroxycholesterol (cerebrosterol) is increased in Alzheimer and vascular demented patients. *J Lipid Res* 2000; **41**: 195–198.
18. Brown J 3rd, Theisler C, Silberman S, Magnuson D, Gottardi-Littell N, Lee JM *et al*. Differential expression of cholesterol hydroxylases in Alzheimer's disease. *J Biol Chem* 2004; **279**: 34674–34681.
19. Kölsch H, Lütjohann D, Tulke A, Björkhem I, Rao ML. The neurotoxic effect of 24-hydroxycholesterol on SH-SY5Y human neuroblastoma cells. *Brain Res* 1998; **818**: 171–175.
20. Walther TC, Farese RV Jr. Lipid droplets and cellular lipid metabolism. *Annu Rev Biochem* 2012; **81**: 687–714.
21. Feng B, Yao PM, Li Y, Devlin CM, Zhang D, Harding HP *et al*. The endoplasmic reticulum is the site of cholesterol-induced cytotoxicity in macrophages. *Nat Cell Biol* 2003; **5**: 781–792.
22. Chang TY, Li BL, Chang CC, Urano Y. Acyl-coenzyme A:cholesterol acyltransferases. *Am J Physiol Endocrinol Metab* 2009; **297**: E1–E9.
23. Bryleva EY, Rogers MA, Chang CC, Buen F, Harris BT, Rousselet E *et al*. ACAT1 gene ablation increases 24(S)-hydroxycholesterol content in the brain and ameliorates amyloid pathology in mice with AD. *Proc Natl Acad Sci USA* 2010; **107**: 3081–3086.
24. Bonilla E, Prella A. Application of Nile blue and Nile red, two fluorescent probes, for detection of lipid droplets in human skeletal muscle. *J Histochem Cytochem* 1987; **35**: 619–621.
25. Chang CC, Sakashita N, Ornvold K, Lee O, Chang ET, Dong R *et al*. Immunological quantitation and localization of ACAT-1 and ACAT-2 in human liver and small intestine. *J Biol Chem* 2000; **275**: 28083–28092.
26. Ikenoya M, Yoshinaka Y, Kobayashi H, Kawamine K, Shibuya K, Sato F *et al*. A selective ACAT-1 inhibitor, K-604, suppresses fatty streak lesions in fat-fed hamsters without affecting plasma cholesterol levels. *Atherosclerosis* 2007; **191**: 290–297.
27. Mei S, Ni HM, Manley S, Bockus A, Kassel KM, Luyendyk JP *et al*. Differential roles of unsaturated and saturated fatty acids on autophagy and apoptosis in hepatocytes. *J Pharmacol Exp Ther* 2011; **339**: 487–498.
28. He MX, He YW. A role for c-FLIP(L) in the regulation of apoptosis, autophagy, and necroptosis in T lymphocytes. *Cell Death Differ* 2013; **20**: 188–197.
29. Feoktistova M, Geserick P, Kellert B, Dimitrova DP, Langlais C, Hupe M *et al*. cIAPs block ripoptosome formation, a RIP1/caspase-8 containing intracellular cell death complex differentially regulated by cFLIP isoforms. *Mol Cell* 2011; **43**: 449–463.
30. Cheng D, Chang CC, Qu X, Chang TY. Activation of acyl-coenzyme A:cholesterol acyltransferase by cholesterol or by oxysterol in a cell-free system. *J Biol Chem* 1995; **270**: 685–695.
31. Zhang Y, Yu C, Liu J, Spencer TA, Chang CC, Chang TY. Cholesterol is superior to 7-ketocholesterol or 7 alpha-hydroxycholesterol as an allosteric activator for acyl-coenzyme A:cholesterol acyltransferase 1. *J Biol Chem* 2003; **278**: 11642–11647.
32. Freeman NE, Rusinol AE, Linton M, Hachey DL, Fazio S, Sinensky MS *et al*. Acyl-coenzyme A:cholesterol acyltransferase promotes oxidized LDL/oxysterol-induced apoptosis in macrophages. *J Lipid Res* 2005; **46**: 1933–1943.
33. Fukunaga M, Nunomura S, Nishida S, Endo K, Gon Y, Hashimoto S *et al*. Mast cell death induced by 24(S),25-epoxycholesterol. *Exp Cell Res* 2010; **316**: 3272–3281.
34. Bao L, Li Y, Deng SX, Landry D, Tabas I. Sitosterol-containing lipoproteins trigger free sterol-induced caspase-independent death in ACAT-competent macrophages. *J Biol Chem* 2006; **281**: 33635–33649.
35. Galluzzi L, Vitale I, Abrams JM, Alnemri ES, Baehrecke EH, Blagosklonny MV *et al*. Molecular definitions of cell death subroutines: recommendations of the Nomenclature Committee on Cell Death 2012. *Cell Death Differ* 2012; **19**: 107–120.
36. Bantel H, Engels IH, Voelter W, Schulze-Osthoff K, Wesselborg S. Mistletoe lectin activates caspase-8/FLICE independently of death receptor signaling and enhances anticancer drug-induced apoptosis. *Cancer Res* 1999; **59**: 2083–2090.
37. von Haefen C, Wieder T, Essmann F, Schulze-Osthoff K, Dörken B, Daniel PT. Paclitaxel-induced apoptosis in BJAB cells proceeds via a death receptor-independent, caspases-3/-8-driven mitochondrial amplification loop. *Oncogene* 2003; **22**: 2236–2247.
38. Xaus J, Comalada M, Villedor AF, Lloberas J, López-Soriano F, Argilés JM *et al*. LPS induces apoptosis in macrophages mostly through the autocrine production of TNF-alpha. *Blood* 2000; **95**: 3823–3831.
39. Saito Y, Nishio K, Ogawa Y, Kinumi T, Yoshida Y, Masuo Y *et al*. Molecular mechanisms of 6-hydroxydopamine-induced cytotoxicity in PC12 cells: involvement of hydrogen peroxide-dependent and -independent action. *Free Radic Biol Med* 2007; **42**: 675–685.
40. Shichiri M, Yoshida Y, Ishida N, Hagihara Y, Iwahashi H, Tamai H *et al*. α -Tocopherol suppresses lipid peroxidation and behavioral and cognitive impairments in the Ts65Dn mouse model of Down syndrome. *Free Radic Biol Med* 2011; **50**: 1801–1811.
41. Urano Y, Watanabe H, Murphy SR, Shibuya Y, Geng Y, Peden AA *et al*. Transport of LDL-derived cholesterol from the NPC1 compartment to the ER involves the trans-Golgi network and the SNARE protein complex. *Proc Natl Acad Sci USA* 2008; **105**: 16513–16518.
42. Urano Y, Hayashi I, Isoo N, Reid PC, Shibasaki Y, Noguchi N *et al*. Association of active gamma-secretase complex with lipid rafts. *J Lipid Res* 2005; **46**: 904–912.



Cell Death and Disease is an open-access journal published by Nature Publishing Group. This work is licensed under a Creative Commons Attribution-NonCommercial-NoDerivs 3.0 Unported License. To view a copy of this license, visit <http://creativecommons.org/licenses/by-nc-nd/3.0/>

Supplementary Information accompanies this paper on Cell Death and Disease website (<http://www.nature.com/cddis>)



Review Article

New aspects of 24(S)-hydroxycholesterol in modulating neuronal cell death



Noriko Noguchi*, Yasuomi Urano, Wakako Takabe, Yoshiro Saito

Systems Life Sciences Laboratory, Department of Medical Life Systems, Faculty of Life and Medical Sciences, Doshisha University, Kyotanabe, Kyoto 610-0394, Japan

ARTICLE INFO

Article history:

Received 24 March 2015

Received in revised form

26 June 2015

Accepted 27 June 2015

Available online 9 July 2015

Keywords:

24(S)-Hydroxycholesterol

CYP46A1

Cholesterol homeostasis

Cell death

Neurodegenerative disease

Free radicals

ABSTRACT

24(S)-Hydroxycholesterol (24S-OHC), which is enzymatically produced in the brain, has been known to play an important role in maintaining cholesterol homeostasis in the brain and has been proposed as a possible biomarker of neurodegenerative disease. Recent studies have revealed diverse functions of 24S-OHC and gained increased attention. For example, 24S-OHC at sublethal concentrations has been found to induce an adaptive response via activation of the liver X receptor signaling pathway, thereby protecting neuronal cells against subsequent oxidative stress. It has also been found that physiological concentrations of 24S-OHC suppress amyloid- β production via downregulation of amyloid precursor protein trafficking in neuronal cells. On the other hand, high concentrations of 24S-OHC have been found to induce a type of nonapoptotic programmed cell death in neuronal cells expressing little caspase-8. Because neuronal cell death induced by 24S-OHC has been found to proceed by a unique mechanism, which is different from but in some ways similar to necroptosis—necroptosis being a type of programmed necrosis induced by tumor necrosis factor α —neuronal cell death induced by 24S-OHC has been called “necroptosis-like” cell death. 24S-OHC-induced cell death is dependent on the formation of 24S-OHC esters but not on oxidative stress. This review article discusses newly reported aspects of 24S-OHC in neuronal cell death and sheds light on the possible importance of controlling 24S-OHC levels in the brain for preventing neurodegenerative disease.

© 2015 Elsevier Inc. All rights reserved.

Contents

1. Introduction	367
2. Oxysterols: oxidation products of cholesterol	367
3. Production of 24S-OHC in health and disease	367
4. Mechanism of protection of neuronal cells by 24S-OHC	368
5. Mechanism of induction of neuronal cell death by 24S-OHC	368
6. Conclusion	370
Acknowledgments	371
References	371

Abbreviations: 24S-OHC, 24(S)-hydroxycholesterol; 5,6-epoxyC, cholesterol-5,6-epoxide; 7-OOHC, 7-hydroperoxycholesterol; 7-OHC, 7-hydroxycholesterol; A β , amyloid- β ; ACAT1, acyl-CoA:cholesterol acyltransferase 1; AD, Alzheimer disease; APP, amyloid precursor protein; CSF, cerebrospinal fluid; CYP46A1, cholesterol 24-hydroxylase; DCFH-DA, dichlorodihydrofluorescein diacetate; GRP78, glucose-regulated protein 78; HD, Huntington disease; JurkatCas8 $^{-/-}$, caspase-8-deficient Jurkat; LCAT, lecithin-cholesterol acyltransferase; LXR, liver X receptor; MLKL, mixed lineage kinase domain-like; MRI, magnetic resonance imaging; PD, Parkinson disease; RIPK, receptor-interacting protein kinase; ROS, reactive oxygen species; RXR, retinoid X receptor; TNF α , tumor necrosis factor α

* Corresponding author. Fax: +81 774 65 6262.

E-mail address: nnoguchi@mail.doshisha.ac.jp (N. Noguchi).<http://dx.doi.org/10.1016/j.freeradbiomed.2015.06.036>

0891-5849/© 2015 Elsevier Inc. All rights reserved.

1. Introduction

The brain is the most cholesterol-rich organ and contains about 25% of the total amount of cholesterol in the body [1]. Brain cholesterol is locally synthesized and its levels are not influenced by the nutritional intake of cholesterol [2, 3]. The blood–brain barrier prevents cholesterol transport between the brain and the peripheral circulation [1, 4–7]. Excess brain cholesterol due to either increased synthesis or cell death needs to be eliminated from the brain into the peripheral circulation by a suitable elimination pathway. To maintain a steady-state level of brain cholesterol, excess cholesterol is converted to 24(S)-hydroxycholesterol (24S-OHC)¹ by the neuronal enzyme cholesterol 24-hydroxylase (CYP46A1) [8, 9]. 24S-OHC penetrates the blood–brain barrier by diffusion or by way of organic anion-transporting polypeptide 2 [10]. The content of 24S-OHC in the brains of mice lacking CYP46A1 was less than 5% of that of wild-type mice [11], suggesting that CYP46A1 is responsible for production of 24S-OHC in the brain. About 30 μM free 24S-OHC has been detected in human brain homogenates [12]. Various oxysterols, including 24S-OHC, can also downregulate cholesterol synthesis by blocking the proteolytic activation of a transcription factor, sterol-regulatory element-binding protein [13]. 24S-OHC is known to be an endogenous ligand of the liver X receptor (LXR) transcription factors, which regulate cholesterol efflux [14]. 24S-OHC in the circulation is transported by low-density lipoprotein to the liver, where it is metabolized to bile acids [15]. It is therefore clear that 24S-OHC is an important physiological molecule for cholesterol metabolism in the human body.

Cholesterol metabolism is thought to be involved in the pathogenesis of Alzheimer disease (AD), and the $\epsilon 4$ allele of apolipoprotein E has been shown to be a genetic risk factor for late-onset AD [16]. A polymorphism in the *CYP46A1* gene that causes an increase in 24S-OHC levels has been reported to be associated with AD [17]. In addition to the concentration of 24S-OHC measured in total brain homogenates [12], Heverin et al. measured the levels of 24S-OHC in four different brain areas of healthy controls and AD patients [18]. They found that 24S-OHC levels in all four areas were about 20 ng/mg tissue in controls and were decreased in AD patients. If we assume that a volume of 1 mg tissue is 1 μl , we can calculate the level of 24S-OHC in brain tissue as approximately 50 μM . Several studies reported that 24S-OHC levels were elevated in the plasma [19, 20] and cerebrospinal fluid (CSF) [21] of AD patients. However, other studies have reported lower levels of plasma 24S-OHC in AD patients [22, 23]. The potential role of 24S-OHC as a biomarker for diagnosis of Parkinson disease (PD) has also been investigated [24, 25]. As with AD, conflicting reports have been observed for PD. Whereas one study reported unchanged levels of 24S-OHC in plasma but significantly increased levels of 24S-OHC in the CSF of patients with PD [24], another study showed markedly reduced levels of 24S-OHC in the plasma of PD patients [25]. The increased levels of 24S-OHC reported in the CSF of PD patients were correlated with longer disease duration [24]. The level of 24S-OHC in plasma from patients with Huntington disease (HD) was observed to decrease in correspondence to the progress of the disease as quantified by magnetic resonance imaging (MRI) measurements of striatal atrophy and striatal volume [26]. Similar to what was observed in HD, levels of 24S-OHC in plasma were found to decrease in proportion to the degree of brain atrophy as measured by MRI in AD and multiple sclerosis [27]. Neurodegeneration, with loss of neurons, would be expected to lead to a reduction in the levels of 24S-OHC in plasma. It is postulated that plasma levels of 24S-OHC may thus be regarded as a surrogate marker for the number of metabolically active neurons located in the gray matter of the brain [28]. Hughes et al. examined a total of 28 studies on plasma 24S-OHC and

neurodegenerative disease and concluded that plasma 24S-OHC might be higher in the early stages of cognitive impairment and lower in advanced stages of AD compared with normal controls owing to loss of neurons [29].

Although it has long been suspected that 24S-OHC might play an important role in the pathogenesis of neurodegenerative disease, the exact functions of 24S-OHC have only recently begun to be investigated. In this review, we summarize the dose-dependent and diverse functions of 24S-OHC, and we explore new models for understanding the role of 24S-OHC in neuronal cell death with a view toward gaining a better grasp of neurodegenerative disease pathologies.

2. Oxysterols: oxidation products of cholesterol

Cholesterol is oxidized enzymatically and nonenzymatically to produce several kinds of oxysterols [30–32]. In nonenzymatic oxidation, cholesterol is attacked by free radicals such as hydroxyl radical, alkoxyl radical, and peroxy radical, which are formed in the decomposition of hydrogen peroxide and hydroperoxides by metal ions such as iron and copper [33]. The free radical-mediated oxidation of cholesterol generates 7-hydroperoxycholesterol (7-OOHC), 7-hydroxycholesterol (7-OHC), 7-ketocholesterol (7-KC), and cholesterol-5,6-epoxide (5,6-epoxyC) as major products. Both α and β forms of 7-OOHC, 7-OHC, and 5,6-epoxyC are formed. 7 β -OHC has been reported to derive in the brain from the oxidation of cholesterol by amyloid- β (A β) and to a lesser extent by amyloid precursor protein (APP) [34]. Singlet oxygen attacks carbon at the 5 position to generate 5 α -hydroxycholesterol specifically. In enzymatic oxidation of cholesterol, several cholesterol hydroxylases produce 24S-OHC, 25-OHC, and 27-OHC, as summarized in Table 1 [33,35]. 7 α -OHC is also produced via an enzymatic mechanism [33,36]. Many of the cholesterol hydroxylases except 25-hydroxylase are cytochrome P450 enzymes. A unique enzyme, 11 β -hydroxysteroid dehydrogenase type 1, catalyzes interconversion between 7-KC and 7 β -OHC [33,37].

3. Production of 24S-OHC in health and disease

In the adult brain, cholesterol is mainly synthesized in astrocytes, from which it is delivered to neurons via ApoE-dependent transportation [38]. CYP46A1 expression is normally restricted to certain neuronal cell types, which include hippocampal principal neurons and some interneuron classes [39]. Abnormal induction of CYP46A1 by glial cells in the brains of AD patients has been reported [40,41].

Transcriptional and posttranscriptional regulation of CYP46A1 activity, as well as 24S-OHC synthesis, is poorly understood. The careful promoter assay conducted by Ohyama et al. failed to determine the transcriptional regulation sites [42]. However, they showed that oxidative stress induced by stimulation of neuronal cells with inflammatory cytokines or tertiary-butylhydroperoxides caused a significant increase in transcriptional activity. The precise mechanisms are not well known yet. In addition to various direct

Table 1
Enzymes involved in oxysterol synthesis

Enzyme	Oxysterol
Cholesterol 7 α -hydroxylase (CYP7A1)	7 α -OHC
Cholesterol 24-hydroxylase (CYP46A1)	24S-OHC
Cholesterol 25-hydroxylase	25-OHC
Sterol 27-hydroxylase (CYP27A1)	27-OHC
11 β -Hydroxysteroid dehydrogenase type 1	7-KC, 7 β -OHC

influences, it is reasonable to suppose that 24S-OHC synthesis will be affected by other cholesterol metabolic pathways, including neurosteroid biosynthesis. Neurosteroids are produced in neurons, astrocytes, and oligodendrocytes—the particular enzymes that are expressed being specific to the type of cell [43,44]. The first step in synthesis of neurosteroids from cholesterol is action of a mitochondrial cholesterol side-chain cleavage enzyme, such as 20- or 21-hydroxylase [45,46]. Because these enzymes and CYP46A1 both take cholesterol as substrate, they will presumably compete with each other for cholesterol [47]. Because CYP46A1 resides in the endoplasmic reticulum (ER), whereas cholesterol side-chain cleavage enzymes reside in mitochondria, cholesterol trafficking to specific organelles could control which pathway is favored under different conditions [48].

In mouse models of AD, neuronal overexpression of CYP46A1 has been found to reduce the amyloid pathology [49]. On the other hand, knockout of the *CYP46A1* gene did not affect amyloid formation in mouse models of AD, although deletion of this gene provided a survival advantage in this mouse model [50]. The CC genotype of the IVS3 + 43C → T polymorphism was associated with increased 24S-OHC/cholesterol ratio in the CSF of AD patients, indicating that the *CYP46A1* gene locus may predispose an individual to AD by increasing the 24S-OHC/cholesterol ratio in the brain [17]. Antifungal agents such as voriconazole have been found to be high-affinity inhibitors of CYP46A1 [51,52], which result might cause one to expect that voriconazole would control 24S-OHC function in the brain [48]. However, increase in CYP46A1 expression in the retina of voriconazole-treated rats has been shown [53], indicating that further investigation will be needed before it will be possible to draw conclusions regarding the compounds that control CYP46A1 activity.

4. Mechanism of protection of neuronal cells by 24S-OHC

It has been demonstrated that certain lipid peroxidation products not only exhibit cytotoxic effects but can also exhibit cytoprotective effects if there is induction of an adaptive response [33,54]. Adaptive response has been defined as a state occurring when a sublethal concentration of an oxidation product significantly enhances cell tolerance with respect to a subsequent oxidative stress [55,56]. Because the highly cytotoxic potential of 7-KC has been demonstrated in neuronal cells [57–59], 7-KC is suspected to be involved in the pathogenesis of neurodegenerative disease. In the case of 24S-OHC, stimulation of a human neuroblastoma cell line (SH-SY5Y cells) with sublethal concentrations of 24S-OHC was found to induce an adaptive response and protect the cells against subsequent cytotoxic stress induced by 7-KC [60]. The cytoprotective effect of 24S-OHC disappeared in LXR β -knocked-down cells, suggesting that LXR β plays a key role in the 24S-OHC-induced adaptive response. LXR forms a functional heterodimer with retinoid X receptor (RXR) and regulates transcription of several genes involved in the cholesterol efflux pathway [61]. Cotreatment with 24S-OHC and 9-*cis*-retinoic acid (the latter being a ligand of RXR) significantly enhanced the adaptive response to prevent 7-KC-induced cell death [60]. Taken together, these results indicate that a sublethal concentration of 24S-OHC protected neuronal cells against subsequent oxidative stress as a result of induction of an adaptive response in which the LXR/RXR was activated.

Accumulation of A β is believed to be the earliest observable event in AD development [62]. A β or A β aggregation has been known to cause neuronal cell death [63,64]. 24S-OHC has been shown to favor the processing of APP to the nonamyloidogenic pathway more preferentially than 27-OHC [65]. The processing of APP into A β by β -secretase and γ -secretase is thought to occur in

the *trans*-Golgi network and endosomes [66–68]. APP budding via coat protein complex II vesicles from the ER was reduced by 70% in 24S-OHC-treated cells [69]. Proteomics and immunoblotting analysis revealed that 24S-OHC induced the expression of glucose-regulated protein 78 (GRP78), an ER chaperone, resulting in the formation of the APP/GRP78 complex. These results suggest that 24S-OHC downregulates APP trafficking via enhancement of the complex formation of APP with upregulated GRP78 in the ER, resulting in suppression of A β production.

5. Mechanism of induction of neuronal cell death by 24S-OHC

There are many studies in the literature that report acceleration of neuronal cell death as a result of A β accumulation [70–72]. 24S-OHC, in some cases, has been shown to enhance A β accumulation. For example, increase in A β accumulation as a result of enhancement of APP expression by 24S-OHC has been shown in neuroblastoma cells [73]. Results of *in vitro* experiments suggest that the balance between the levels of 24S-OHC and 27-OHC may be of importance for generation of A β peptides [6]. It has been reported that high CSF concentrations of cholesterol, 24S-OHC, and 27-OHC are associated with increase in production of both soluble (s) APP forms, i.e., sAPP α and sAPP β , in AD patients [74]. Enhancement of A β production via ABCA1 induction by 24S-OHC has also been reported [75].

In addition to the enhancing effect of 24S-OHC on A β production, acceleration of A β cytotoxicity by oxidative stress and/or 24S-OHC has been reported [76,77]. It has also been reported that 24S-OHC in the close vicinity of amyloid plaques appears to enhance the adhesion of large amounts of A β to the plasma membrane of neurons and then to amplify the neurotoxic action of A β by locally increasing reactive oxygen species (ROS) steady-state levels [32,78]. The interaction of the A β molecule with the hydrophobic part of 24S-OHC has been observed [79].

Direct cytotoxicity of 24S-OHC in differentiated SH-SY5Y cell has been shown by Kölsch et al. [80]. 24S-OHC caused apoptosis as indicated by caspase-3 activation and partially prevented by the radical-scavenging antioxidant vitamin E in SH-SY5Y cells differentiated by treatment with retinoic acid [81]. When we treated undifferentiated SH-SY5Y cells with 24S-OHC, we observed that 24S-OHC exhibited cytotoxicity in a concentration-dependent manner (Fig. 1) [60,82,83]. 24S-OHC at concentrations higher than 10 μ M significantly caused cell death in which caspase-3 and caspase-9 were not activated [83]. Cell death induced by 24S-OHC was not suppressed by several kinds of antioxidants such as α -tocotrienol; an analogue of α -tocopherol, BO-653; deferoxamine; curcumin; and *N*-acetylcysteine (Fig. 2A) [83]. We used

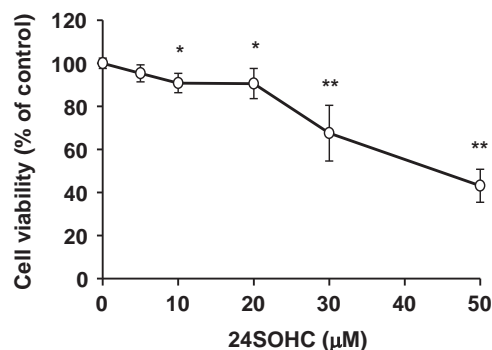


Fig. 1. Cell death induced by 24S-OHC in SH-SY5Y cells. SH-SY5Y cells were treated with variable concentrations of 24S-OHC for 24 h, and cell viability was measured by WST-8 assay. Each bar represents the mean \pm SD ($n = 3$). * $p < 0.05$, ** $p < 0.01$, compared with vehicle control.

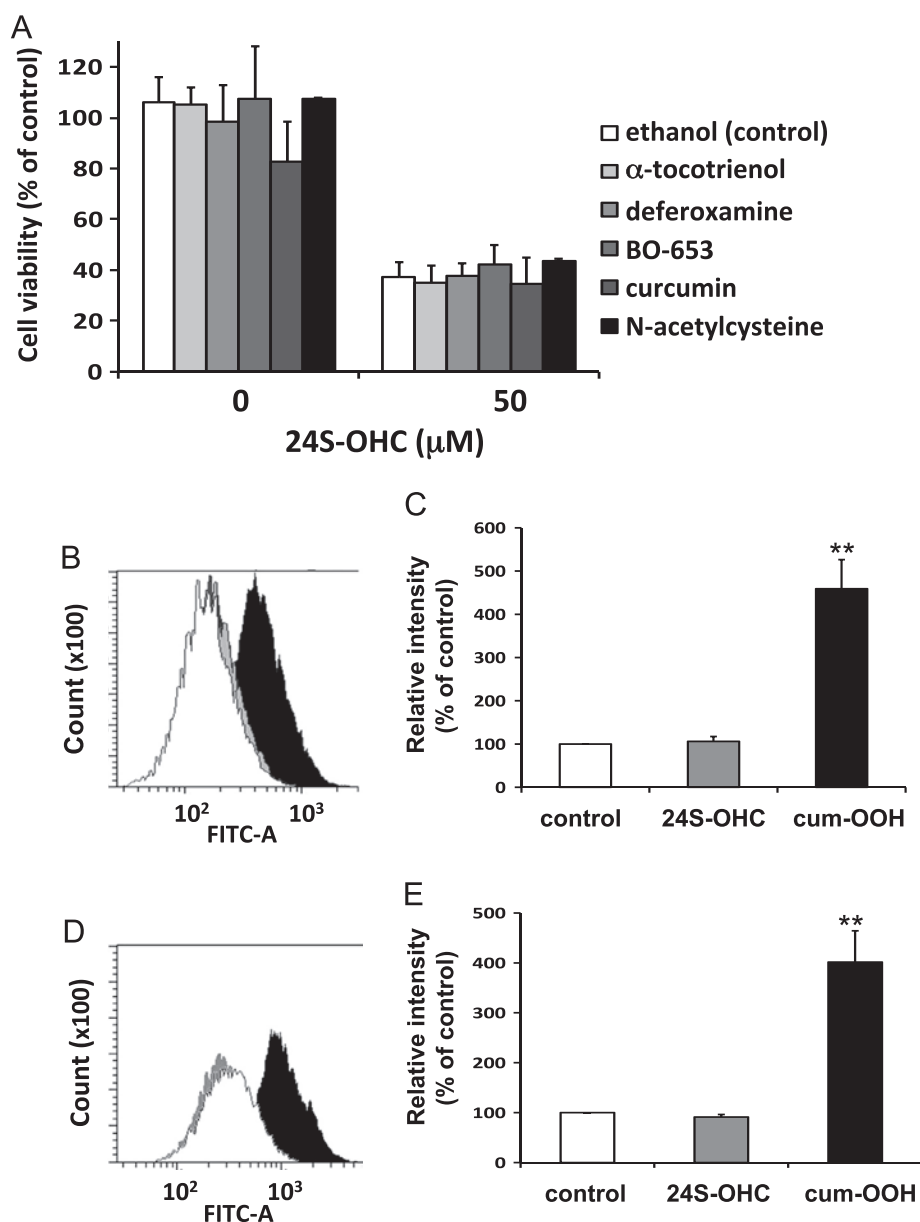


Fig. 2. Oxidative stress induced by 24S-OHC in SH-SY5Y cells. (A) Effects of antioxidants against 24S-OHC toxicity in SH-SY5Y cells were assessed. After treatment of cells with various antioxidants, α -tocotrienol, 10 μ M; deferoxamine, 10 μ M; BO-653, 10 μ M; curcumin, 10 μ M; and *N*-acetylcysteine, 2 mM, for 24 h, cells were treated with 24S-OHC for 24 h, and the viability was measured by MTT assay. (B–E) Increase in intracellular ROS levels was measured using fluorescent probes, DCFH-DA (B, C) and Liperfluo (D, E), by flow cytometry. Cells were treated with ethanol (control; white), 50 μ M 24S-OHC (gray), or 100 μ M cumene-hydroperoxide (cum-OOH; black) for 6 h. Mean \pm SD ($n = 3$), ** $p < 0.01$, Tukey, ANOVA compared with vehicle control.

dichlorodihydrofluorescein diacetate (DCFH-DA; Figs. 2B and 2C) and 2-(4-diphenylphosphanylphenyl)-9-(3,6,9,12-tetraoxatridecyl) anthra[2,1,9-def:6,5,10-d'e'f']diisoquinoline-1,3,8,10-tetraone (Liperfluo; Figs. 2D and 2E) to detect free radical and lipid hydroperoxides [84], respectively. No increase in the ROS levels in cells treated with 24S-OHC was observed, whereas a significant increase was shown by treatment with cumene hydroperoxide. This discrepancy may be explained by different cell conditions between undifferentiated and differentiated with retinoic acid, which was shown to induce caspase-8 in neuroblastoma cells [85].

As summarized in Fig. 3, our recent studies have revealed that 24S-OHC induces a type of nonapoptotic programmed cell death in neuronal cells expressing little caspase-8 [83]. The term “necroptosis” has been used to describe a type of programmed necrosis in which activation of receptor-interacting protein kinase 1 (RIPK1), RIPK3, and mixed-lineage kinase domain-like (MLKL) is

involved in the signaling pathway in a human T-lymphoma cell line, Jurkat cells, upon exposure to tumor necrosis factor α (TNF α) [86,87]. RIPK1 has been known to be activated by autophosphorylation [88]. It has been shown that RIPK1 phosphorylation is involved in 24S-OHC-induced cell death in SH-SY5Y cells [83]. We recently found that RIPK1 but neither RIPK3 nor MLKL was expressed in neuronal SH-SY5Y cells [89]. Using caspase-8-deficient Jurkat (Jurkat^{Cas8^{-/-}}) cells expressing these three proteins, we showed that TNF α -induced cell death was dependent on RIPK1, RIPK3, and MLKL [89] as reported in the literature [86,87]. In contrast, of three kinase inhibitors tested, which respectively targeted the kinase activities of RIPK1, RIPK3, and MLKL, only RIPK1 kinase inhibitor was found to cause significant suppression of 24S-OHC-induced cell death in Jurkat^{Cas8^{-/-}} cells. Almost as surprising was the fact that in Jurkat^{Cas8^{-/-}} cells, knockdown of either RIPK1 or RIPK3 caused moderate but significant suppression of 24S-OHC-

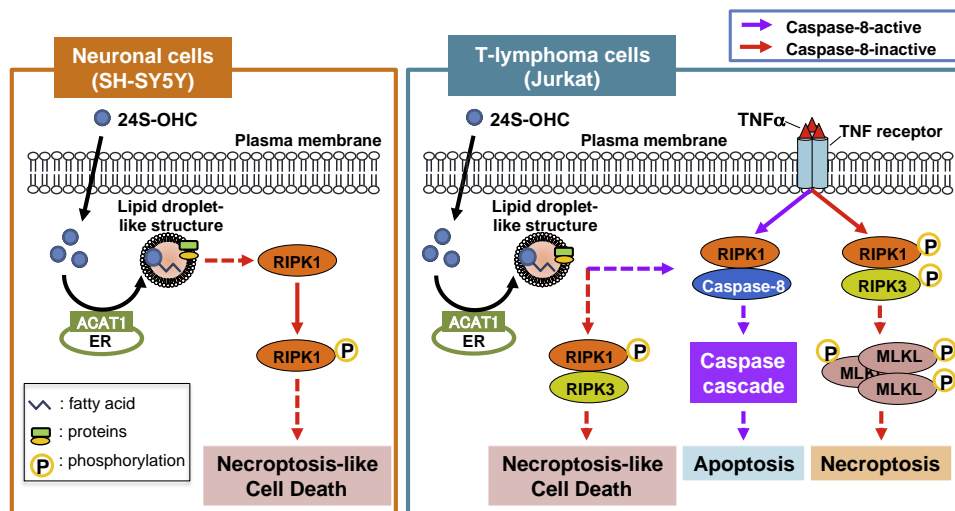


Fig. 3. Summary of the proposed mechanism of cell death induced by 24S-OHC in neuronal cells and T-lymphoma cells. 24S-OHC is esterified by ACAT1 at the ER resulting in formation of lipid droplet-like structures. In SH-SY5Y cells expressing little caspase-8, 24S-OHC induces necroptosis-like cell death, which is dependent on RIPK1 phosphorylation. In Jurkat cells, 24S-OHC can induce either apoptosis or necroptosis-like cell death, as determined by caspase-8 activity. Whereas TNF α induces necroptosis, which is dependent on the kinase activity of RIPK1, RIPK3, and MLKL, 24S-OHC induces necroptosis-like cell death, which is dependent on RIPK1 kinase activity and RIPK3 protein (not kinase activity), but not on MLKL kinase activity.

induced cell death, but knockdown of MLKL showed no such effect. Taking into consideration especially the fact that the RIPK3 inhibitor did not display inhibitory effect, we concluded that 24S-OHC-induced cell death was dependent on RIPK1 kinase activity and RIPK3 protein (not kinase activity), but not on MLKL kinase activity in Jurkat^{Cas8^{-/-}} cells. Taken collectively, these results indicate that in the absence of caspase-8 activity, 24S-OHC induces necroptosis-like cell death that is RIPK1-dependent but MLKL-independent (Fig. 3).

We previously showed that 24S-OHC induces caspase-dependent apoptosis in Jurkat cells, which endogenously express caspase-8 [90]. When caspase-8 was inactivated in Jurkat cells by treatment with the pancaspase inhibitor ZVAD-fmk (ZVAD), 24S-OHC was found to induce caspase-independent cell death, and it was furthermore found that this was significantly inhibited by RIPK1 kinase inhibitor or knockdown of RIPK1 or RIPK3, as had been observed separately in Jurkat^{Cas8^{-/-}} cells. These results suggest that 24S-OHC can induce either apoptosis or necroptosis-like cell death, and which of the two is induced is determined by caspase-8 activity in T-lymphoma Jurkat cells (Fig. 3).

Regardless of the presence or absence of ZVAD, 24S-OHC treatment was found to induce the formation of lipid droplet-like structures and cell death in Jurkat cells and SH-SY5Y cells, and it was furthermore found that this was suppressed by treatment with an inhibitor of acyl-CoA:cholesterol acyltransferase 1 (ACAT1) [90]. ACAT1 catalyzes esterification of cholesterol with unsaturated fatty acid at the ER [91]. Analysis using gas chromatography–mass spectrometry revealed that the 24S-OHC-treated cells exhibited accumulation of 24S-OHC esters but not of cholesteryl esters and that accumulation of 24S-OHC esters was reduced when ACAT1 was inhibited either by ACAT1 inhibitor or by siRNA for ACAT1 [90]. Together with the disappearance of lipid droplet-like structures that resulted from inhibition of ACAT1 activity, recovery of cell viability was observed. Collectively, these results suggest that ACAT1-catalyzed 24S-OHC esterification and the resulting formation of lipid droplet-like structures are initial key events in 24S-OHC-induced cell death. Therapeutic strategies that might employ ACAT1 inhibitors to treat neurodegenerative disease could therefore be promising. Marca et al. showed that esterification of 24S-OHC by the lecithin-cholesterol acyltransferase (LCAT) activity of apolipoprotein A-I suppressed the

neurotoxicity of 24S-OHC by preventing 24S-OHC from entering into the cell [92]. This protecting mechanism using LCAT activity against the cytotoxicity of 24S-OHC may play a role when 24S-OHC released from neurons attacks the neurons or other cells.

It is still unclear whether the esterified form of 24S-OHC is itself cytotoxic or whether it is the formation of lipid droplet-like structures that triggers cell death signaling. It is possible to hypothesize that certain proteins that suppress cell death, e.g., cellular FLICE inhibitory protein [93] or cellular inhibitor of apoptosis [94], might collect within lipid droplet-like structures and cause the induction of cell death. Another possibility is that the lipid droplet-like structures could serve as an intracellular platform to permit association of certain proteins that might then presumably promote cell death signaling.

6. Conclusion

The different forms of cell death that are induced by 24S-OHC may contribute to different pathogenesises. 24S-OHC has diverse functions, as described above and as summarized in the graphic abstract, and these diverse functions may account for some of the conflicting results observed in connection with the pathologies of various neurodegenerative diseases. Under normal conditions or during the early stages of neurodegenerative disease, it would seem that low levels of 24S-OHC act protectively, but that as 24S-OHC levels increase, a point is reached at which 24S-OHC no longer acts protectively but instead functions causally to induce cell death. After such a period, because a large number of neuronal cells will have died, this fact may itself be sufficient to explain why 24S-OHC levels are thereafter observed to decrease. It is difficult to determine the range of physiological and pathological concentrations of 24S-OHC in the brain. Although it is hoped that control of 24S-OHC levels in the brain might one day play a role in preventing neurodegenerative disease, we must at the same time remember that it is likely to be only as a result of gaining a clear understanding of the “big picture” of cell death signaling that we will be able to establish effective therapeutic strategies.

Acknowledgments

We thank Gerry Peters (JTT K.K., Takatsuki, Japan) for his careful editing of the manuscript. This work was supported in part by KAKENHI Grant-in-Aid for Young Scientists (B) 25830041 to Y.U., the Adaptable and Seamless Technology Transfer Program through target-driven R&D, JST, to Y.U., the Foundation of Cosmetology Research to N.N., and the MEXT-Supported Program for the Strategic Research Foundation at Private Universities in Japan for the years 2012–2016.

References

- [1] I. Björkhem, S. Meaney, Brain cholesterol: long secret life behind a barrier, *Arterioscler. Thromb. Vasc. Biol.* 24 (2004) 806–815.
- [2] H. Jurevics, P. Morell, Cholesterol for synthesis of myelin is made locally, not imported into brain, *J. Neurochem.* 64 (1995) 895–901.
- [3] J.M. Dietschy, S.D. Turley, Thematic review series: brain lipids. Cholesterol metabolism in the central nervous system during early development and in the mature animal, *J. Lipid Res.* 45 (2004) 1375–1397.
- [4] F.W. Pfrieger, N. Ungerer, Cholesterol metabolism in neurons and astrocytes, *Prog. Lipid Res.* 50 (2011) 357–371.
- [5] A.A. Saeed, G. Genové, T. Li, D. Lütjohann, M. Olin, N. Mast, I.A. Pikuleva, P. Crick, Y. Wang, W. Griffiths, C. Betsholtz, I. Björkhem, Effects of a disrupted blood–brain barrier on cholesterol homeostasis in the brain, *J. Biol. Chem.* 289 (2014) 23712–23722.
- [6] I. Björkhem, A. Cedazo-Minguez, V. Leoni, S. Meaney, Oxysterols and neurodegenerative diseases, *Mol. Aspects Med.* 30 (2009) 171–179.
- [7] D.W. Russell, R.W. Halford, D.M. Ramirez, R. Shah, T. Kotti, Cholesterol 24-hydroxylase: an enzyme of cholesterol turnover in the brain, *Annu. Rev. Biochem.* 78 (2009) 1017–1040.
- [8] I. Björkhem, D. Lütjohann, O. Breuer, A. Sakinis, A. Wennmalm, Importance of a novel oxidative mechanism for elimination of brain cholesterol, *J. Biol. Chem.* 272 (1997) 30178–30184.
- [9] I. Björkhem, U. Diczfalussy, D. Lütjohann, Removal of cholesterol from extrahepatic sources by oxidative mechanisms, *Curr. Opin. Lipidol.* 10 (1999) 161–165.
- [10] S. Ohtsuki, S. Ito, A. Matsuda, S. Hori, T. Abe, T. Terasaki, Brain-to-blood elimination of 24S-hydroxycholesterol from rat brain is mediated by organic anion transporting polypeptide 2 (oatp2) at the blood–brain barrier, *J. Neurochem.* 103 (2007) 1430–1438.
- [11] E.G. Lund, C. Xie, T. Kotti, S.D. Turley, J.M. Dietschy, D.W. Russell, Knockout of the cholesterol 24-hydroxylase gene in mice reveals a brain-specific mechanism of cholesterol turnover, *J. Biol. Chem.* 278 (2003) 22980–22988.
- [12] D. Lütjohann, O. Breuer, G. Ahlborg, I. Nennesmo, A. Sidén, U. Diczfalussy, I. Björkhem, Cholesterol homeostasis in human brain: evidence for an age-dependent flux of 24S-hydroxycholesterol from the brain into the circulation, *Proc. Natl. Acad. Sci. USA* 93 (1996) 9799–9804.
- [13] A. Radhakrishnan, Y. Ikeda, H.J. Kwon, M.S. Brown, J.L. Goldstein, Sterol-regulated transport of SREBPs from endoplasmic reticulum to Golgi: oxysterols block transport by binding to Insig, *Proc. Natl. Acad. Sci. USA* 104 (2007) 6511–6518.
- [14] S.B. Joseph, E. McKilligin, L. Pei, M.A. Watson, A.R. Collins, B.A. Laffitte, M. Chen, G. Noh, J. Goodman, G.N. Hagger, J. Tran, T.K. Tippin, X. Wang, A. J. Lusis, W.A. Hsueh, R.E. Law, J.L. Collins, T.M. Willson, P. Tontonoz, Synthetic LXR ligand inhibits the development of atherosclerosis in mice, *Proc. Natl. Acad. Sci. USA* 99 (2002) 7604–7609.
- [15] F. Gosselet, J. Saint-Pol, L. Fenart, Effects of oxysterols on the blood–brain barrier: implications for Alzheimer's disease, *Biochem. Biophys. Res. Commun.* 446 (2014) 687–691.
- [16] D.E. Schmechel, A.M. Saunders, W.J. Strittmatter, B.J. Crain, C.M. Hulette, S. H. Joo, M.A. Pericak-Vance, D. Goldgaber, A.D. Roses, Increased amyloid beta-peptide deposition in cerebral cortex as a consequence of apolipoprotein E genotype in late-onset Alzheimer disease, *Proc. Natl. Acad. Sci. USA* 90 (1993) 9649–9653.
- [17] H. Kölsch, D. Lütjohann, M. Ludwig, A. Schulte, U. Ptok, F. Jessen, K. von Bergmann, M.L. Rao, W. Maier, R. Heun, Polymorphism in the cholesterol 24S-hydroxylase gene is associated with Alzheimer's disease, *Mol. Psychiatry* 7 (2002) 899–902.
- [18] M. Heverin, N. Bogdanovic, D. Lütjohann, T. Bayer, I. Pikuleva, L. Bretillon, U. Diczfalussy, B. Winblad, I. Björkhem, Changes in the levels of cerebral and extracerebral sterols in the brain of patients with Alzheimer's disease, *J. Lipid Res.* 45 (2004) 186–193.
- [19] D. Lütjohann, A. Papassotiropoulos, I. Björkhem, S. Locatelli, M. Bagli, R. D. Oehring, U. Schlegel, F. Jessen, M.L. Rao, K. von Bergmann, R. Heun, Plasma 24S-hydroxycholesterol (cerebrosterol) is increased in Alzheimer and vascular demented patients, *J. Lipid Res.* 41 (2000) 195–198.
- [20] G. Zuliani, M.P. Donnorso, C. Bosi, A. Passaro, N.E. Dalla, A. Zurlo, F. Bonetti, A. F. Mozzi, C. Cortese, Plasma 24S-hydroxycholesterol levels in elderly subjects with late onset Alzheimer's disease or vascular dementia: a case–control study, *BMC Neurol.* 11 (2011) 121.
- [21] M. Shafaati, A. Solomon, M. Kivipelto, I. Björkhem, V. Leoni, Levels of ApoE in cerebrospinal fluid are correlated with Tau and 24S-hydroxycholesterol in patients with cognitive disorders, *Neurosci. Lett.* 425 (2007) 78–82.
- [22] L. Bretillon, A. Sidén, L.O. Wahlund, D. Lütjohann, L. Minthon, M. Crisby, J. Hillert, C.G. Groth, U. Diczfalussy, I. Björkhem, Plasma levels of 24S-hydroxycholesterol in patients with neurological diseases, *Neurosci. Lett.* 293 (2000) 87–90.
- [23] H. Kölsch, R. Heun, A. Kerksiek, K.V. Bergmann, W. Maier, D. Lütjohann, Altered levels of plasma 24S- and 27-hydroxycholesterol in demented patients, *Neurosci. Lett.* 368 (2004) 303–308.
- [24] I. Björkhem, A. Lövgren-Sandblom, V. Leoni, S. Meaney, L. Brodin, L. Salveson, et al., Oxysterols and Parkinson's disease: evidence that levels of 24S-hydroxycholesterol in cerebrospinal fluid correlates with the duration of the disease, *Neurosci. Lett.* 555 (2013) 102–105.
- [25] C.Y. Lee, R.C. Seet, S.H. Huang, L.H. Long, B. Halliwell, Different patterns of oxidized lipid products in plasma and urine of dengue fever, stroke, and Parkinson's disease patients: cautions in the use of biomarkers of oxidative stress, *Antioxid. Redox Signaling* 11 (2009) 407–420.
- [26] V. Leoni, J.D. Long, J.A. Mills, S. Di Donato, J.S. Paulsen, Plasma 24S-hydroxycholesterol correlation with markers of Huntington disease progression, *Neurobiol. Dis.* 55 (2013) 37–43.
- [27] V. Leoni, C. Caccia, Oxysterols as biomarkers in neurodegenerative diseases, *Chem. Phys. Lipids* 164 (2011) 515–524.
- [28] I. Björkhem, Crossing the barrier, oxysterols as cholesterol transporters and metabolic modulators in the brain, *J. Intern. Med.* 260 (2006) 493–508.
- [29] T.M. Hughes, C. Rosano, R.W. Evans, L.H. Kuller, Brain cholesterol metabolism, oxysterols, and dementia, *J. Alzheimers Dis.* 33 (2013) 891–911.
- [30] B. Sottero, P. Gamba, S. Gargiulo, S. Leonarduzzi, G. Poli, Cholesterol oxidation products and disease: an emerging topic of interest in medicinal chemistry, *Curr. Med. Chem.* 16 (2009) 685–705.
- [31] L. Juliano, Pathways of cholesterol oxidation via non-enzymatic mechanisms, *Chem. Phys. Lipids* 164 (2011) 457–458.
- [32] G. Poli, F. Biasi, G. Leonarduzzi, Oxysterols in the pathogenesis of major chronic diseases, *Redox Biol* 1 (2013) 125–130.
- [33] E. Niki, Lipid peroxidation: physiological levels and dual biological effects, *Free Radic. Biol. Med.* 47 (2009) 469–484.
- [34] T.J. Nelson, D.L. Alkon, Oxidation of cholesterol by amyloid precursor protein and beta-amyloid peptide, *J. Biol. Chem.* 280 (2005) 7377–7387.
- [35] A. Vejux, L. Malvitte, G. Lizard, Side effects of oxysterols: cytotoxicity, oxidation, inflammation, and phospholipidosis, *Braz. J. Med. Biol. Res.* 41 (2008) 545–556.
- [36] Y. Saito, N. Noguchi, 7-Hydroxycholesterol as a possible biomarker of cellular lipid peroxidation: difference between cellular and plasma lipid peroxidation, *Biochem. Biophys. Res. Commun.* 446 (2014) 741–744.
- [37] T. Mitić, R. Andrew, B.R. Walker, P.W. Hadoko, 11 β -Hydroxysteroid dehydrogenase type 1 contributes to the regulation of 7-oxysterol levels in the arterial wall through the inter-conversion of 7-ketocholesterol and 7 β -hydroxycholesterol, *Biochimie* 95 (2013) 548–555.
- [38] J. Poirier, A. Baccichet, D. Dea, S. Gauthier, Cholesterol synthesis and lipoprotein reuptake during synaptic remodelling in hippocampus in adult rats, *Neuroscience* 55 (1993) 81–90.
- [39] D.M. Ramirez, S. Andersson, D.W. Russell, Neuronal expression and subcellular localization of cholesterol 24-hydroxylase in the mouse brain, *J. Comp. Neurol.* 507 (2008) 1676–1693.
- [40] N. Bogdanovic, L. Bretillon, E.G. Lund, U. Diczfalussy, L. Lannfelt, B. Winblad, D. W. Russell, I. Björkhem, On the turnover of brain cholesterol in patients with Alzheimer's disease: abnormal induction of the cholesterol-catabolic enzyme CYP46 in glial cells, *Neurosci. Lett.* 314 (2001) 45–48.
- [41] J. 3rd Brown, C. Theisler, S. Silberman, D. Magnuson, N. Gottardi-Littell, J. M. Lee, D. Yager, J. Crowley, K. Sambamurti, M.M. Rahman, A.B. Reiss, C. B. Eckman, B. Wolozin, Differential expression of cholesterol hydroxylases in Alzheimer's disease, *J. Biol. Chem.* 279 (2004) 34674–34681.
- [42] Y. Ohyama, S. Meaney, M. Heverin, L. Ekström, A. Brafman, M. Shafir, U. Andersson, M. Olin, G. Eggertsen, U. Diczfalussy, E. Feinstein, I. Björkhem, Studies on the transcriptional regulation of cholesterol 24-hydroxylase (CYP46A1), *J. Biol. Chem.* 281 (2006) 3810–3820.
- [43] C. Patte-Mensah, A.G. Mensah-Nyagan, Peripheral neuropathy and neurosteroid formation in the central nervous system, *Brain Res. Rev.* 57 (2008) 454–459.
- [44] S.R. Doodipala, Neurosteroids: endogenous role in the human brain and therapeutic potentials, *Prog. Brain Res.* 186 (2010) 113–137.
- [45] J.L. Do Rego, J.Y. Seong, D. Burel, J. Leprince, V. Luu-The, K. Tsutsui, M.C. Tonon, G. Pelletier, H. Vaudry, Neurosteroid biosynthesis: enzymatic pathways and neuroendocrine regulation by neurotransmitters and neuropeptides, *Front. Neuroendocrinol.* 30 (2009) 259–301.
- [46] I.H. Zwain, S.S. Yen, Neurosteroidogenesis in astrocytes, oligodendrocytes, and neurons of cerebral cortex of rat brain, *Endocrinology* 140 (1999) 3843–3852.
- [47] M. Chisari, L.N. Eisenman, D.F. Covey, S. Mennerick, C.F. Zorumski, The sticky issue of neurosteroids and GABA_A receptors, *Trends Neurosci.* 33 (2010) 299–306.
- [48] M.Y. Sun, A.J. Linsenbardt, C.M. Emmett, L.N. Eisenman, Y. Izumi, C.F. Zorumski, S. Mennerick, 24(S)-hydroxycholesterol as a modulator of neuronal signaling and survival, *Neuroscientist* (2015) 1–13.
- [49] E. Hudry, D. Van Dam, W. Kulik, P.P. De Deyn, F.S. Stet, O. Ahouansou, A. Benraiss, A. Delacourte, P. Bougnères, P. Aubourg, N. Cartier, Adeno-

- associated virus gene therapy with cholesterol 24-hydroxylase reduces the amyloid pathology before or after the onset of amyloid plaques in mouse models of Alzheimer's disease, *Mol. Ther.* 18 (2010) 44–53.
- [50] R.W. Halford, D.W. Russell, Reduction of cholesterol synthesis in the mouse brain does not affect amyloid formation in Alzheimer's disease, but does extend lifespan, *Proc. Natl. Acad. Sci. USA* 106 (2009) 3502–3506.
- [51] N. Mast, C. Charvet, I.A. Pikuleva, C.D. Stout, Structural basis of drug binding to CYP46A1, an enzyme that controls cholesterol turnover in the brain, *J. Biol. Chem.* 285 (2010) 31783–31795.
- [52] M. Shafaati, N. Mast, O. Beck, R. Nayef, G.Y. Heo, L. Björkhem-Bergman, D. Lütjohann, I. Björkhem, I.A. Pikuleva, The antifungal drug voriconazole is an efficient inhibitor of brain cholesterol 24S-hydroxylase in vitro and in vivo, *J. Lipid Res.* 51 (2010) 318–323.
- [53] C. Fourgeux, L. Martine, N. Acar, A.M. Bron, C.P. Creuzot-Garcher, L. Bretillon, In vivo consequences of cholesterol-24S-hydroxylase (CYP46A1) inhibition by voriconazole on cholesterol homeostasis and function in the rat retina, *Biochem. Biophys. Res. Commun.* 446 (2014) 775–781.
- [54] Y. Huang, W. Li, A.N. Kong, Anti-oxidative stress regulator NF-E2-related factor 2 mediates the adaptive induction of antioxidant and detoxifying enzymes by lipid peroxidation metabolite 4-hydroxynonenal, *Cell Biosci* 2 (2012) 40.
- [55] Z.H. Chen, Y. Yoshida, Y. Saito, A. Sekine, N. Noguchi, E. Niki, Induction of adaptive response and enhancement of PC12 cell tolerance by 7-hydroxycholesterol and 15-deoxy-delta(12,14)-prostaglandin J2 through up-regulation of cellular glutathione via different mechanisms, *J. Biol. Chem.* 281 (2006) 14440–14445.
- [56] Y. Saito, K. Nishio, Y. Numakawa, Y. Ogawa, Y. Yoshida, N. Noguchi, E. Niki, Protective effects of 15-deoxy-Delta12,14-prostaglandin J2 against glutamate-induced cell death in primary cortical neuron cultures: induction of adaptive response and enhancement of cell tolerance primarily through up-regulation of cellular glutathione, *J. Neurochem.* 102 (2007) 1625–1634.
- [57] M.L. Rao, D. Lütjohann, M. Ludwig, H. Kölsch, Induction of apoptosis and necrosis in human neuroblastoma cells by cholesterol oxides, *Ann. N.Y. Acad. Sci.* 893 (1999) 379–381.
- [58] D.E. Kim, Y.C. Youn, Y.K. Kim, K.M. Hong, C.S. Lee, Glycyrrhizin prevents 7-ketocholesterol toxicity against differentiated PC12 cells by suppressing mitochondrial membrane permeability change, *Neurochem. Res.* 34 (2009) 1433–1442.
- [59] E.R. Jang, C.S. Lee, 7-Ketocholesterol induces apoptosis in differentiated PC12 cells via reactive oxygen species-dependent activation of NF- κ B and Akt pathways, *Neurochem. Int.* 58 (2011) 52–59.
- [60] A. Okabe, Y. Urano, S. Itoh, N. Suda, R. Kotani, Y. Nishimura, Y. Saito, N. Noguchi, Adaptive responses induced by 24S-hydroxycholesterol through liver X receptor pathway reduce 7-ketocholesterol-caused neuronal cell death, *Redox Biol.* 2 (2013) 28–35.
- [61] P.J. Willy, K. Umeson, E.S. Ong, R.M. Evans, R.A. Heyman, D.J.L.X. R. Mangelsdorf, a nuclear receptor that defines a distinct retinoid response pathway, *Genes Dev.* 9 (1995) 1033–1045.
- [62] J. Hardy, D.J. Selkoe, The amyloid hypothesis of Alzheimer's disease: progress and problems on the road to therapeutics, *Science* 297 (2002) 353–356.
- [63] D.T. Loo, A. Copani, C.J. Pike, E.R. Whittemore, A.J. Walencewicz, C.W. Cotman, Apoptosis is induced by beta-amyloid in cultured central nervous system neurons, *Proc. Natl. Acad. Sci. USA* 90 (1993) 7951–7955.
- [64] S. Estus, H.M. Tucker, C. van Rooyen, S. Wright, E.F. Brigham, M. Wogulis, R. E. Rydel, Aggregated amyloid-beta protein induces cortical neuronal apoptosis and concomitant "apoptotic" pattern of gene induction, *J. Neurosci.* 17 (1997) 7736–7745.
- [65] J.R. Prasanthi, A. Huls, S. Thomasson, A. Thompson, E. Schommer, O. Ghribi, Differential effects of 24-hydroxycholesterol and 27-hydroxycholesterol on beta-amyloid precursor protein levels and processing in human neuroblastoma SH-SY5Y cells, *Mol. Neurodegener* 4 (2009) 1.
- [66] D. Cai, J.Y. Leem, J.P. Greenfield, P. Wang, B.S. Kim, R. Wang, K.O. Lopes, S. H. Kim, H. Zheng, P. Greengard, S.S. Sisodia, G. Thinakaran, H. Xu, Presenilin-1 regulates intracellular trafficking and cell surface delivery of beta-amyloid precursor protein, *J. Biol. Chem.* 278 (2003) 3446–3454.
- [67] J. Kim, S. Hamamoto, M. Ravazzola, L. Orzi, R. Schekman, Uncoupled packaging of amyloid precursor protein and presenilin 1 into coat protein complex II vesicles, *J. Biol. Chem.* 280 (2005) 7758–7768.
- [68] Y. Urano, I. Hayashi, N. Isoo, P.C. Reid, Y. Shibasaki, N. Noguchi, T. Tomita, T. Iwatsubo, T. Hamakubo, T. Kodama, Association of active gamma-secretase complex with lipid rafts, *J. Lipid Res.* 46 (2005) 904–912.
- [69] Y. Urano, S. Ochiai, N. Noguchi, Suppression of amyloid- β production by 24S-hydroxycholesterol via inhibition of intracellular amyloid precursor protein trafficking, *FASEB J* 27 (2013) 4305–4315.
- [70] V. Cavallucci, M. D'Amelio, F. Ceconi, A β toxicity in Alzheimer's disease, *Mol. Neurobiol.* 45 (2012) 366–378.
- [71] E. Hubin, N.A. van Nuland, K. Broersen, K. Pauwels, Transient dynamics of A β contribute to toxicity in Alzheimer's disease, *Cell Mol. Life Sci.* 71 (2014) 3507–3521.
- [72] Q. Wang, X. Yu, L. Li, J. Zheng, Inhibition of amyloid- β aggregation in Alzheimer's disease, *Curr. Pharm. Des* 20 (2014) 1223–1243.
- [73] P. Gamba, M. Guglielmotto, G. Testa, D. Monteleone, C. Zerbinati, S. Gargiulo, F. Biasi, L. Iuliano, G. Giaccone, A. Mauro, G. Poli, E. Tamagno, G. Leonarduzzi, Up-regulation of β -amyloidogenesis in neuron-like human cells by both 24- and 27-hydroxycholesterol: protective effect of N-acetyl-cysteine, *Aging Cell* 13 (2014) 561–572.
- [74] J. Popp, P. Lewczuk, H. Kölsch, S. Meichsner, W. Maier, J. Kornhuber, F. Jessen, D. Lütjohann, Cholesterol metabolism is associated with soluble amyloid precursor protein production in Alzheimer's disease, *J. Neurochem.* 123 (2012) 310–316.
- [75] H. Fukumoto, A. Deng, M.C. Irizarry, M.L. Fitzgerald, G.W. Rebeck, Induction of the cholesterol transporter ABCA1 in central nervous system cells by liver X receptor agonists increases secreted Abeta levels, *J. Biol. Chem.* 277 (2002) 48508–48513.
- [76] P. Ferrera, O. Mercado-Gómez, M. Silva-Aguilar, M. Valverde, C. Arias, Cholesterol potentiates beta-amyloid-induced toxicity in human neuroblastoma cells: involvement of oxidative stress, *Neurochem. Res.* 33 (2008) 1509–1517.
- [77] Z. Kristofiková, V. Kopecký Jr, K. Hofbauerová, P. Hovorková, D. Rířová, Complex of amyloid beta peptides with 24-hydroxycholesterol and its effect on hemicholinium-3 sensitive carriers, *Neurochem. Res.* 33 (2008) 412–421.
- [78] P. Gamba, G. Leonarduzzi, E. Tamagno, M. Guglielmotto, G. Testa, B. Sottero, S. Gargiulo, F. Biasi, A. Mauro, J. Viña, G. Poli, Interaction between 24-hydroxycholesterol, oxidative stress, and amyloid- β in amplifying neuronal damage in Alzheimer's disease: three partners in crime, *Aging Cell* 10 (2011) 403–417.
- [79] Z. Kristofiková, Z. Kríz, D. Rířová, J. Kocá, Interactions of amyloid β peptide 1–40 and cerebrosterol, *Neurochem. Res.* 37 (2012) 604–613.
- [80] H. Kölsch, D. Lütjohann, A. Tulke, I. Björkhem, M.L. Rao, The neurotoxic effect of 24-hydroxycholesterol on SH-SY5Y human neuroblastoma cells, *Brain Res.* 818 (1999) 171–175.
- [81] H. Kölsch, M. Ludwig, D. Lütjohann, M.L. Rao, Neurotoxicity of 24-hydroxycholesterol, an important cholesterol elimination product of the brain, may be prevented by vitamin E and estradiol-17 β , *J. Neural Transmission* 108 (2001) 475–488.
- [82] N. Noguchi, Y. Saito, Y. Urano, Diverse functions of 24(S)-hydroxycholesterol in the brain: a special issue on oxysterols, *Biochem. Biophys. Res. Commun.* 446 (2014) 692–696.
- [83] K. Yamanaka, Y. Saito, T. Yamamori, Y. Urano, N. Noguchi, 24(S)-Hydroxycholesterol induces neuronal cell death through necroptosis, a form of programmed necrosis, *J. Biol. Chem.* 286 (2011) 24666–24673.
- [84] K. Yamanaka, Y. Saito, J. Sakiyama, Y. Ohuchi, F. Oseto, N. Noguchi, A novel fluorescent probe with high sensitivity and selective detection of lipid hydroperoxides in cells, *RSC Adv* 2 (2012) 7894–7900.
- [85] M. Jiang, K. Zhu, J. Grenet, J.M. Lahti, Retinoic acid induces caspase-8 transcription via phospho-CREB and increases apoptotic responses to death stimuli in neuroblastoma cells, *Biochim. Biophys. Acta* 1783 (2008) 1055–1067.
- [86] L. Sun, H. Wang, Z. Wang, S. He, S. Chen, D. Liao, L. Wang, J. Yan, W. Liu, X. Lei, X. Wang, Mixed lineage kinase domain-like protein mediates necrosis signaling downstream of RIP3 kinase, *Cell* 148 (2012) 213–227.
- [87] H. Wang, L. Sun, L. Su, J. Rizo, L. Liu, L.F. Wang, F.S. Wang, X. Wang, Mixed lineage kinase domain-like protein MLKL causes necrotic membrane disruption upon phosphorylation by RIP3, *Mol. Cell* 54 (2014) 133–146.
- [88] A. Degtarev, J. Hitomi, M. Gernscheid, I.L. Ch'en, O. Korkina, X. Teng, D. Abbott, G.D. Cunny, C. Yuan, G. Wagner, S.M. Hedrick, S.A. Gerber, A. Lugovskoy, J. Yuan, Identification of RIP1 kinase as a specific cellular target of necrostatins, *Nat. Chem. Biol.* 4 (2008) 313–321.
- [89] D.K. Vo, Y. Urano, W. Takabe, Y. Saito, N. Noguchi, 24(S)-Hydroxycholesterol induces RIPK1-dependent but MLKL-independent cell death in the absence of caspase-8, *Steroids* 99 (2015) 230–237.
- [90] K. Yamanaka, Y. Urano, W. Takabe, Y. Saito, N. Noguchi, Induction of apoptosis and necroptosis by 24(S)-hydroxycholesterol is dependent on activity of acyl-CoA:cholesterol acyltransferase 1, *Cell Death Dis.* 5 (2014) e990.
- [91] T.Y. Chang, B.L. Li, C.C. Chang, Y. Urano, A. Acyl-coenzyme, cholesterol acyltransferases, *Am. J. Physiol. Endocrinol. Metab.* 297 (2009) E1–9.
- [92] V.L. Marca, M.S. Spagnuolo, L. Cigliano, D. Marasco, P. Abrescia, The enzyme lecithin-cholesterol acyltransferase esterifies cerebrosterol and limits the toxic effect of this oxysterol on SH-SY5Y cells, *J. Neurochem.* 130 (2014) 97–108.
- [93] M.X. He, Y.W. He, A role for c-FLIP(L) in the regulation of apoptosis, autophagy, and necroptosis in T lymphocytes, *Cell Death Differ.* 20 (2013) 188–197.
- [94] M. Feoktistova, P. Gericke, B. Kellert, D.P. Dimitrova, C. Langlais, M. Hupe, K. Cain, M. MacFarlane, G. Häcker, M. Leverkus, cIAPs block Ripoptosome formation, a RIP1/caspase-8 containing intracellular cell death complex differentially regulated by cFLIP isoforms, *Mol. Cell* 43 (2011) 449–463.

Esterification of 24S-OHC induces formation of atypical lipid droplet-like structures, leading to neuronal cell death^S

Wakako Takabe,* Yasuomi Urano,^{1,*} Diep-Khanh Ho Vo,* Kimiyuki Shibuya,[†] Masaki Tanno,[§] Hiroaki Kitagishi,[§] Toyoshi Fujimoto,** and Noriko Noguchi^{1,*}

Department of Medical Life Systems, Faculty of Life and Medical Sciences,* and Department of Molecular Chemistry and Biochemistry, Faculty of Sciences and Technology,[§] Doshisha University, Kyoto 610-0394, Japan; Tokyo New Drug Research Laboratories,[†] Pharmaceutical Division, Kowa Company, Ltd., Tokyo 189-0022, Japan; and Department of Anatomy and Molecular Cell Biology,** Nagoya University Graduate School of Medicine, Nagoya 466-8550, Japan

Abstract The 24(S)-hydroxycholesterol (24S-OHC), which plays an important role in maintaining brain cholesterol homeostasis, has been shown to possess neurotoxicity. We have previously reported that 24S-OHC esterification by ACAT1 and the resulting lipid droplet (LD) formation are responsible for 24S-OHC-induced cell death. In the present study, we investigate the functional roles of 24S-OHC esters and LD formation in 24S-OHC-induced cell death, and we identify four long-chain unsaturated fatty acids (oleic acid, linoleic acid, arachidonic acid, and DHA) with which 24S-OHC is esterified in human neuroblastoma SH-SY5Y cells treated with 24S-OHC. Here, we find that cotreatment of cells with 24S-OHC and each of these four unsaturated fatty acids increases prevalence of the corresponding 24S-OHC ester and exacerbates induction of cell death as compared with cell death induced by treatment with 24S-OHC alone. Using electron microscopy, we find in the present study that 24S-OHC induces formation of LD-like structures coupled with enlarged endoplasmic reticulum (ER) lumina, and that these effects are suppressed by treatment with ACAT inhibitor. Collectively, these results illustrate that ACAT1-catalyzed esterification of 24S-OHC with long-chain unsaturated fatty acid followed by formation of atypical LD-like structures at the ER membrane is a critical requirement for 24S-OHC-induced cell death.—Takabe, W., Y. Urano, D.-K. H. Vo, K. Shibuya, M. Tanno, H. Kitagishi, T. Fujimoto, and N. Noguchi. Esterification of 24S-OHC induces formation of atypical lipid droplet-like structures, leading to neuronal cell death. *J. Lipid Res.* 2016. 57: 2005–2014.

Supplementary key words acyl-CoA:cholesterol acyltransferase • Alzheimer's disease • electron microscopy • mass spectrometry • oxysterols • 24(S)-hydroxycholesterol

This work was supported in part by the Adaptable and Seamless Technology Transfer Program through target-driven R&D, Japan Science and Technology Agency Grant AS2532313Q (to Y.U.), and the Ministry of Education, Culture, Sports, Science, and Technology-supported Program for the Strategic Research Foundation at Private Universities in Japan for the years 2012–2016 and 2015–2019.

Manuscript received 16 May 2016 and in revised form 29 August 2016.

Published, JLR Papers in Press, September 19, 2016
DOI 10.1194/jlr.M068775

Copyright © 2016 by the American Society for Biochemistry and Molecular Biology, Inc.

This article is available online at <http://www.jlr.org>

The brain contains about 25% of the total amount of cholesterol in the human body (1). As the blood-brain barrier prevents cholesterol translocation between the brain and the circulation, brain cholesterol is locally produced. To maintain cholesterol homeostasis in the brain, cholesterol 24-hydroxylase (CYP46A1) converts excess amounts of cholesterol into 24(S)-hydroxycholesterol (24S-OHC), which readily crosses the blood-brain barrier (2). CYP46A1 mRNA and protein are present in neurons, but not in support cells (3). It has been reported that free 24S-OHC is present at concentrations of about 4–15 ng/mg wet weight in the human brain (4). Another report showed that 24S-OHC in four different brain areas of healthy controls was about 20 ng/mg tissue (5); assuming a volume of 1 μ l per 1 mg tissue, this would imply a concentration of 24S-OHC in brain tissue that is approximately 50 μ M. Several lines of evidence suggest that dysregulation of cholesterol and 24S-OHC metabolism in the brain has been linked to the development of neurodegenerative diseases such as Alzheimer's disease (AD) and Parkinson's disease (6–11). Several studies reported that 24S-OHC levels increase or decrease in plasma and cerebrospinal fluid of patients with AD or mild cognitive impairment (11–13); although inconclusive, the differing degrees of progression of disease may account for the different results observed. Selective expression of CYP46A1 around neuritic plaques has also been reported

Abbreviations: AA, arachidonic acid; AD, Alzheimer's disease; ADRP, adipose differentiation-related protein; CYP46A1, cholesterol 24-hydroxylase; DART, direct analysis in real time; ER, endoplasmic reticulum; EtOH, ethanol; LA, linoleic acid; LD, lipid droplet; MLKL, mixed lineage kinase domain-like; OA, oleic acid; PA, palmitic acid; RIPK, receptor-interacting protein kinase; SA, stearic acid; SCD1, stearoyl-CoA desaturase 1; 24S-OHC, 24(S)-hydroxycholesterol.

¹To whom correspondence should be addressed.

e-mail: yurano@mail.doshisha.ac.jp (Y.U.); nnoguchi@mail.doshisha.ac.jp (N.N.)

^SThe online version of this article (available at <http://www.jlr.org>) contains a supplement.

(14). Moreover, in the brains of patients with AD, increased CYP46A1 expression in astrocytes has been observed (15, 16). Furthermore, we and other groups have shown that 24S-OHC possesses a potent neurotoxicity that may be involved in the etiology of neurodegenerative disease (17, 18). We have also shown that high concentrations of 24S-OHC can induce caspase-independent cell death in human neuroblastoma SH-SY5Y cells and rat primary cortical neuronal cells (18).

Necroptosis is a form of caspase-independent programmed necrosis (19–21). Necroptosis can be caused by death receptor ligands or stimuli that induce expression of death receptor ligands under apoptotic-deficient conditions such as absence of functional caspase-8. This regulated cell death requires three proteins, these being: receptor-interacting protein kinase (RIPK)1, RIPK3, and mixed lineage kinase domain-like (MLKL). We have shown that necrostatin-1 (a specific inhibitor of RIPK1 kinase activity) or knockdown of RIPK1 significantly suppresses 24S-OHC-induced cell death (18). We further showed that RIPK1, but neither RIPK3 nor MLKL, was expressed in SH-SY5Y cells, suggesting that 24S-OHC induces RIPK1-dependent necroptosis-like cell death (22). Interestingly, we found that the neuronal cells used did not express caspase-8, which we understood to be the reason why 24S-OHC induced necroptosis-like cell death and not apoptosis. When we induced the expression of caspase-8 in SH-SY5Y cells by treating the cells with all-*trans*-retinoic acid, we found that apoptosis could be induced by 24S-OHC (23). We have also shown that 24S-OHC induces apoptosis in human T lymphoma Jurkat cells that endogenously express caspase-8, and that 24S-OHC induces RIPK1-dependent, but MLKL-independent, necroptosis-like cell death in caspase-8-deficient Jurkat cells (22). Despite clues drawn from the foregoing research, however, the specific molecular mechanisms responsible for induction of cell death have remained unclear.

ACAT1, an enzyme located in the endoplasmic reticulum (ER), forms cholesteryl esters to store or prevent cytotoxic build-up of cholesterol (24). We had previously found that ACAT1 catalyzes 24S-OHC esterification to produce at least four varieties of 24S-OHC esters, leading to formation of lipid droplets (LDs) that stained positive with the fluorescent probe, Nile red, in SH-SY5Y cells (25). Because selective ACAT1 inhibitor or ACAT1 siRNA suppresses both 24S-OHC-induced LD formation and cell death, we postulated that ACAT1-catalyzed esterification of 24S-OHC might be responsible for initiation of cell death signaling. However, even if our postulated explanation was correct, it was still unclear to us which varieties of 24S-OHC esters might have formed in the cells treated with 24S-OHC because, at the time of our previous study, no useful method had as yet been established for identifying oxysterol esters and no compounds suitable for use as 24S-OHC ester reference standards were as yet available. Moreover, it was still unclear to us at that time whether the cell death that we observed might be due to the specific cytotoxic effect of some particular 24S-OHC ester or whether it might be the accumulation of total 24S-OHC ester regardless of the

variety that was responsible. It was also unknown to us at that time whether it was accumulation of 24S-OHC ester or formation of LDs (or some other unknown phenomenon) that was responsible for cell death signaling.

In the present study, we investigate the precise association between 24S-OHC-induced cell death and the ACAT1-catalyzed 24S-OHC esterification that is responsible for LD formation. We find that there are increased amounts of esters produced by esterification of 24S-OHC with four varieties of long-chain unsaturated fatty acid in 24S-OHC-treated SH-SY5Y cells. We further show that 24S-OHC induces formation of atypical LD-like structures coupled with enlarged ER lumina in SH-SY5Y cells. We conclude that formation of atypical LD-like structures and the accompanying abnormal ER morphology, both of which are caused by accumulation of 24S-OHC esters, play an important role in 24S-OHC-induced cell death.

MATERIAL AND METHODS

Materials

ACAT inhibitor F12511 was the generous gift of Dr. Ta-Yuan Chang (Dartmouth Medical School, Hanover, NH). The 24S-OHC and various forms of esterified 24S-OHC were synthesized as we previously reported (26). All fatty acids and Nile red were obtained from Sigma-Aldrich (St. Louis, MO). BODIPY 493/503 and DAPI were from Thermo Fisher Scientific (Waltham, MA). Stearoyl-CoA desaturase 1 (SCD1) inhibitor was from BioVision (Milpitas, CA). All other chemicals, of analytical grade, were obtained from Sigma-Aldrich or Wako (Osaka, Japan).

Cell culture

Human neuroblastoma cells from the SH-SY5Y cell line were purchased from American Type Culture Collection (Manassas, VA). Cells were maintained in Dulbecco's modified Eagle's medium/nutrient mixture F-12 (Thermo Fisher Scientific), which contained 10% fetal bovine serum (Hyclone, Logan, UT) and antibiotics (100 U/ml penicillin, 100 mg/ml streptomycin; Thermo Fisher Scientific). Cells were grown at 37°C in an atmosphere of 5% CO₂.

Cell treatment

The 24S-OHC and oleic acids (OAs) were dissolved in ethanol (EtOH) and stored at –20°C. To examine toxicity or esterification of 24S-OHC in SH-SY5Y cells, cells were treated with 50 μM 24S-OHC (final concentration of EtOH in the medium was 0.5%) in the presence or absence of 50 μM of each fatty acid under study for the indicated period. To evaluate LD formation, cells were treated with 50 μM 24S-OHC or 200 μM OA for the indicated period. Control cells were treated with EtOH.

Knockdown of ACAT1 and RIPK1 by siRNA

Stealth siRNA targeting human RIPK1 (18), ACAT1 (25), and Stealth RNAi negative control were obtained from Thermo Fisher Scientific. Cells were transfected with siRNAs using Lipofectamine RNAiMax (Thermo Fisher Scientific) as previously described (18, 25). Forty-eight hours after transfection, cells were used for further analyses.

Neutral lipid staining

Neutral lipids were stained with Nile red as previously described (25) and fluorescence images were obtained using an inverted

fluorescence microscope (OLYMPUS IX71; Tokyo, Japan). To clarify the localization of neutral lipid-rich structures, cells were stained with BODIPY 493/503 (Thermo Fisher Scientific). Briefly, cells were fixed in a mixture of 3% formaldehyde and 0.025% glutaraldehyde in 0.1 M phosphate buffer (pH 7.4) for 15 min. Cells were then stained with 0.5 $\mu\text{g}/\text{ml}$ BODIPY 493/503 for 15 min at room temperature. Nuclei were counterstained by DAPI and images were obtained using confocal microscopy (Zeiss LSM710; Oberkochen, Germany).

Lipid extraction and HPLC analysis

Cellular lipids were extracted and HPLC analysis was performed as described previously (25). Briefly, after the treatment, the medium was removed and the cells were washed with PBS three times, lysed in 0.2 M NaOH, and neutralized immediately with 3 M HCl and 1 M KH_2PO_4 . The Folch method (2:1, v/v chloroform/methanol) was thereafter used to extract lipids, the chloroform phase being evaporated in a nitrogen gas environment. The dry residue was then dissolved in eluent without water, and this was subjected to HPLC analysis. HPLC was carried out using an Inertsil ODS-3 column (5 μm , 4.6 \times 250 mm; GL Science, Tokyo, Japan) in combination with a pump (PU-980 Intelligent HPLC pump; Nihon Bunko, Tokyo, Japan), an UV detector outputting a signal in units of millivolts (UV-970 Intelligent UV/VIS detector; Nihon Bunko), and a data processor (EPC-500; Eicom, Kyoto, Japan) under conditions such that flow rate of eluent (acetonitrile/2-propanol/water, 43/53/4) was 1.0 ml/min.

Direct analysis in real time-MS analysis

Synthesized 24S-OHC esters were dissolved in CHCl_3 at concentrations of approximately 10^{-4} M and the resulting solutions were subjected to measurement of mass spectra. For cellular extract, lipid extracts were fractionated by HPLC, the eluent was removed using nitrogen gas, the dry residue was dissolved in CHCl_3 (approximately 100 μl), and the resulting CHCl_3 solutions were subjected to MS analysis. Measurement of mass spectra was carried out using an LCMS 2020 instrument (Shimadzu, Kyoto, Japan) equipped with a direct analysis in real time (DART)-SVP ion source (IonSense, Inc., Saugus, MA). Helium was used as ionization gas at a temperature of 500°C. Mass spectra were obtained with the instrument set to positive ion mode.

Determination of cell viability

To determine cell viability, WST-8 assay was performed using a Cell Counting Kit-8 (Dojindo, Kumamoto, Japan) according to the manufacturer's protocol. MTT assay was performed as described previously (18). Data were expressed as percentages relative to cells treated with vehicle serving as control.

Isolation of LD-enriched fraction

Cells were resuspended in buffer A [25 mM Tris-HCl (pH 7.4), 100 mM KCl, 1 mM EDTA, 1 mM EGTA] with protease inhibitor cocktail (Nacalai Tesque, Kyoto, Japan). Cells were disrupted under high pressure by nitrogen bomb at 800 psi for 15 min, and the lysate was centrifuged for 10 min at 1,000 g at 4°C. The postnuclear supernatant was mixed with an equal volume of 1.08 M sucrose in buffer A (final sucrose concentration was 0.54 M). This postnuclear supernatant (1.25 ml) in 0.54 M sucrose in buffer A, 1.25 ml of 0.27 M sucrose in buffer A, 1.25 ml of 0.135 M sucrose in buffer A, and 1.25 ml of buffer A without KCl were layered sequentially in 5 ml tubes for ultracentrifugation (Beckman Coulter, Brea, CA). Tubes were centrifuged at 34,000 rpm at 4°C for 1 h using an Optima L-90K Ultracentrifuge (Beckman Coulter) with a swing rotor (SW 55 Ti). Following centrifugation, fractionated samples were collected at 0.5 ml intervals from the top of each tube.

Immunoblotting and MS analysis

Equal aliquots from each fraction were subjected to SDS-PAGE and immunoblotting by using primary antibodies specific for adipose differentiation-related protein (ADRP; Fitzgerald Industries International, Acton, MA), ribophorin-1 (Santa Cruz Biotechnologies, Dallas, TX), and RIPK1 (BD Biosciences, San Jose, CA) with appropriate secondary antibodies. Immunoblotting was visualized with enhanced chemiluminescence (Millipore, Billerica, MA). For each set of conditions, i.e., EtOH, 24S-OHC, and OA as indicated in Fig. 6B, the top three fractions were subjected to SDS-PAGE and were detected by silver staining using a Dodeca silver stain kit (Bio-Rad, Berkeley, CA). Visible bands obtained by silver staining were manually cut and subjected to LC-MS as described previously (6).

Electron microscopy analysis

For electron microscopy, cells cultured on glass coverslips were fixed for more than 2 h in a mixture of 2% formaldehyde and 2.5% glutaraldehyde in 0.1 M HEPES-NaOH (pH 7.4), to which 1 mM CaCl_2 had been added, and were thereafter postfixed for 1 h in a mixture of 1% osmium tetroxide and 0.1% potassium ferrocyanide in 0.1 M sodium cacodylate buffer (27), following which they were dehydrated and embedded in epoxy resin. Ultrathin sections were observed using a JEM1011 electron microscope (JEOL, Tokyo, Japan) operated at 100 kV.

Statistical analysis

Data are reported as mean \pm SD of at least three independent experiments. The statistical significance of the difference between the determinations was calculated by an ANOVA using Tukey's test for multiple comparisons. The difference was considered significant at $P < 0.05$.

RESULTS

The 24S-OHC-induced neutral lipid-rich structure formation occurred upstream of RIPK1 signaling in SH-SY5Y cells

We have previously shown that siRNA knockdown of either ACAT1 or RIPK1 significantly suppresses 24S-OHC-induced cell death (18, 25). In the present study, to examine the relationship between 24S-OHC-induced LD formation and RIPK1 activation, cells were transfected with ACAT1 (siACAT1), RIPK1 (siRIPK1), or negative control siRNA oligos for 48 h, and were then treated with 50 μM 24S-OHC or vehicle (0.5% EtOH) for a further 6 h. Consistent with previous findings, knockdown of ACAT1 was found to suppress 24S-OHC-induced Nile red-positive LD formation (Fig. 1). In contrast, knockdown of RIPK1 did not affect 24S-OHC-induced LD formation. These data suggested that 24S-OHC-induced LD formation was occurring upstream of RIPK1 signaling.

Esterified forms of 24S-OHC in which 24S-OHC was esterified with four varieties of unsaturated fatty acid were identified in SH-SY5Y cells treated with 24S-OHC

Because we had previously observed that LD formation due to accumulation of 24S-OHC esters occurs in the early stage of 24S-OHC-induced cell death (25), we next focused on identifying which fatty acids it was that were esterifying with 24S-OHC. We previously reported being able to detect

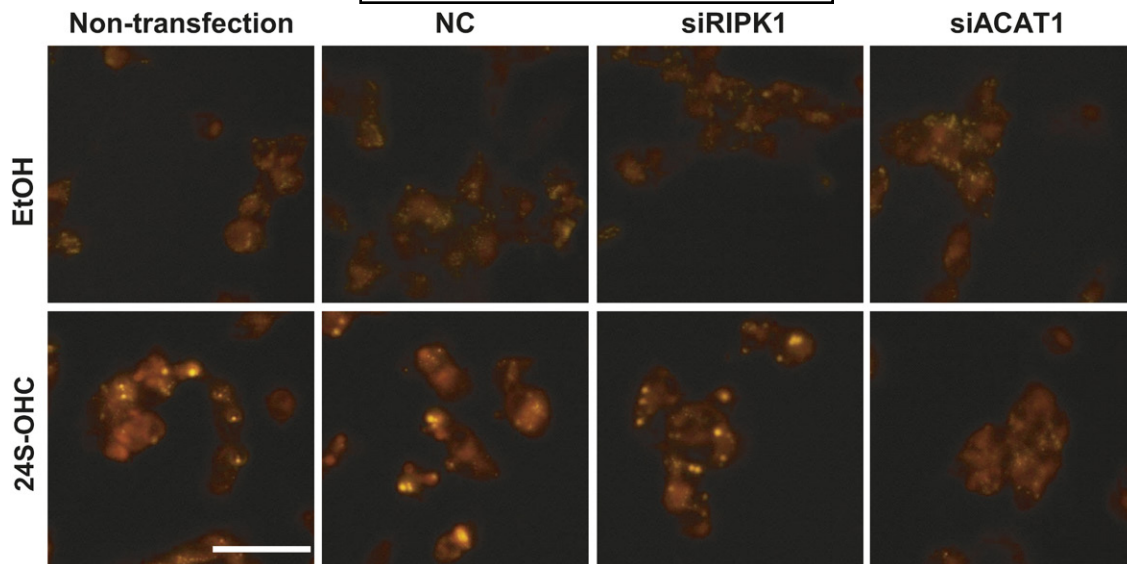


Fig. 1. Formation of Nile red-positive structure induced by 24S-OHC, which was attenuated by knockdown of ACAT1, but not by knockdown of RIPK1. SH-SY5Y cells were transfected with RIPK1 (siRIPK1), ACAT1 (siACAT1), or negative control (NC), siRNA oligo, for 48 h, and the cells were then treated with 50 μ M 24S-OHC for 6 h and were thereafter stained with Nile red. Representative images are shown. Scale bar, 50 μ m.

at least four different varieties of esterified 24S-OHC using HPLC in SH-SY5Y cells when cells were treated with 24S-OHC (25). In that study, we also confirmed that formation of 24S-OHC esters was diminished by ACAT inhibitor. Using the same technique as in our previous study, we first investigated those fatty acids which we had reason to expect might participate in 24S-OHC esterification. We focused on abundant fatty acids in the brain, such as DHA, arachidonic acid (AA), linoleic acid (LA), OA, stearic acid (SA), and palmitic acid (PA). In this first part of our present study, for each fatty acid under study, cells were cotreated with 50 μ M fatty acid and 50 μ M 24S-OHC for 6 h, and lipid extracts were thereafter subjected to HPLC analysis. As observed previously, significant increases in peak area were observed at four peaks in 24S-OHC-treated cells (Fig. 2A, 24S-OHC) as compared with the vehicle control condition (EtOH). When cells were cotreated with DHA, a marked increase in the area under peak 1 was observed (Fig. 2A, peak 1'). Similarly, treatment of cells with AA, LA, or OA showed marked increase in the area under peak 2, 3, or 4, respectively (Fig. 2A, peaks 2'–4'). In contrast, cotreatment with SA or PA did not affect the corresponding peak (Fig. 2B). These results suggested that ACAT1 favors unsaturated fatty acids for esterification of 24S-OHC.

For further identification of these four peaks, we synthesized candidate 24S-OHC esters (26), such as 24S-OHC-DHA, 24S-OHC-AA, 24S-OHC-LA, and 24S-OHC-OA (supplemental Fig. S1). We performed spiking experiments using these synthesized 24S-OHC esters by adding each synthesized 24S-OHC ester to lipid extract from 24S-OHC-treated cells, and then subjecting the ester-containing extract samples to HPLC analysis. When the lipid extract sample that contained 24S-OHC-DHA was analyzed, it was found that the area under peak 1 had increased as compared with lipid extract alone (Fig. 3, peak 1"). Similarly, lipid extract

samples that contained 24S-OHC-AA, 24S-OHC-LA, or 24S-OHC-OA showed a marked increase in the area under the respective peak 2, 3, or 4, as compared with lipid extract alone (Fig. 3, peaks 2"–4"). Note that we also measured the retention times of the peaks observed with synthesized 24S-OHC-SA and 24S-OHC-PA, and found that neither of these corresponded to any of the retention times measured for peaks 1–4 (data not shown).

Finally, we employed a novel mass spectrometric technique for yet further identification of the respective 24S-OHC esters. Prior to settling on the mass spectrometric technique that is reported below, we first tried to use gas chromatography-MS, matrix-assisted laser desorption/ionization time-of-flight-MS, and electrospray ionization-MS; despite our best attempts with each of these methods, however, we were unable to detect mass spectrographic patterns corresponding to the 24S-OHC esters due to difficulties experienced in ionizing these esters. But as we had recently established a novel technique using DART-MS that permits specific ion peaks derived from synthesized 24S-OHC esters to be detected (26), we decided to apply our DART-MS technique to identification of the 24S-OHC esters formed in SH-SY5Y cells using synthesized 24S-OHC esters as reference standards. Using a procedure similar to that described above with reference to Fig. 2, for each fatty acid under study, cells were treated with 50 μ M fatty acid and 50 μ M 24S-OHC for 6 h, following which each of the four peaks (peaks 1'–4') was collected by HPLC, and these were thereafter subjected to DART-MS analysis. For all DART-MS measurements, our instrument was operated in positive ion mode under conditions such that synthesized 24S-OHC esters were detected as $[M+NH_4]^+$ adduct ions (Fig. 4A). For example, synthesized 24S-OHC-DHA was detected by the presence of the parent ion peak at m/z 731 in the resulting spectra. The fragment ion peak at m/z 385

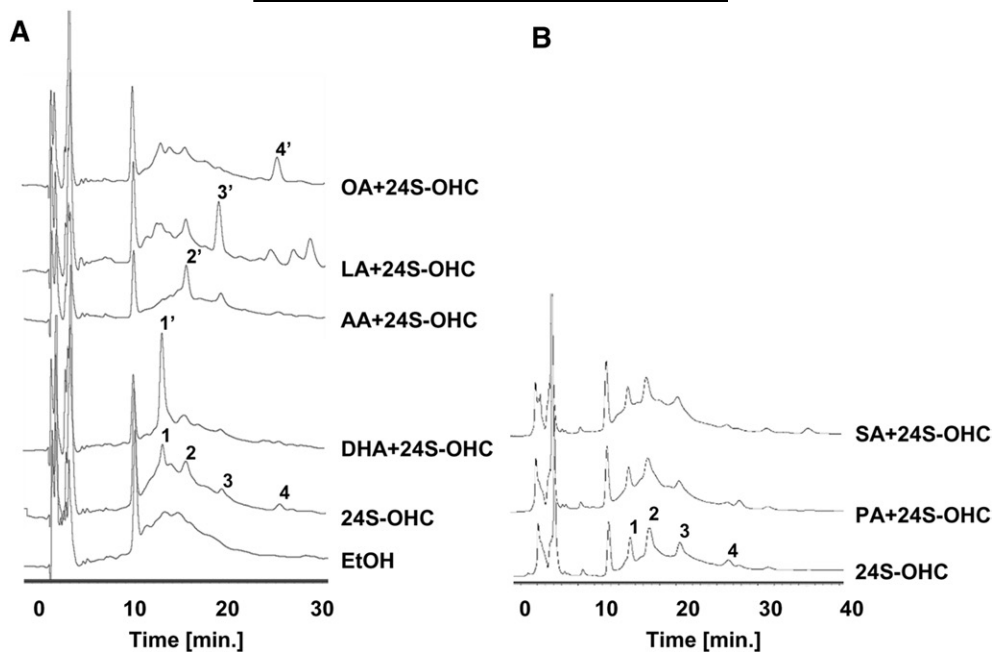


Fig. 2. The 24S-OHC preferentially formed esters with unsaturated fatty acids rather than saturated fatty acids in SH-SY5Y cells. A, B: SH-SY5Y cells were treated with vehicle (EtOH) or 50 μM 24S-OHC in the presence or absence of 50 μM unsaturated fatty acid (A) or 50 μM saturated fatty acid (B) for 6 h. Lipid extracts were subjected to HPLC analysis.

was attributed to the ester linkage. Based on comparison with synthesized 24S-OHC-DHA, -AA, -LA, -OA (Fig. 4A), and 24S-OHC-PA, -SA (supplemental Fig. S2), the adduct ion of m/z 731 at peak 1' (Fig. 4B) was found to be identical to that of synthesized 24S-OHC-DHA. Similarly, the adduct ion of m/z 707 at peak 3', m/z 683 at peak 2', and m/z 685 at peak 4' were respectively found to be identical to those of synthesized 24S-OHC-AA, 24S-OHC-LA, and 24S-OHC-OA. Collectively, these data suggest that DHA, AA, LA, and OA are fatty acids that are used for esterification of 24S-OHC in 24S-OHC-treated SH-SY5Y cells.

Effect that cotreatment with fatty acid had on 24S-OHC-induced cell death in SH-SY5Y cells

Because it was our observation that at least four varieties of 24S-OHC ester accumulate in 24S-OHC-treated cells, we considered it important to determine whether any particular 24S-OHC ester had specific cytotoxic effect or whether it was the formation of LD that triggered cell death signaling regardless of the variety of 24S-OHC ester. Unfortunately, synthesized 24S-OHC esters could not be introduced directly into cells due to their high hydrophobicity (data not shown). To evaluate the cytotoxic properties of these four varieties of 24S-OHC ester, for each unsaturated fatty acid under study, we therefore evaluated the effect of cotreatment with 24S-OHC and 50 μM unsaturated fatty acid for 24 h (Fig. 5) in SH-SY5Y cells, because in the present study we had already confirmed that there was increase of the corresponding 24S-OHC ester under the same treatment for 6 h (Fig. 2). WST-8 assay was performed to determine the effect of cotreatment with 24S-OHC and fatty acid on cell death. As a result, we found that cotreatment with 24S-OHC and each of the fatty acids under

study, except DHA, decreased cell viability as compared with treatment with 24S-OHC alone. Because we found that, at the concentration employed, none of the fatty acids induced cell death in SH-SY5Y cells, this supports our conclusion that, for all fatty acids under study for which reduction of cell viability was observed, it was cotreatment with the fatty acid and not any cytotoxicity on the part of the fatty acid itself that was responsible for the reduction of cell viability that we observed. These data suggest that it may be the accumulation of total esterified 24S-OHC and the resulting LD formation that causes cell death, independent of any specificity on the part of the ester employed for cotreatment.

The 24S-OHC induced LD-like structures along with swollen ER in SH-SY5Y cells

It is generally believed that LDs are formed to store excess lipids and protect cells against toxicity of lipids (28, 29). However, our present study showed that 24S-OHC-derived LD formation might actually be a cause of cell death. To compare 24S-OHC-induced LDs that we observed with fatty acid-induced TG-rich typical LDs, treatment with OA at high concentration (200 μM) was employed to induce LD formation. We first investigated the localization of LDs in SH-SY5Y cells in response to 50 μM 24S-OHC or 200 μM OA for 6 h by using Nile red (Fig. 6A) or the fluorescent probe, BODIPY 493/503, both of which stain neutral lipids (supplemental Fig. S3). We found as a result of our investigation that OA-treated cells had abundant LDs, these being dispersed throughout the cytoplasm, while 24S-OHC-treated cells had only a limited number of LDs, these being present near the nuclei. Cotreatment with 24S-OHC and 50 μM OA, which decreased cell viability as

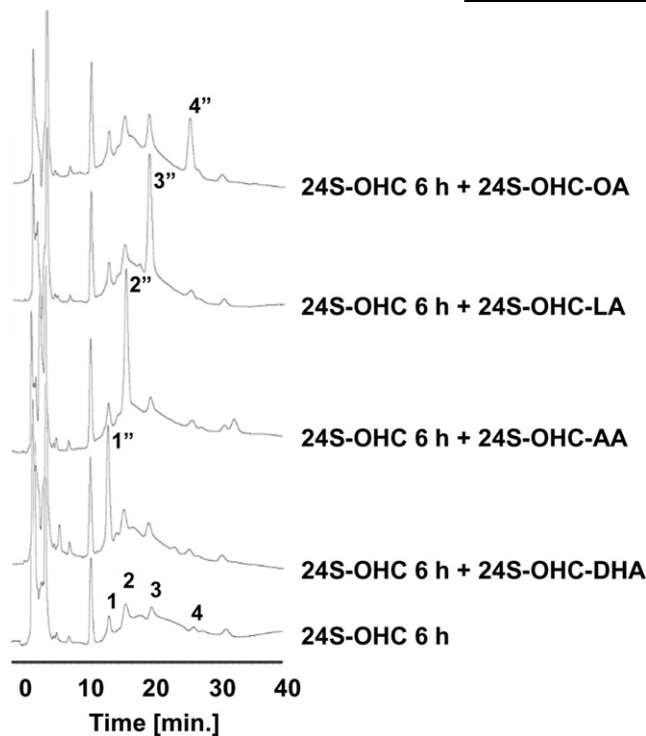


Fig. 3. Retention times of four synthesized 24S-OHC esters corresponded to those of four peaks observed in 24S-OHC-treated cells. SH-SY5Y cells were treated with 50 μ M 24S-OHC for 6 h. Lipid extracts were mixed with synthesized 4 nmol 24S-OHC-DHA, -LA, -OA, or 2 nmol 24S-OHC-AA for spiking and were thereafter subjected to HPLC analysis.

compared with treatment with 24S-OHC alone (Fig. 5), showed increases in both the number and the size of Nile red-positive LDs (Fig. 6A).

To further evaluate 24S-OHC-treated cells versus OA-treated cells with respect to formation of LDs, we applied sucrose density gradient centrifugation to attempt to isolate LD-enriched fractions from 24S-OHC-treated cells and OA-treated cells. ADRP, which is an LD-associated protein (28), was used as marker for LDs. LDs were generally recovered at the top surface, while other organelles were recovered at lower fractions along the gradient. The results showed that, for OA-treated cells, ADRP was detected at the top fraction (fraction #1), whereas the ER marker protein, ribophorin-1, and the cytosolic protein, RIPK1, were enriched in the bottom fractions (fractions #9, #10) (Fig. 6B, right panel). However, no ADRP was observed in any fraction recovered from 24S-OHC-treated cells (Fig. 6B, center panel), even though Nile red-positive and BODIPY-positive structures were observed in those cells (Figs. 1, 6A). Three fractions from the top in each condition were further subjected to silver staining and MS analysis (supplemental Fig. S4). The results showed that various proteins reported to exist in LDs (29) were detected in the top fraction obtained from OA-treated cells, but were not detected in the top fraction obtained from 24S-OHC-treated cells. Cell viability assays of 24S-OHC-treated cells and OA-treated cells showed that while significant cell death occurred in cells treated with 24S-OHC for 24 h, treatment with OA for 24 h did not induce cell death (Fig. 6C), suggesting that

typical LD formation itself was not a cytotoxic event in SH-SY5Y cells.

To further examine 24S-OHC-induced LDs in SH-SY5Y cells, we performed morphological analysis using electron microscopy. Cells were treated with either 50 μ M 24S-OHC or 200 μ M OA for 6 h, following which conventional ultrathin sections were prepared. While no LD structure was observed in EtOH-treated control cells (Fig. 7A), typical LD structures were observed in the cytoplasm of OA-treated cells (Fig. 7B). In contrast to the typical LD structures observed in OA-treated cells, in 24S-OHC-treated cells we observed atypical LD-like structures (Fig. 7C, white asterisk) that appeared to be attached to some sort of enlarged membrane structure (black star). Because our observations suggested that these enlarged membrane structures were connected to the ER membrane (Fig. 7C, arrow), we theorized that these structures might have formed as a result of enlargement of the ER lumen. Cells cotreated with 50 μ M OA and 24S-OHC showed an increased amount of 24S-OHC-OA (Fig. 2A) and decreased cell viability (Fig. 5), and it was further observed that there was an increase in the size of the atypical LD-like structures (Fig. 7D, white asterisk) that were attached to the enlarged membrane structures (Fig. 7D, black star). When cells were treated with 24S-OHC in the presence of F12511, an ACAT inhibitor, the 24S-OHC-induced atypical LD-like structures disappeared, but unknown multilamellar structures were observed (Fig. 7E, arrowhead). These observations led us to conclude that 24S-OHC induces ACAT-dependent atypical LD-like structures along with enlarged ER lumina, these being features that are different from typical OA-induced LDs, in SH-SY5Y cells.

DISCUSSION

ACAT generally catalyzes the esterification of free cholesterol with fatty acid to yield cholesteryl ester in the ER (19). Two ACAT isoenzymes, ACAT1 and ACAT2, have been identified. ACAT1 is the main isoenzyme in the brain (30). We have found that *ACAT1* mRNA, but not *ACAT2* mRNA, is expressed in SH-SY5Y cells (25). One study reported that ACAT1 showed a slight preference for oleoyl-CoA, compared with palmitoyl-, linoleoyl-, or arachidonyl-CoA, as substrate in insect cells expressing human ACAT1 (31). Another study has shown that microsomes isolated from human ACAT1-expressing CHO cells showed strong substrate preference for oleoyl-CoA, compared with linolenoyl-, arachidonyl-, or eicosapentaenoyl-CoA (32). In our present study, we showed that ACAT1 preferentially utilizes long-chain unsaturated fatty acids (OA, LA, AA, and DHA) rather than saturated fatty acids (PA and SA) for esterification of 24S-OHC. Our previous (25) and present results suggest that 24S-OHC ester forms in SH-SY5Y cells in relative amounts such that 24S-OHC-OA > 24S-OHC-LA > 24S-OHC-AA > 24S-OHC-DHA, but there was no significant difference among these four fatty acids in terms of any observed preference as substrate for ACAT1. The present study showed that at least four varieties of 24S-OHC ester

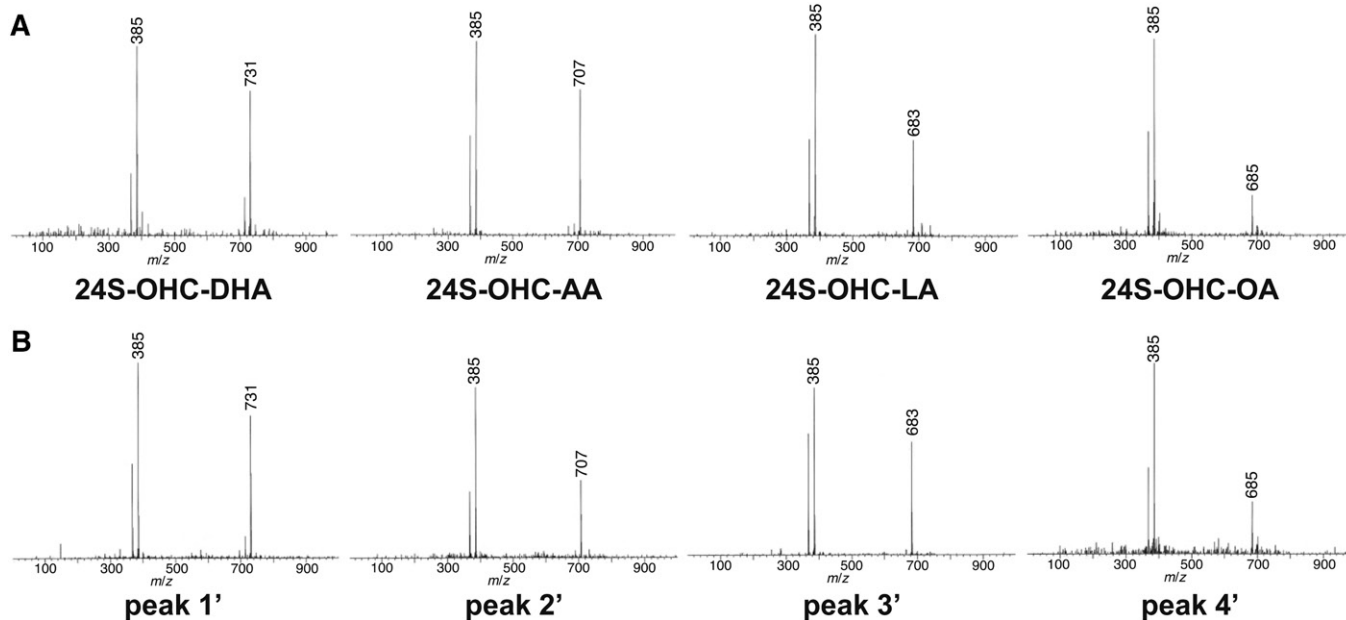


Fig. 4. DART-MS spectra of synthesized 24S-OHC esters and of fractions collected by HPLC from 24S-OHC-treated cells. For each unsaturated fatty acid under study, SH-SY5Y cells were treated with 50 μ M 24S-OHC and 50 μ M fatty acid for 6 h as in Fig. 2. Lipid extracts were subjected to HPLC analysis. Synthesized 24S-OHC esters (A) and fractions collected by HPLC (B) were further subjected to DART-MS analysis.

accumulated in 24S-OHC-treated cells, though it is possible that other minor esterified forms of 24S-OHC may also have formed in the cells. We also found that cotreatment with 24S-OHC and any of the four unsaturated fatty acids tested resulted in a cell death that was enhanced as compared with that which was induced by 24S-OHC alone. Specific enhancement of 24S-OHC-induced cell death as a result of cotreatment with any particular one of the unsaturated fatty acids tested was not observed, suggesting that it was the accumulation of total 24S-OHC ester regardless of variety, and not the specific cytotoxicity of any particular 24S-OHC ester, that was responsible for the 24S-OHC-induced cell death that we observed. We also found that 24S-OHC-induced cell death was significantly reduced when cells were cotreated with an inhibitor of SCD1 (supplemental Fig. S5); because SCD1 catalyzes the synthesis of mono-unsaturated fatty acids from saturated fatty acids, this supported the idea that esterification of 24S-OHC with unsaturated fatty acid is responsible for 24S-OHC-induced cell death. Interestingly, extracellular esterification of 24S-OHC by lecithin:cholesterol acyltransferase reduces the cytotoxic effect of 24S-OHC by limiting uptake of 24S-OHC esters by cells (33), suggesting that ACAT1-catalyzed intracellular esterification of 24S-OHC plays an important role in 24S-OHC-induced cell death.

In our present study, biochemical and morphological analysis revealed that ACAT1-mediated 24S-OHC esterification induced formation of atypical LD-like structures coupled with what appeared to be a swollen ER structure, but that the presence of OA induced typical LD formation without affecting cell viability in SH-SY5Y cells. Many lines of evidence suggest that LDs are formed within the ER membrane (28, 29). Most conventional models have assumed that formation of LDs occurs with an initial accumulation

of TG or sterol ester between the two leaflets of the ER membrane. It is believed that at some point the prenascent LD structure presumably buds off from the ER, forming a nascent LD, followed by growth of the LD. Because ACAT1 is localized in the ER membrane, the conventional thinking has been that newly produced 24S-OHC esters might accumulate between the two membrane leaflets of the ER in similar fashion as would be the case with a cholesteryl ester. However, unlike cholesteryl esters, which are entirely hydrophobic, 24S-OHC esters have a hydroxyl group at position 24 in their steroid side chain (supplemental Fig. S1). It is therefore plausible that the polar moiety at the side chain and the nonpolar moiety at the sterol ring in combination with the fatty acid portion of the 24S-OHC ester might act together to upset orientation of the 24S-OHC

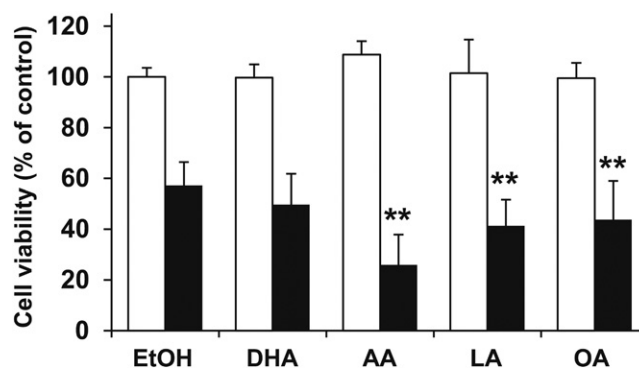


Fig. 5. Cotreatment with unsaturated fatty acid and 24S-OHC enhanced 24S-OHC-induced cell death. For each fatty acid under study, SH-SY5Y cells were treated with 50 μ M 24S-OHC in the presence or absence of 50 μ M fatty acid for 24 h. Cell viability was measured by WST-8 assay. ** $P < 0.01$, when compared with cells with 24S-OHC and EtOH.

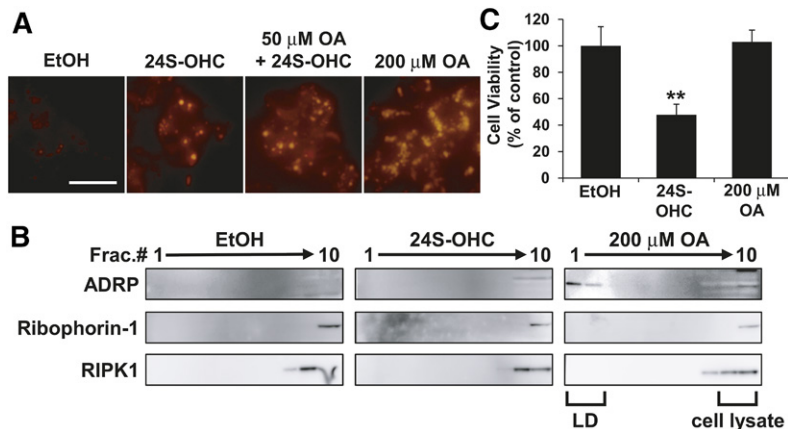


Fig. 6. The 24S-OHC-induced LD-like structures were different from OA-induced TG-rich LDs. A–C: SH-SY5Y cells were treated with 50 μM 24S-OHC or 200 μM OA for 6 h (A), 16 h (B), or 24 h (C). A: Cells were also cotreated with 50 μM 24S-OHC and 50 μM OA for 6 h. Cells were thereafter stained with Nile red. Representative images are shown. Scale bar, 20 μm. B: The postnuclear supernatants were fractionated by using ultracentrifugation with different densities of sucrose. Equal aliquots from each fraction were subjected to immunoblotting with appropriate antibodies as indicated. C: Cell viability was measured by MTT assay. ***P* < 0.01, when compared with cells with EtOH.

ester in the membrane bilayer, thereby disturbing ER membrane integrity and causing LD formation to become atypical. Because it has been reported that dysregulation of ER function, such as that which is caused by severe ER stress, can induce cell death (34–36), we postulated that disturbance of ER homeostasis by accumulation of 24S-OHC ester could trigger cell death signaling. Another possibility is that the atypical LD-like structures and/or swollen ER structures that we observed could be providing an intracellular platform to permit association of certain proteins that promote cell death signaling. Further experiments will be required to address these possibilities. It is noted that unknown multilamellar structures were observed in 24S-OHC-treated cells that had been cotreated with ACAT inhibitor. It is thought that formation of such unknown multilamellar structures might occur as a result of accumulation of free 24S-OHC. Because ACAT inhibitor suppressed

24S-OHC-induced cell death, these unknown multilamellar structures were not thought to be associated with cell death signaling. Interestingly, it has been reported that treatment with polar oxysterol (7-ketocholesterol, 7β-hydroxycholesterol, cholesterol-5β, 6β epoxide) induced a multilamellar cytoplasmic structure that was predominantly lysosomal in origin in various cell types (37, 38). Further studies are needed to characterize the multilamellar structures that were observed in the present study.

With respect to methodology, in our present study we found that we were able to effectively ionize 24S-OHC esters using the DART method. Although mass spectrometric analysis is a powerful tool to investigate unknown biochemical compounds, inability to ionize esterified forms of sterols and sterol derivatives has forced many researchers to employ the saponification method, which unfortunately only permits evaluation of total sterol content (25, 39). In

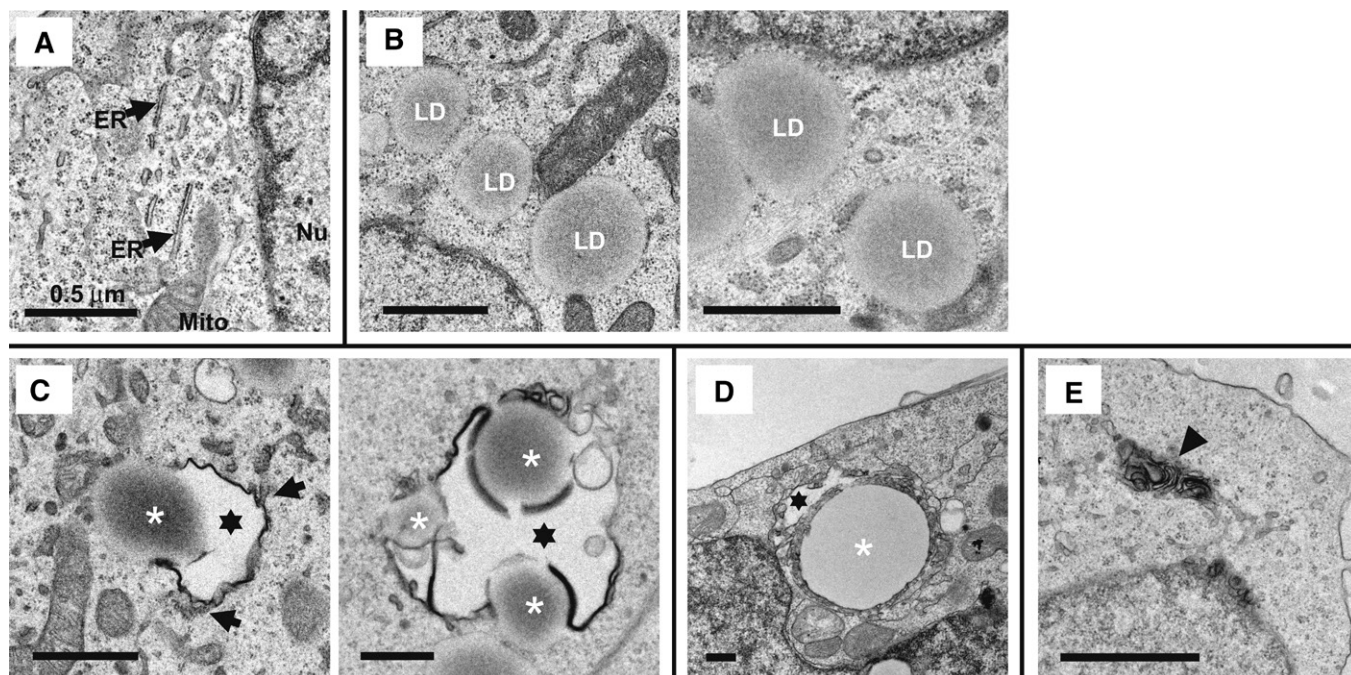


Fig. 7. The 24S-OHC induced atypical LD-like structures in SH-SY5Y cells. A–E: SH-SY5Y cells were treated with EtOH (A), 200 μM OA (B), 50 μM 24S-OHC (C), 50 μM 24S-OHC with 50 μM OA (D), or 50 μM 24S-OHC with 5 μM F-12511 (E) for 6 h. Cells were subjected to electron microscopy. Representative images are shown. Scale bar, 0.5 μm. Arrows indicate ER. White asterisks indicate LD-like structures. Black star indicates swelling of ER lumen. Arrowhead indicates unknown multilamellar structure.

contrast, with DART analysis, it is possible to detect the parent ion peak of molecules as they exist in their esterified form, without the need for additives, pretreatment, or other such potentially sample-altering methods of preparation. Because DART-MS analysis cannot easily distinguish between different isomers under current conditions, DART-MS analysis must be coupled with a chromatographic technique, such as HPLC, using a suitable column and the synthetic standard compounds if it to be used for identification of compounds. We propose that DART-MS analysis may serve as a useful tool for investigation not just of 24S-OHC esters, as in our present study, but of a wide variety of esters of sterols and fatty acids. For example, there has been growing interest in oxysterol research because there are a number of bioactivities of oxysterols that have received much attention (40, 41), and oxysterols also have potential for use as biomarkers of neurodegenerative diseases (10, 42, 43). Although it will be necessary to devise appropriate techniques before DART-MS can be used for precise quantitative analysis, it is thought that the DART-MS method will ultimately be valuable for evaluation not only of free oxysterol, but also of oxysterol esters in the tissue, plasma, and cerebrospinal fluid of patients suffering from neurodegenerative disease.

Because we have previously shown that ACAT1-mediated 24S-OHC esterification occurs upstream of the switching point at which the determination is made as to whether cell death will be apoptotic or necroptosis-like (22, 25), the atypical LD-like structures and swollen ER that we observed to form as a result of treatment with 24S-OHC should also play an important role in 24S-OHC-induced caspase-dependent apoptosis. Unlike the extrinsic pathway for programmed cell death in which the cell surface death receptor is stimulated by its ligand (44), the morphological abnormalities that we observed to occur as a result of treatment with 24S-OHC, i.e., atypical LD-like structures and swollen ER, are intracellular events. It is therefore thought likely that the cell death machinery that is activated in 24S-OHC-induced cell death is different from that which is activated in death receptor-mediated cell death. In line with our observations, it has recently been reported that ER stress induces ligand-independent necroptosis in L929 mouse fibroblast cells (45). It should be noted, however, with regard to physiological relevance, that it is not clear that the changes observed in our present study would necessarily occur in accompaniment to the increase in CYP46A1 expression (14–16) or the increase in brain 24S-OHC level that has been observed in early- and middle-stage AD (11–13). Whereas LD structures have been observed in brain tissue from AD patients and in AD mouse models (46–48), there remains a need to elucidate whether an increase in 24S-OHC esters and formation of atypical LD-like structures, as reported in our present study, occur in vivo as a consequence of the normal progression of AD. In conclusion, our present study suggests that ACAT1-mediated esterification of 24S-OHC with long-chain unsaturated fatty acid and formation of atypical LD-like structures with abnormal ER morphology play important roles in 24S-OHC-induced cell death in SH-SY5Y cells. 

The authors thank Dr. Ta-Yuan Chang for providing valuable reagents. The authors also thank Norie Kato and Kyoko Urano for research support and Gerry Peters (JTT K.K., Takatsuki, Japan) for his careful editing of the manuscript.

REFERENCES

- Dietschy, J. M., and S. D. Turley. 2004. Cholesterol metabolism in the central nervous system during early development and in the mature animal. *J. Lipid Res.* **45**: 1375–1397.
- Russell, D. W., R. W. Halford, D. M. Ramirez, R. Shah, and T. Kotti. 2009. Cholesterol 24-hydroxylase: an enzyme of cholesterol turnover in the brain. *Annu. Rev. Biochem.* **78**: 1017–1040.
- Lund, E. G., J. M. Guileyardo, and D. W. Russell. 1999. cDNA cloning of cholesterol 24-hydroxylase, a mediator of cholesterol homeostasis in the brain. *Proc. Natl. Acad. Sci. USA.* **96**: 7238–7243.
- Lütjohann, D., O. Breuer, G. Ahlborg, I. Nennesmo, A. Sidén, U. Diczfalusy, and I. Björkhem. 1996. Cholesterol homeostasis in human brain: evidence for an age-dependent flux of 24S-hydroxycholesterol from the brain into the circulation. *Proc. Natl. Acad. Sci. USA.* **93**: 9799–9804.
- Heverin, M., N. Bogdanovic, D. Lütjohann, T. Bayer, I. Pikuleva, L. Bretillon, U. Diczfalusy, B. Winblad, and I. Björkhem. 2004. Changes in the levels of cerebral and extracerebral sterols in the brain of patients with Alzheimer's disease. *J. Lipid Res.* **45**: 186–193.
- Noguchi, N., Y. Saito, and Y. Urano. 2014. Diverse functions of 24(S)-hydroxycholesterol in the brain. *Biochem. Biophys. Res. Commun.* **446**: 692–696.
- Noguchi, N., Y. Urano, W. Takabe, and Y. Saito. 2015. New aspects of 24(S)-hydroxycholesterol in modulating neuronal cell death. *Free Radic. Biol. Med.* **87**: 366–372.
- Urano, Y., S. Ochiai, and N. Noguchi. 2013. Suppression of amyloid- β production by 24S-hydroxycholesterol via inhibition of intracellular amyloid precursor protein trafficking. *FASEB J.* **27**: 4305–4315.
- Okabe, A., Y. Urano, S. Itoh, N. Suda, R. Kotani, Y. Nishimura, Y. Saito, and N. Noguchi. 2013. Adaptive responses induced by 24S-hydroxycholesterol through liver X receptor pathway reduce 7-ketocholesterol-caused neuronal cell death. *Redox Biol.* **2**: 28–35.
- Jeitner, T. M., I. Voloshyna, and A. B. Reiss. 2011. Oxysterol derivatives of cholesterol in neurodegenerative disorders. *Curr. Med. Chem.* **18**: 1515–1525.
- Sun, M. Y., A. J. Linsenbardt, C. M. Emmett, L. N. Eisenman, Y. Izumi, C. F. Zorumski, and S. Mennerick. 2016. 24(S)-Hydroxycholesterol as a modulator of neuronal signaling and survival. *Neuroscientist.* **22**: 132–144.
- Shafaati, M., A. Solomon, M. Kivipelto, I. Björkhem, and V. Leoni. 2007. Levels of ApoE in cerebrospinal fluid are correlated with Tau and 24S-hydroxycholesterol in patients with cognitive disorders. *Neurosci. Lett.* **425**: 78–82.
- Lütjohann, D., A. Papassotiropoulos, I. Björkhem, S. Locatelli, M. Bagli, R. D. Oehring, U. Schlegel, F. Jessen, M. L. Rao, K. von Bergmann, et al. 2000. Plasma 24S-hydroxycholesterol (cerebrosterol) is increased in Alzheimer and vascular demented patients. *J. Lipid Res.* **41**: 195–198.
- Brown 3rd, J., C. Theisler, S. Silberman, D. Magnuson, N. Gottardi-Littell, J. M. Lee, D. Yager, J. Crowley, K. Sambamurti, M. M. Rahman, et al. 2004. Differential expression of cholesterol hydroxylases in Alzheimer's disease. *J. Biol. Chem.* **279**: 34674–34681.
- Bogdanovic, N., L. Bretillon, E. G. Lund, U. Diczfalusy, L. Lannfelt, B. Winblad, D. W. Russell, and I. Björkhem. 2001. On the turnover of brain cholesterol in patients with Alzheimer's disease. Abnormal induction of the cholesterol-catabolic enzyme CYP46 in glial cells. *Neurosci. Lett.* **314**: 45–48.
- Tian, G., Q. Kong, L. Lai, A. Ray-Chaudhury, and C. L. Lin. 2010. Increased expression of cholesterol 24S-hydroxylase results in disruption of glial glutamate transporter EAAT2 association with lipid rafts: a potential role in Alzheimer's disease. *J. Neurochem.* **113**: 978–989.
- Kölsch, H., D. Lütjohann, A. Tulke, I. Björkhem, and M. L. Rao. 1999. The neurotoxic effect of 24-hydroxycholesterol on SH-SY5Y human neuroblastoma cells. *Brain Res.* **818**: 171–175.
- Yamanaka, K., Y. Saito, T. Yamamori, Y. Urano, and N. Noguchi. 2011. 24(S)-hydroxycholesterol induces neuronal cell death through

- necroptosis, a form of programmed necrosis. *J. Biol. Chem.* **286**: 24666–24673.
19. Christofferson, D. E., and J. Yuan. 2010. Necroptosis as an alternative form of programmed cell death. *Curr. Opin. Cell Biol.* **22**: 263–268.
20. Vandenabeele, P., L. Galluzzi, T. Vanden Berghe, and G. Kroemer. 2010. Molecular mechanisms of necroptosis: an ordered cellular explosion. *Nat. Rev. Mol. Cell Biol.* **11**: 700–714.
21. Vanden Berghe, T., A. Linkermann, S. Jouan-Lanhouet, H. Walczak, and P. Vandenabeele. 2014. Regulated necrosis: the expanding network of non-apoptotic cell death pathways. *Nat. Rev. Mol. Cell Biol.* **15**: 135–147.
22. Vo, D. K., Y. Urano, W. Takabe, Y. Saito, and N. Noguchi. 2015. 24(S)-Hydroxycholesterol induces RIPK1-dependent but MLKL-independent cell death in the absence of caspase-8. *Steroids*. **99(Pt B)**: 230–237.
23. Nakazawa, T., Y. Miyonoki, Y. Urano, M. Uehara, Y. Saito, and N. Noguchi. Effect of vitamin E on 24(S)-hydroxycholesterol-induced necroptosis-like cell death and apoptosis. *J. Steroid Biochem. Mol. Biol.* Epub ahead of print. March 4, 2016; doi:10.1016/j.jsbmb.2016.03.003.
24. Chang, T. Y., B. L. Li, C. C. Chang, and Y. Urano. 2009. Acyl-coenzyme A:cholesterol acyltransferases. *Am. J. Physiol. Endocrinol. Metab.* **297**: E1–E9.
25. Yamanaka, K., Y. Urano, W. Takabe, Y. Saito, and N. Noguchi. 2014. Induction of apoptosis and necroptosis by 24(S)-hydroxycholesterol is dependent on activity of acyl-CoA:cholesterol acyltransferase 1. *Cell Death Dis.* **5**: e990.
26. Shibuya, K., T. Watanabe, Y. Urano, W. Takabe, N. Noguchi, and H. Kitagishi. 2016. Synthesis of 24(S)-hydroxycholesterol esters responsible for the induction of neuronal cell death. *Bioorg. Med. Chem.* **24**: 2559–2566.
27. White, D. L., J. E. Mazurkiewicz, and R. J. Barnett. 1979. A chemical mechanism for tissue staining by osmium tetroxide-ferrocyanide mixtures. *J. Histochem. Cytochem.* **27**: 1084–1091.
28. Walther, T. C., and R. V. Farese, Jr. 2012. Lipid droplets and cellular lipid metabolism. *Annu. Rev. Biochem.* **81**: 687–714.
29. Ohsaki, Y., J. Cheng, M. Suzuki, Y. Shinohara, A. Fujita, and T. Fujimoto. 2009. Biogenesis of cytoplasmic lipid droplets: from the lipid ester globule in the membrane to the visible structure. *Biochim. Biophys. Acta.* **1791**: 399–407.
30. Bryleva, E. Y., M. A. Rogers, C. C. Chang, F. Buen, B. T. Harris, E. Rousselet, N. G. Seidah, S. Oddo, F. M. LaFerla, T. A. Spencer, et al. 2010. ACAT1 gene ablation increases 24(S)-hydroxycholesterol content in the brain and ameliorates amyloid pathology in mice with AD. *Proc. Natl. Acad. Sci. USA.* **107**: 3081–3086.
31. Cases, S., S. Novak, Y. W. Zheng, H. M. Myers, S. R. Lear, E. Sande, C. B. Welch, A. J. Lusis, T. A. Spencer, B. R. Krause, et al. 1998. ACAT-2, a second mammalian acyl-CoA:cholesterol acyltransferase. Its cloning, expression, and characterization. *J. Biol. Chem.* **273**: 26755–26764.
32. Seo, T., P. M. Oelkers, M. R. Giattina, T. S. Worgall, S. L. Sturley, and R. J. Deckelbaum. 2001. Differential modulation of ACAT1 and ACAT2 transcription and activity by long chain free fatty acids in cultured cells. *Biochemistry.* **40**: 4756–4762.
33. La Marca, V., M. S. Spagnuolo, L. Cigliano, D. Marasco, and P. Abrescia. 2014. The enzyme lecithin-cholesterol acyltransferase esterifies cerebrosterol and limits the toxic effect of this oxysterol on SH-SY5Y cells. *J. Neurochem.* **130**: 97–108.
34. Tabas, I., and D. Ron. 2011. Integrating the mechanisms of apoptosis induced by endoplasmic reticulum stress. *Nat. Cell Biol.* **13**: 184–190.
35. Hetz, C. 2012. The unfolded protein response: controlling cell fate decisions under ER stress and beyond. *Nat. Rev. Mol. Cell Biol.* **13**: 89–102.
36. Sano, R., and J. C. Reed. 2013. ER stress-induced cell death mechanisms. *Biochim. Biophys. Acta.* **1833**: 3460–3470.
37. Miguet-Alfonsi, C., C. Prunet, S. Monier, G. Bessède, S. Lemaire-Ewing, A. Berthier, F. Ménétrier, D. Néel, P. Gambert, and G. Lizard. 2002. Analysis of oxidative processes and of myelin figures formation before and after the loss of mitochondrial transmembrane potential during 7beta-hydroxycholesterol and 7-ketocholesterol-induced apoptosis: comparison with various pro-apoptotic chemicals. *Biochem. Pharmacol.* **64**: 527–541.
38. Vejux, A., E. Kahn, F. Ménétrier, T. Montange, J. Lherminier, J. M. Riedinger, and G. Lizard. 2007. Cytotoxic oxysterols induce caspase-independent myelin figure formation and caspase-dependent polar lipid accumulation. *Histochem. Cell Biol.* **127**: 609–624.
39. Griffiths, W. J., and Y. Wang. 2009. Analysis of neurosterols by GC-MS and LC-MS/MS. *J. Chromatogr. B Analyt. Technol. Biomed. Life Sci.* **877**: 2778–2805.
40. Luu, W., L. J. Sharpe, I. Capell-Hattam, I. C. Gelissen, and A. J. Brown. 2016. Oxysterols: old tale, new twists. *Annu. Rev. Pharmacol. Toxicol.* **56**: 447–467.
41. Olsen, B. N., P. H. Schlesinger, D. S. Ory, and N. A. Baker. 2012. Side-chain oxysterols: from cells to membranes to molecules. *Biochim. Biophys. Acta.* **1818**: 330–336.
42. Hughes, T. M., C. Rosano, R. W. Evans, and L. H. Kuller. 2013. Brain cholesterol metabolism, oxysterols, and dementia. *J. Alzheimers Dis.* **33**: 891–911.
43. Leoni, V., and C. Caccia. 2011. Oxysterols as biomarkers in neurodegenerative diseases. *Chem. Phys. Lipids.* **164**: 515–524.
44. Galluzzi, L., I. Vitale, J. M. Abrams, E. S. Alnemri, E. H. Baehrecke, M. V. Blagosklonny, T. M. Dawson, V. L. Dawson, W. S. El-Deiry, S. Fulda, et al. 2012. Molecular definitions of cell death subroutines: recommendations of the Nomenclature Committee on Cell Death 2012. *Cell Death Differ.* **19**: 107–120.
45. Saveljeva, S., S. L. Mc Laughlin, P. Vandenabeele, A. Samali, and M. J. Bertrand. 2015. Endoplasmic reticulum stress induces ligand-independent TNFR1-mediated necroptosis in L929 cells. *Cell Death Dis.* **6**: e1587.
46. Gómez-Ramos, P., and M. Asunción Morán. 2007. Ultrastructural localization of intraneuronal Abeta-peptide in Alzheimer disease brains. *J. Alzheimers Dis.* **11**: 53–59.
47. Hamilton, L. K., A. Aumont, C. Julien, A. Vadnais, F. Calon, and K. J. Fernandes. 2010. Widespread deficits in adult neurogenesis precede plaque and tangle formation in the 3xTg mouse model of Alzheimer's disease. *Eur. J. Neurosci.* **32**: 905–920.
48. Yang, D. S., P. Stavrides, M. Saito, A. Kumar, J. A. Rodriguez-Navarro, M. Pawlik, C. Huo, S. U. Walkley, M. Saito, A. M. Cuervo, et al. 2014. Defective macroautophagic turnover of brain lipids in the TgCRND8 Alzheimer mouse model: prevention by correcting lysosomal proteolytic deficits. *Brain.* **137**: 3300–3318.

Supplemental figure legends

Figure S1 Chemical structures of 24S-OHC esters

The molecular weight of each 24S-OHC ester is indicated.

Figure S2 DART-MS spectra of synthesized 24S-OHC-PA and 24S-OHC-SA.

Synthesized 24S-OHC esters (24S-OHC-PA and 24S-OHC-SA) were analyzed by DART-MS analysis.

Figure S3 Bodipy 493/503 staining of 24S-OHC-induced LD-like structures.

SH-SY5Y cells were treated with 50 μ M 24S-OHC or 200 μ M oleic acid for 6 h as in Figure 6A. Cells were stained with Bodipy 493/503 (green) and DAPI (blue). Representative images are shown. Bar, 20 μ m.

Figure S4 Silver staining and MS analysis of LD-enriched fraction.

SH-SY5Y cells were treated with 50 μ M 24S-OHC or 200 μ M oleic acid for 16 h as in Figure 6B. The post-nuclear supernatants were fractionated by using ultracentrifugation with different densities of sucrose. The top fraction for each set of conditions was subjected to MS analysis.

Figure S5 SCD1 inhibitor suppressed 24S-OHC-induced cell death in SH-SY5Y cells.

SH-SY5Y cells were pretreated with SCD1 inhibitor for 15 min and were then treated with 50 μ M 24S-OHC for 24 h. Cell viability was measured by WST-8 assay. *, $p < 0.05$, when compared with cells with 24S-OHC without SCD1 inhibitor.

Figure S1

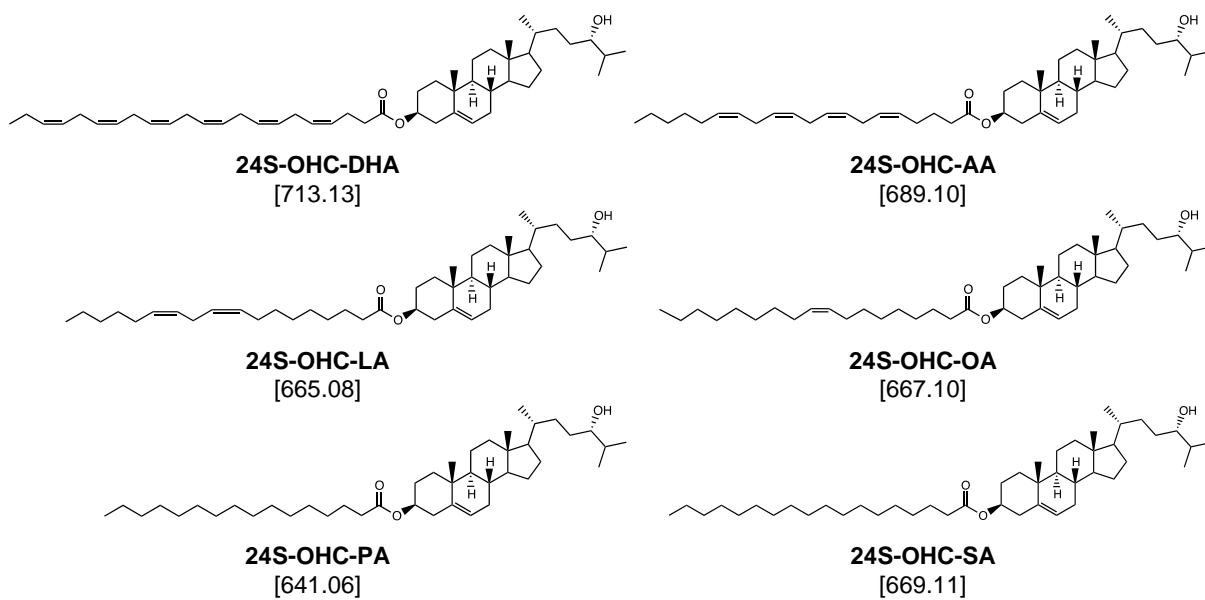


Figure S2

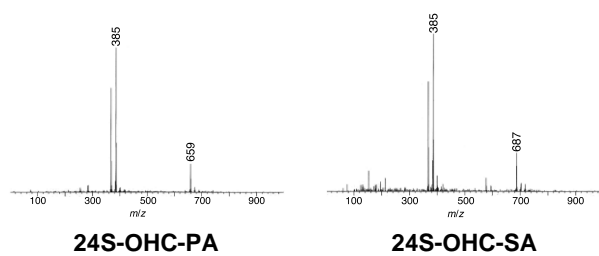


Figure S3

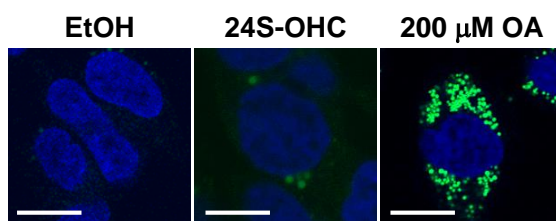


Figure S4

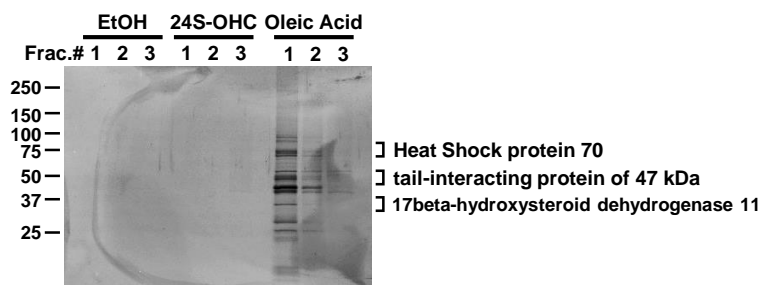
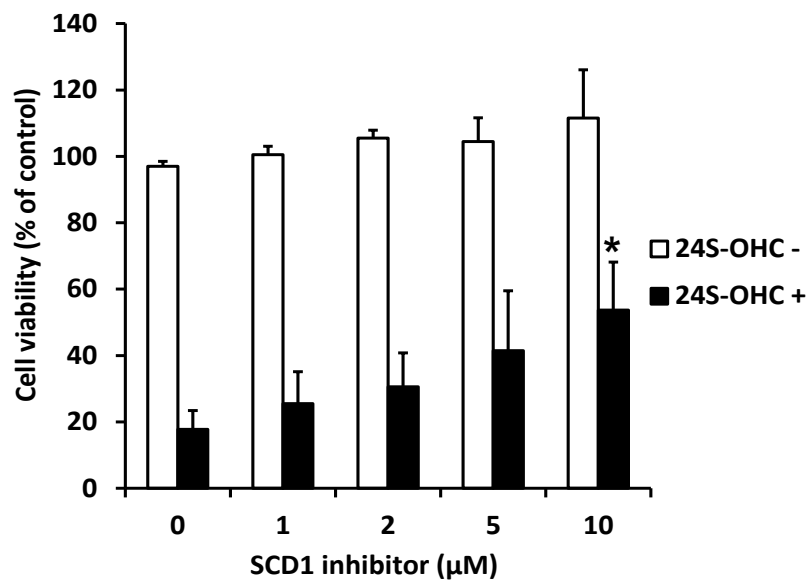


Figure S5



神経病理におけるイオンチャネルの役割と 細胞内輸送の異常についての研究

御園生裕明（脳科学研究科・教授）

廣野守俊（研究開発推進機構・特任准教授）

渡辺祥司（研究開発推進機構・特任助教）

1. はじめに

高次神経機能障害研究センターにおける当研究プロジェクトの目的は、神経機能障害における電位依存性イオンチャネルおよびその細胞内輸送機構の役割を明らかにすることである。特に、興奮性障害とアルツハイマー病に焦点を当て研究を行ってきた。

電位依存性イオンチャネルは神経細胞機能に不可欠の分子であり、その分子機能の阻害は重篤な神経機能障害を引き起こす。実際にてんかんを含む多くの神経障害が、これらチャネル遺伝子の異常から生じることが明らかになってきており、チャネロパシーという疾患概念が生まれている。本研究では、(1) 小脳運動失調に関与する Ca^{2+} 依存性 BK チャネルによる、軸索興奮性の制御メカニズム、(2) イオンチャネルの細胞内輸送メカニズムの解明とその病理的破綻について研究を行い、いくつかの重要な成果を得た。また、(3) 細胞内輸送に関わり、またアルツハイマー病の病原因子であるタウについても研究を行い、正常な状態でのタウの軸索局在化メカニズムと、病的な状態においてどのようにこのメカニズムが破綻するのかについて検討を行った。

2. 研究の背景

(1) BK チャネル遺伝子 KCNMA1 を欠失したマウスは小脳性運動失調を呈する。また BK チャネルの阻害がプルキンエ細胞の活動電位発火を顕著に変化させることから、その小脳における役割が特に注目されている。BK チャネルはプルキンエ細胞の細胞体と樹上突起に顕著に発現している (Misonou et al., 2005, J. Comp. Neurol.)。BK チャネルが生理的な範囲の膜電位

で開くためには細胞内 Ca^{2+} 濃度の上昇が必要であり、 Ca^{2+} 変動がほとんど見られない軸索ではなく、 Ca^{2+} チャネルが豊富な細胞体に局在していることは機能的な妥当性がある。しかしわれわれは独自に、BK チャネルがプルキンエ細胞の有髄軸索上で、ランビエ絞輪 (node) の近傍である paranodal junction に局在していることを見いだした (図1)。本研究では、「プルキンエ軸索には Ca^{2+} シグナリングが存在し、BK チャネルによって、跳躍伝導の各点で局所的な活動電位の制御が行われている」と仮説し、その検証を行った。また、その機能障害によって軸索内活動電位伝搬が以上を呈することを明らかにした。

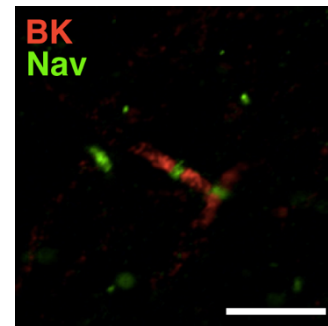


図1 Paranode への軸索 BK チャネルの局在。BK チャネルはランビエ絞輪に局在する電位依存性 Na^+ チャネル (Nav) を挟む paranode に局在する。

(2) 細胞内小胞輸送はイオンチャネルや受容体など、神経細胞機能に不可欠な膜タンパク質を輸送し、シナプスや神経終末等の特異的な膜ドメインへと局在化させる極めて重要な機構であり、その分子メカニズムの研究が活発に行われている。またアルツハイマー病やハンチントン病の神経病理において小胞輸送機構に異常が生じることが示唆されており、その詳細なメカニズムの解明は喫緊の課題となっている。しかし、輸送小胞へのタンパク質の選別や、小胞を特定の膜ドメインに輸送し融合させるメカニズムなど、その分子機構については未知の部分が多い。そこで本研究では、最先端の生細胞内蛍光イメージング技術を用いて、異なった膜ドメインに局在する様々なイオンチャネル分子の細胞内小胞輸送を可視化・解析し、神経細胞における小胞輸送メカニズムの研究を行った。特に、てんかんと関わりが知られている2つの電位依存性 K^+ チャネルについて、これらのチャネルが細胞膜に輸送されるメカニズムを明らかにした。

(3) 神経細胞内小胞輸送メカニズム研究の一端として、軸索内輸送に関わっていると考えられている微小管結合タンパク質タウについての研究を行った。タウは通常軸索に局在するが、アルツハイマー病などの神

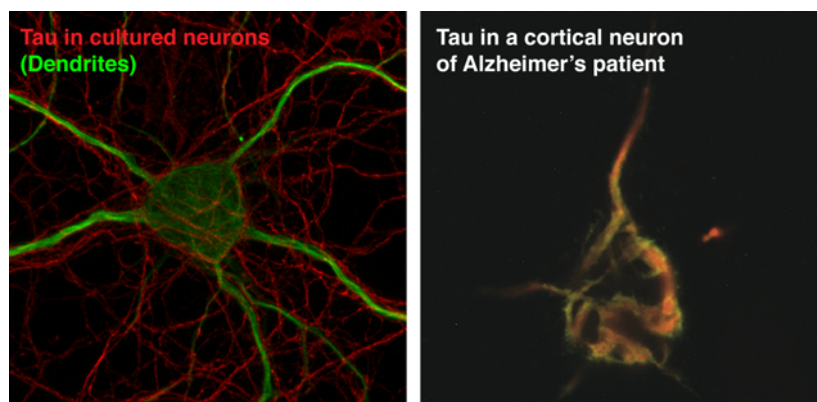


図2 タウの局在とその異常。左、内在性タウの培養神経細胞における局在。軸索に特異的に局在している。右、アルツハイマー病脳におけるタウ局在化の異常。細胞体と樹状突起にタウが蓄積している。

経変性疾患では樹状突起への局在異常を示す (図2)。われわれは正常な状態でのタウの局在化メカニズムを明らかにし、病的な状態においてどのようにこのメカニズムが破綻するのかについて検討を行った。

3. 結果

(1) BK チャンネルによる軸索内活動電位伝搬の制御

軸索 BK チャンネルの役割を検討するためには、軸索からの電気生理学的記録が必要になる。我々は、細胞外電極からの刺激により軸索内で活動電位を惹起し、逆行性に軸索を伝導する活動電位を細胞体より記録する手法を用いた (図3)。

この記録中に BK チャンネルの阻害剤を途中の軸索に局所投与することにより、BK チャンネルが軸索内活動電位伝導にどのような役割を持つかを検討することができる。まず我々は、この手法で記録できる逆行性活動電位の特性について調べた。その結果、軸索に高頻度刺激を行うと、100 Hz 程度までは刺激によく追従した活動電位が記録できるが、それ以上の頻度では発火に至らず、失敗する例 (failure) が見られた。ここで BK チャンネルの阻害剤である paxilline および Penitrem A を局所的に軸索に投与すると、この failure が増える、すなわち発火に失敗する確率が増大することが明らかになった (図4)。この結果は、有髄軸索の paranode に局在する BK チャンネルが、軸索内活動電位の高頻度発火及び伝導を支えていることを示唆している。

また、この軸索 BK チャンネルによる制御が、プルキンエ細胞の最終的な出力である、小脳核細胞へのシナプス伝達に影響を与えているかどうかについても検討を行った。この実験では、細胞外電極からの刺激により

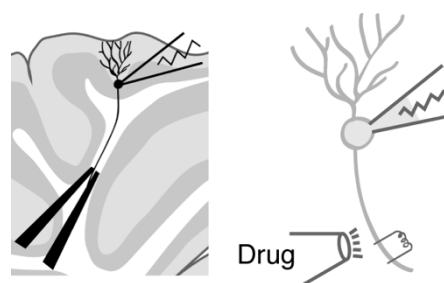


図3 電気生理学記録の概要。(左) 小脳スライス内のプルキンエ細胞軸索への刺激と、細胞体からの逆行性活動電位の記録の模式図。(右) 局所的な BK チャンネル阻害剤投与の模式図。

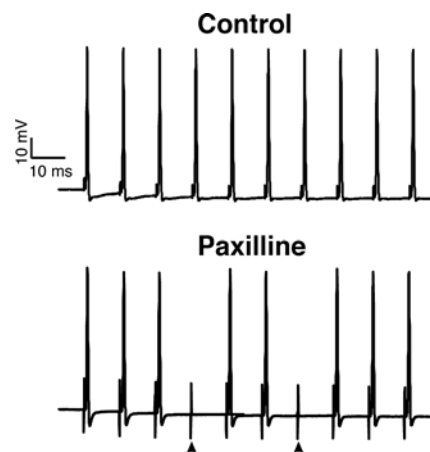


図4 軸索BKチャンネル阻害による活動電位の発火忠実性の低下。阻害前は100 Hz 刺激に対して忠実に発火が起こったが、BK チャンネル阻害剤である paxilline を軸索に局所的に投与すると、failureが増加した。

同様に軸索内に活動電位を惹起する。そして、シナプス後細胞である小脳核細胞からシナプス後電位を記録し、軸索の BK チャンネルを局所的に阻害することにより、プルキンエ細胞から小脳核細胞への出力がどのような影響を受けるかについて検討した。その結果、軸

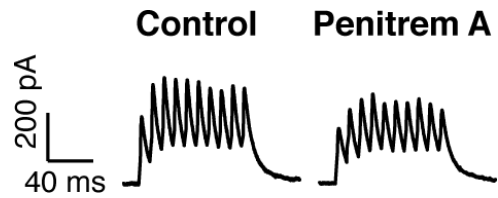


図5 軸索BKチャンネルの阻害によるシナプス出力の減少。

索 BK チャンネルを阻害することにより、小脳核細胞におけるシナプス後電位が減少することが分かった (図5)。小脳核細胞は複数のプルキンエ細胞軸索から入力を受けるので、軸索 BK チャンネル阻害により活動電位の failure が増大し、結果としてシナプス伝達が阻害されたと考えられる。以上の結果からわれわれは、軸索 BK チャンネルは、小脳プルキンエ細胞の有髄軸索における高頻度発火に不可欠の役割を果たしていると結論した。

BK チャンネルは通常、その開口に高濃度の Ca^{2+} を必要とする。そのため、軸索に局在する BK チャンネルも、その近傍に Ca^{2+} チャンネルを必要とすると考えられる。そこでわれわれは、 Ca^{2+} チャンネル阻害剤を軸索上に局所投与し、逆行性の活動電位伝搬にどのような影響があるかを調べることにした。もし軸索に Ca^{2+} チャンネルが局在し、BK チャンネルに Ca^{2+} を供給しているとすると、 Ca^{2+} チャンネル阻害剤は BK チャンネル阻害剤と同様に、軸索内活動電位の高頻度発火を妨げるはずである。特定の種類の Ca^{2+} チャンネルを阻害するニッケルを局所投与しても、同様の高頻度発火阻害がみられた。以上の結果から、軸索上には Ca^{2+} チャンネル、特にニッケル感受性のチャンネルが存在し、BK チャンネルを介して活動電位を制御していることが示唆される。今後 Ca^{2+} チャンネルの分子種の同定を行う予定である。

さらに、われわれは予備実験として、脳虚血後に、小脳白質で軸索 BK チャンネルが顕著に減少する結果を得ている。今後このような変化が小脳失調の神経病理に関与するかについて検討を行う予定である。

(2) Kv チャンネルの細胞内輸送の可視化

神経細胞の細胞膜は、樹状突起 (近位、遠位)、スパイン、軸索起始部、ランビエ絞輪、神経終末などの、機能的に異なったいくつものマイクロドメインに分かれている。そしてイオンチャンネルや受容体といった機能分子は、それぞれが特異的な膜ドメインに局在することでその機能

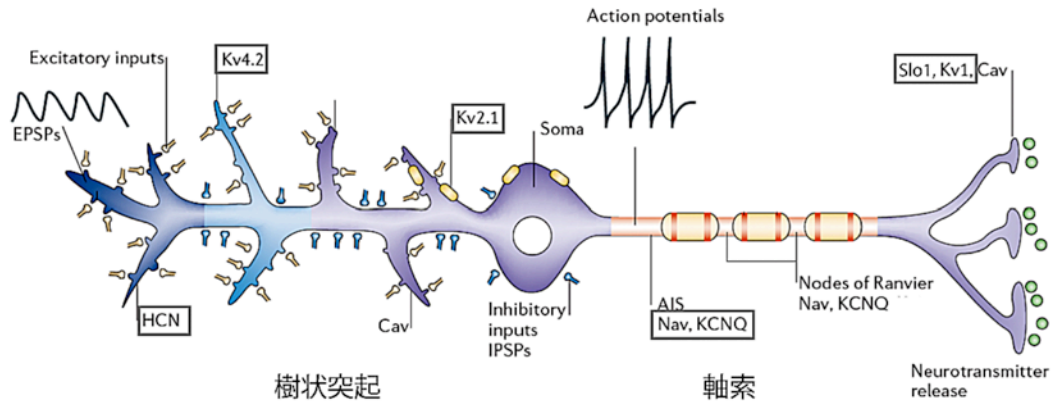


図6 様々な神経細胞内局在を示す電位依存性イオンチャネル。本研究では四角で囲んだチャネルを、各膜ドメインに局在するモデル分子として用いる。Lai and Jan (2006) Nature Neuroscience Reviews より改変。

を果たす (図6)。われわれは、蛍光タンパク質を付加したイオンチャネルを培養海馬神経細胞に一過性に発現させ、低温培養を行うことにより、チャネル分子をゴルジ体に集積させる手法を開発した。さらに温度を生理的温度にもどすことで、チャネルを含む輸送小胞がゴルジ体から一斉に出芽して、細胞内を運ばれていく様子を可視化し、速度や動きなどの性質を定量的に解析することに成功した (図7)。この手法を用いて、てんかんなどの興奮性神経疾患に関与す

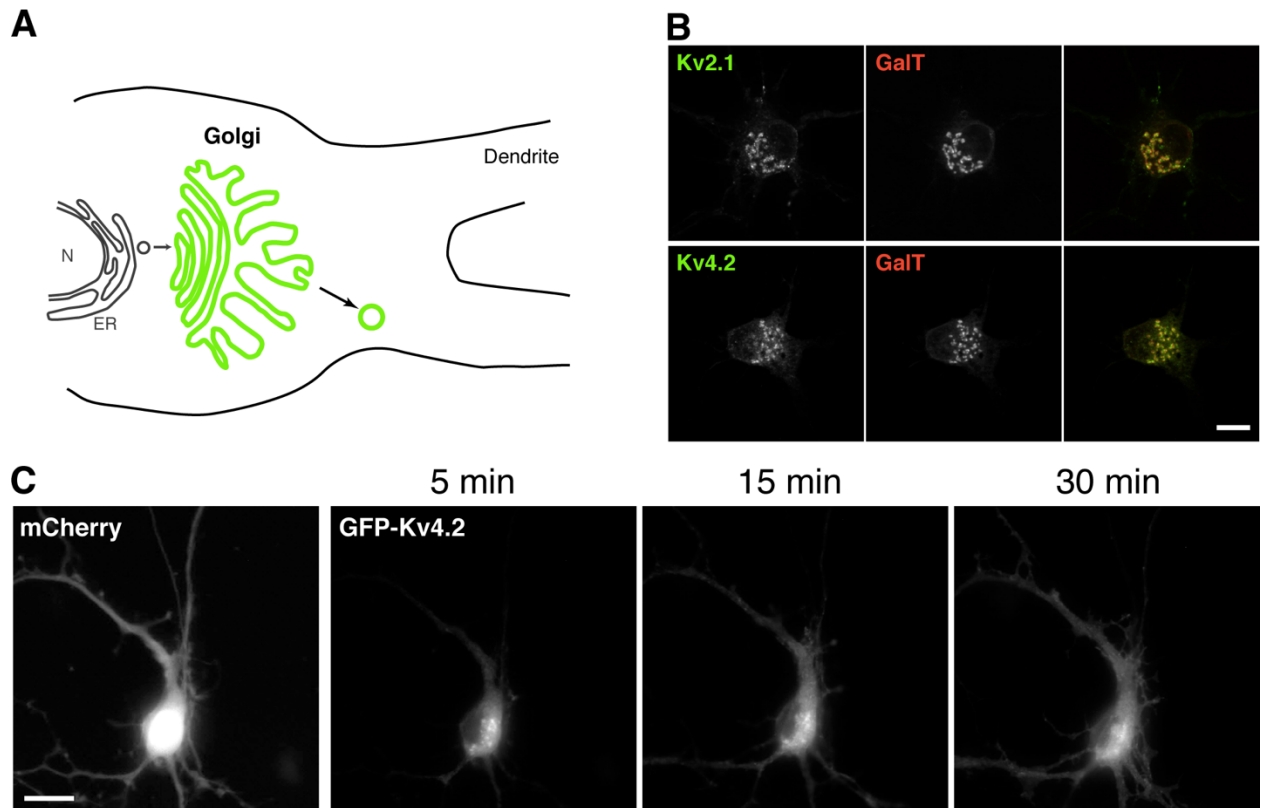


図7 小胞輸送の可視化手法。A、GFP を付加したチャネルを低温培養によりゴルジ体に蓄積させ、生理的温度に戻した時に、同期して輸送が始まるようにする。これにより小胞の可視化が容易になる。B、実際にゴルジ体に蓄積したチャネル。C、生理的温度に戻すと、徐々に細胞体からチャネルが輸送される様子が観察できる。

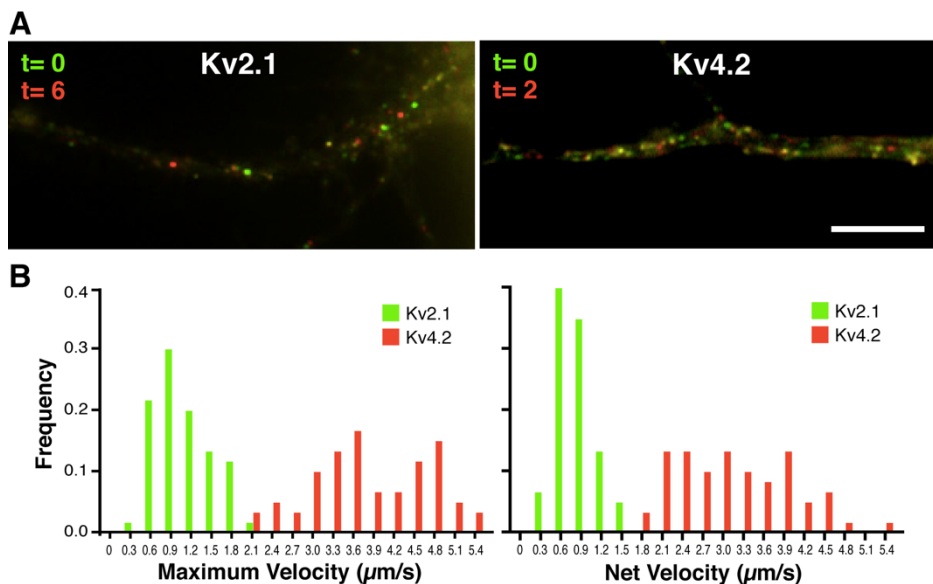


図8 Kv2.1とKv4.2を輸送する小胞の解析。A、小胞の動きを色で表現している。緑が時間0での、赤が6秒後もしくは2秒後の小胞の位置を表す。B、各小胞の移動速度の分布。それぞれのチャンネルを運ぶ小胞は、非常に異なった速度を示す。

ることの知られている Kv2.1 と Kv4.2 チャンネルの輸送メカニズムについて研究を行った。各チャンネルを輸送する小胞の速度を解析することにより、これらのチャンネルが性質の異なる輸送小胞に梱包され、特定の分子メカニズムにより、細胞内の異なった部位に運ばれていくことを示唆する結果を得（図8）、学術誌に発表した（Jensen et al., 2014）。また、神経細胞が過興奮状態に陥ると、これらの小胞輸送メカニズムが阻害されることを示唆する結果を得ている。今後、このような異常が神経細胞の機能と病理に与える影響について研究を行う。

将来的には、アルツハイマー病原因子である異常型タウ（下記参照）や酸化ストレスにも着目し、これらの病理因子がイオンチャンネルの小胞輸送メカニズムにどのような異常を引き起こすかを明らかにしていきたい。

（3）細胞内輸送に関わる微小管結合タンパク質タウの局在化と異常のメカニズム

細胞内小胞輸送は主に微小管と微小管結合タンパク質（モータータンパク質と MAPs など）によって行われている。その中でもタウは軸索に特異的に局在する MAP であり、軸索内輸送との関わりが示唆されている。またアルツハイマー病ではタウが細胞体および樹状突起に高度に蓄積凝集する（図2参照）。これらの知見から、アルツハイマー病の病理において、何らかの異常がタウの局在の変化を引き起こし、それに伴って細胞内輸送が乱されて神経細胞の機能以上が起こるといふ仮説も提唱されている。そこでわれわれは、研究グループ3の宮坂らと、①タ

ウが軸索に局在化するメカニズムと、②アルツハイマー病においてそのメカニズムがどのような異常をきたすのか、の2点について明らかにするために共同研究を行った。

まずわれわれは、蛍光タンパク質 GFP を付加したヒトタウを培養神経細胞に発現させ、タウ局在化メカニズム研究のモデルとすることを試みた。しかし、内在性のタウは軸索に特異的に

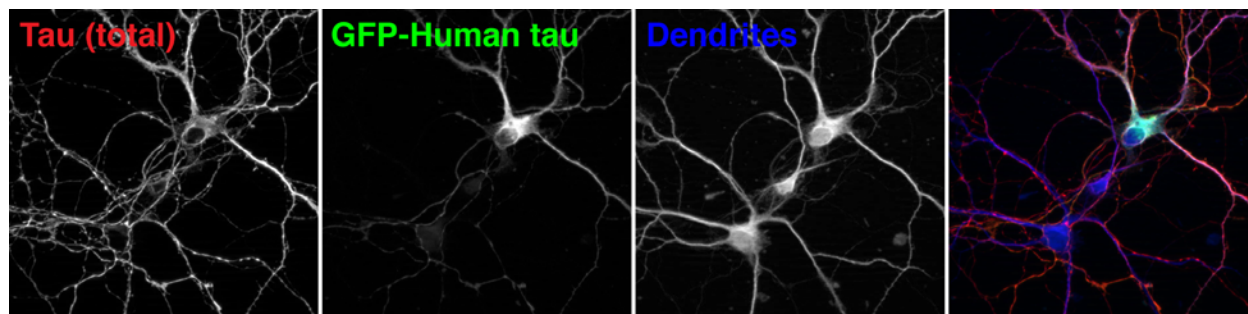


図9 GFP-タウの局在異常。左下の細胞は内在性タウのみを発現しており、細胞体や樹状突起にはタウの染色はほとんど検出されない。一方 GFP-タウは細胞体と樹状突起に顕著に検出される。

検出されるにもかかわらず、GFP タウは主に細胞体と樹状突起に蓄積していた (図9)。これはヒトのタウを用いたことが原因ではなく、マウスタウをマウスの神経細胞に発現させても同様であった。

そこで、内在性タウの局在化メカニズムについての知見を得る目的で、神経細胞の分化発達に伴うタウの軸索への局在化を、免疫染色により詳細に解析した。その結果、タウの局在化は、発達初期の軸索決定直後にすでに始まっていること、そしてタウの発現が神経細胞の発達に伴い減少することを見いだした。これらの結果からわれわれは、タウの軸索への局在化は発達初期に大部分が完了すると考え、現在神経細胞の発達初期にのみタウを発現させることを試みた。発現誘導が可能な発現ベクターに GFP タウを挿入したものを作成し、内在性タウの発現と同様の時期にのみ GFP タウを一過性に発現させた。その結果、GFP タウを軸索に特異的に局

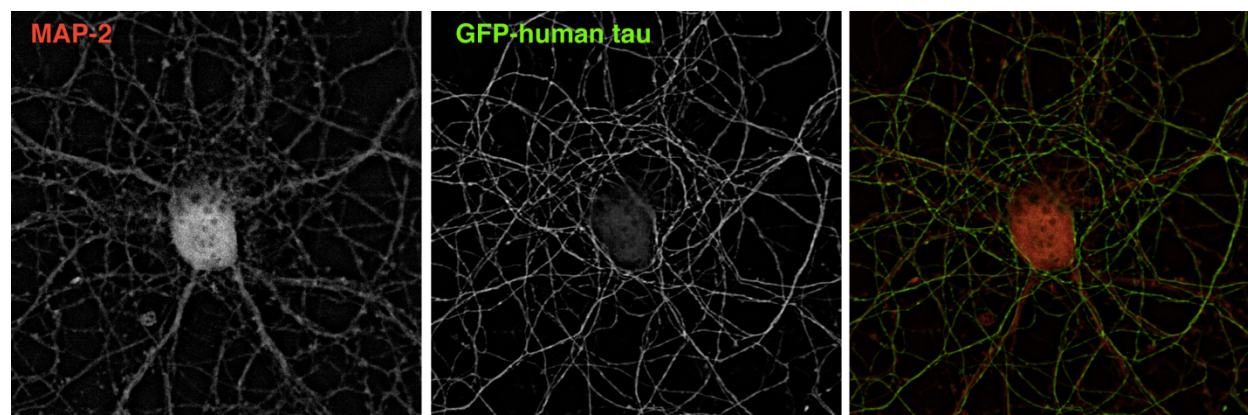


図10 発達初期限定的な発現制御による、GFP タウの軸索特異的局在。GFP タウは樹状突起マーカーの MAP2 陰性の軸索にのみ検出された。

在化させることが可能になった（図10）。

この結果は、タウの発現制御と軸索局在の間に緊密な関係があることを示唆している。すなわち、タウ発現の破綻と異所的な発現によって、タウの局在が破綻する可能性がある。実際、同じ発現誘導系を用いて、内在性タウの発現は低下している成熟細胞に GFP タウを一過性に発現させると、恒常的に発現させた場合と同様に、GFP タウが細胞体と樹状突起に蓄積することが分かった（図11）。以上のことから、われわれは、「タウの発現制御こそが、タウの軸索特異的局在を決定する重要な因子の一つであり、その破綻によりタウの異常局在が引き起こされる」、という仮説を立てている。今後、タウ発現制御因子の探索、タウ軸索局在を発達初期に限局するメカニズムの探索を行い、アルツハイマー病患者脳でこれらのメカニズムの破綻が実際に観察されるかどうかを検証していく。

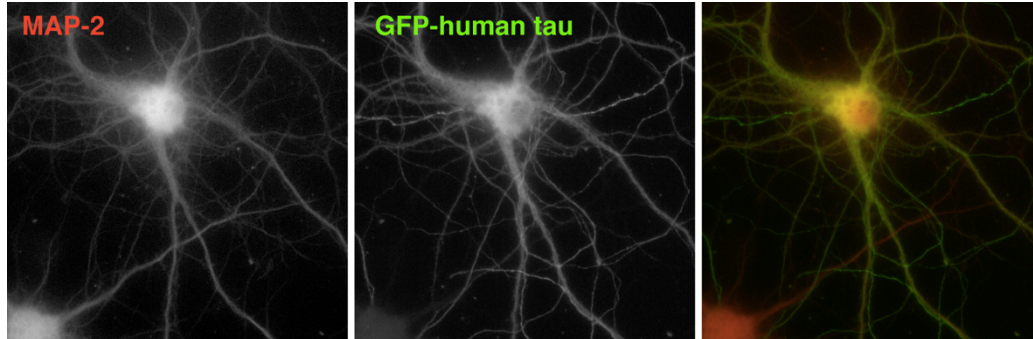


図11 発達期を超えて発現させた GFP タウの異常局在

4. 論文・学会発表

1) 原著論文

1. Bishop, H.I., Guan, D., Bocksteins, E., Parajuli, L.K., Murray, K.D., Cobb, M.M., Misonou, H., Zito, K., Foehring, R.C., and Trimmer, J.S. (2015) Distinct, cell- and layer-specific expression patterns and independent regulation of Kv2 channel subtypes in cortical pyramidal neurons. *J. Neurosci*, in press.
2. Hirono, M., Ogawa, Y., Misono, K., Zollinger, D.R., Trimmer, J.S., Rasband, M.N., and Misonou, H. (2015) BK channels localize to the paranodal junction and regulate action potentials in myelinated axons of cerebellar Purkinje cells. *J. Neurosci.* 35, 7082-7094.
3. Trimmer, J.S. and Misonou H. (2015) Phosphorylation of voltage-gated ion channels. In *Handbook of Ion Channels* (M Trudeau and J Zhang ed) in press. Boca Raton: CRC Press.
4. Jensen, C.S. and Misonou H. (2015) Live-cell imaging of post-Golgi transport vesicles in cultured hippocampal neurons. *Cell. Mol. Neurobiol.* 35, 123-135.
5. Jensen, C.S., Watanabe, S., Rasmussen, H.B., Schmitt, N., Olesen, S.P., Frost, N.A., Blanpied, T.A., and Misonou H. (2014) Specific Sorting and Post-Golgi trafficking of Dendritic Potassium Channels in Living Neurons. *J. Biol. Chem.* 289, 10566-10581.
6. Nomura, T., Watanabe, S., Kaneko, K., Yamanaka, K., Nukina, N., Furukawa, Y. (2014) Intranuclear Aggregation of Mutant FUS/TLS as a Molecular Pathomechanism of Amyotrophic Lateral Sclerosis. *J. Biol. Chem.* 289, 1192-202.
7. Hermansteyne, T.O., Subedi, K., Li, W.W., Hoffman, G.E., Meredith, A.L., Mong, J.A., and Misonou, H. (2013) Kv2.2: A novel molecular target to study the role of basal forebrain GABAergic neurons in the sleep-wake cycle. *Sleep* 36, 1839-1848.
8. Furukawa, Y., Kaneko, K., Watanabe, S., Yamanaka, K., Nukina, N. (2013) Intracellular seeded aggregation of mutant Cu,Zn-superoxide dismutase associated with amyotrophic lateral sclerosis. *FEBS Lett.* 587, 2500-2505.

2) 図書

James S. Trimmer and Hiroaki Misonou "Phosphorylation of Voltage-gated Ion Channels" in

Handbook of Ion Channels, Zheng and Trudeau ed., CRC Press.

3) 学会発表 (国外・国内)

2012年 北米神経化学会第43回大会 コロキウムチェアー “Unique trafficking mechanisms govern neuronal ion channel localization” (メリーランド)

イギリス生理学会シンポジスト “Kv2.1- a key regulator of neuronal excitability” (エジンバラ)

2013年 日本神経科学会 Neuro2013 シンポジウムチェアー 「チャネルの細胞内局在を制御する分子メカニズム」 (京都)

2015年 FASEB meeting Ion Channel Regulation "Axonal BK channels regulate action potentials in myelinated axons of cerebellar Purkinje cells" (コロラド)

2016年 日本生化学会大会 「神経細胞におけるアルツハイマー病原因蛋白質タウの軸索局在の分子機序」 (仙台)

日本認知症学会 「神経細胞におけるタウ蛋白質の軸索局在化機構の解明」 (東京)

4) その他の研究成果等

特記なし。

Specific Sorting and Post-Golgi Trafficking of Dendritic Potassium Channels in Living Neurons^{*[5]}

Received for publication, November 13, 2013, and in revised form, February 21, 2014. Published, JBC Papers in Press, February 25, 2014, DOI 10.1074/jbc.M113.534495

Camilla Stampe Jensen^{‡S1}, Shoji Watanabe[¶], Hanne Borger Rasmussen[‡], Nicole Schmitt[‡], Søren-Peter Olesen[‡], Nicholas A. Frost^{||}, Thomas A. Blanpied^{||}, and Hiroaki Misonou^{S¶12}

From the [‡]Department of Biomedical Sciences, University of Copenhagen, Blegdamsvej 3, DK-2200 Copenhagen N, Denmark, Departments of ^SNeural and Pain Sciences and ^{||}Physiology, University of Maryland, Baltimore, Maryland 21201, and [¶]Unit for Brain Pathology, Graduate School of Brain Science, Doshisha University, Kyoto 619-02225, Japan

Background: Voltage-gated K⁺ (Kv) channels are localized in specific dendritic subcompartments of neurons to regulate dendritic excitability.

Results: Dendritic Kv channels are sorted and trafficked in distinct populations of post-Golgi transport vesicles.

Conclusion: Sorting of Kv channels and their subsequent trafficking by unique mechanisms are crucial for their specific localizations within dendrites.

Significance: Our study reveals the existence of novel subcompartment-specific trafficking pathways for dendritic ion channels.

Proper membrane localization of ion channels is essential for the function of neuronal cells. Particularly, the computational ability of dendrites depends on the localization of different ion channels in specific subcompartments. However, the molecular mechanisms that control ion channel localization in distinct dendritic subcompartments are largely unknown. Here, we developed a quantitative live cell imaging method to analyze protein sorting and post-Golgi vesicular trafficking. We focused on two dendritic voltage-gated potassium channels that exhibit distinct localizations: Kv2.1 in proximal dendrites and Kv4.2 in distal dendrites. Our results show that Kv2.1 and Kv4.2 channels are sorted into two distinct populations of vesicles at the Golgi apparatus. The targeting of Kv2.1 and Kv4.2 vesicles occurred by distinct mechanisms as evidenced by their requirement for specific peptide motifs, cytoskeletal elements, and motor proteins. By live cell and super-resolution imaging, we identified a novel trafficking machinery important for the localization of Kv2.1 channels. Particularly, we identified non-muscle myosin II as an important factor in Kv2.1 trafficking. These findings reveal that the sorting of ion channels at the Golgi apparatus and their subsequent trafficking by unique molecular mechanisms are crucial for their specific localizations within dendrites.

The somatodendritic compartment of neurons receives and integrates incoming synaptic information. These physiological processes are underpinned by a number of receptors and voltage-gated ion channels that are targeted specifically to this compartment. The highly controlled expression of receptors

and ion channels and their accurate positioning within the dendrites are therefore important for dendritic computation. However, despite this importance, the mechanisms underlying intracellular trafficking and precise targeting of these molecules remain poorly understood.

Previous studies suggest that membrane proteins localized in dendrites are selectively delivered from the soma to the dendrites by vesicular transport (1, 2) and are prevented from entering the axon at the axon initial segment (3, 4). However, it is still uncertain how receptors and ion channels are targeted to more confined areas within the dendrites, such as proximal dendrites, distal dendrites, and dendritic spines (5).

In the present study, we hypothesized that, within dendrites, multiple biosynthetic trafficking mechanisms exist to target membrane proteins to different and specific subcompartments. To test this hypothesis, we focused on Kv2.1³ and Kv4.2 channels based on their distinct localizations in dendrites. Kv2.1 channels are widely expressed in the mammalian brain where they exhibit restricted localization on soma and proximal parts of the dendrites (6). In contrast, Kv4.2 channels are expressed in distal parts of the dendrites with increasing expression levels from the soma (7). These Kv channels, therefore, serve as excellent model proteins to study targeting to different subcompartments of neuronal dendrites (8).

We first developed quantitative live cell imaging methods to investigate whether different ion channels are sorted into distinct transport vesicles at the Golgi apparatus. Using Kv channels tagged with fluorescent proteins, we here demonstrate a novel approach to synchronize the release of transport vesicles from the Golgi apparatus by a modified temperature arrest method. With this approach, we uncovered that Kv2.1 and Kv4.2 channels are sorted into different types of transport vesicles, which display different movement dynamics and distribu-

* This work was supported in part by a grant from the Epilepsy Foundation (to H. M.), the Takeda Science Foundation (to H. M.), the Naito Foundation (to H. M.), and a framework grant from the Danish Medical Research Council (to S. P. O.).

[5] This article contains supplemental Movies 1–7.

¹ Supported by the Lundbeck Foundation.

² To whom correspondence should be addressed: Unit for Brain Pathology, Graduate School of Brain Science, Doshisha University, Kyoto 619-02225, Japan. Tel.: 81-774-65-7886; Fax: 81-774-73-1902; E-mail: h_misonou@mac.com.

³ The abbreviations used are: Kv, Voltage-gated K⁺; DIV, days *in vitro*; MyoIIb, non-muscle myosin IIB; CCD, charge-coupled device; PALM, photoactivated localization microscopy; PA-TagRFP, photoactivatable red fluorescent protein; AIS, axon initial segment; LatA, latrunculin A; MAP-2, microtubule-associated protein-2.

tions. The specific sorting into vesicles was found to be dictated by previously reported peptide targeting motifs present in Kv2.1 (9) and Kv4.2 (10). Quantitative analysis revealed that the differential targeting of Kv2.1 and Kv4.2 post-Golgi transport vesicles is mediated by distinct molecular mechanisms. Particularly, we identified a novel actin-myosin-based trafficking mechanism for Kv2.1 of which disruption caused a marked change in the expression of the channel. Our imaging study, therefore, provides insight into how dendritic ion channels are localized to specific subcompartments in neuronal cells. The novel imaging technique introduced here also provides a basis for future investigations of vesicular trafficking of a broader spectrum of membrane signaling proteins in neurons.

EXPERIMENTAL PROCEDURES

cDNA Constructs—Kv2.1, Kv4.2, KChIP2, and Kv2.1 S586A cDNAs were generous gifts from Dr. Trimmer. The coding sequences of Kv2.1 and Kv4.2 were cloned into EGFP-C1 and mCherry-C1 vectors from Clontech. Kv2.1 S586A was cloned into the EGFP-C1 vector. mCherry-GalT was generated from Venus-GalT (Addgene, Cambridge, MA). Green fluorescent protein (GFP)-tagged microtubule-associated protein-2C (MAP-2C) was a generous gift from Dr. Kaech (11). The Arf1 Q71I mutant was a generous gift from Dr. Jeyfous but was originally constructed by the El-Husseini laboratory. The dominant negative mutant of nonmuscle myosin IIB was provided by Dr. Takashi Tsuboi. hCD4-hKv7.3CT in pcDNA3.1 was generated as reported (12). Small hairpin RNAs for rat myosin IIB were designed as follows: 1, GGAAGAAAGCGATGGTCAA (196–214 bp in NCBI Reference Sequence accession number NM_031520); 2, GCTGCAGTTTGGAAACATC (1058–1076 bp); and 3, GCGAATGATCCGAGCTTTA (2243–2261 bp). Control small hairpin RNA (shRNA) for luciferase was GTGCGTTGCTAGTACCAAC. All of these sequences were cloned into pBasi-hU6 Pur vector (Takara Biotechnology, Shiga, Japan) for mammalian expression.

Cell Culture and Transfection—Dissociated cultures of embryonic rat hippocampal neurons (E18) were prepared from female timed pregnant rats as described previously (13) with minor modifications. All animal use was approved by the institutional animal care and use committee. Neurons were transiently transfected at 7–10 days *in vitro* (DIV) using Lipofectamine 2000 transfection reagent (Invitrogen). In all experiments with GFP-Kv4.2 and mCherry-Kv4.2, we co-expressed the β subunit KChIP2, which is required for efficient export of Kv4.2 from the endoplasmic reticulum (14). For live cell imaging, these plasmids were used at 1 μ g/coverslip (diameter, 25 mm). In the experiments with shRNA, neurons were transfected with an shRNA construct (0.25 μ g/coverslip) together with a GFP expression vector as a marker (0.5 μ g/coverslip).

Drug Experiments—Latrunculin A (Invitrogen) was dissolved in DMSO and added to Hanks' balanced salt solution to a final concentration of 1 μ M (0.1% DMSO). Colchicine (Sigma) was also dissolved in DMSO. Neurons were imaged before and 5 min after the treatment. A working solution of blebbistatin (50 μ M; Tocris) was prepared from a 50 mM stock solution (in DMSO) by rapidly mixing 2 μ l of the stock solution with 300 μ l of Hanks' balanced salt solution to prevent the formation of

fluorescent precipitates. The solution was briefly centrifuged to remove any remaining precipitates and then added to the imaging medium at 50 μ M.

Immunofluorescence Staining—Neurons were fixed in 4% paraformaldehyde, 4% sucrose, PBS and blocked in 4% milk, Tris-buffered saline in the presence of 0.1% Triton X-100 (TBST). Neurons were incubated overnight with primary antibodies and subsequently for 1 h with Alexa Fluor-conjugated IgG-specific secondary antibodies (Invitrogen; 1 μ g/ml), both diluted in 4% milk, TBST. Primary antibodies used were anti-MAP-2 mouse monoclonal antibody (Sigma-Aldrich; clone AP-20; 1:2000), rabbit anti-Kv2.1 antiserum (at 1:5000) (15), mouse anti-Kv4.2 monoclonal antibody (K57 from NeuroMab, Davis, CA; 5 μ g/ml), and rabbit anti-myosin IIB polyclonal antibody (Covance, Berkeley, CA).

Immunoprecipitation—Brains from adult Wistar rats were homogenized in ice-cold homogenization buffer (10% sucrose, 5 mM EDTA, 2.5 mM EGTA, 10 mM NaCl, 10 mM KCl, 50 mM Tris-HCl, pH 7.4) with protease inhibitors. The postnuclear supernatant (1 mg/ml) was incubated in a solubilization buffer (150 mM NaCl, 1% Triton X-100, 20 mM Tris-HCl, pH 7.9 with protease inhibitors) on ice for 30 min. Extracts were then cleared by centrifugation at 20,000 \times *g* for 10 min to remove insoluble material. The brain lysates were preincubated with Dynabeads-Protein G (Invitrogen) for 1 h at 4 °C with agitation. The precleared lysates were further incubated with 2.0 μ g of 1) mouse anti-Kv2.1 monoclonal antibody (K89 from NeuroMab), 2) rabbit anti-myosin IIB polyclonal antibody, 3) mouse anti-Kv2.1 external antibody (K39 from NeuroMab), 4) rabbit anti-Kv4.2 polyclonal antibody (Alomone Laboratory, Israel), or 5) normal rabbit IgG (Santa Cruz Biotechnology, Santa Cruz, CA). Dynabeads-Protein G were added, and the incubation was continued for 2 h. Dynabeads were collected using a magnetic stand and washed four times in the solubilization buffer. Proteins were eluted from the Dynabeads by incubating for 3 min at 70 °C in an SDS sample buffer (2% SDS, 5% 2-mercaptoethanol, 10% glycerol, 62.5 mM Tris-HCl, pH 6.8).

Pulldown Assay—We generated cytoplasmic N- (amino acid residues 1–181) and C-terminal (431–853) fragments of rat Kv2.1 tagged with HaloTag (Promega, Madison, WI) and the DDK tag (DYKDDDDK). These fragments and human non-muscle myosin IIB (MyoIIB) were cloned into pFN18A (Promega) vector for bacterial expression. *Escherichia coli* Rosetta2 (DE3)/pLysS were transformed with the Kv2.1 fragments or MyoIIB expression vector. Transformed *E. coli* cells were grown at 30 °C in LB medium. When the culture reached mid-log phase, protein expression was induced with 100 mM isopropyl 1-thio- β -D-galactopyranoside for 3 h. Cells were then collected at 10,000 \times *g* for 5 min and then resuspended in a solubilization buffer (25 mM Tris-HCl, pH 7.4, 300 mM NaCl, 1 mg/ml lysozyme, 0.5 mM EDTA, 10 mM 2-mercaptoethanol, 1% Triton X-100, Complete protease inhibitor mixture EDTA-free (Roche Applied Science)). After 20-min incubation on ice, MgCl₂ (10 mM) and 50 units of Benzonase were added to the lysate followed by 20-min incubation. The soluble fraction was obtained as a supernatant after centrifugation at 20,000 \times *g* for 10 min. A soluble fraction containing either the N- or the C-terminal fragment was incubated with a HaloTag ligand with bio-

Distinct Sorting and Trafficking of Dendritic Kv Channels

tin (PEG-biotin) according to the manufacturer's instruction (Promega). This was then mixed with a bacterial lysate expressing MyoIIB or a lysate from HEK293 cells. The total protein concentration in the reaction mixture was ~6 mg/ml. After 2-h incubation at room temperature, biotin-labeled proteins were purified using 50 μ l of streptavidin magnetic beads (Thermo Scientific, Waltham, MA). Magnetic beads were washed three times with 25 mM Tris-HCl, pH 7.4, 1% Triton X-100, Complete protease inhibitor mixture EDTA-free. Bound proteins were eluted with the SDS sample buffer, separated by 7.5% SDS-PAGE, and then detected by Western blotting using anti-DDK or MyoIIB antibody.

Western Blotting—Proteins were separated in 4–15% SDS-polyacrylamide gels and transferred to PVDF membranes. The membranes were washed, blocked in PBS containing 4% nonfat dry milk for 1 h, and then incubated with primary antibodies overnight in the blocking buffer at room temperature. We used mouse anti-Kv2.1 C-terminal monoclonal antibody (1 μ g/ml; K89 from NeuroMab), rabbit anti-myosin IIB polyclonal antibody (1:2,000; Covance), and anti-DDK antibody (1:2,000; Medical and Biological Laboratories Co., Ltd., Japan). The membranes were washed and probed with HRP-conjugated secondary antibodies according to the manufacturer's instructions. Immunoreactive bands were detected with enhanced chemiluminescence (PerkinElmer Life Sciences) and visualized by exposing the membranes to x-ray films (GE Healthcare). NeuroMab antibodies are available from the University of California Davis/National Institutes of Health NeuroMab Facility supported by National Institutes of Health Grant U24NS050606 and maintained by the Department of Neurobiology, Physiology and Behavior, College of Biological Sciences, University of California, Davis.

Temperature Block Procedure and Live Cell Imaging—Cultured neurons were transfected with either GFP-Kv2.1 or GFP-Kv4.2 and non-tagged mCherry, which served as a cell fill dye to access the morphology of neurons and to identify axons. Three hours after transfection, neurons were transferred to dishes with Hanks' balanced salt solution (Invitrogen) containing 10 mM HEPES, pH 7.3 and then incubated at 19.5 °C for 3–5 h. After the temperature block, a coverslip with neurons was transferred to an imaging chamber (Warner Instruments, Hamden, CT) and imaged in Hanks' balanced salt solution prewarmed to 37 °C. The temperature of the imaging solution was kept at 35–37 °C using an Air Stream Incubator (Nevtek, Williamsville, VA), and the chamber temperature was continuously monitored using a probe thermometer (Physitemp, Clifton, NJ). Neurons were visualized under epifluorescence illumination using an interline CCD camera installed on an Axiovert 200M microscope (Zeiss, Thornwood, NY) with a 63 \times objective lens (1.4 numerical aperture). Time lapse images were obtained with a typical CCD exposure time of 150 ms using Axiovision software. Time lapse images were acquired using either 1- (GFP-Kv2.1) or 5-Hz (GFP-Kv4.2) acquisition rates. We chose cells that had morphological characteristics of pyramidal neurons and of which the axon could be identified by mCherry labeling. Simultaneous dual color imaging was carried out by installing an image splitter (Andor Technology, South

Windsor, CT) in front of the CCD camera. Images were transferred as JPEG files to NIH Image software ImageJ.

Image Analysis—The velocity, processivity, and distribution of transport vesicles were analyzed in live cell images. The analysis was restricted to anterograde moving vesicles in dendrites (<100 μ m from the soma). We manually tracked individual vesicles for the analysis using the Manual Tracking plug-in in ImageJ. Signal intensity in each image frame was adjusted using a best fit algorithm to compensate for photobleaching and to reduce the background signal as well as to amplify the signal from small vesicles. We chose processes that were thick (>1.5 μ m) and distinguishable from the axon in an mCherry image for each imaged neuron. Velocity measurements were performed in the following steps. 1) Mobile vesicular structures in the processes were selected from time lapse image stacks. 2) The tracking was restricted to vesicles that showed at least 1- μ m displacement through a minimum of five frames. Intracellular puncta that appeared immobile through the time lapse sequences were not tracked and included in the analysis. 3) The net and maximum velocities of a vesicle were determined as follows.

$$V_{\text{net}} = D_{\text{total}}/t_{\text{total}} \quad (\text{Eq. 1})$$

$$V_{\text{max}} = D_{\text{max}}/t_{\text{interval}} \quad (\text{Eq. 2})$$

D_{total} represents the distance the vesicle traveled during the duration for which the vesicle was tracked (t_{total}) in Equation 1. D_{max} represents the maximum displacement the vesicle showed between two consecutive frames separated by an interval (t_{interval}) in Equation 2. Velocities of individual vesicles were averaged per neuron, and then these values were averaged among 10 neurons. Alternatively, velocity distributions of all vesicles analyzed were presented. For the measurement of processivity, we determined the distance that vesicles traveled without any cessation of movement. Obtained values were averaged among 10 neurons.

Spatial distribution of vesicles in the dendrites was analyzed as follows. We chose dendrites that were 1) thick, 2) were distinguishable from the axon, and 3) showed their entire length in an image frame. We then measured the signal intensity of GFP along the dendrites, from the base to the tip, using the line profiling function of ImageJ. The signal intensity was divided by that of mCherry to compensate for changes in volume and then plotted against the distance. We then obtained the ratio of the signal intensity near the tip over that at the base of the dendrite. These values (distal enrichment indices) were averaged among 11 neurons and compared between GFP-Kv2.1- and GFP-Kv4.2-expressing neurons.

Image subtraction used to assess the drug effects was performed as follows (see also [supplemental Movie 3](#)). First, all image frames of a live cell imaging set were averaged in ImageJ. Then, this average image was subtracted from each image frame to remove signals from the background and immobile structures, like the Golgi apparatus, and to leave only that from mobile vesicles. Maximum projection was then created from the subtracted images to visualize trajectories of transport vesicles. The number of mobile anterograde vesicles that showed more than 1- μ m displacement in the dendrites of a cell was

manually counted in the subtracted live cell images and averaged among several neurons.

In the experiments with shRNA, images of immunofluorescence staining were acquired with a fixed exposure time. Signal intensity was measured within the soma using ImageJ and expressed as a percentage of the control (average signal intensity in non-transfected neurons).

Photoactivated Localization Microscopy (PALM) Imaging and Analysis—Tracking of individual actin molecules in filamentous actin in living neurons was performed using PALM (16). Cultured hippocampal neurons were transfected with actin tagged with a photoactivatable red fluorescent protein (PA-TagRFP). GFP-tagged markers of the axon initial segment (GFP-AIS) or the proximal dendrites (GFP-Kv2.1) were co-expressed with actin-PA-TagRFP to identify axons and dendrites, respectively. Imaging was conducted on an Olympus IX81 inverted microscope with a 100 \times /1.45 total internal reflection fluorescence oil immersion objective. The temperature was kept near 37 °C with an objective heater, and the imaging chamber was covered to avoid evaporation. The live cell imaging medium contained 120 mM NaCl, 3 mM KCl, 10 mM HEPES, 2 mM CaCl₂, 2 mM MgCl₂, and 10 mM glucose, pH 7.35. Fluorescence emission was detected with an iXon DV887ECS-BV back-thinned EM-CCD camera (Andor Technology) placed after the 1.6 \times magnification optic in the microscope body. The 16.0- μ m pixels of the camera thus covered 100 nm in the imaging plane. GFP was excited with a 488 nm argon ion laser and PA-TagRFP with a 568 nm helium-neon laser. Photoactivation of PA-TagRFP was achieved with a SpectraPhysics MaiTai titanium sapphire laser tuned to 405 nm. Before PALM acquisition, GFP-positive neurons were located in total internal reflection fluorescence, and the background red fluorescence was bleached. We acquired time lapse images of red fluorescence actin-PA-TagRFP photoconverted with low intensity 405-nm excitation. The molecules were then imaged during consecutive frames before their stepwise disappearance in a time lapse series of a total of 300–1000 frames. Images of activated molecules were acquired every second (1 Hz) using 150-ms exposure. Molecules were localized by fitting a two-dimensional elliptical Gaussian function to a 9 \times 9-pixel array surrounding the peak, and the locations were assembled into tracks using freely available algorithms (17). All subsequent analysis was written in Matlab. To identify potential molecules, the raw data were bandpass-filtered and thresholded to select only high intensity peaks. To ensure that orientation was reliably measured, we limited analysis to molecules that were tracked over distances exceeding 100 nm. The number of tracked molecules was between 36 and 160. To determine the orientation of actin filaments, the net angle of each track (see red tracks from detected actin-PA-TagRFP molecules in Fig. 9E) was determined relative to the axis of either the dendrite or the axon. The angle score was then generated for each angle by computing the cosine of the angle.

Statistical Analysis—All data are presented as actual data points, the mean \pm S.E., or a frequency distribution. Normality of data was examined by Kolmogorov-Smirnov test. Maximum and net velocities of GFP-Kv2.1 and GFP-Kv4.2 (cell averages) and the processivity were compared by Student's *t* test

(unpaired, two-tailed). Comparison of the numbers of mobile vesicles in drug-treated neurons was done using the paired *t* test (two-tailed). Mann-Whitney test was used for the comparison of velocity distributions and that of spatial distributions of vesicles in the dendrites (the distal enrichment index). A *p* value less than 0.05 was considered to be statistically significant in all cases. It should be noted that one-way analysis of variance of velocities of all groups with Tukey post hoc analysis also yielded consistent results. Immunofluorescence data were analyzed with the Kruskal-Wallis test and Dunn's multiple comparison post hoc tests. Actual *p* values are shown in the text and figure legends except for those smaller than 0.0001 and for post hoc tests. All statistical analyses were carried out with GraphPad Prism software (La Jolla, CA).

RESULTS

Probing Post-Golgi Traffic in Neurons by Live Cell Imaging—To investigate vesicular trafficking of Kv2.1 and Kv4.2 channels in living neurons, we added a GFP tag to the N termini of channel polypeptides and verified their localization in cultured hippocampal neurons. Consistent with the localization of endogenous Kv2.1 and Kv4.2 channels (Fig. 1A), GFP-tagged Kv2.1 and Kv4.2 were targeted to distinct subdomains in the dendrites of neurons (Fig. 1B). It should be noted that GFP-Kv4.2 was co-expressed with KCHIP2 because it is trapped in the endoplasmic reticulum without a β subunit (14, 18). GFP-Kv2.1 exhibited a proximal and clustered localization, whereas GFP-Kv4.2 showed uniform dendritic localization toward distal parts of the dendrites (Fig. 1C). Both GFP-Kv2.1 and GFP-Kv4.2 were functionally intact as they elicited the delayed rectifier (Kv2.1) (19) and transient A-type (Kv4.2) K⁺ currents (18) as expected when expressed in HEK293 cells (Fig. 1D). These findings demonstrate that GFP-tagged Kv2.1 and Kv4.2 are assembled in functional channels and that they are targeted to their respective subcellular locations in cultured neurons.

To investigate protein sorting at the Golgi apparatus, we developed a method by which we could selectively detect and analyze post-Golgi transport vesicles. The principle of the method is as follows (see also Fig. 2A). First, neurons were transfected and allowed to express GFP-tagged channel proteins for 3 h. At this time point, the expression of GFP was barely detectable. Then, neurons were incubated at 19.5 °C at which temperature the exit of membrane proteins from the Golgi apparatus is suppressed. Therefore, newly synthesized GFP-tagged channels would be accumulated in the Golgi apparatus. Indeed, after 3–5 h at 19.5 °C, we observed that GFP-Kv2.1 and GFP-Kv4.2 were highly concentrated in perinuclear organelles positive for a Golgi marker, the N-terminal fragment of galactosyltransferase (amino acids 1–60) tagged with mCherry (mCherry-GalT) as shown in Fig. 2B. This accumulation in the Golgi was not observed in neurons that were not subjected to the low temperature incubation after transfection (Fig. 2C). These results suggest that our temperature block method trapped most of the newly synthesized GFP-Kv2.1 in the Golgi apparatus with minimal levels of the protein in other organelles and in the surface membrane.

We then promoted a synchronized release of GFP-tagged channels from the Golgi apparatus in transport vesicles by

Distinct Sorting and Trafficking of Dendritic Kv Channels

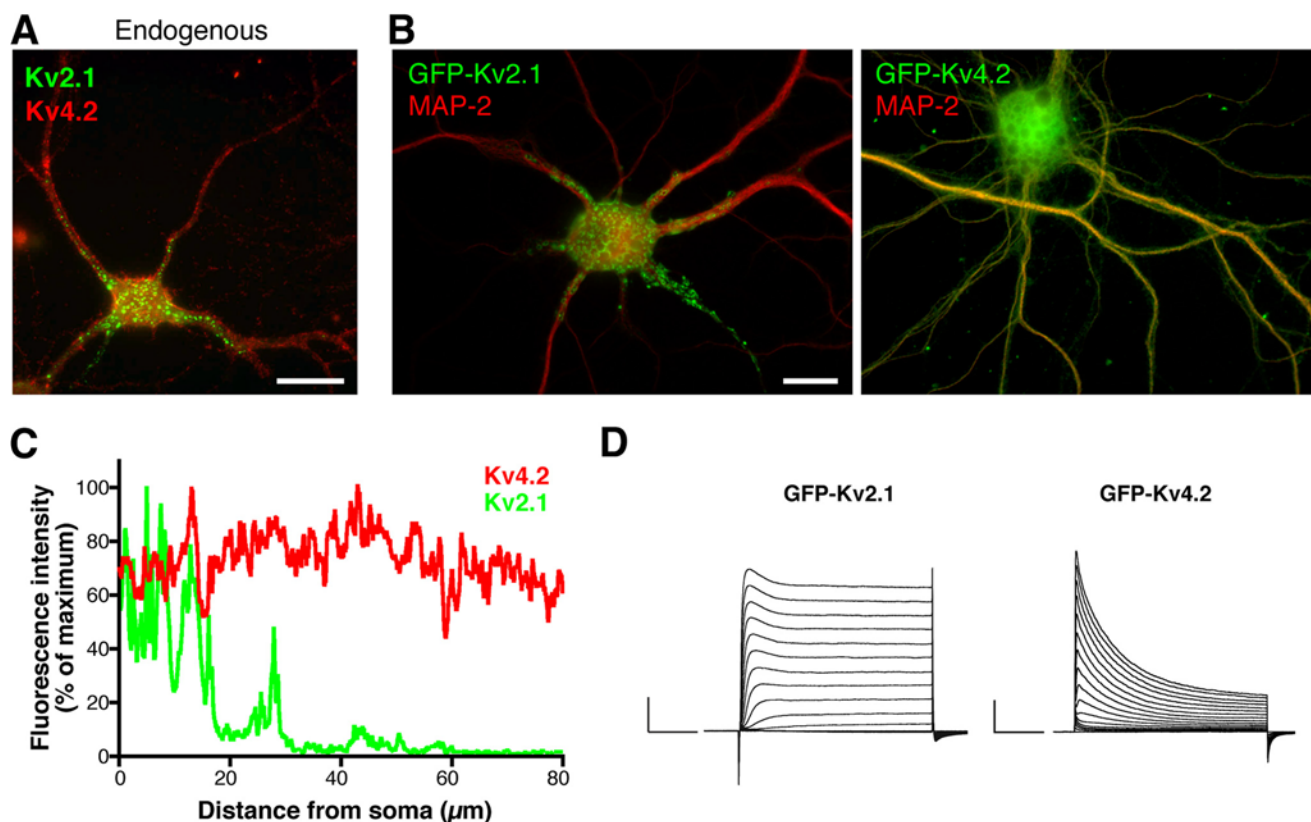


FIGURE 1. Validation of GFP-tagged Kv2.1 and Kv4.2 channels for live cell imaging. *A*, localization of Kv2.1 and Kv4.2 channels endogenously expressed in cultured hippocampal neurons 18 DIV. Scale bar, 20 μm . *B*, localization of GFP-tagged Kv2.1 and Kv4.2 channels. Neurons were transfected at 10 DIV, fixed at 18 DIV, and immunostained for GFP and MAP-2. Scale bar, 10 μm . *C*, fluorescence detection of GFP-Kv2.1 (green trace) and GFP-Kv4.2 (red trace) channel expression from base to tip of dendritic branches. *D*, macroscopic currents of GFP-Kv2.1 and GFP-Kv4.2 recorded from transfected HEK293 cells. Scale, 1 nA and 50 ms.

shifting the incubation temperature to 37 °C. Analysis of the released vesicles would reveal whether Kv2.1 and Kv4.2 are sorted into distinct pools of transport vesicles at the Golgi apparatus and whether they are trafficked by different mechanisms. To initiate sorting of vesicles from the Golgi after the temperature arrest, we incubated neurons for 15 min at 37 °C and visualized by live cell imaging how GFP-positive puncta appeared (see [supplemental Movie 1](#) (GFP-Kv2.1) and [supplemental Movie 2](#) (GFP-Kv4.2)). Occasionally, we observed puncta emerging directly from perinuclear organelles, presumably the Golgi apparatus (Fig. 2*D*). The mobile puncta in both GFP-Kv2.1- and GFP-Kv4.2-transfected neurons were transported out from the perinuclear region and into dendrites. However, this was particularly apparent with GFP-Kv4.2 as the vesicles traveled far into dendrites (Fig. 2*E*).

To test whether these mobile puncta are indeed post-Golgi transport vesicles, we co-expressed a mutant of Arf1 (Arf1 Q71I) that inhibits the release of vesicles from the Golgi apparatus (20, 21). We found that co-expression of Arf1 Q71I dramatically reduced the number of mobile GFP-Kv2.1 and GFP-Kv4.2 puncta. To better visualize the effect, we processed live cell images using an image subtraction method to reveal trajectories of mobile puncta (see Fig. 3*A*, [supplemental Movie 3](#), and “Experimental Procedures” for the image processing information). Although control neurons exhibited a number of trajectories for both GFP-Kv2.1 (Fig. 3*B*) and GFP-Kv4.2 (Fig. 3*C*), neurons co-expressing Arf1 Q71I showed virtually no trajec-

tries, indicating that the mobile puncta are post-Golgi transport vesicles. Taken together, these results suggest that our temperature block method is suitable for probing post-Golgi transport vesicles, which mediate the transport of Kv2.1 and Kv4.2 channels, respectively.

Distinct Sorting of Kv2.1 and Kv4.2 Channels—We then quantitatively analyzed individual vesicles to determine whether GFP-Kv2.1 and GFP-Kv4.2 are sorted into distinct transport vesicles at the Golgi apparatus. As shown in [supplemental Movie 1](#) (GFP-Kv2.1) and [supplemental Movie 2](#) (GFP-Kv4.2), many GFP-positive vesicles were trafficked in the soma and dendrites (Fig. 4*A*). We observed that GFP-Kv2.1 vesicles were trafficked in both anterograde and retrograde directions, whereas the majority of GFP-Kv4.2 vesicles appeared anterogradely transported.

GFP-Kv2.1 and GFP-Kv4.2 vesicles appeared to be transported at different velocities. To quantify the difference, we tracked individual transport vesicles through several frames to obtain their movement velocities. The average net and maximum velocities (see “Experimental Procedures” for definitions) of GFP-Kv2.1 vesicles in individual neurons were 0.79 ± 0.04 and $1.09 \pm 0.06 \mu\text{m/s}$ ($n = 10$ cells), whereas those of GFP-Kv4.2 vesicles were 3.17 ± 0.14 and $3.85 \pm 0.13 \mu\text{m/s}$ ($n = 10$ cells), respectively (Fig. 4*B*). The frequency distributions of the net and maximum velocities of GFP-Kv2.1 vesicles were significantly smaller than those of GFP-Kv4.2 vesicles ($p < 0.0001$, $n = 60$) (Fig. 4*C*). These results indicate that GFP-Kv2.1 and

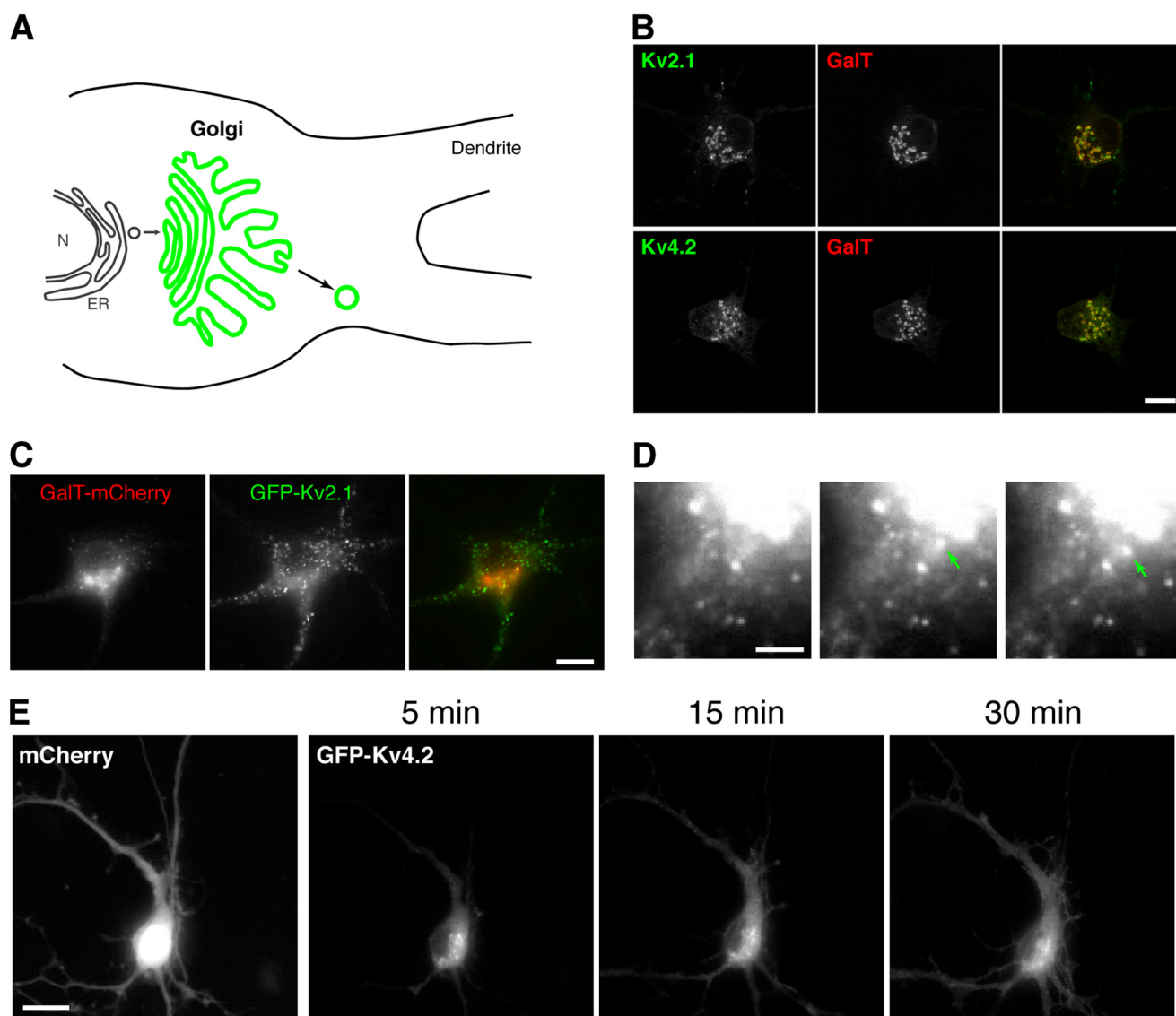


FIGURE 2. A temperature block assay to probe post-Golgi vesicular trafficking of membrane proteins. *A*, the principle of the method using temperature block. *N*, nucleus; *ER*, endoplasmic reticulum. *B*, effects of the temperature block. Transfected neurons were incubated for 3–5 h at 19.5 °C and imaged at room temperature. The Golgi marker, galactosyltransferase tagged with mCherry (*GalT*), was co-expressed. *C*, without the temperature block procedure, GFP-Kv2.1 channels escape to the surface membrane. Neurons were transfected and imaged 5 h later. *D*, emergence of mobile puncta from the Golgi apparatus. When sorting was restored after the temperature block, mobile puncta emerged from the Golgi apparatus. Time lapse images from GFP-Kv2.1-transfected neurons are shown. *E*, visualization of mobile puncta. After changing the incubation temperature to 37 °C, GFP-Kv4.2 signal started to invade dendrites but not the axon, indicating the synchronized formation of post-Golgi transport vesicles. The image of cell fill mCherry represents the morphology of the neuron. Scale bars, 10 μ m.

GFP-Kv4.2 are sorted into different populations of post-Golgi transport vesicles. We noted that these velocity values are comparable with values reported previously for vesicular carriers (22–25) and with those of vesicular stomatitis virus G (VSVG)-GFP post-Golgi vesicles in our experiments (Fig. 4, *D* and *E*).

Next, we investigated the spatial distribution of GFP-Kv2.1 and GFP-Kv4.2 vesicles. The distribution of GFP signal along dendrites was measured in neurons that were incubated for 30 min at 37 °C following the temperature block (Fig. 5*A*). The fluorescence intensity was normalized to that of co-expressed mCherry for volume correction. Then the intensity in the distal 50- μ m segment of the dendrites was divided by that in the proximal 50- μ m segment to assess the enrichment of GFP-positive vesicles in distal dendrites. We found that the spatial distribution of GFP-Kv2.1 vesicles was more restricted to the

proximal segment than that of GFP-Kv4.2 vesicles as evidenced by the significant difference in the distal enrichment indices between GFP-Kv2.1 and GFP-Kv4.2 vesicles (Fig. 5*B*). This further indicates that they are sorted and transported in distinct pools of vesicles.

To directly test whether neurons sort Kv2.1 and Kv4.2 channels in different vesicles, we co-expressed mCherry-tagged Kv4.2 with GFP-Kv2.1 for simultaneous dual color live cell imaging. GFP-Kv2.1 and mCherry-Kv4.2 were present in non-overlapping populations of transport vesicles that moved independently of each other (Fig. 5*C* and [supplemental Movie 4](#)). We also measured the fluorescence intensity along a line drawn in a proximal segment of a dendrite (20 μ m). Peaks of fluorescence signals corresponding to vesicles containing GFP-Kv2.1 or mCherry-Kv4.2 did not overlap (Fig. 5*D*). Similar results

Distinct Sorting and Trafficking of Dendritic Kv Channels

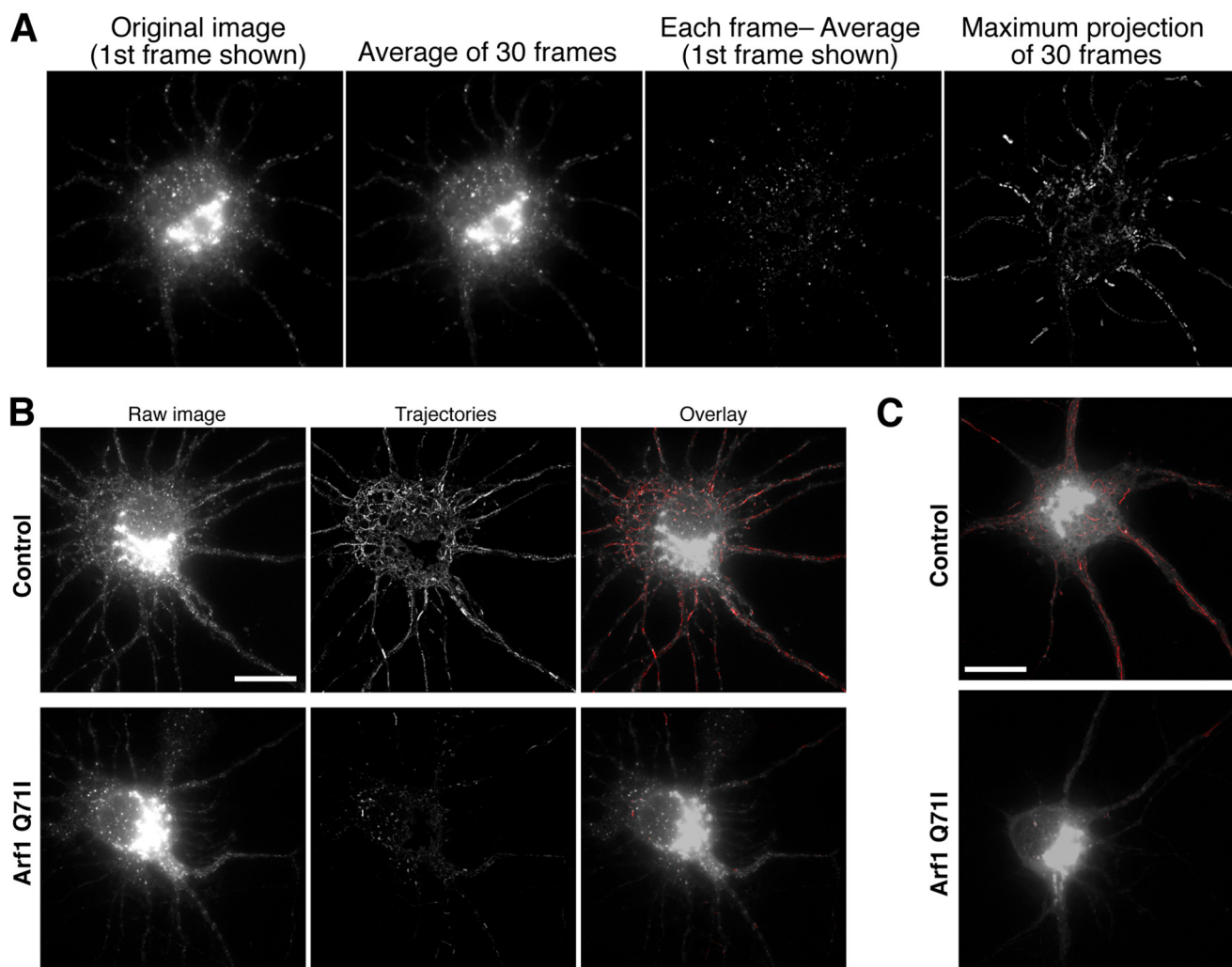


FIGURE 3. Post-Golgi vesicular trafficking of Kv2.1 and Kv4.2. *A*, image processing procedure used for the analysis of vesicular motility. First, all image frames of a live cell imaging set (*leftmost* image) were averaged in ImageJ. This average image (*second left* image) was then subtracted from each image frame to remove signals from the background and immobile structures, like the Golgi apparatus, and to leave only that from mobile vesicles (*second right* image). Maximum projection was then created from the subtracted images to visualize trajectories of transport vesicles (*rightmost* image). *B* and *C*, mobile puncta represent post-Golgi transport vesicles. Formation of mobile puncta was inhibited by co-expression of Arf1 Q711, indicating that these puncta represent post-Golgi transport vesicles. After temperature block, neurons expressing GFP-Kv2.1 (*B*) and GFP-Kv4.2 (*C*) were imaged without (*Control*) or with Arf1 Q711. By an image subtraction method (see "Experimental Procedures"), trajectories from moving puncta were extracted to represent the effect of Arf1 Q711. Scale bars, 10 μm .

were obtained with neurons from at least three different cultures ($n = 10$). It should be noted that only GFP-Kv2.1 vesicles appeared in the axon (Fig. 5C, *arrow*), consistent with the localization of Kv2.1 in the axon initial segment (9, 26). These data demonstrate that neurons strictly sort GFP-Kv2.1 and mCherry-Kv4.2 into different populations of transport vesicles at the Golgi apparatus.

Specific Sorting of Kv2.1 and Kv4.2 Dictated by Peptide Motifs—Previous studies have identified peptide motifs in the cytoplasmic C-terminal tails of Kv2.1 and Kv4.2 in which mutations result in mislocalization of the channels without apparent changes in their surface expression (9, 10). However, it is not known how these peptide motifs contribute to the specific localizations of Kv2.1 and Kv4.2 in dendrites. We hypothesized that mutation in Kv2.1 and Kv4.2 peptide motifs would alter their localizations due to disrupted sorting and subsequent post-Golgi trafficking. To test this, we analyzed Kv2.1 S586A (9) and Kv4.2 LL/AV (10) tagged with GFP. Kv2.1 S586A muta-

tion resulted in uniform localization of the channel throughout the dendritic membrane (9) unlike the clustered localization of wild-type Kv2.1 in the soma and proximal dendrites (Fig. 6A). In the Kv4.2 LL/AV mutant, the replacement of the dileucine targeting motif with Ala and Val resulted in both axonal and somatodendritic localization (Fig. 6B) (10).

We performed live cell imaging of these mutant channel subunits using our temperature block method to assess their sorting and post-Golgi traffic (**supplemental Movies 5 and 6**). We found that the vesicles carrying GFP-Kv2.1 S586A showed a marked change in the velocity distribution as compared with that of wild-type GFP-Kv2.1. The maximum (Fig. 7A) velocity distribution was significantly greater from that of wild-type GFP-Kv2.1 vesicles ($p < 0.0001$, $n = 60$). In addition, average maximum velocity in individual neurons ($3.12 \pm 0.20 \mu\text{m/s}$) was significantly greater ($p < 0.0001$, $n = 10$). In contrast, the velocity distribution of the vesicles carrying GFP-Kv4.2 LL/AV was significantly ($p = 0.0006$, $n = 60$) shifted to

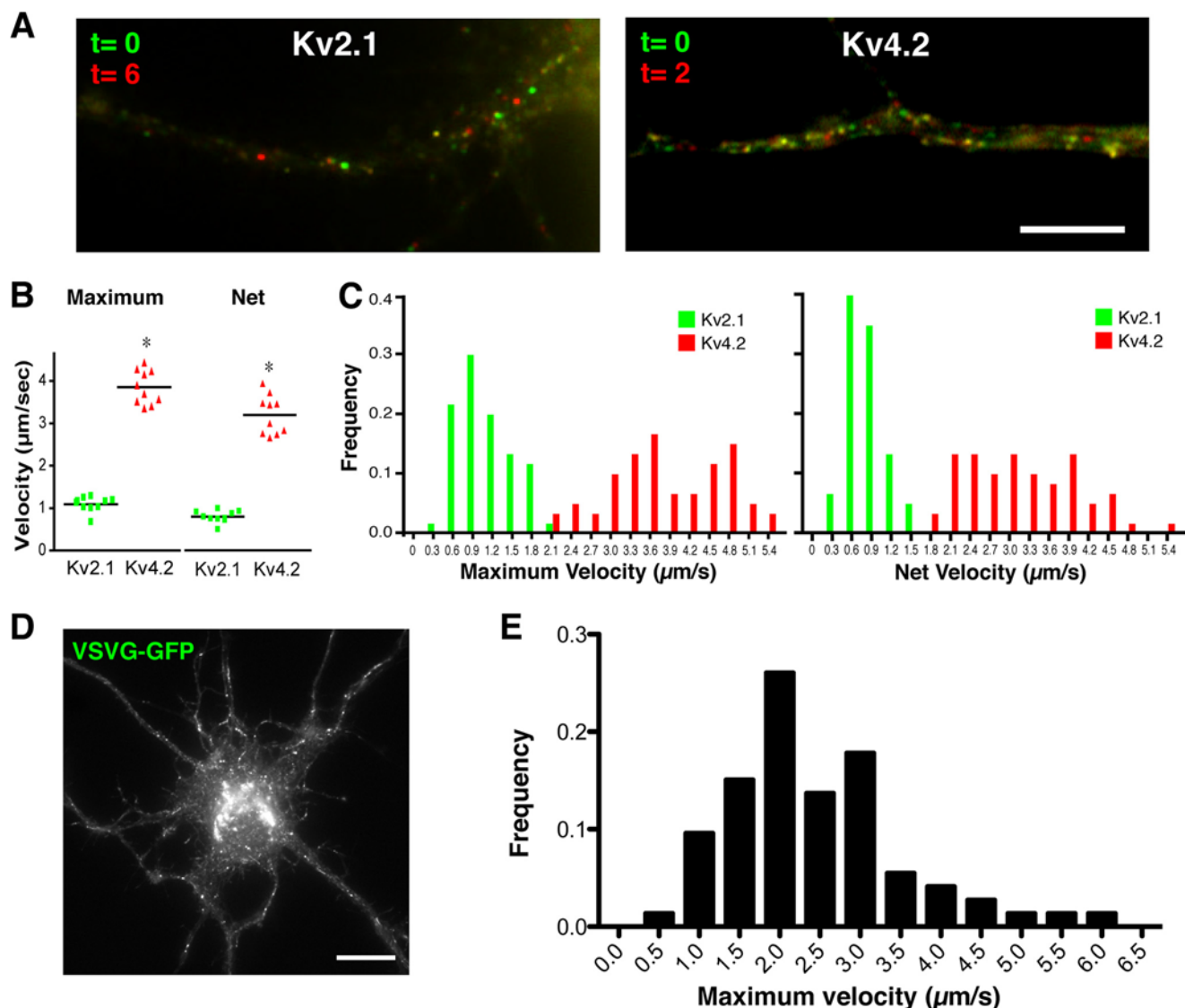


FIGURE 4. Characterization of post-Golgi transport vesicles. *A*, mobile vesicles appeared after the temperature block. The movements of vesicles in the dendrites are illustrated by merging two image frames separated by a certain interval in two different colors: frame 1 (*green*) corresponds to time 0, and frame 2 (*red*) corresponds to 6 and 2 s later for GFP-Kv2.1 and GFP-Kv4.2, respectively. *Scale bar*, 5 μm . *B*, maximum and net velocities of vesicles carrying GFP-Kv2.1 and GFP-Kv4.2 in individual neurons. Velocities of individual vesicles were averaged per cell, and then these values were averaged in 10 cells. The *horizontal bars* indicate the averages. *, $p < 0.0001$. *C*, frequency distributions of the maximum and net velocities of GFP-Kv2.1 vesicles and GFP-Kv4.2 vesicles. *D* and *E*, velocities of vesicular stomatitis virus G (VSVG) vesicles were measured for comparison with values acquired for Kv2.1 and Kv4.2 vesicles. *Scale bar*, 10 μm .

slower velocities than that of wild-type Kv4.2 vesicles (Fig. 7A). The average maximum velocity in individual neurons ($3.22 \pm 0.16 \mu\text{m/s}$) was also significantly slower ($p = 0.006$, $n = 10$). These results indicate that the PRC motif and the dileucine motif act as specific sorting signals for Kv2.1 and Kv4.2, respectively.

In addition, we found that the spatial distributions of mutant GFP-Kv2.1 S586A and GFP-Kv4.2 LL/AV vesicles were disrupted. The distal enrichment index of GFP-Kv2.1 S586A was significantly increased ($p = 0.008$, $n = 6$) compared with wild-type Kv2.1 (1.91 ± 0.35 versus 0.80 ± 0.07), indicating that the vesicles carrying the targeting mutant are not restricted to the proximal dendrites but transported more distally in the dendrites. Furthermore, unlike wild-type GFP-Kv4.2, post-Golgi vesicles containing GFP-Kv4.2 LL/AV were readily detected in both the dendrites and in the axon (Fig. 7B), which was further

evidenced by line scan analysis (Fig. 7C). Together, these results indicate that specific sorting mediated by the peptide motifs is crucial in the targeted transport of vesicles and therefore in the specific localization of Kv2.1 and Kv4.2.

Kv2.1 and Kv4.2 Are Trafficked by Distinct Mechanisms—The different velocities of Kv2.1 and Kv4.2 vesicles suggest that they are trafficked by distinct molecular mechanisms in dendrites. Therefore, we addressed the mechanisms underlying their vesicular trafficking. First, we investigated whether the actin cytoskeleton would be involved in the transport of Kv2.1 vesicles because an actin-myosin transport system was previously demonstrated to mediate short range transport of ionotropic glutamate receptors in dendrites (27, 28). Therefore, by use of an actin-depolymerizing toxin, latrunculin A (LatA), we examined whether intact actin filaments are required for the movement of Kv2.1 vesicles.

Distinct Sorting and Trafficking of Dendritic Kv Channels

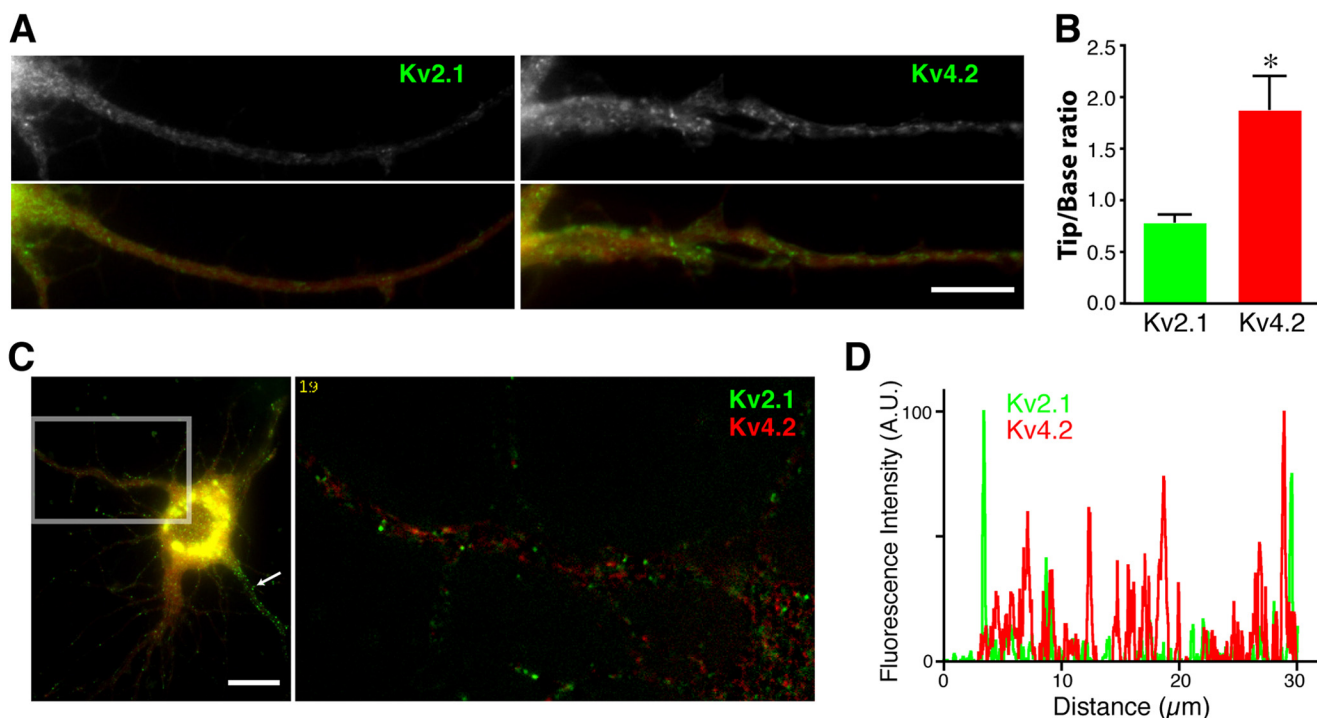


FIGURE 5. Kv2.1 and Kv4.2 in distinct transport vesicles. *A*, spatial distributions of vesicles along the dendrites. Co-expression of GFP-Kv2.1 and GFP-Kv4.2 with cell fill mCherry (red in the lower panels) is shown. Scale bar, 10 μm . *B*, GFP fluorescence intensity in the dendrites was measured for each channel and normalized to volume changes using mCherry fluorescence. The distal enrichment index was calculated as the normalized fluorescence intensity in the distal 50- μm segment of the dendrite divided by that in the proximal 50- μm segment of the dendrites. The distal enrichment index was significantly higher for GFP-Kv4.2 vesicles than for GFP-Kv2.1 vesicles (*, $p = 0.0006$; $n = 11$). Data shown are the means \pm S.E. *C*, GFP-Kv2.1 and mCherry-Kv4.2 in non-overlapping vesicles. The image represents the first frame in the time lapse image of a proximal dendrite. Scale bar, 10 μm . *D*, the fluorescence intensities of GFP-Kv2.1 and mCherry-Kv4.2 vesicles plotted along a line (30 μm) drawn in the proximal dendrites.

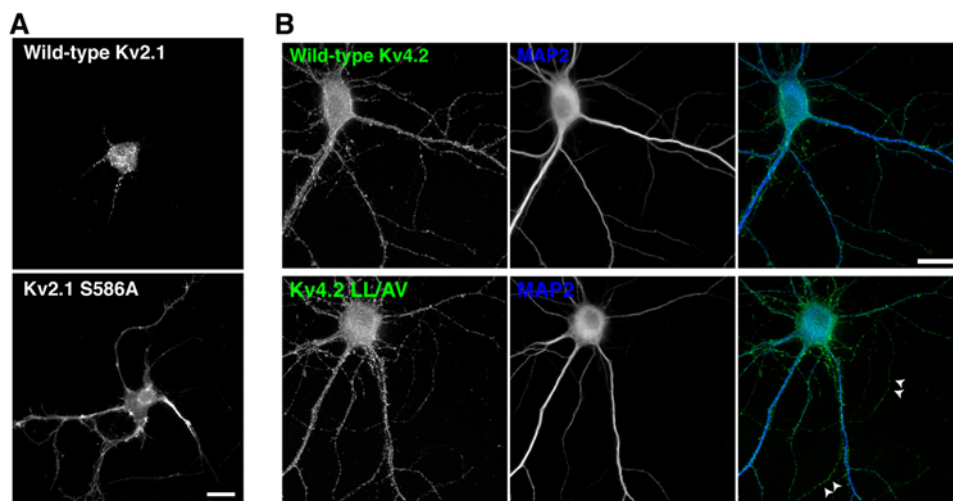


FIGURE 6. Mislocalization of Kv2.1 and Kv4.2 mutants. *A*, the restricted and clustered localization of GFP-Kv2.1 (upper) is disrupted for the targeting mutant GFP-Kv2.1 S586A (lower). Neurons were transfected at 10 DIV, fixed at 18 DIV, and immunostained for GFP. Scale bar, 10 μm . *B*, mutation of the dileucine motif in Kv4.2 channels results in both axonal and dendritic localization. Neurons were transfected at 10 DIV, fixed at 18 DIV, and immunostained for GFP and MAP2. Arrows point to the MAP2-negative axonal compartment. Scale bar, 20 μm .

Neurons transfected with GFP-Kv2.1 were subjected to temperature block and then imaged before and after a 5-min treatment with 1 μM LatA. We verified that this treatment effectively reduced the level of filamentous actin as evidenced by a substantial reduction in phalloidin staining ($100 \pm 16\%$ in control versus $24 \pm 2\%$ in LatA-treated cells, $n = 3$). This acute LatA treatment dramatically attenuated the motility of GFP-Kv2.1 vesicles (Fig. 8A, upper panel, and supplemental Movie

7). In contrast, the motion of GFP-Kv4.2 vesicles was not significantly affected by LatA (Fig. 8A, lower panel).

To quantify the effect of LatA, we analyzed live cell images using the image processing method (see “Experimental Procedures” and Fig. 3A). The processing allowed us to count the number of post-Golgi vesicles in dendrites under different conditions for quantification. Before LatA treatment, many trajectories of GFP-Kv2.1 vesicles were detected in proximal den-

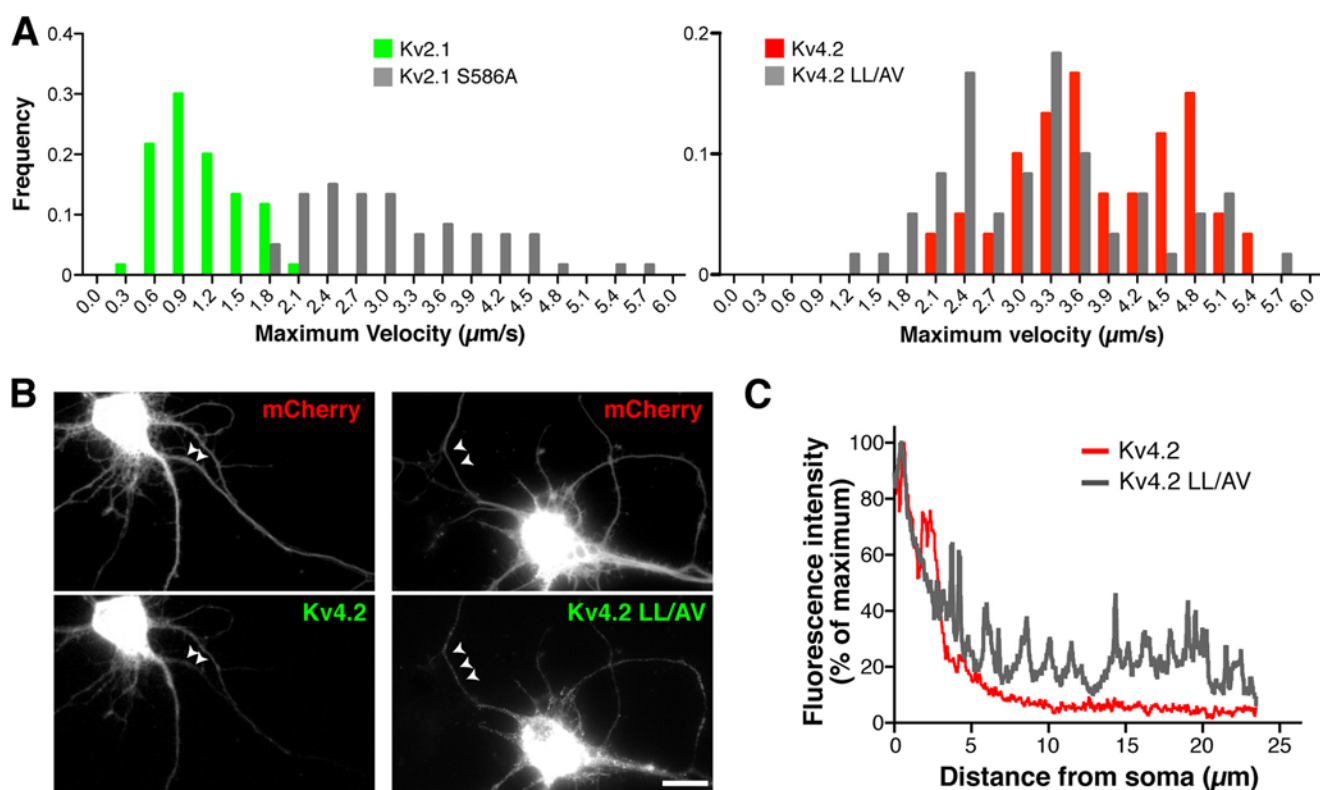


FIGURE 7. Missorting of Kv2.1 and Kv4.2 mutants. *A*, frequency distributions of the maximum velocities of vesicles carrying GFP-Kv2.1 S586A (*left*) and GFP-Kv4.2 LL/AV (*right*). There was a significant difference in the velocity distribution between wild-type Kv2.1 and Kv2.1 S586A ($p < 0.0001$) as well as between Kv4.2 and Kv4.2 LL/AV ($p < 0.0001$). *B*, mistargeting of vesicles carrying GFP-Kv4.2 LL/AV to the axons indicated by the arrowheads. Scale bar, 10 μm . *C*, fluorescence intensity of GFP-Kv4.2 and GFP-Kv4.2 LL/AV along 23- μm segments of the axons.

drifts (Fig. 8*B*). However, after LatA treatment, virtually no trajectories were visible (Fig. 8*B* and supplemental Movie 7). Consistently, the number of mobile vesicles was significantly reduced after LatA treatment (Fig. 8*C*). In contrast, depolymerization of microtubules with colchicine (100 μM ; 20 min) did not elicit significant effects on the motility of GFP-Kv2.1 vesicles (Fig. 8*C*). Interestingly, the motility of vesicles carrying GFP-Kv2.1 S586A was not affected by LatA (Fig. 8*C*), further supporting the notion that the PRC mutant is sorted into a population of transport vesicles distinct from wild-type GFP-Kv2.1 vesicles. These data suggest that the specific population of post-Golgi vesicles carrying Kv2.1 depends on actin filaments for their transport.

It was shown previously that dendritic localization of Kv4.2 channels depends on a kinesin motor protein (KIF17) that transports cargo along microtubules (29). Consistently, upon depolymerization of microtubules with colchicine, we found a significant reduction in the number of moving GFP-Kv4.2 vesicles, whereas LatA did not cause any significant effect (Fig. 8, *D* and *E*). Together, these results strongly indicate that Kv2.1 and Kv4.2 channels are trafficked by distinct vesicular transport mechanisms within the somatodendritic compartment of neurons.

Unique Mode of Trafficking of GFP-Kv2.1 Vesicles and Its Underlying Mechanism—Our finding that the distribution of GFP-Kv2.1 vesicles was restricted to soma and the proximal parts of dendrites was striking and novel. To understand the basis of this, we first analyzed the processivity of individual

post-Golgi transport vesicles, a parameter defined by the distance each vesicle moves without cessation. The average maximum processivity of GFP-Kv2.1 vesicles in individual neurons was significantly smaller than that of GFP-Kv4.2 vesicles (Fig. 9*A*). Interestingly, we also found that GFP-Kv2.1 vesicles changed direction frequently, whereas most of the GFP-Kv4.2 vesicles moved unidirectionally toward either the soma or the distal dendrites (Fig. 9, *B* and *C*). In the example shown in Fig. 9*C*, the net travel distance in 18 s was only about 1 μm even though the vesicle traveled with a maximum velocity of 1.9 $\mu\text{m/s}$. These results suggest that the actin-based trafficking of Kv2.1 is characterized by the intermittent and bidirectional motions of transport vesicles.

Therefore, we speculated that filaments with diverse orientations in this dendritic region could account for the unique bidirectional motion of GFP-Kv2.1 vesicles. Proximal dendrites contain numerous actin filaments (30), but their directionality is unknown. To determine the orientation of individual actin filaments, we used PALM (31) to track single molecules in live cells (16, 17). We noted that actin polymerization at filament barbed ends drives the flow of monomers along the filament away from the site of polymerization (32). Thus, trajectories of individual polymerized molecules reflect filament directionality, and we used this to compare filament organization in different subcompartments of neurons (Fig. 9*D*). Neurons were transfected with actin tagged with PA-TagRFP (33) and a marker of the axon initial segment (GFP-tagged ankyrin G-binding motif of Kv7.3 fused to CD4) (12). Tagged actin mol-

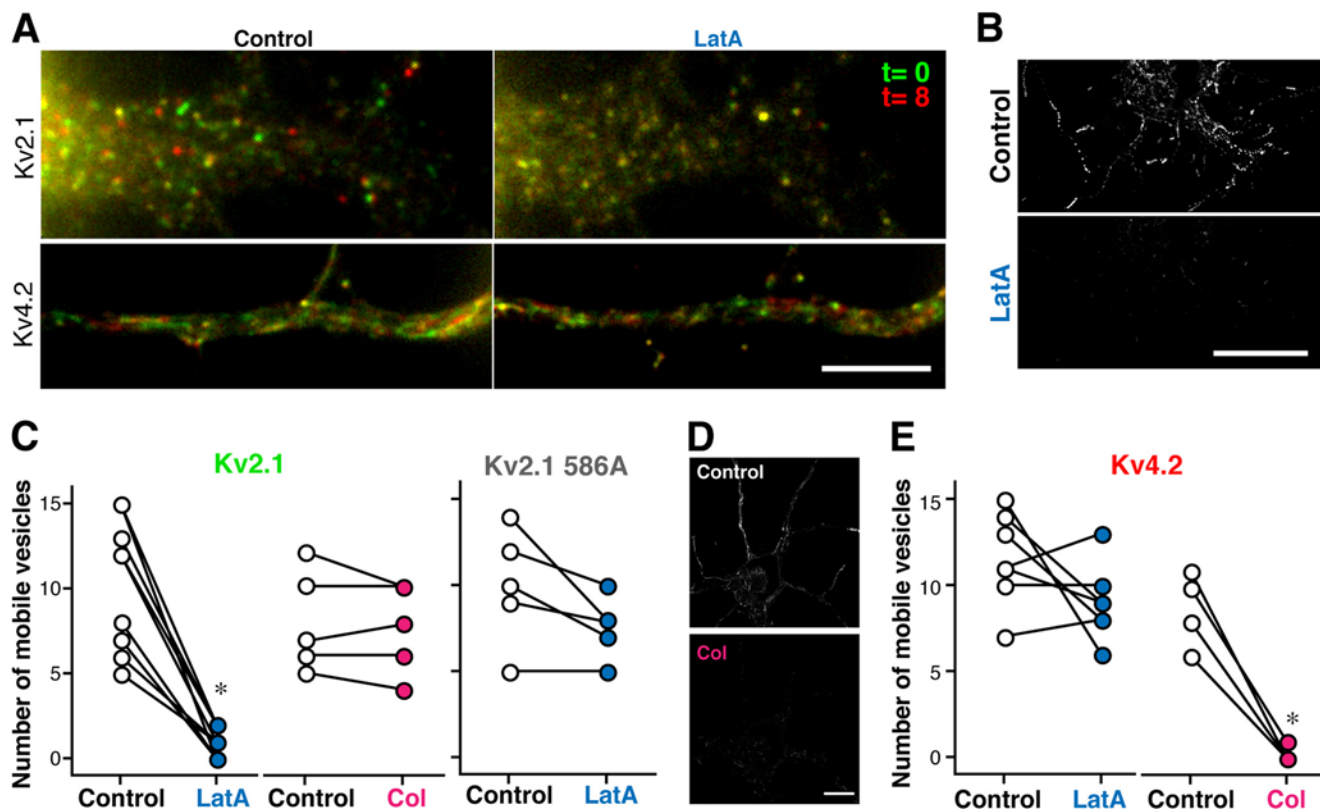


FIGURE 8. Kv2.1 and Kv4.2 channels are trafficked by distinct molecular mechanisms. *A*, neurons transfected with GFP-Kv2.1 or GFP-Kv4.2 were imaged before (*Control*) and after a 5-min treatment with $1 \mu\text{M}$ LatA. The movements of vesicles are illustrated by merging two image frames separated by 8 s in two different colors. *Scale bar*, $5 \mu\text{m}$. *B*, trajectories from moving GFP-Kv2.1 vesicles before (*Control*) and after LatA treatment. *Scale bar*, $10 \mu\text{m}$. *C*, the average number of mobile GFP-Kv2.1 vesicles in the dendrites was significantly reduced after treatment with LatA (*, $p < 0.0001$; $n = 10$ cells), whereas there were no significant changes in neurons treated with $100 \mu\text{M}$ colchicine (*Col*; $n = 5$). The effect of LatA on GFP-Kv2.1 S586A vesicles was negligible ($n = 6$). *D*, trajectories from moving GFP-Kv4.2 vesicles before (*Control*) and after treatment with colchicine (*Col*). *Scale bar*, $10 \mu\text{m}$. *E*, the average number of mobile GFP-Kv4.2 vesicles was significantly reduced after treatment with colchicine (*Col*; $n = 5$) but not with LatA ($n = 6$).

ecules were photoactivated, localized, and tracked as reported previously (Fig. 9E) (16). The direction of movement was measured as the angle relative to the axis of the dendrite. We then computed the cosine of each angle and used it as an angle score. We predicted that if actin filaments are oriented randomly in proximal dendrites then the average angle score would be zero. On the contrary, if actin filaments are oriented uniformly along the axis of the dendrite then the average angle score would be significantly greater than 0 with a maximum value of 1. In addition, we computed the angle scores relative to a perpendicular axis of dendrites in case actin filaments were oriented along this axis. For comparison, we simulated randomly oriented actin filaments with typical numbers of tracked particles (35–160) and obtained the angle scores, which were virtually zero (0.001 ± 0.114 (mean \pm S.D.)). The mean angle score obtained from actin filaments in the proximal dendrites was not significantly greater than zero ($p > 0.8$), suggesting that actin filaments are randomly orientated in this compartment of neurons. Consistently, when the axis for angle score determination was rotated 90° , the values were not significantly different from zero ($p > 0.9$). In contrast, the mean angle score in the axon initial segment was 0.194 ± 0.052 , suggesting an organized arrangement of actin filaments consistent with a recent study using electron microscopy (4). This score was significantly higher than the values from proximal dendrites and random simulations (Fig. 9F). These results suggest that actin filaments

are more uniformly oriented in the axon initial segment than in the proximal dendrites. Taken together, these findings indicate that the characteristic intermittent and bidirectional motion of GFP-Kv2.1 vesicles in the somatodendritic compartment results from their traffic along randomly oriented actin filaments.

Role of Non-muscle Myosin II in GFP-Kv2.1 Trafficking—Our data also provide evidence that non-muscle myosin II (myosin II hereafter) is involved in the transport of Kv2.1 vesicles. Fig. 10, *A* and *B*, illustrate a significant reduction in the number of mobile GFP-Kv2.1 vesicles after treatment with $50 \mu\text{M}$ blebbistatin, a specific myosin II inhibitor (34, 35). We furthermore confirmed that a dominant-negative mutant of myosin IIB also reduced the motility of GFP-Kv2.1 vesicles (10.2 ± 1.7 in control versus 4.6 ± 1.1 with the dominant negative, $p = 0.02$).

Consistently, we found that endogenous Kv2.1 binds to endogenous myosin IIB in native rat brain tissues using a co-immunoprecipitation assay (Fig. 10C). In a reciprocal approach, an antibody against the extracellular epitope of Kv2.1 successfully co-immunoprecipitated myosin IIB. This binding was specific to Kv2.1 as endogenous Kv4.2 was not detected in the immunoprecipitate of myosin IIB (Fig. 10D).

To determine whether the binding between Kv2.1 and myosin IIB is direct, we performed a pull-down assay. Cytoplasmic N (1–186 amino acid residues) and C termini (431–853) of rat Kv2.1 were tagged with HaloTag (36) and

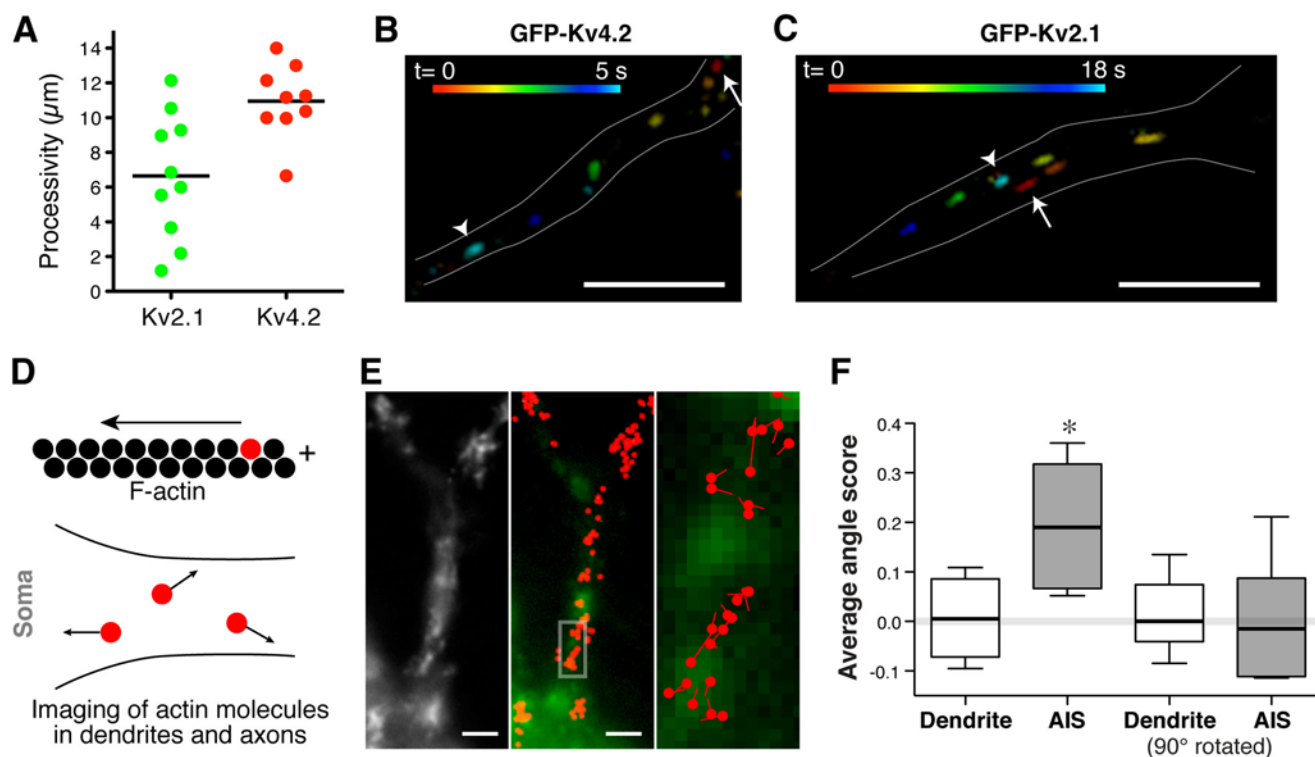


FIGURE 9. Unique motion of Kv2.1 vesicles and the organization of dendritic actin filaments. *A*, the average processivity of GFP-Kv4.2 vesicles in individual neurons was significantly greater than that of GFP-Kv2.1 ($p = 0.006$). The horizontal bars indicate the means. *B*, unidirectional motion of a Kv4.2 vesicle. A single vesicle carrying GFP-Kv4.2 was imaged over 5 s. Positions of the vesicle at different time points are shown in different colors. The arrow indicates the original position of the filament at time 0, and the arrowhead indicates the position in the last frame. Scale bar, 5 μm . *C*, bidirectional motion of Kv2.1 vesicles. Note the net travel distance of $\sim 1 \mu\text{m}$ in 18 s. Scale bar, 5 μm . *D*, determination of actin filament orientation. If a fluorescent actin molecule moves to the left in a filament, the right side of the filament is the plus-end. *E*, representative result of PALM imaging. *Left panel*, diffraction-limited image of PA-TagRFP-actin in proximal dendrites. *Middle panel*, actin molecules with track lengths greater than 100 nm (red dots) are overlaid with GFP-Kv2.1. Scale bars, 2 μm . *Right panel*, the boxed region in the middle panel is magnified to show the net direction of each actin molecule. Red dots represent the original positions of the actin molecules, and lines indicate the net directions and the net distances. *F*, directions of motions were determined relative to the axis of the dendrites. Angle scores were calculated as the cosine of these angles. Averaged angle scores obtained in proximal dendrites and AIS are shown. Angle scores were also calculated with the axis rotated 90°. Data are presented with a box plot (the error bars indicate the 10th and 90th percentile). *, $p = 0.0002$ with analysis of variance.

expressed in *E. coli*. The bacterial lysates were mixed with a lysate either from *E. coli* expressing recombinant myosin IIB or from HEK293 cells. Recombinant Kv2.1 fragments were purified using a biotin ligand for HaloTag and a streptavidin column. We found that recombinant myosin IIB as well as endogenous myosin IIB from HEK293 cells was co-purified with either of the Kv2.1 fragments (Fig. 10E). These results indicate that myosin IIB can directly bind to Kv2.1 and that the binding involves both N and C termini of Kv2.1.

To test the significance of myosin IIB in Kv2.1 trafficking, we applied the temperature block to neurons transfected with GFP-Kv2.1 and then treated them without or with blebbistatin for 18 h. Control neurons showed typical clustering of GFP-Kv2.1, indicating its surface expression. However, GFP-Kv2.1 signal appeared cytoplasmic in neurons treated with blebbistatin (Fig. 10E).

Furthermore, to investigate whether the trafficking of endogenous Kv2.1 also depends on myosin IIB, we used shRNA to knock down myosin IIB and investigated its effect on Kv2.1. We tested three different shRNAs and found that they all reduced the expression levels of endogenous myosin IIB significantly as evidenced by immunofluorescence staining (Fig. 11, A and B). We then examined whether the expression of endogenous Kv2.1 in the somatodendritic region is altered by the shRNAs. Neurons were transfected with shRNA at 7 DIV, fixed at 9 DIV,

and immunostained for Kv2.1. We found that neurons transfected with the shRNAs of myosin IIB had significantly lower immunofluorescence signals than those transfected with a control shRNA or untransfected neurons (Fig. 11, C and D). As it has been shown with a number of ion channels that trafficking-defective channels are rapidly degraded (for example, see Ref. 14), the result indicates that the reduction of myosin IIB disrupts Kv2.1 trafficking. Collectively, these results suggest that myosin II has a unique role in the post-Golgi trafficking of endogenous Kv2.1 in neurons.

DISCUSSION

In this study, we developed a novel imaging approach and used it to probe protein sorting and vesicular transport of dendritic Kv channels in living neurons. Our approach, based on the temperature block, resulted in the effective accumulation of GFP-tagged channel proteins in the Golgi apparatus, thereby allowing semipulse-chase imaging of the post-Golgi vesicular trafficking of Kv channels. By combining this approach with a number of quantitative analyses, we provided evidence that two dendritic ion channels, Kv2.1 and Kv4.2, are precisely sorted into distinct pools of transport vesicles that are targeted to specific dendritic subcompartments by different molecular mechanisms. Previous work has demonstrated that membrane proteins targeted to either axonal or somatodendritic compart-

Distinct Sorting and Trafficking of Dendritic Kv Channels

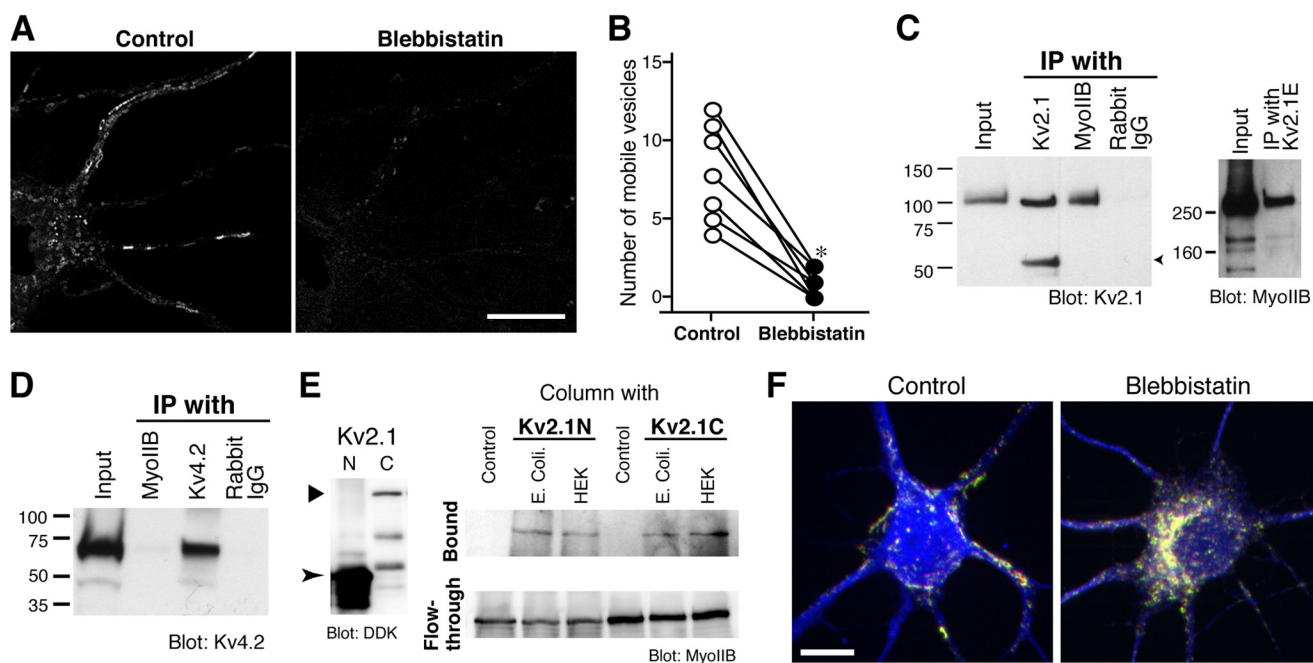


FIGURE 10. The role of non-muscle MyoIIB in Kv2.1 trafficking. *A*, the motility of GFP-Kv2.1 vesicles is attenuated upon treatment with blebbistatin. GFP-Kv2.1 vesicles were imaged before (*Control*) and after treatment with 50 μM blebbistatin for 5 min. *Scale bar*, 10 μm . *B*, the number of mobile GFP-Kv2.1 vesicles was significantly reduced ($*$, $p = 0.0006$; $n = 7$) upon treatment. *C*, interaction between Kv2.1 and MyoIIB. MyoIIB and Kv2.1 were immunoprecipitated (*IP*) from brain lysate. Normal rabbit IgG was used as a control. The immunoprecipitates were subjected to Western blotting (*Blot*) using the anti-MyoIIB antibody (*left*) and an antibody raised against the extracellular region of Kv2.1 (*Kv2.1E*) (*middle*). The arrowhead indicates the mouse IgG band. *Right panel*, co-immunoprecipitation of myosin IIB by an antibody against the extracellular region of Kv2.1 (*Kv2.1E*). *D*, lack of Kv4.2 binding to myosin IIB. *E*, pull-down assay with recombinant Kv2.1 fragments and MyoIIB. *Left panel*, the expression of Kv2.1 fragments in *E. coli*. *Right panel*, pull-down assay with Kv2.1 lysates and either the bacterial lysate with myosin IIB (*E. coli*) or HEK293 cell (*HEK*) lysate. *Control* represents the pull-down of the myosin IIB bacterial lysate with the streptavidin column in the absence of Kv2.1 lysate. Representative results from three independent experiments are shown. *F*, effect of blebbistatin on the steady-state localization of GFP-Kv2.1. Neurons were transfected with GFP-Kv2.1 for 3 h, incubated at 19.5 $^{\circ}\text{C}$ for 3 h, and treated with 10 μM blebbistatin for 18 h. Cells were then fixed and immunostained for GFP (*green*), Kv2.1 (*red*), and MAP-2 (*blue*). *Scale bar*, 20 μm .

ments, such as the transferrin receptor and neuroglia cell adhesion molecule (NgCAM) are sorted in distinct populations of transport vesicles (1), a result that has also been supported by recent studies (37, 38). Our study further extends this compartment-specific trafficking model to ion channels that are localized to specific subcompartments within the dendrites. Based on our findings, we propose a selective dendritic transport model (Fig. 11*E*) in which proximal Kv2.1 and distal Kv4.2 are sorted into unique populations of vesicles at the Golgi apparatus and delivered by distinct transport machineries.

The significance of the specific sorting in establishing the distinct localizations of Kv2.1 and Kv4.2 is supported by our experiments using localization mutants. We showed that the mutants, which have been reported to mislocalize in neuronal membranes (9, 10), were indeed impaired in the protein sorting process. They appeared to be still efficiently packaged into post-Golgi transport vesicles but not into their designated populations. Consequently, these vesicles carrying missorted proteins were transported to improper locations, such as the distal dendrites for Kv2.1 S586A and the axon for Kv4.2 LL/AV. These results indicate that sorting to a specific population of transport vesicles at the Golgi apparatus is a crucial step in localizing these Kv channels to specific dendritic subcompartments.

Interestingly, our studies also shed light on how efficiently and precisely neurons sort dendritic ion channels into post-Golgi vesicles. Ample evidence suggests that the binding of a specific set of coat proteins to a peptide sorting signal is the common mechanism whereby membrane proteins are concen-

trated and packaged into a specific population of vesicles at the Golgi apparatus (39, 40). A recent study also reported that the μ1A subunit of adaptor protein-1 complex prevents somatodendritic proteins from being packaged into axonal transport vesicles at the Golgi apparatus (41). Although we currently do not know the molecular mechanism whereby dendritic Kv2.1 and Kv4.2 are separated into specific vesicular carriers, our results that an Arf1 mutant inhibits the formation of both types of vesicles indicate that adaptor protein-1 or other clathrin-associated sorting proteins recruited by Arf1 (40, 42) might be involved in the sorting events.

The velocities of post-Golgi transport vesicles obtained in this study (0.5–6 $\mu\text{m/s}$) are much greater than the values reported for single myosin IIB molecules (<0.1 $\mu\text{m/s}$) (43) and kinesin motors (up to 2 $\mu\text{m/s}$) (44), which have been measured mostly *in vitro*. As our results with vesicular stomatitis virus G-GFP showed velocities comparable with those measured previously in living cells (22–25), we concluded that our measurements are genuine. It should also be noted that the most classical type of vesicular transport in neurons, the fast axonal transport, has been shown to operate at the speed of $\sim 5 \mu\text{m/s}$ (400 mm/day). Therefore, there may be unknown factors that accelerate molecular motors, presumably their hydrolysis cycle (45), in the native cellular environment. However, these remain to be identified.

Previous studies have characterized mobile structures positive for Kv2.1 in neurons using live cell imaging (46, 47). However, because vesicles mediate the transport of membrane

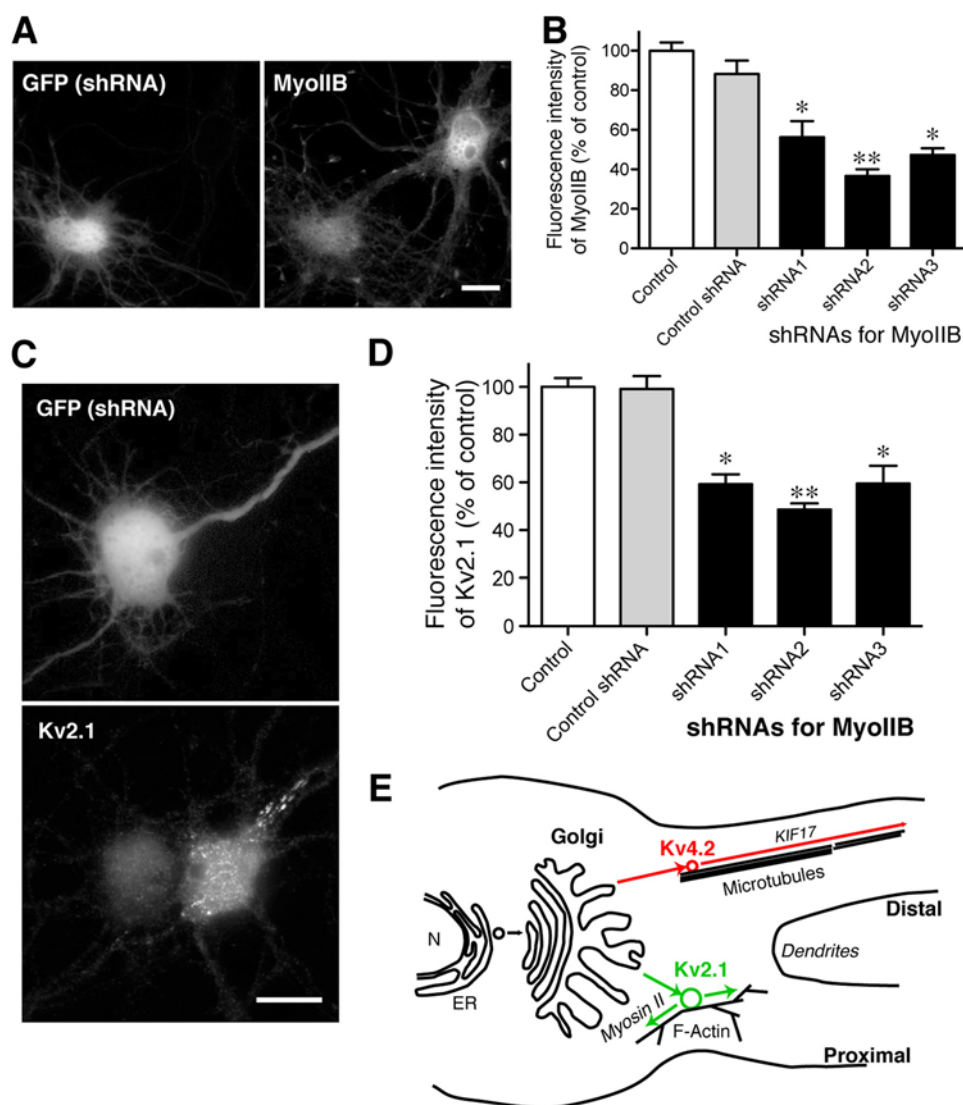


FIGURE 11. Significance of MyoIIB in Kv2.1 trafficking. *A*, knockdown of endogenous MyoIIB with shRNA. Neurons were transfected with shRNA and GFP at 7 DIV and fixed at 9 DIV for immunostaining of MyoIIB. Note that the GFP-positive neuron exhibits less immunofluorescence signal. Scale bar, 20 μ m. *B*, quantification of the effects of shRNAs. The immunofluorescence signal of MyoIIB was measured in neurons expressing shRNA for luciferase (*Control shRNA*) or three independent shRNAs for rat MyoIIB (*shRNA1–3*). Non-transfected neurons were also used as controls. Asterisks indicate statistically significant differences as compared with control with Kruskal-Wallis test and Dunn's multiple comparison post hoc tests (*, $p < 0.05$; **, $p < 0.01$). Data shown are the means \pm S.E. *C*, immunofluorescence staining of endogenous Kv2.1 in neurons transfected with MyoIIB shRNA together with GFP. Scale bar, 20 μ m. *D*, quantification of the effects of shRNAs on Kv2.1. Quantification and analysis were done as for *B*. Data shown are the means \pm S.E. *E*, the model. Selective transport mechanisms in the somatodendritic compartment are shown. Kv2.1 and Kv4.2 are sorted into distinct populations of transport vesicles at the Golgi apparatus and transported to specific subdomains of the dendrites by distinct transport mechanisms. N, nucleus; ER, endoplasmic reticulum.

proteins between several compartments, such as from endoplasmic reticulum to Golgi or from the surface to endosomes, simple live cell imaging does not provide direct insight into the post-Golgi trafficking of Kv2.1. Our approach combining temperature block with quantitative live cell imaging allowed us to detect and analyze post-Golgi transport vesicles preferentially. Here, we provided evidence that GFP-Kv2.1 is sorted into a specific pool of vesicles at the Golgi apparatus that differs from the vesicle population carrying GFP-Kv4.2. Furthermore, GFP-Kv2.1 vesicles were trafficked by a unique mechanism involving myosin IIB and actin filaments. The molecular interaction detected between endogenous Kv2.1 and myosin IIB in brain tissue suggests that this novel trafficking mechanism identified for GFP-Kv2.1 also applies to the native channel. This was further supported by the results that shRNAs for myosin IIB

caused significant changes in the expression of endogenous Kv2.1.

The binding between Kv2.1 and myosin IIB appears to be direct. This was evidenced by the results that recombinant myosin IIB expressed in *E. coli* was able to bind to recombinant cytoplasmic fragments of Kv2.1. This is comparable with the direct binding of the KIF17 motor protein to Kv4.2 (29). Also, the binding may involve both cytoplasmic tails of Kv2.1 as myosin IIB was co-purified with both of the fragments. This is interesting in light of the previous work demonstrating that the N and C termini of Kv2.1 can form a polypeptide complex and facilitate Kv2.1 trafficking in heterologous cells (48).

It has been shown that Kv2.1 is also localized in the proximal region of the axon, the AIS (9, 26). Although the S586A muta-

Distinct Sorting and Trafficking of Dendritic Kv Channels

tion disrupted the proximal localization of Kv2.1 in dendrites, it did not affect its restricted localization at the AIS (see Fig. 3A) (9). This suggests that the mechanism that localizes Kv2.1 to the AIS differs from the mechanism mediating the restricted somatodendritic localization of Kv2.1.

Our live PALM study provided evidence that actin filaments are oriented randomly in proximal dendrites. This is consistent with the random motion of Kv2.1 vesicles presumably mediated by a myosin motor. Although we do not know exactly how long actin filaments are, actin filament length in neurons varies widely, ranging from a few micrometers to 100 nm (30, 49). Therefore, motor molecules (and Kv2.1 vesicles) may have to change tracks frequently in the proximal dendrites. The random orientation and the short track length would cause frequent stalls and changes of direction of Kv2.1 transport vesicles in accordance with our observation. Alternatively, the myosin motor itself may reverse direction as observed by single molecule imaging of myosin IIB (43).

In summary, using quantitative imaging approaches, we provide evidence that neurons sort dendritic ion channels into multiple trafficking pathways, thereby resulting in destination-specific targeting and localization. In addition, these approaches would be useful in future studies to determine vesicular trafficking of other membrane signaling molecules in living neurons.

Acknowledgments—We thank Drs. James Trimmer, Stephanie Kaeck, Mark Rizzo, Takashi Tsuboi, and Don Arnold for generously providing precious reagents. We also thank Matthew Rasband and Scott Thompson for critical reading and helpful discussion.

REFERENCES

- Burack, M. A., Silverman, M. A., and Banker, G. (2000) The role of selective transport in neuronal protein sorting. *Neuron* **26**, 465–472
- Sampo, B., Kaeck, S., Kunz, S., and Banker, G. (2003) Two distinct mechanisms target membrane proteins to the axonal surface. *Neuron* **37**, 611–624
- Al-Bassam, S., Xu, M., Wandless, T. J., and Arnold, D. B. (2012) Differential trafficking of transport vesicles contributes to the localization of dendritic proteins. *Cell Rep.* **2**, 89–100
- Watanabe, K., Al-Bassam, S., Miyazaki, Y., Wandless, T. J., Webster, P., and Arnold, D. B. (2012) Networks of polarized actin filaments in the axon initial segment provide a mechanism for sorting axonal and dendritic proteins. *Cell Rep.* **2**, 1546–1553
- Lai, H. C., and Jan, L. Y. (2006) The distribution and targeting of neuronal voltage-gated ion channels. *Nat. Rev. Neurosci.* **7**, 548–562
- Murakoshi, H., and Trimmer, J. S. (1999) Identification of the Kv2.1 K⁺ channel as a major component of the delayed rectifier K⁺ current in rat hippocampal neurons. *J. Neurosci.* **19**, 1728–1735
- Menegola, M., Misonou, H., Vacher, H., and Trimmer, J. S. (2008) Dendritic A-type potassium channel subunit expression in CA1 hippocampal interneurons. *Neuroscience* **154**, 953–964
- Jensen, C. S., Rasmussen, H. B., and Misonou, H. (2011) Neuronal trafficking of voltage-gated potassium channels. *Mol. Cell. Neurosci.* **48**, 288–297
- Lim, S. T., Antonucci, D. E., Scannevin, R. H., and Trimmer, J. S. (2000) A novel targeting signal for proximal clustering of the Kv2.1 K⁺ channel in hippocampal neurons. *Neuron* **25**, 385–397
- Rivera, J. F., Ahmad, S., Quick, M. W., Liman, E. R., and Arnold, D. B. (2003) An evolutionarily conserved dileucine motif in Shal K⁺ channels mediates dendritic targeting. *Nat. Neurosci.* **6**, 243–250
- Kaeck, S., Ludin, B., and Matus, A. (1996) Cytoskeletal plasticity in cells expressing neuronal microtubule-associated proteins. *Neuron* **17**, 1189–1199
- Gilling, M., Rasmussen, H. B., Calloe, K., Sequeira, A. F., Baretto, M., Oliveira, G., Almeida, J., Lauritsen, M. B., Ullmann, R., Boonen, S. E., Brondum-Nielsen, K., Kalscheuer, V. M., Tümer, Z., Vicente, A. M., Schmitt, N., and Tommerup, N. (2013) Dysfunction of the heteromeric KV7.3/KV7.5 potassium channel is associated with autism spectrum disorders. *Front. Genet.* **4**, 54
- Kaeck, S., and Banker, G. (2006) Culturing hippocampal neurons. *Nat. Protoc.* **1**, 2406–2415
- Shibata, R., Misonou, H., Campomanes, C. R., Anderson, A. E., Schrader, L. A., Doliveira, L. C., Carroll, K. I., Sweatt, J. D., Rhodes, K. J., and Trimmer, J. S. (2003) A fundamental role for KChIPs in determining the molecular properties and trafficking of Kv4.2 potassium channels. *J. Biol. Chem.* **278**, 36445–36454
- Trimmer, J. S. (1991) Immunological identification and characterization of a delayed rectifier K⁺ channel polypeptide in rat brain. *Proc. Natl. Acad. Sci. U.S.A.* **88**, 10764–10768
- Frost, N. A., Shroff, H., Kong, H., Betzig, E., and Blanpied, T. A. (2010) Single-molecule discrimination of discrete perisynaptic and distributed sites of actin filament assembly within dendritic spines. *Neuron* **67**, 86–99
- Manley, S., Gillette, J. M., Patterson, G. H., Shroff, H., Hess, H. F., Betzig, E., and Lippincott-Schwartz, J. (2008) High-density mapping of single-molecule trajectories with photoactivated localization microscopy. *Nat. Methods* **5**, 155–157
- An, W. F., Bowlby, M. R., Betty, M., Cao, J., Ling, H. P., Mendoza, G., Hinson, J. W., Mattsson, K. I., Strassle, B. W., Trimmer, J. S., and Rhodes, K. J. (2000) Modulation of A-type potassium channels by a family of calcium sensors. *Nature* **403**, 553–556
- Frech, G. C., VanDongen, A. M., Schuster, G., Brown, A. M., and Joho, R. H. (1989) A novel potassium channel with delayed rectifier properties isolated from rat brain by expression cloning. *Nature* **340**, 642–645
- Dascher, C., and Balch, W. E. (1994) Dominant inhibitory mutants of ARF1 block endoplasmic reticulum to Golgi transport and trigger disassembly of the Golgi apparatus. *J. Biol. Chem.* **269**, 1437–1448
- Jeyifous, O., Waites, C. L., Specht, C. G., Fujisawa, S., Schubert, M., Lin, E. I., Marshall, J., Aoki, C., de Silva, T., Montgomery, J. M., Garner, C. C., and Green, W. N. (2009) SAP97 and CASK mediate sorting of NMDA receptors through a previously unknown secretory pathway. *Nat. Neurosci.* **12**, 1011–1019
- Hirschberg, K., Miller, C. M., Ellenberg, J., Presley, J. F., Siggia, E. D., Phair, R. D., and Lippincott-Schwartz, J. (1998) Kinetic analysis of secretory protein traffic and characterization of Golgi to plasma membrane transport intermediates in living cells. *J. Cell Biol.* **143**, 1485–1503
- Toomre, D., Keller, P., White, J., Olivo, J. C., and Simons, K. (1999) Dual-color visualization of trans-Golgi network to plasma membrane traffic along microtubules in living cells. *J. Cell Sci.* **112**, 21–33
- Polishchuk, E. V., Di Pentima, A., Luini, A., and Polishchuk, R. S. (2003) Mechanism of constitutive export from the Golgi: bulk flow via the formation, protrusion, and en bloc cleavage of large trans-Golgi network tubular domains. *Mol. Biol. Cell* **14**, 4470–4485
- Lock, J. G., and Stow, J. L. (2005) Rab11 in recycling endosomes regulates the sorting and basolateral transport of E-cadherin. *Mol. Biol. Cell* **16**, 1744–1755
- Sarmiere, P. D., Weigle, C. M., and Tamkun, M. M. (2008) The Kv2.1 K⁺ channel targets to the axon initial segment of hippocampal and cortical neurons in culture and *in situ*. *BMC Neurosci.* **9**, 112
- Brown, J. R., Stafford, P., and Langford, G. M. (2004) Short-range axonal/dendritic transport by myosin-V: a model for vesicle delivery to the synapse. *J. Neurobiol.* **58**, 175–188
- Osterweil, E., Wells, D. G., and Mooseker, M. S. (2005) A role for myosin VI in postsynaptic structure and glutamate receptor endocytosis. *J. Cell Biol.* **168**, 329–338
- Chu, P. J., Rivera, J. F., and Arnold, D. B. (2006) A role for Kif17 in transport of Kv4.2. *J. Biol. Chem.* **281**, 365–373
- Xu, K., Zhong, G., and Zhuang, X. (2013) Actin, spectrin, and associated proteins form a periodic cytoskeletal structure in axons. *Science* **339**, 452–456
- Betzig, E., Patterson, G. H., Sougrat, R., Lindwasser, O. W., Olenych, S., Bonifacino, J. S., Davidson, M. W., Lippincott-Schwartz, J., and Hess, H. F.

- (2006) Imaging intracellular fluorescent proteins at nanometer resolution. *Science* **313**, 1642–1645
32. Pollard, T. D., and Borisy, G. G. (2003) Cellular motility driven by assembly and disassembly of actin filaments. *Cell* **112**, 453–465
 33. Subach, F. V., Patterson, G. H., Renz, M., Lippincott-Schwartz, J., and Verkhusa, V. V. (2010) Bright monomeric photoactivatable red fluorescent protein for two-color super-resolution sptPALM of live cells. *J. Am. Chem. Soc.* **132**, 6481–6491
 34. Straight, A. F., Cheung, A., Limouze, J., Chen, I., Westwood, N. J., Sellers, J. R., and Mitchison, T. J. (2003) Dissecting temporal and spatial control of cytokinesis with a myosin II inhibitor. *Science* **299**, 1743–1747
 35. Allingham, J. S., Smith, R., and Rayment, I. (2005) The structural basis of blebbistatin inhibition and specificity for myosin II. *Nat. Struct. Mol. Biol.* **12**, 378–379
 36. Los, G. V., Encell, L. P., McDougall, M. G., Hartzell, D. D., Karassina, N., Zimprich, C., Wood, M. G., Learish, R., Ohana, R. F., Urh, M., Simpson, D., Mendez, J., Zimmerman, K., Otto, P., Vidugiris, G., Zhu, J., Darzins, A., Klauert, D. H., Bulleit, R. F., and Wood, K. V. (2008) HaloTag: a novel protein labeling technology for cell imaging and protein analysis. *ACS Chem. Biol.* **3**, 373–382
 37. Lewis, T. L., Jr., Mao, T., Svoboda, K., and Arnold, D. B. (2009) Myosin-dependent targeting of transmembrane proteins to neuronal dendrites. *Nat. Neurosci.* **12**, 568–576
 38. Song, A. H., Wang, D., Chen, G., Li, Y., Luo, J., Duan, S., and Poo, M. M. (2009) A selective filter for cytoplasmic transport at the axon initial segment. *Cell* **136**, 1148–1160
 39. Bonifacino, J. S., and Lippincott-Schwartz, J. (2003) Coat proteins: shaping membrane transport. *Nat. Rev. Mol. Cell Biol.* **4**, 409–414
 40. Traub, L. M. (2005) Common principles in clathrin-mediated sorting at the Golgi and the plasma membrane. *Biochim. Biophys. Acta* **1744**, 415–437
 41. Farías, G. G., Cuitino, L., Guo, X., Ren, X., Jarnik, M., Mattera, R., and Bonifacino, J. S. (2012) Signal-mediated, AP-1/clathrin-dependent sorting of transmembrane receptors to the somatodendritic domain of hippocampal neurons. *Neuron* **75**, 810–823
 42. Edeling, M. A., Smith, C., and Owen, D. (2006) Life of a clathrin coat: insights from clathrin and AP structures. *Nat. Rev. Mol. Cell Biol.* **7**, 32–44
 43. Norstrom, M. F., Smithback, P. A., and Rock, R. S. (2010) Unconventional processive mechanics of non-muscle myosin IIB. *J. Biol. Chem.* **285**, 26326–26334
 44. Hirokawa, N., Noda, Y., Tanaka, Y., and Niwa, S. (2009) Kinesin superfamily motor proteins and intracellular transport. *Nat. Rev. Mol. Cell Biol.* **10**, 682–696
 45. Howard, J. (2001) *Mechanics of Motor Proteins and the Cytoskeleton*, Sinauer Associates, Inc., Sunderland, MA
 46. Nakata, T., and Hirokawa, N. (2003) Microtubules provide directional cues for polarized axonal transport through interaction with kinesin motor head. *J. Cell Biol.* **162**, 1045–1055
 47. Tamkun, M. M., O'Connell, K. M., and Rolig, A. S. (2007) A cytoskeletal-based perimeter fence selectively corrals a sub-population of cell surface Kv2.1 channels. *J. Cell Sci.* **120**, 2413–2423
 48. Mohapatra, D. P., Siino, D. F., and Trimmer, J. S. (2008) Interdomain cytoplasmic interactions govern the intracellular trafficking, gating, and modulation of the Kv2.1 channel. *J. Neurosci.* **28**, 4982–4994
 49. Korobova, F., and Svitkina, T. (2010) Molecular architecture of synaptic actin cytoskeleton in hippocampal neurons reveals a mechanism of dendritic spine morphogenesis. *Mol. Biol. Cell* **21**, 165–176

Live-cell Imaging of Post-Golgi Transport Vesicles in Cultured Hippocampal Neurons

Camilla Stampe Jensen · Hiroaki Misonou

Received: 12 May 2014 / Accepted: 23 August 2014 / Published online: 3 September 2014
© Springer Science+Business Media New York 2014

Abstract The subcellular localization of neuronal membrane signaling molecules such as receptors and ion channels depends on intracellular trafficking mechanisms. Essentially, vesicular trafficking mechanisms ensure that a large number of membrane proteins are correctly targeted to different subcellular compartments of neurons. In the past two decades, the establishment and advancement of fluorescent protein technology have provided us with opportunities to study how proteins are trafficked in living cells. However, live imaging of trafficking processes in neurons necessitate imaging tools to distinguish the several different routes that neurons use for protein trafficking. Here we provide a novel protocol to selectively visualize post-Golgi transport vesicles carrying fluorescent-labeled ion channel proteins in living neurons. Further, we provide a number of analytical tools we developed to quantify characteristics of different types of transport vesicles. We demonstrate the application of our protocol to investigate whether ion channels are sorted into distinct vesicular populations at the Golgi apparatus. We also demonstrate

how these techniques are suitable for pharmacological dissection of the transport mechanisms by which post-Golgi vesicles are trafficked in neurons. Our protocol uniquely combines the classic temperature-block with close monitoring of the transient expression of transfected protein tagged with fluorescent proteins, and provides a quick and easy way to study protein trafficking in living neurons. We believe that the procedures described here are useful for researchers who are interested in studying molecular mechanisms of protein trafficking in neurons.

Keywords Hippocampal neurons · Ion channels · Live-cell imaging · Post-Golgi vesicles · Intracellular transport · Analysis and quantification

Introduction

Neurons are one of the most morphologically complex cell types in the body due to their highly elaborated and branched network of dendrites and elongated axons, which further develop multiple sub-compartments, such as dendritic spines, the axon initial segments, and the node of Ranvier. Despite this complex composition, neurons are capable of localizing a number of membrane signaling molecules, such as neurotransmitter receptors and ion channels, to specific destinations, thereby realizing unique functions in each membrane sub-compartment (Lai and Jan 2006). This destination-specific distribution of signaling molecules is largely achieved by the secretory trafficking pathway as in other types of cells (Horton and Ehlers 2003b; Namba et al. 2011).

In the secretory pathway, receptors and ion channels are synthesized in the rough endoplasmic reticulum (ER) and transported to the Golgi apparatus for posttranslational

Electronic supplementary material The online version of this article (doi:10.1007/s10571-014-0103-4) contains supplementary material, which is available to authorized users.

C. S. Jensen · H. Misonou
Department of Neural and Pain Sciences, University of Maryland, Baltimore, MD 21201, USA

C. S. Jensen
Department of Biomedical Sciences, The Panum Institute, University of Copenhagen, Blegdamsvej 3, 2200 Copenhagen N, Denmark

H. Misonou (✉)
Graduate School of Brain Science, Doshisha University, 4-1-1 Kizudawadai, Kizugawa-Shi, Kyoto 6190225, Japan
e-mail: h_misonou@mac.com

processing. At the Golgi apparatus and in the *trans*-Golgi network, membrane signaling molecules are packaged into transport vesicles which can be targeted to a specific compartment, either dendrites or the axon, by two different trafficking mechanisms (Horton and Ehlers 2003b; Jensen et al. 2011). In the first scenario, transport vesicles are delivered to or near the final destination of the cargo proteins. This “selective trafficking” has been shown to underlie polarized dendritic localization of the transferrin receptor. The transferrin receptor was found to reside in transport vesicles which were delivered to dendrites and excluded from the axon (Burack et al. 2000; Silverman et al. 2001; Sampo et al. 2003). The second scenario is not as simple. Here, transport vesicles are not targeted to a specific membrane compartment but rather delivered non-specifically. In this case, the specific localization of the membrane protein is achieved by a downstream mechanism. This downstream mechanism can be either (1) compartment-specific exocytosis where insertion of the protein occurs exclusively in a specific membrane compartment even though vesicles were delivered non-specifically (Burack et al. 2000), or (2) compartment-specific endocytosis where insertion of the protein initially occurs non-specifically followed by endocytosis from the compartment which is not the final destination (Sampo et al. 2003). A number of studies have been conducted to understand the trafficking mechanisms underlying polarized membrane distribution of membrane proteins in neurons. However, except from the fact that neurons can use these distinct mechanisms in membrane protein targeting, our knowledge on how they are utilized for a broader number of membrane signaling proteins, is yet largely unknown.

To address which trafficking pathway a given protein takes, one needs to visualize and analyze how the protein is trafficked dynamically from the Golgi apparatus, where different trafficking pathways emerge. Here, we report a new protocol to image selectively the post-Golgi vesicles which traffic membrane proteins in living hippocampal neurons. The membrane proteins were fluorescently labeled and transiently expressed in neurons. Shortly after the transfection, the expressed membrane proteins were concentrated in the Golgi apparatus. This concentration was achieved by close monitoring the temporal expression profile of the proteins and by blocking their exit from the Golgi apparatus with low-temperature incubation of the neurons (Dotti and Simons 1990). When physiological temperature was subsequently restored, the membrane proteins were synchronously released from the Golgi apparatus in transport vesicles. Live-cell imaging of these vesicular carriers and quantitative analyses of their traffic characteristics allowed us to dissect the mechanisms of membrane protein trafficking in neurons. Our protocol

therefore provides a simple and easy way to probe the post-Golgi trafficking of neuronal transmembrane proteins.

Here, we demonstrate the applicability of the protocol to investigate the trafficking mechanisms using voltage-gated potassium (Kv) channels. These ion channels exhibit a diverse, yet precise pattern of localizations in defined sub-compartments of the neuronal surface membrane (Misonou and Trimmer 2004; Trimmer and Rhodes 2004; Vacher et al. 2007) and therefore serve as excellent model proteins to study the heterogeneity in neuronal trafficking mechanisms. Using the protocol, we recently reported that two Kv channels that are both localized to dendrites are sorted in separate pools of post-Golgi transport vesicles and trafficked by different molecular mechanisms (Jensen et al. 2014). Here, we wish to provide a detailed description of our techniques and hope that the protocol serves the research fields to advance our understanding of neuronal protein trafficking mechanisms.

Materials and Methods

Primary Cultures of Rat Hippocampal Neurons

Our culture method is derived from the low-density culture method described by Goslin and Banker (Goslin et al. 1998; Kaeck and Banker 2006) with some modifications (Misonou and Trimmer 2005; Jensen et al. 2014). Although this is a co-culture system of neurons and glia in principle, they need to be separately prepared and cultured as described below. All animal use and procedures have been approved by the institutional animal use committees.

Preparation of Culture Reagents

Hippocampal neurons were cultured in two types of culture media: A plating medium consisting of modified Eagles medium (MEM) containing 10 % (v/v) donor horse serum, 0.6 % (w/v) glucose, and 1 µg/ml penicillin and streptomycin, and a maintenance medium consisting of MEM supplemented with 0.6 % (w/v) glucose, the N2 supplement, 1 % B27 supplement (Invitrogen), and 1 mM sodium pyruvate.

Preparation of Astrocytes for Co-culture with Hippocampal Neurons

The astrocytes used in the co-culturing were prepared from cortices of newborn rat pups (P1 or P2). Pieces of cortical hemispheres were dissected and incubated with 0.25 % trypsin in Dulbecco's phosphate buffered saline without Ca^{2+} and Mg^{2+} (DPBS) for 20 min at 37 °C. The tissues were collected by centrifugation, and cells were dissociated in the plating medium. About 300,000 cells per dish were

plated into 10 cm tissue culture dishes coated overnight with 25 µg/ml poly-L-lysine and cultured for 7–10 days in a humidified CO₂ incubator at 37 °C. The astrocytes were harvested with 0.05 % trypsin/EDTA when the cultures reached 80 % confluence (i.e., 80 % of the tissue culture dish surface area covered with astrocytes). Upon resuspension in the plating media supplemented with 10 % dimethylsulfoxide (DMSO), the cells were frozen and stored in 1 ml aliquots (1 ml from a 10 cm tissue culture dish) in liquid nitrogen. One week prior to the preparation of hippocampal neurons, astrocytes were thawed and resuspended in the plating medium. Cells were collected by centrifugation (at 120×g for 5 min), resuspended in 10 ml of glial plating medium, and plated at 30,000 cells per well in 6-well tissue culture plates which were coated overnight with 25 µg/ml poly-L-lysine. The cells were cultured in the plating medium for 7 days. One day before the preparation of neurons, the culture medium was replaced with the maintenance medium.

Preparation of Rat Embryonic Hippocampal Neurons

A timed pregnant rat was euthanized in a CO₂ euthanization chamber. E18 embryos were obtained from the uterus, and their heads were collected in ice cold DPBS. Brains were carefully isolated and placed in a new dish with fresh DPBS on ice. Hippocampi were dissected and kept on ice until the dissection of all hippocampi was completed. Hippocampi were transferred to a 15-ml tube and incubated with 0.25 % trypsin in 5 ml of DPBS for 15 min at 37 °C. The reaction was terminated by adding 5 ml of the plating medium. The hippocampi were centrifuged at 120×g for 5 min, and the supernatant was carefully removed. The hippocampal tissue was slowly triturated (in the plating medium) using a 1-ml plastic pipette tip until the tissue was completely dissociated (about 20–25 strokes). Approximately 250,000–400,000 cells should be obtained from each hippocampus. Neurons were plated onto 25-mm-diameter round glass coverslips treated as follows. Prior to their use, coverslips were placed in porcelains racks and washed overnight in 1 N nitric acid. The next day coverslips were washed three times with purified water and autoclaved. To separate neurons from astrocytes in the co-culture, wax pedestals were added near the edge of the coverslips. Then, they were coated overnight with 1 mg/ml poly-L-lysine in 100 mM borate buffer (pH 8.5) and washed. Six coverslips were placed in a 10-cm petri dish and covered with 12 ml plating media. Neurons were plated at 50,000 cells per coverslip and incubated 3–6 h in a humidified 5 % CO₂ incubator at 37 °C. After the incubation, each coverslip was transferred to a well of the 6-well plates with astrocytes (with neurons

facing down toward the astrocytes). Two days after the plating, cytosine arabinoside was added to each well at a final concentration of 5 µM to prevent proliferation of non-neuronal cells.

Transient Transfection of Cultured Neurons

Neurons cultured for 7–11 days were transiently transfected using Lipofectamine 2000 (Invitrogen). Prior to transfection, 1.5 ml of the culture media was transferred from each well of 6-well plates into new 6-well plates. Coverslips were transferred to the new 6-well plates with the neuronal side facing up. Lipofectamine 2000/cDNA cocktails were prepared in MEM in accordance with the manufacturer's instructions. The amount of cDNA was carefully optimized for each protein for appropriate expression levels. Typically we used 0.5–1.0 µg cDNA and 2 µl of Lipofectamine 2000 reagent in 100 µl MEM per coverslip. The transfection cocktail was added directly onto the neurons, and neurons were incubated for 1.5 h in a 5 % CO₂ incubator at 37 °C. Subsequently, the coverslips were transferred back to the original 6-well plates and the co-culture with astrocytes was continued until neurons were subjected to the temperature-block procedure.

Temperature-block Procedure and Live-cell Imaging

The timing of the temperature-block initiation was carefully considered as membrane proteins exhibits different temporal expression patterns (see details in “Results” section). The temperature-block was performed by transferring coverslips to 35-mm dishes with pre-cooled (to 19.5 °C) Hank's balanced salt solution (HBSS, Invitrogen) containing 10 mM 4-(2-hydroxyethyl)-1-piperazineethanesulfonic acid (HEPES, pH 7.3). The dishes were then placed in a water bath set to a temperature that made the HBSS temperature at 19.5 °C and incubated for 3–5 h. Subsequently, to release neurons from the temperature-arrest, coverslips were mounted in an imaging chamber (Warner Instruments, Hamden, CT) with HBSS pre-warmed to 37 °C, and the chamber was secured on a microscope stage warmed up using an air stream incubator (Nevtek, Williamsville, VA). The temperature of the imaging solution was continuously monitored using a probe thermometer (Physitemp, Clifton, NJ) and kept at 35–37 °C. Neurons were visualized under epifluorescence illumination using an inter-line-CCD camera installed on an Axiovert 200 M microscope (Zeiss, Thornwood, NY) with a 63X objective lens (1.4 NA). Time-lapse images (typically 40–100 frames) were taken at a 0.5–5 Hz acquisition rate with a typical CCD exposure time of 150 ms using Axiovision software. Only neurons with a morphology characteristic of pyramidal neurons were selected for imaging and the cells were kept on the imaging stage for

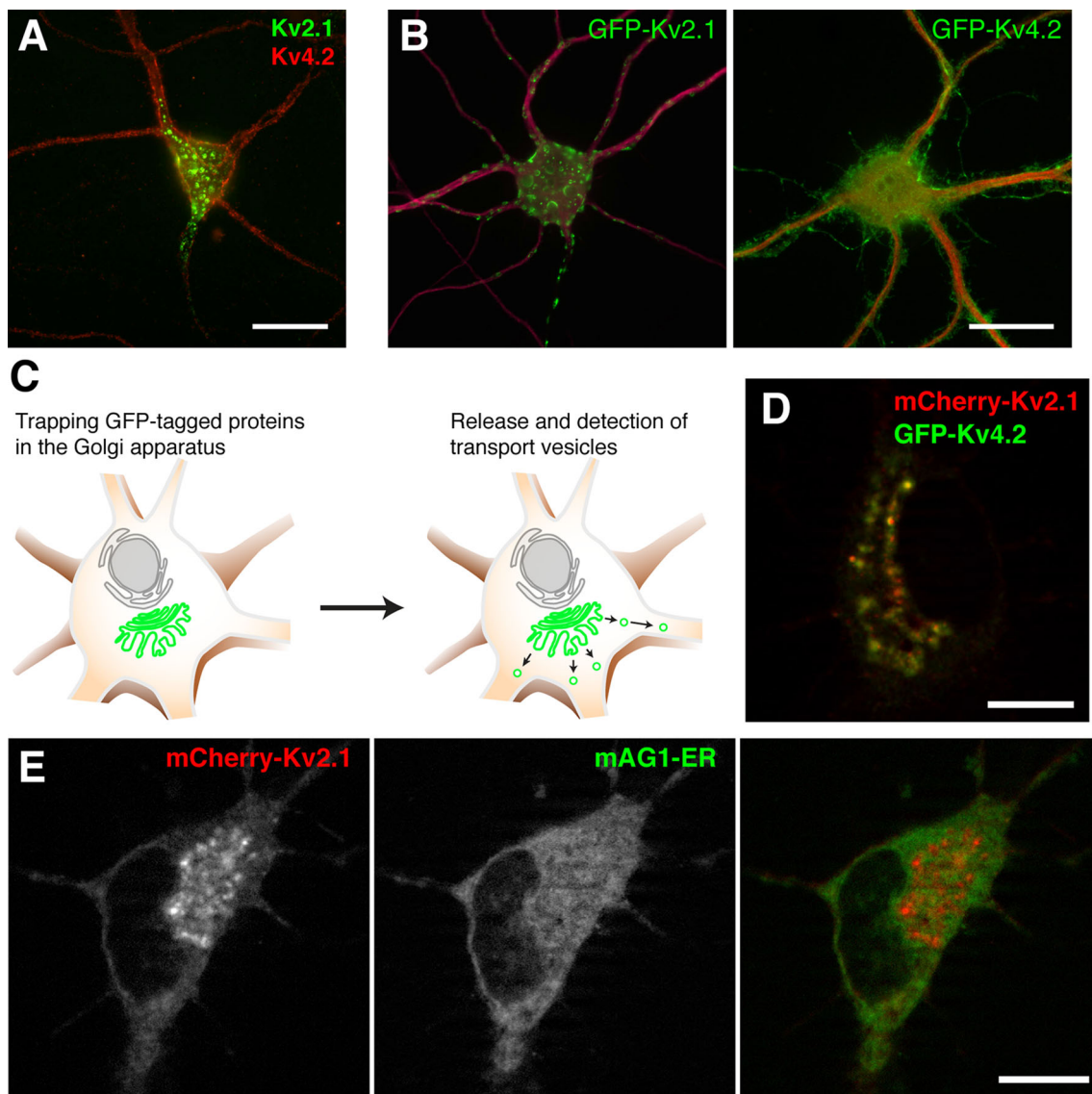


Fig. 1 Temperature-block to concentrate ion channel proteins in the Golgi apparatus. **a** Localization of endogenous Kv2.1 and Kv4.2 channels. Cultured neurons were immunostained with specific antibodies for each potassium channel protein. *Scale bar*, 20 μ m. **b** Expression and steady-state localization of GFP-tagged Kv2.1 (*left*) and Kv4.2 (*right*). Transfected neurons were immunostained for a dendritic marker MAP-2 and imaged for GFP signals and immunolabeling. *Scale bar*, 20 μ m. **c** Graphical presentation of our protocol.

d Accumulation of mCherry-Kv2.1 and GFP-Kv4.2 in perinuclear structures by the temperature-block. Neurons transfected with these tagged channel proteins were subjected to the temperature-block and then imaged live at the room temperature. *Scale bar*, 10 μ m. **e** Non-overlapping distribution of mCherry-Kv2.1 and mAG fluorescent protein with an ER localization signal (KDEL). Neurons were transfected, subjected to the temperature-block and then imaged live at the room temperature. *Scale bar*, 10 μ m

maximum of 1 h. Images were exported as JPEG files to the NIH Image software, ImageJ.

Image Analyses

Analysis of Vesicle Velocities

To obtain the velocity of transport vesicles, all frames from a time-lapse image stack were imported in ImageJ and analyzed using the “Manual Tracking” plug-in. Only

anterograde moving vesicles in the proximal region of dendrites (<100 μ m from the soma) were selected for tracking analysis. To amplify the signal to noise ratio and to compensate for photobleaching, the signal intensity in each image frame was adjusted using a best-fit algorithm in ImageJ. The analysis was restricted to dendrites, which were thick (>1.5 μ m) and distinguishable from the axon when visualized using the mCherry cell-fill image (see Fig. 3c). Six transport vesicles were selected per neuron and tracked through the movie for a minimum of five

frames. The net and maximum velocities of a vesicle were determined as follows.

$$V_{\text{net}} = D_{\text{total}}/t_{\text{total}} \quad (1)$$

$$V_{\text{max}} = D_{\text{max}}/t_{\text{interval}} \quad (2)$$

D_{total} represents the distance the vesicle traveled during the duration for which the vesicle was tracked (t_{total}) in Eq. (1). D_{max} represents the maximum displacement the vesicle showed between two consecutive frames separated by an interval (t_{interval}) in Eq. (2). Velocities of individual vesicles were averaged per neuron, and then these values were averaged among ten neurons. Alternatively, velocity distributions of all vesicles analyzed were presented and analyzed.

Analysis of the Number of Mobile Vesicles

The image-subtraction method used to assess the drug effects was performed as follows. First, all image frames from a time-lapse image stack were averaged in ImageJ. This averaged image was then subtracted from each of the original image frames to remove signals from relatively immobile objects, like the Golgi apparatus. This subtraction results in series of imaging frames where only mobile objects are represented (as demonstrated in Fig. 4b). A maximum projection from this set of subtracted imaging frames was then created to visualize trajectories of transport vesicles. The number of mobile anterograde vesicles, showing more than a 1 μm displacement in the dendrites of a cell was manually counted in the subtracted live-cell images and averaged among several neurons. In this paper, we analyzed the number of moving GFP-Kv2.1 and GFP-HCN1 vesicles in the absence and presence of latrunculin A (LatA; Invitrogen). LatA was dissolved in DMSO and applied to the imaging solution at a final concentration of 1 μM . Neurons were imaged before and 5 min after the treatment with LatA.

Analysis of the Travel Distance

Net travel distances were obtained from the subtracted movies. Vesicles near the base of the dendrites were followed to see how far they reached. The termination point was the position where vesicles were immobile for at least five frames. The maximum cut-off value is 100 μm due to the size of the imaging area.

Statistical Analysis

All data are presented as actual data points, the mean \pm s.e.m, or as a frequency distribution. Normality of data was

examined by Kolmogorov–Smirnov test. Comparison of the numbers of mobile vesicles in drug-treated neurons was done using the paired t test (two tailed). ANOVA was used to compare the velocity distributions of three groups. A P value less than 0.05 was considered to be statistically significant in all cases.

Immunofluorescence Staining

Neurons were fixed in 4 % paraformaldehyde/4 % sucrose/PBS in 20 min. Then, washed in PBS and blocked in 4 % milk/Tris-buffered saline in the presence of 0.1 % Triton X-100 (TBST). Primary antibodies were applied during overnight incubation at 4 °C. The primary antibodies employed were; anti-MAP-2 mouse monoclonal antibody (Sigma-Aldrich; clone AP-20; 1:2000), K89 anti-Kv2.1 mouse monoclonal antibody (NeuroMab, Davis, CA), K57 anti-Kv4.2 mouse monoclonal antibody (NeuroMab), a mouse monoclonal antibody generated against tubulin (Sigma, clone DM1A, 1:2000), and a mouse monoclonal antibody against GM130 (BD Biosciences, clone 35, 1:500). Secondary antibodies were Alexa-conjugated IgG-specific antibodies (Invitrogen; 1:2000). Both primary and secondary antibodies were diluted in 4 % milk/TBST. Neurons were mounted on microscope slides using Pro-Long Gold antifade reagent (Invitrogen).

cDNA Expression Constructs

Kv2.1 (NM_013186), Kv4.2 (NM_031730) and KChIP2 (NM_020095) cDNA were generous gifts from Dr. James Trimmer. The coding sequences were cloned into the EGFP-C1 or mCherry-C1 vectors from Clontech (Mountain View, CA). In experiments with GFP-Kv4.2, the beta subunit KChIP2 were co-expressed to promote the surface expression of Kv4.2 channels (Shibata et al. 2003). mCherry-GalT was generated from Venus-GalT (Addgene, Cambridge, MA). Monomeric Azami Green fused with the signal peptide and the ER-retention signal of calreticulin was purchased from MBL (Nagoya, Japan). Wild-type Arf1, Arf1 Q71I, and GFP-tagged MAP2C were generous gifts from Dr. Jeyifous and Dr. Kaech, respectively (Jeyifous et al. 2009; Kaech et al. 1996). GFP-HCN1 was a gift from Dr. Siegelbaum (Santoro et al. 2011).

Results

Temperature-block of Newly Synthesized GFP-tagged Ion Channel Proteins in the Golgi Apparatus

To study protein trafficking of neuronal ion channels, we have used a low-density culture system of primary rat

hippocampal neurons (Goslin et al. 1998). This culture system is ideal for imaging of individual transport vesicles due to their low-density plating and their optical clarity. All experiments were performed on neurons cultured for 7–11 days.

Our goal with this protocol was to visualize post-Golgi traffic of Kv channels that we tagged with fluorescent proteins. Being able to image selectively post-Golgi vesicles, we aimed to investigate (1) whether different Kv channels are sorted into different transport vesicles, (2) whether and how vesicles are targeted, and (3) the molecular mechanisms by which the vesicles are transported and targeted in living neurons. Here, as target examples, we employed two dendritic Kv channels, Kv2.1 and Kv4.2, which exhibits very distinct localizations in neuronal dendrites (Fig. 1a) (Jensen et al. 2011). First, we verified that addition of a fluorescent protein tag, like the green fluorescent protein (GFP) would not impact the targeting and localization of Kv2.1 and Kv4.2 channels in hippocampal neurons. In consistence with previous studies (Sheng et al. 1992; Murakoshi and Trimmer 1999; Menebola et al. 2008), we found that these fluorescent protein-tagged channels localized properly (Fig. 1b) like their endogenous counterparts (Fig. 1a) at the steady-state (>24 h after transfection).

To probe selectively the population of post-Golgi transport vesicles carrying ion channel proteins, we employed the classical temperature-block technique (Matlin and Simons 1983; Cid-Arregui et al. 1995) in combination with controlled transient expression of fluorescent protein-tagged proteins (Fig. 1c). It has previously been shown that incubating cultured neurons at 19.5 °C will inhibit the export of proteins from the Golgi apparatus, thereby trapping them in the organelle. Therefore, initiation of a temperature-block around the time when newly synthesized fluorescent protein-tagged Kv subunits are detectable should result in trapping of the majority of GFP-tagged proteins in the Golgi apparatus with only negligible levels trafficked to later organelles such as the plasma membrane. To determine the optimal time point to initiate the temperature-block, we first monitored the temporal expression of the fluorescent protein-tagged ion channel proteins from the onset of transfection. Neurons were transfected with cDNA encoding either GFP-tagged Kv2.1 or Kv4.2 channels using Lipofectamine 2000. Although we were not able to quantify the expression levels because of the low transfection efficiency of the method and variable expression levels among cells, the signals of fluorescent proteins (under the CMV promoter) became apparent typically between 2 and 3 h. We therefore chose the 3 h time point to start the temperature-block. In our hands, initiation of the temperature-block 3 h after transfection was appropriate for a number of membrane proteins other than Kv2.1

and Kv4.2, including HCN1 (see below), vesicular stomatitis virus G (VSVG) (Jensen et al. 2014), and the transferrin receptor (data not shown). However, we recommend a verification of whether this time frame of temperature-block is appropriate for other membrane proteins.

After the transfection period, we transferred glass coverslips with neurons to dishes containing HBSS pre-cooled to 19.5 °C. Hereafter, neurons were kept at this temperature for the temperature-block for 1–6 h using a cooled circulating water bath. We found that 2–3 h of temperature-block was sufficient for effective accumulation of both mCherry-Kv2.1 and GFP-Kv4.2 in perinuclear structures (Fig. 1d), and that this accumulation was consistently observed even after a 6 h incubation. We chose 3–5 h temperature-block for the following experiments as described in the “Materials and Methods” section.

These perinuclear structures were apparently distinct from the ER, as accumulated mCherry-Kv2.1 did not colocalize with monomeric Azami GFP containing the signal peptide and the ER-retention signal of calreticulin (Fig. 1e) (Karasawa et al. 2003). In contrast, GFP-Kv2.1 showed a partial colocalization with mCherry fused with the N-terminal region (aa 1–60) of the human galactosyl-transferase (GalT-mCherry) (Zaal et al. 1999), which has been shown to localize in medial-trans cisternae of Golgi stacks (Sciaky et al. 1997), as shown in Fig. 2a. We also observed a partial colocalization of GFP-Kv2.1 and GM130, a cis-Golgi matrix protein (Nakamura et al. 1995) (Fig. 2b). The perinuclear accumulation of GFP-tagged channels promoted by the temperature-block was not observed in control cells kept at 37 °C during the incubation period (Fig. 2c). These results suggest that our temperature-block protocol effectively accumulate fluorescent protein-tagged Kv channel proteins in the Golgi apparatus.

Addition of a protein synthesis inhibitor, cycloheximide, during the temperature-block did not provide any significant improvement in the Golgi accumulation (data not shown). Therefore, we concluded that the translation may be greatly reduced in neurons incubated at 19.5 °C in HBSS, which does not contain any amino acids. Therefore, the following experiments were performed without cycloheximide.

Imaging of Post-Golgi Transport Vesicles Carrying GFP-tagged Proteins

Given that the GFP-tagged Kv channels were highly accumulated in the Golgi apparatus, we next tested whether the protein trafficking could be restored after the temperature-block. To this end, we performed time-lapse imaging of neurons expressing GFP-Kv4.2 after the temperature shift from 19.5 to 37 °C. We chose Kv4.2 in this experiment because it is localized to distal dendrites as compared

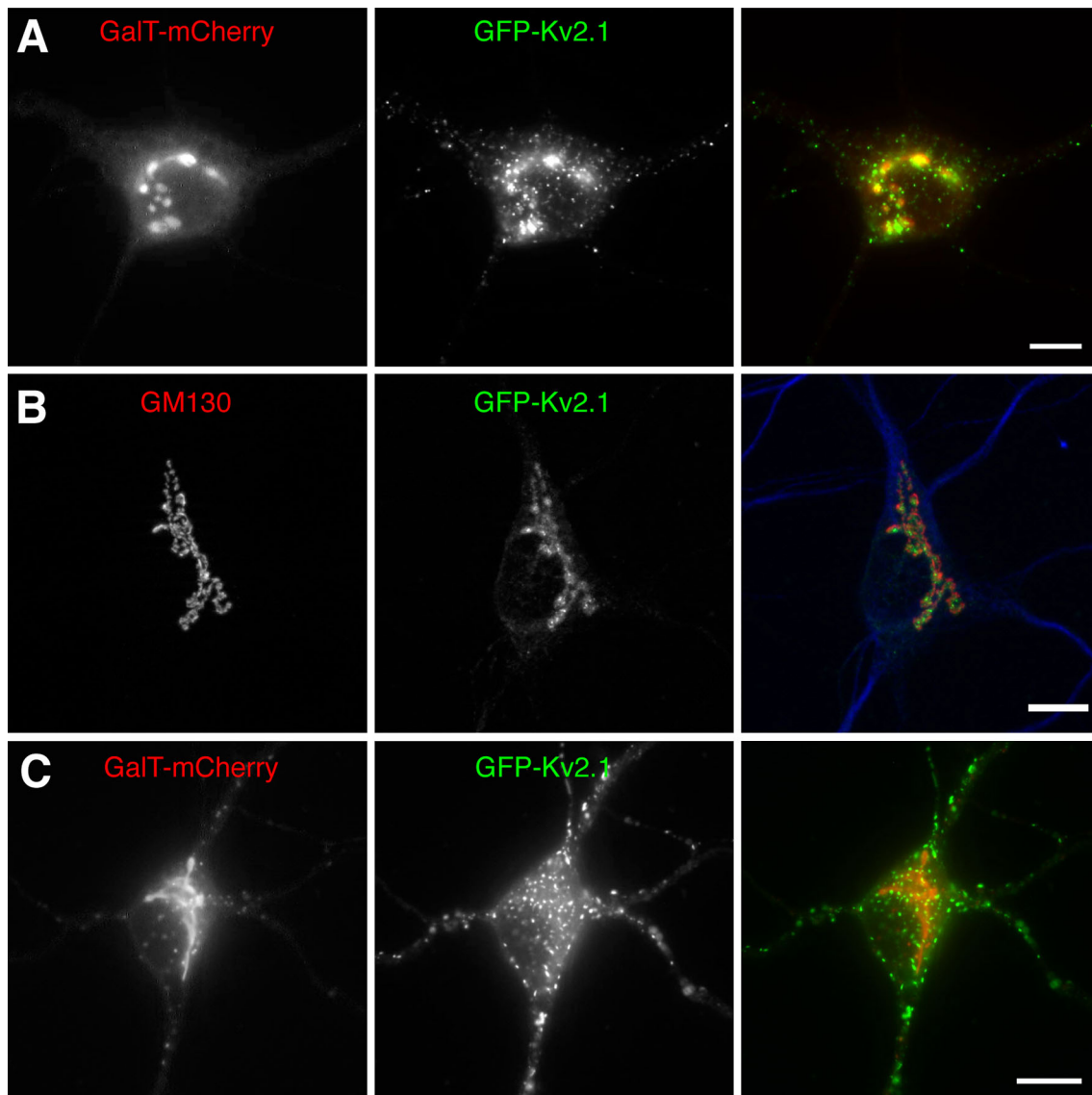


Fig. 2 Accumulation of ion channel proteins in the Golgi apparatus. **a** Partial colocalization of GFP-Kv2.1 and GalT-mCherry after the temperature-block. Neurons transfected with GFP-Kv2.1 and GalT-mCherry were subjected to the temperature-block and then imaged live at the room temperature. *Scale bar*, 5 μm . **b** Partial colocalization of GFP-Kv2.1 and GM130 after the temperature-block. Neurons

transfected with GFP-Kv2.1 were subjected to the temperature-block, fixed, and immunostained for GM130 and MAP-2 (in blue). *Scale bar*, 10 μm . **c** Non-overlapping localization of GFP-Kv2.1 and GalT-mCherry without the temperature-block at 6 h after transfection. *Scale bar*, 10 μm (Color figure online)

to the proximal localization of Kv2.1 (see Fig. 1a and b). Therefore, the bulk transport of the fluorescent proteins from the Golgi apparatus in the soma to distal dendrites could be easily visualized as a gradual shift of the GFP signals from the soma to dendrites if vesicular transport from the Golgi recovers. We confirmed that GFP-Kv4.2 is accumulated in the Golgi apparatus with mCherry-Kv2.1 as shown in Fig. 3a and in the line-scanning analysis (Fig. 3b). Likewise, immediately after the temperature-block, GFP signals were observed mostly in the soma, presumably in the Golgi apparatus (Fig. 3c). However,

after 15 min of incubation at 37 $^{\circ}\text{C}$, GFP signals appeared in more distal regions of the dendrites (Fig. 3c). Measurement of GFP fluorescence intensity along a dendrite revealed this time-dependent increase in fluorescent intensity (Fig. 3d), indicating that vesicular trafficking of GFP-Kv4.2 was restored after the temperature-block.

To visualize individual transport vesicles at a higher spatial and temporal resolution, we performed time-lapse imaging of neurons expressing GFP-tagged channels. Figure 4a (Control) shows an example of the time-lapse images of GFP-Kv2.1 expressing neurons (see the

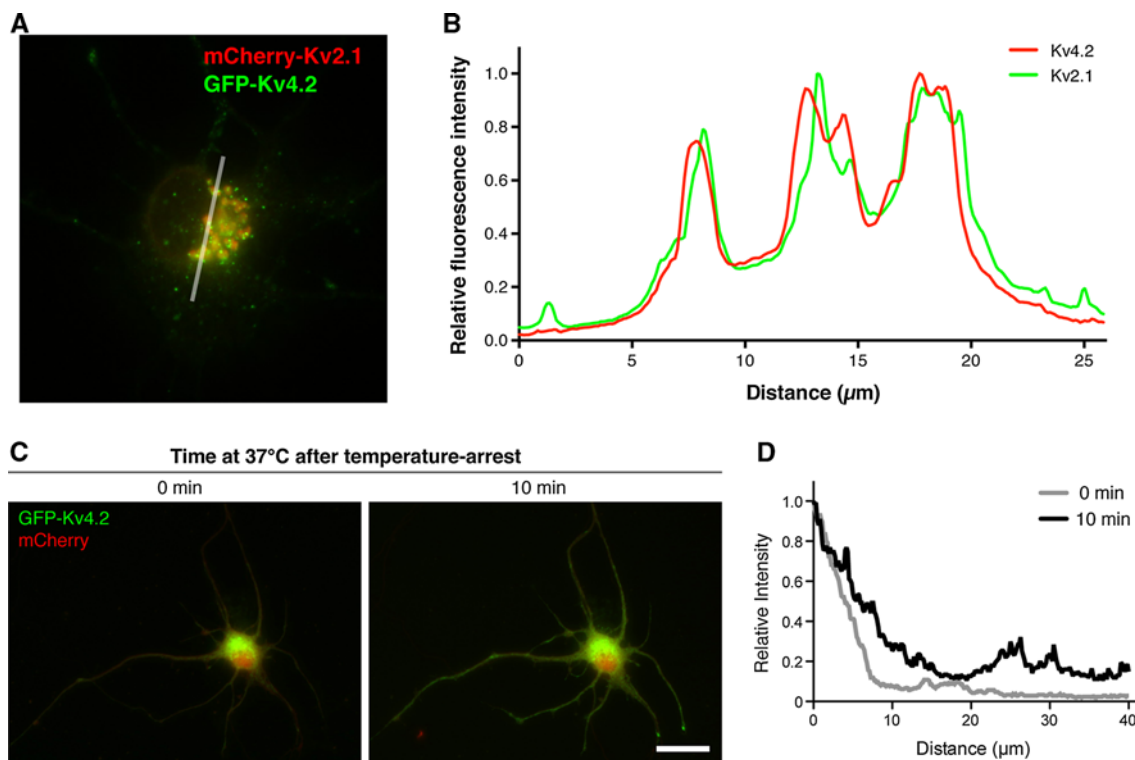


Fig. 3 Export of ion channels from the Golgi apparatus upon releasing cells from the temperature-block. **a** Colocalization of GFP-Kv2.1 and mCherry-Kv2.1 in the Golgi apparatus. **b** Fluorescence intensity of GFP-Kv4.2 and mCherry-Kv2.1 was measured over the *line* indicated in **a**. **c** A representative neuron expressing mCherry and GFP-Kv4.2. Neurons were subjected to the temperature-block

and then imaged live at two different time points (0 and 15 min) after release from the block. *Scale bar*, 20 μm . **d** Quantification of GFP-Kv4.2 fluorescence toward distal dendrites in neurons released from the temperature-block. A *line* was drawn from soma and 40 μm into a dendrite at two time points (0 and 10 min) after the temperature-block. A representative trace is shown. *Scale bar*, 25 μm

Supplementary Movie). After the temperature-block, cells were incubated for 15 min at 37 °C to allow vesicles to emerge from the Golgi apparatus. The images were acquired every 6 s and overlaid with different colors to visualize the displacement of transport vesicles. In the composite image, immobile structures are shown in white, whereas mobile structures exhibit distinct colors. These mobile structures were not observed when neurons were co-transfected with a mutant of Arf1 (Arf1 Q71I) (Fig. 4a), which has been shown to block the fission of transport vesicles from the Golgi apparatus (Dascher and Balch 1994; Jeyifous et al. 2009). Co-expression of wild-type Arf1 did not exhibit any noticeable effects (Fig. 4a). These results demonstrate that our protocol provides a way to achieve synchronous release of transport vesicles from the Golgi apparatus.

Analysis of Transport Vesicles

To test hypotheses regarding the nature of vesicular transport, one needs to quantify specific properties of transport vesicles such as velocity, travel distance and motion. For this purpose, we have developed a number of

image processing methods to obtain quantitative measures from the time-lapse image series. First, we utilized an image-subtraction method (Fig. 4b). From our time-lapse movies consisting of a number of frames, we generated an averaged image. In this image, the signal intensity of mobile vesicles is expected to be greatly reduced due to the averaging, whereas that of immobile structures would not be altered substantially. Next, the averaged image was subtracted from each frame (of original time-lapse stack), which resultantly removes the signals from immobile structures (Fig. 4b). Therefore, the color-coded image generated from the image-subtraction represents mobile vesicles without the background of immobile structures (Fig. 4b). To obtain an image representing the motility of vesicles in a time-lapse movie, we generated a maximum projection image from all the subtracted frames. This resulted in the representation of trajectories of moving transport vesicles (Fig. 4b). Using these processed images, we applied different analytical applications to obtain quantitative measures of vesicular trafficking as described below.

Velocity of vesicles is a useful measure for statistical comparison of vesicle characteristics. To obtain the

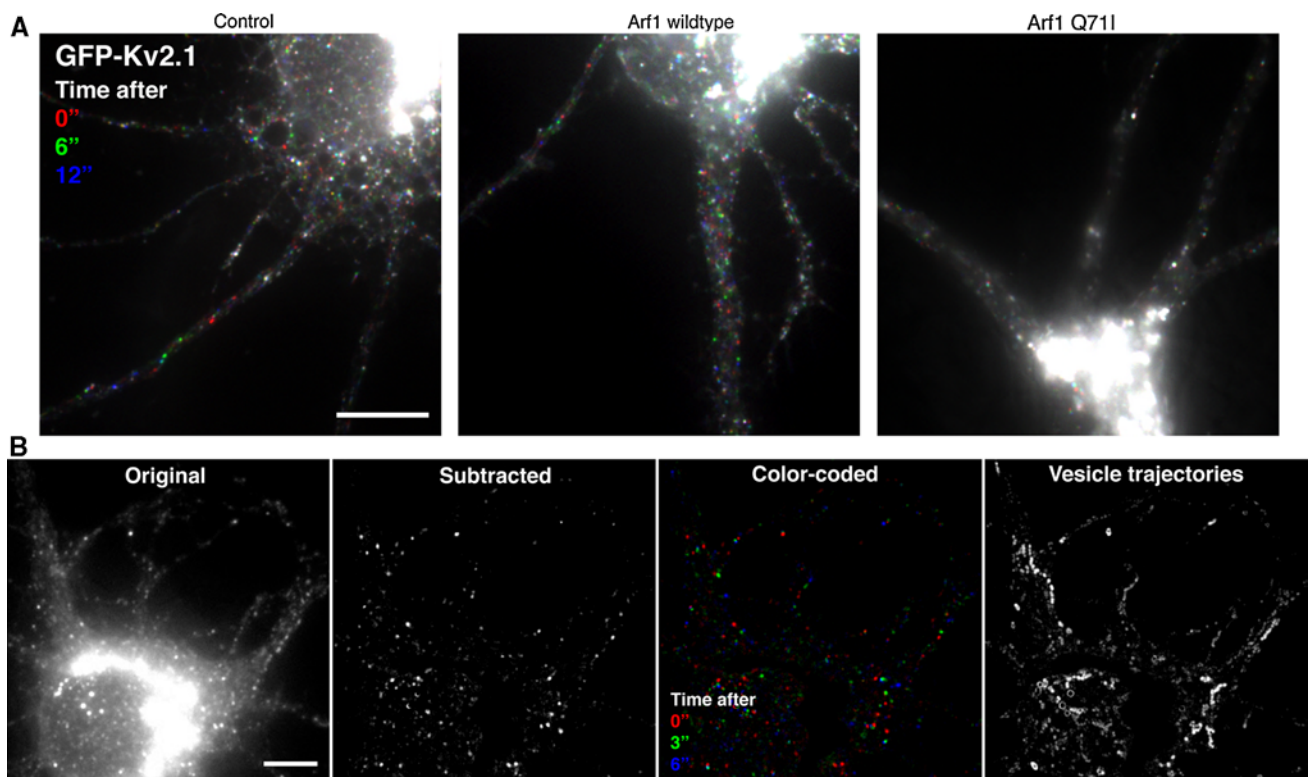


Fig. 4 Visualization and analyses of post-Golgi transport vesicles. **a** Emergence of mobile puncta carrying GFP-Kv2.1 after the temperature-block and its dependence to Arf1. Neurons were transfected with GFP-Kv2.1 and an empty vector (Control), Arf1, or Arf1 Q71I mutant. To demonstrate the mobility of the puncta, time-lapse frames are color-coded at different time points (0, 6 and 12 s) after the temperature-block. *Scale bar*, 10 μm. **b** Image processing of time-lapse image stacks. Example shown is from imaging of post-Golgi vesicles carrying GFP-Kv2.1. First, an averaged image representing all frames from a time-lapse image

stack was generated in ImageJ (not shown). This image was then subtracted from each frame in the live imaging sequence (Original) to remove signals from stationary objects. That processing resulted in a live imaging sequence of mobile post-Golgi vesicles (Subtracted). Color-coding of consecutive frames demonstrate the vesicle mobility and reveal the direction of movement when these frames are overlaid (Color-coded). Finally, a maximum projection image was generated to obtain the movement tracks from individual post-Golgi vesicles (Vesicle trajectories). *Scale bar*, 5 μm

velocity, we tracked individual vesicles using the “Manual Tracking” function of the software ImageJ in a time-lapse sequence. For this, we used either the original images or the processed images. Briefly, we tracked post-Golgi vesicles through several imaging frames (≥ 5). With this, we have obtained both average (or net) and maximum vesicle velocities calculated according to the imaging frame acquisition time. To demonstrate the power of the analysis, we measured the velocities of vesicles carrying three dendritic ion channels, GFP-Kv2.1, Kv4.2, and HCN1. It should be noted that the velocities of GFP-Kv2.1 and Kv4.2 vesicles have been already published (Jensen et al. 2014), but are re-analyzed and compared here with the newly measured velocity of GFP-HCN1 vesicles to demonstrate the usefulness of our method. Figure 5a shows that GFP-HCN1 was also efficiently accumulated in the Golgi apparatus like GFP-Kv2.1 with the temperature-block. These results, in Fig. 5b, that the vesicles carrying different dendritic ion channels exhibit distinct velocities, indicate

that these vesicles are different populations. Here, one needs to pay attention to the fact that the velocities can vary dramatically from 0.6 to 6 μm/s. Therefore, the acquisition rate has to be carefully chosen for the membrane protein studied (we used 1 and 5 Hz acquisition rate for GFP-Kv2.1 and HCN1, and 5 Hz for GFP-Kv4.2).

From the vesicle trajectories, we obtained and measured the net travel distance of vesicles (Fig. 5c). To do so, we first identified vesicles near the base of dendrites and tracked them to measure how far they can reach in the dendrites. Dendrites were distinguished from the axon using untagged mCherry as a cell-fill dye and based on their morphology. The net travel distance was measured from the base of dendrites to the point where the vesicle becomes immobile for at least five frames. We analyzed the mean travel distance of vesicles carrying GFP-Kv2.1 and those of GFP-Kv4.2 as shown in Fig. 5c and averaged them in each cell. The analysis showed that the mean travel distance of GFP-Kv4.2 vesicles (80 ± 12 μm) was

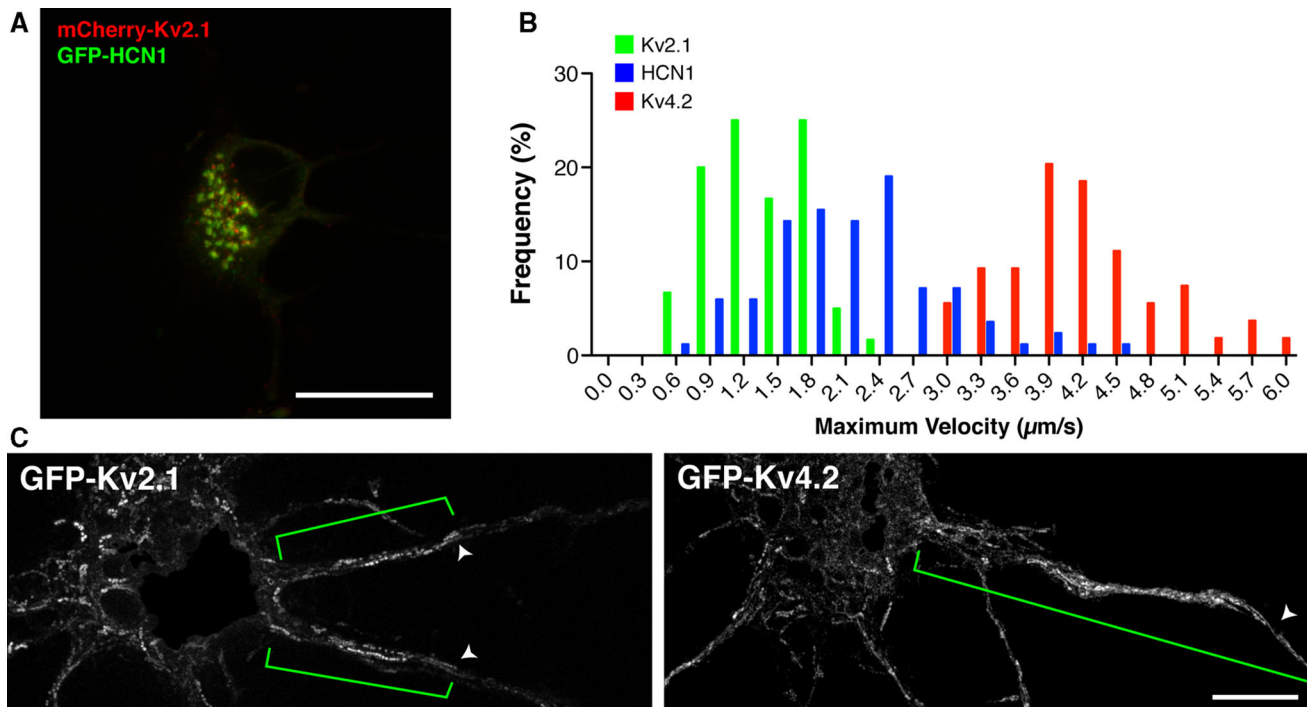


Fig. 5 Analyses of post-Golgi transport vesicles carrying dendritic ion channels. **a** Accumulation of GFP-HCN1 to perinuclear structures with mCherry-Kv2.1 after the temperature-block. *Scale bar*, 20 μm . **b** Velocities of post-Golgi transport vesicles. Post-Golgi vesicles were tracked in several consecutive frames and the maximum velocities calculated from the image acquisition rate. A distribution of maximum velocities of vesicles carrying GFP-Kv2.1, GFP-Kv4.2,

and GFP-HCN1 is shown (for each protein; 6 vesicles were tracked in 10 different cells). **c** Measuring post-Golgi travel distances. By use of the subtraction method we can obtain the net travel distance of vesicles into dendrites. As demonstrated here, GFP-Kv2.1 vesicles traffic with a mean travel distance of $24 \pm 7 \mu\text{m}$ whereas that of GFP-Kv4.2 vesicles is significantly greater ($80 \pm 12 \mu\text{m}$) ($P < 0.05$, $n = 3$, unpaired t test). *Scale bar*, 10 μm

significantly greater than that of GFP-Kv2.1 vesicles ($24 \pm 7 \mu\text{m}$, $P < 0.05$, $n = 3$ cells). Hence, the analysis reveals that GFP-Kv2.1 and GFP-Kv4.2 vesicle populations are transported and targeted differently in neurons.

Pharmacological Intervention

Our ability to image selectively post-Golgi transport vesicles also allows for dissection of the mechanisms underlying vesicular transport of a given protein using acute pharmacological treatments. We have recently shown that the motility of transport vesicles carrying GFP-Kv2.1 depends on intact actin filaments (Jensen et al. 2014), evidenced by the attenuation of motility with an actin depolymerizing agent, latrunculin A (LatA) (Spector et al. 1983). Here, we tested whether the motility of vesicles carrying HCN1 is also sensitive to LatA. LatA effectively reduced the levels of actin filaments in neurons treated for 5 min at 1 μM (Fig. 6a and b). As shown in Fig. 6c, neurons expressing either GFP-Kv2.1 or GFP-HCN1 showed a number of vesicle trajectories. However, after the LatA treatment, the numbers of mobile vesicles and vesicle trajectories for GFP-Kv2.1 were significantly reduced in the

same cells (Fig. 6c). In contrast, GFP-HCN1 vesicle motility did not change substantially before and after the treatment (Fig. 6d). These results suggest that the transport of HCN1 vesicles does not rely on intact actin filaments and demonstrates the usefulness of our methods in studying the characteristics and mechanisms of vesicular trafficking in living neurons.

Discussion

Here, we present a protocol to study the post-Golgi trafficking of transmembrane proteins in living cultured hippocampal neurons. Our protocol relies on the combination of low-temperature incubation (temperature-block) and monitoring of transient expression of GFP-tagged proteins. Although the temperature-block has previously been used to study protein trafficking in neuronal cells (for example, (Dotti and Simons 1990; Horton and Ehlers 2003a)), this combination makes our protocol unique. In a relatively simple manner, which is not based on extensive modification of the protein of interest, we can efficiently probe post-Golgi trafficking in living neurons. Using Kv channels as

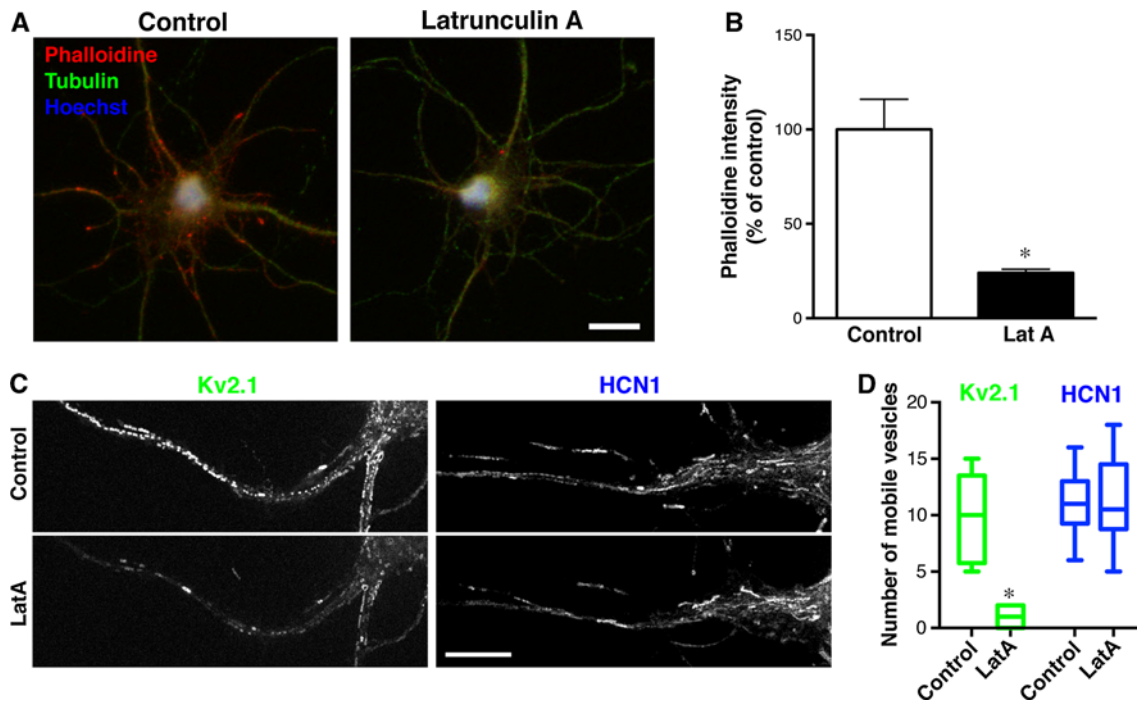


Fig. 6 Pharmacological dissection of post-Golgi trafficking. **a** Effect of latrunculin A on actin filaments. Neurons were treated with 1 μ M latrunculin A for 5 min, fixed, and labeled with phalloidine (for actin filament), anti-tubulin antibody, and Hoechst 33258 (DNA). *Scale bar*, 20 μ m. **b** Reduction of actin filaments evidenced by the decreased phalloidine staining. Fluorescence signals were measured in the somata and proximal dendrites, and normalized to the control. $*P < 0.05$ ($n = 3$). **c** Neurons were transfected with either GFP-

Kv2.1 or GFP-HCN1 and the experiment conducted after 3 h temperature-block. Neurons were imaged before and after treatment with 1 μ M latrunculin A (LatA) for 5 min. Time-lapse series were processed to obtain the number of mobile vesicles before and after the treatment. *Scale bar*, 10 μ m. **d** Disruption of actin filaments with LatA was found to significantly reduce the number of moving vesicles with GFP-Kv2.1 but not those with GFP-HCN1. $*P < 0.002$ ($n = 10$)

model proteins, we demonstrated that newly synthesized proteins become highly concentrated in the Golgi apparatus during the temperature-block and that they were synchronously trafficked out from the Golgi apparatus in transport vesicles when neurons were released from the temperature-block.

How can we be sure that the imaged vesicles truly represent post-Golgi transport vesicles? First, we strictly monitored the temporal expression of GFP tagged Kv channels and initiated the temperature-block before substantial expression occurred to ensure that most of newly synthesized GFP-tagged channels were trapped in the Golgi compartment. As we observed most of the signals in the Golgi apparatus, the vesicles we detected were mostly from the Golgi apparatus but not from the ER, the plasma membrane (endocytic vesicles), or other organelles. This is further supported by the absence of mobile vesicles when the Arf1 Q71I mutant was co-expressed, as Arf1 has been shown to be critical for transport vesicles to emerge from the Golgi apparatus (Dascher and Balch 1994; Jeyifous et al. 2009). Collectively, these results suggest that we have been able to probe post-Golgi trafficking preferentially using the modified temperature-block method.

A number of modern techniques have recently been developed to synchronize protein trafficking in a controlled fashion by optical or chemical means (Rivera et al. 2000; Boncompain and Perez 2013; Chen et al. 2013). In the context of these techniques, we believe that our protocol is a useful and complementary approach in dissecting post-Golgi trafficking mechanisms for neuronal membrane proteins. First, it is based on an approach compatible with the use of simple GFP-tagged proteins, which currently have been generated for many neuronal proteins in laboratories around the world. Second, our method can readily be applied to these proteins, and therefore provide a quick and easy way to obtain preliminary data regarding post-Golgi trafficking of a protein of interest. Thirdly, our protocol synchronizes the protein trafficking at the level of the Golgi apparatus. The recently developed state-of-the-art techniques primarily synchronize protein trafficking at the ER by taking advantage of cell's intrinsic mechanism of retaining aggregated proteins in the ER (Rivera et al. 2000; Al-Bassam et al. 2012; Boncompain and Perez 2013; Chen et al. 2013). Therefore, our protocol would complement these modern techniques in studying protein sorting and post-Golgi trafficking and can also be

combined with them to further refine the control of protein trafficking.

Although this protocol sufficiently worked to reveal the post-Golgi trafficking of the dendritic ion channels, it may not work for every protein of interest. Our protocol requires the temperature-block to be started before GFP-tagged proteins are expressed substantially and that they proceed to the Golgi apparatus efficiently during the temperature-block. Therefore, proteins that intrinsically require a long time for folding and ER transit may not be suitable targets for this procedure. Combining our method with photoactivatable fluorescent proteins (Lippincott-Schwartz et al. 2003) may enable us to label these proteins in the Golgi specifically and to probe their post-Golgi trafficking. Another potentially useful combination would be with the super-ecliptic pHluorin (Sankaranarayanan et al. 2000). The synchronous post-Golgi trafficking achieved with our protocol would facilitate the detection of surface insertion of transmembrane proteins which are extracellularly tagged with Super-ecliptic pHluorin.

It has become increasingly clear that trafficking to distinct neuronal compartments is a tightly controlled process which constantly operates to ensure that proteins are at the right place at the right time (Horton and Ehlers 2003b). Trafficking is therefore not only a matter of understanding how membrane proteins are delivered to the surface membrane, but also, to reveal how it is regulated in response to neuronal activity. Our protocol also allows for such investigations as we can image and quantify how vesicles behave in response to different activity-related input. This opens up for a number of potential applications which collectively will improve our current knowledge within the field of neuronal protein trafficking.

Acknowledgments We thank Drs. James Trimmer, Stephanie Kaech, Okunola Jeyifous, and Stephen Siegelbaum for generously providing precious reagents. We also thank Dr. Shoji Watanabe for his technical assistance. The work was supported by Takeda Science Foundation (H.M.) and the Naito Foundation (H.M.). C.S.J was supported by the Lundbeck Foundation.

Conflict of interest Hiroaki Misono and Camilla Jensen has no financial conflict of interest.

References

- Al-Bassam S, Xu M, Wandless TJ, Arnold DB (2012) Differential trafficking of transport vesicles contributes to the localization of dendritic proteins. *Cell Rep* 2:89–100
- Boncompain G, Perez F (2013) Fluorescence-based analysis of trafficking in mammalian cells. *Methods Cell Biol* 118:179–194
- Burack MA, Silverman MA, Banker G (2000) The role of selective transport in neuronal protein sorting. *Neuron* 26:465–472

- Chen D, Gibson ES, Kennedy MJ (2013) A light-triggered protein secretion system. *J Cell Biol* 201:631–640
- Cid-Arregui A, Parton RG, Simons K, Dotti CG (1995) Nocodazole-dependent transport, and brefeldin A-sensitive processing and sorting, of newly synthesized membrane proteins in cultured neurons. *J Neurosci* 15:4259–4269
- Dascher C, Balch WE (1994) Dominant inhibitory mutants of ARF1 block endoplasmic reticulum to Golgi transport and trigger disassembly of the Golgi apparatus. *J Biol Chem* 269:1437–1448
- Dotti CG, Simons K (1990) Polarized sorting of viral glycoproteins to the axon and dendrites of hippocampal neurons in culture. *Cell* 62:63–72
- Goslin K, Asmussen H, Banker G (1998) Rat hippocampal neurons in low-density culture. In: Goslin K, Banker GA (eds) *Culturing nerve cells*. MIT Press, Cambridge, pp 339–370
- Horton AC, Ehlers MD (2003a) Dual modes of endoplasmic reticulum-to-Golgi transport in dendrites revealed by live-cell imaging. *J Neurosci* 23:6188–6199
- Horton AC, Ehlers MD (2003b) Neuronal polarity and trafficking. *Neuron* 40:277–295
- Jensen CS, Rasmussen HB, Misonou H (2011) Neuronal trafficking of voltage-gated potassium channels. *Mol Cell Neurosci* 48:288–297
- Jensen CS, Watanabe S, Rasmussen HB, Schmitt N, Olesen SP, Frost NA et al (2014) Specific sorting and post-golgi trafficking of dendritic potassium channels in living neurons. *J Biol Chem* 289:10566–10581
- Jeyifous O, Waites CL, Specht CG, Fujisawa S, Schubert M, Lin EI et al (2009) SAP97 and CASK mediate sorting of NMDA receptors through a previously unknown secretory pathway. *Nat Neurosci* 12:1011–1019
- Kaech S, Banker G (2006) Culturing hippocampal neurons. *Nat Protoc* 1:2406–2415
- Kaech S, Ludin B, Matus A (1996) Cytoskeletal plasticity in cells expressing neuronal microtubule-associated proteins. *Neuron* 17:1189–1199
- Karasawa S, Araki T, Yamamoto-Hino M, Miyawaki A (2003) A green-emitting fluorescent protein from Galaxeidae coral and its monomeric version for use in fluorescent labeling. *J Biol Chem* 278:34167–34171
- Lai HC, Jan LY (2006) The distribution and targeting of neuronal voltage-gated ion channels. *Nat Rev Neurosci* 7:548–562
- Lippincott-Schwartz J, Patterson GH (2003) Development and use of fluorescent protein markers in living cells. *Science* 300:87–91
- Matlin KS, Simons K (1983) Reduced temperature prevents transfer of a membrane glycoprotein to the cell surface but does not prevent terminal glycosylation. *Cell* 34:233–243
- Menegola M, Misonou H, Vacher H, Trimmer JS (2008) Dendritic A-type potassium channel subunit expression in CA1 hippocampal interneurons. *Neuroscience* 154:953–964
- Misonou H, Trimmer JS (2004) Determinants of voltage-gated potassium channel surface expression and localization in mammalian neurons. *Crit Rev Biochem Mol Biol* 39:125–145
- Misonou H, Trimmer JS (2005) A primary culture system for biochemical analyses of neuronal proteins. *J Neurosci Methods* 144:165–173
- Murakoshi H, Trimmer JS (1999) Identification of the Kv2.1 K⁺ channel as a major component of the delayed rectifier K⁺ current in rat hippocampal neurons. *J Neurosci* 19:1728–1735
- Nakamura N, Rabouille C, Watson R, Nilsson T, Hui N, Slusarewicz P et al (1995) Characterization of a cis-Golgi matrix protein, GM130. *J Cell Biol* 131:1715–1726

- Namba T, Nakamuta S, Funahashi Y, Kaibuchi K (2011) The role of selective transport in neuronal polarization. *Dev Neurobiol* 71:445–457
- Rivera VM, Wang X, Wardwell S, Courage NL, Volchuk A, Keenan T et al (2000) Regulation of protein secretion through controlled aggregation in the endoplasmic reticulum. *Science* 287:826–830
- Sampo B, Kaech S, Kunz S, Banker G (2003) Two distinct mechanisms target membrane proteins to the axonal surface. *Neuron* 37:611–624
- Sankaranarayanan S, De Angelis D, Rothman JE, Ryan TA (2000) The use of pHluorins for optical measurements of presynaptic activity. *Biophys J* 79:2199–2208
- Santoro B, Hu L, Liu H, Saponaro A, Pian P, Piskorowski RA et al (2011) TRIP8b regulates HCN1 channel trafficking and gating through two distinct C-terminal interaction sites. *J Neurosci* 31:4074–4086
- Sciaky N, Presley J, Smith C, Zaal KJ, Cole N, Moreira JE et al (1997) Golgi tubule traffic and the effects of brefeldin A visualized in living cells. *J Cell Biol* 139:1137–1155
- Sheng M, Tsaur ML, Jan YN, Jan LY (1992) Subcellular segregation of two A-type K⁺ channel proteins in rat central neurons. *Neuron* 9:271–284
- Shibata R, Misonou H, Campomanes CR, Anderson AE, Schrader LA, Doliveira LC et al (2003) A fundamental role for KChIPs in determining the molecular properties and trafficking of Kv4.2 potassium channels. *J Biol Chem* 278:36445–36454
- Silverman MA, Kaech S, Jareb M, Burack MA, Vogt L, Sonderegger P et al (2001) Sorting and directed transport of membrane proteins during development of hippocampal neurons in culture. *Proc Natl Acad Sci USA* 98:7051–7057
- Spector I, Shochet NR, Kashman Y, Groweiss A (1983) Latrunculins: novel marine toxins that disrupt microfilament organization in cultured cells. *Science* 219:493–495
- Trimmer JS, Rhodes KJ (2004) Localization of voltage-gated ion channels in mammalian brain. *Annu Rev Physiol* 66:477–519
- Vacher H, Misonou H, Trimmer JS, (eds) (2007) Determinants of voltage-gated potassium channel distribution in neurons. Elsevier Academic Press, London
- Zaal KJ, Smith CL, Polishchuk RS, Altan N, Cole NB, Ellenberg J et al (1999) Golgi membranes are absorbed into and reemerge from the ER during mitosis. *Cell* 99:589–601

BK Channels Localize to the Paranodal Junction and Regulate Action Potentials in Myelinated Axons of Cerebellar Purkinje Cells

Moritoshi Hirono,¹ Yasuhiro Ogawa,³  Kaori Misono,² Daniel R. Zollinger,³  James S. Trimmer,⁴ Matthew N. Rasband,³ and Hiroaki Misonou^{1,2}

¹Graduate School of Brain Science, Doshisha University, Kyoto 619-0225, Japan, ²Department of Neural and Pain Sciences, Dental School, University of Maryland, Baltimore, Maryland 21201, ³Department of Neuroscience, Baylor College of Medicine, Houston, Texas 77030, and ⁴Department of Neurobiology, Physiology, and Behavior, University of California, Davis, Davis, California 95616

In myelinated axons, K⁺ channels are clustered in distinct membrane domains to regulate action potentials (APs). At nodes of Ranvier, Kv7 channels are expressed with Na⁺ channels, whereas Kv1 channels flank nodes at juxtaparanodes. Regulation of axonal APs by K⁺ channels would be particularly important in fast-spiking projection neurons such as cerebellar Purkinje cells. Here, we show that BK/Slo1 channels are clustered at the paranodal junctions of myelinated Purkinje cell axons of rat and mouse. The paranodal junction is formed by a set of cell-adhesion molecules, including Caspr, between the node and juxtaparanodes in which it separates nodal from internodal membrane domains. Remarkably, only Purkinje cell axons have detectable paranodal BK channels, whose clustering requires the formation of the paranodal junction via Caspr. Thus, BK channels occupy this unique domain in Purkinje cell axons along with the other K⁺ channel complexes at nodes and juxtaparanodes. To investigate the physiological role of novel paranodal BK channels, we examined the effect of BK channel blockers on antidromic AP conduction. We found that local application of blockers to the axon resulted in a significant increase in antidromic AP failure at frequencies above 100 Hz. We also found that Ni²⁺ elicited a similar effect on APs, indicating the involvement of Ni²⁺-sensitive Ca²⁺ channels. Furthermore, axonal application of BK channel blockers decreased the inhibitory synaptic response in the deep cerebellar nuclei. Thus, paranodal BK channels uniquely support high-fidelity firing of APs in myelinated Purkinje cell axons, thereby underpinning the output of the cerebellar cortex.

Key words: action potential; axon; cerebellum; potassium channel

Introduction

Voltage-activated ion channels are uniquely situated in myelinated axons of mammalian neurons (Lai and Jan, 2006). Voltage-activated Na⁺ (Nav) channels are localized precisely at the node of Ranvier to generate action potentials (APs). Voltage-activated K⁺ (Kv) channels are also expressed at and near the node and

may regulate axonal APs (Rasband and Shrager, 2000; Devaux et al., 2003; Pan et al., 2006). Among them, Kv7.2/7.3 channels are localized at the node (Pan et al., 2006) and thought to regulate the overall excitability of the nodal membrane (Schwarz et al., 2006). In contrast, Kv1.1/1.2 channels are localized in regions flanking the node called the juxtaparanode (Wang et al., 1993; Rhodes et al., 1997; Rasband et al., 1998). Because this area is covered completely with the myelin sheath, juxtaparanodal Kv1 channels are considered mostly inert under normal conditions (Kocsis and Waxman, 1980) but can be functional during development and when the myelin sheath is retracted in pathological situations, such as multiple sclerosis (Poliak and Peles, 2003; Rasband, 2004). Here, we show that Slo1/BK channels are also found in myelinated axons.

The Slo1/KCa1.1/BK K⁺ channel is unique in its coincident activation by changes in membrane potential and intracellular Ca²⁺ concentration ([Ca²⁺]_i; Salkoff et al., 2006). The BK channel also has an exceptionally large single-channel conductance compared with other K⁺ channels (Salkoff et al., 2006). Therefore, its expression in a specific neuronal compartment, in which BK channels can be exposed to local increases in [Ca²⁺]_i, would be expected to significantly affect the local membrane excitability. BK channels are found predominantly in presynaptic termi-

Received Sept. 5, 2014; revised March 2, 2015; accepted April 1, 2015.

Author contributions: M.H., M.N.R., and H.M. designed research; M.H., Y.O., K.M., D.R.Z., J.S.T., M.N.R., and H.M. performed research; M.H., Y.O., K.M., D.R.Z., M.N.R., and H.M. analyzed data; M.H., J.S.T., M.N.R., and H.M. wrote the paper.

We thank Drs. Takafumi Miki, Shinya Kawaguchi, Tomoyuki Takahashi, Shoji Watanabe, and Takeshi Sakaba for their technical assistance and critical discussion. This work was supported by NIH grant NS069688 (MNR), NS34383 (JST), Takeda Science Foundation (MH and HM), Naito Foundation (HM), Core-to-Core Program A Advanced Research Networks, and MEXT/JSPS KAKENHI Grant 26640017 (HM).

The authors declare no competing financial interests.

Correspondence should be addressed to either of the following: Hiroaki Misonou, Graduate School of Brain Science, Doshisha University, 4-1-1 Kizugawadai, Kizugawa-shi, Kyoto 619-0225, Japan, E-mail: h_misonou@mac.com; or Matthew Rasband, Department of Neuroscience, Baylor College of Medicine, One Baylor Plaza, Houston, TX 77030, E-mail: rasband@bcm.edu.

Y. Ogawa's present address: Department of Pharmacology, Meiji Pharmaceutical University, Tokyo 204-8588, Japan.

K. Misonou's present address: Department of Ophthalmology and Visual Sciences, Kyoto University, Kyoto 606-8501, Japan.

DOI:10.1523/JNEUROSCI.3778-14.2015

Copyright © 2015 the authors 0270-6474/15/357082-13\$15.00/0

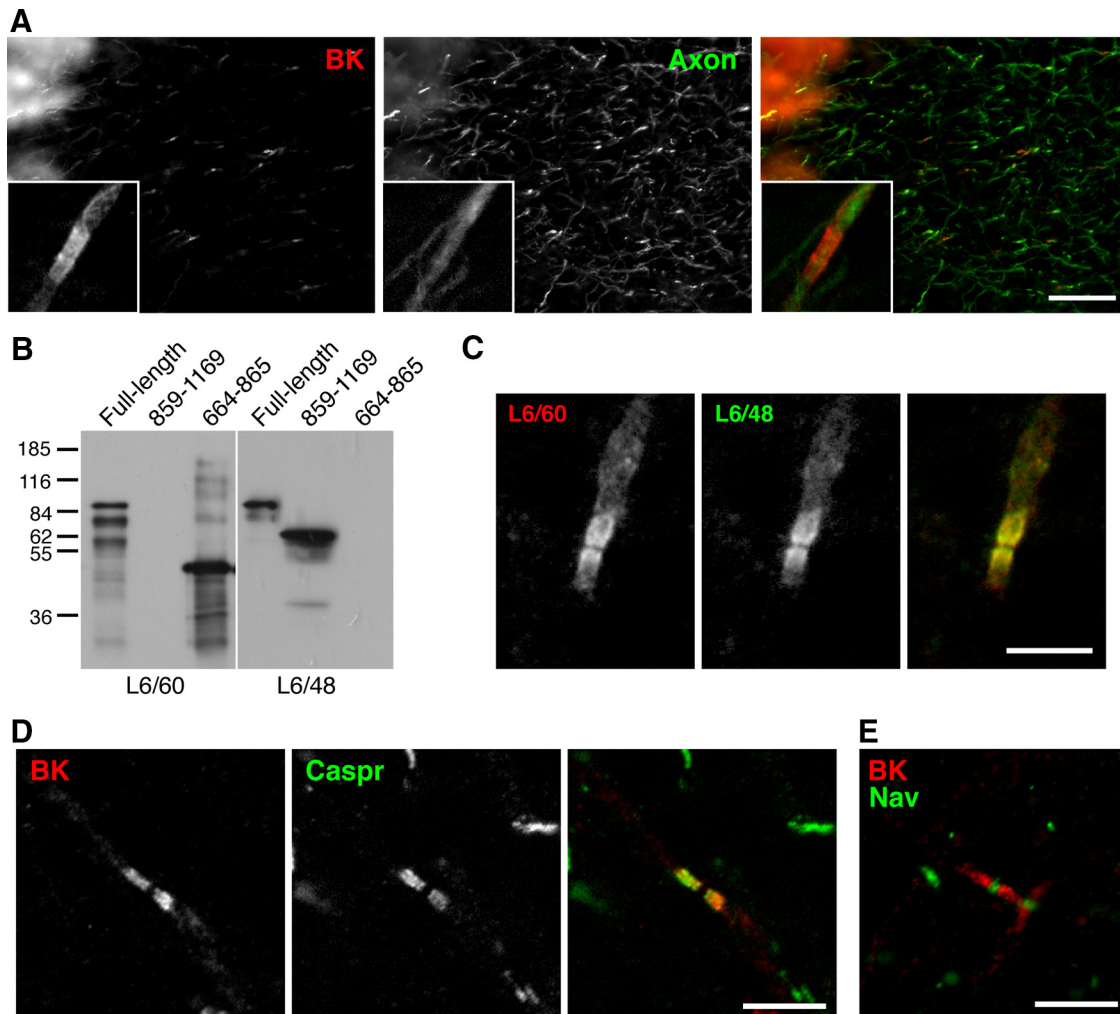


Figure 1. Paranodal localization of BK channels in the rat cerebellum. **A**, Non-uniform compact localization of BK channels in axons in the granule layer of the cerebellum. Rat cerebellar sections were immunolabeled with the L6/60 mouse mAb against BK (Slo1.1, red) and an antibody against an axonal marker, unphosphorylated neurofilament (Axon, green). Insets show magnified views of the immunolabeling. Scale bar, 50 μm . **B**, Two mAbs against BK recognize two distinct epitopes. Immunoblot of recombinant full-length BK channels and fragments representing residues 859–1169 and residues 664–865, probed with L6/60 and L6/48 mAbs. **C**, The compact localization of BK channels in axons verified by immunolabeling with two distinct mAbs (L6/60, red; L6/48, green). Scale bar, 5 μm . **D**, Double immunolabeling with L6/60 (red) and an anti-Caspr antibody (green) showing their colocalization in the paranode. Scale bar, 5 μm . **E**, Immunolabeling for Nav1.6 (green) is present in the gap between the paired paranodal BK channel immunolabeling (red). Scale bar, 5 μm .

nals in brain neurons and less prominently in somata and dendrites (Vacher et al., 2008; Trimmer, 2015). We and others have shown that, in cerebellar Purkinje cells, BK channels are highly expressed in the dendrites and soma (Misonou et al., 2006; Sausbier et al., 2006). Studies using BK blockers and Slo1 knock-out mice have suggested that, in Purkinje cells, somatodendritic BK channels contribute to the afterhyperpolarization (AHP) in the soma (Sausbier et al., 2004) and regulation of Ca^{2+} spikes in dendrites in Purkinje cells (Faber and Sah, 2003; Swensen and Bean, 2003; Womack and Khodakhah, 2004).

Here, we show that BK channels are also present in the myelinated axons of cerebellar Purkinje cells. Specifically, we show that BK channels colocalize at paranodes with Caspr, an axonal cell-adhesion molecule required for the paranodal axoglial junction (Einheber et al., 1997; Menegoz et al., 1997; Bhat et al., 2001). The paranode differs from the juxtaparanode in that small molecules and ions may be more accessible to the paranode (Mierzwa et al., 2010), such that paranodal ion channels would be fully functional under normal physiological conditions. Based on these findings, we tested whether paranodal BK channels regulate APs in Purkinje cell axons. Our results suggest that paranodal BK

channels have a significant role in the myelinated axons of Purkinje cells to support reliable high-frequency conduction of APs.

Materials and Methods

Antibodies against BK channels. The production and validation of monoclonal antibodies (mAbs) against Slo1/KCa1.1/BK have been described previously (Misonou et al., 2006). Briefly, L6/48 and L6/60 mAbs against the mouse Slo1 (mSlo) channel subunit were raised against a GST–mSlo1 fusion protein corresponding to amino acids 690–1196 of mSlo1 (GenBank accession number AAA39746). Within this fragment, L6/48 binds within amino acids 859–1169, and L6/60 binds within amino acids 690–715 (Fig. 1). Conditioned media from hybridoma clones were screened by chemiluminescence ELISA against COS-1 cells expressing full-length human Slo1 (Meera et al., 1997) and then further selected based on immunofluorescence labeling of COS-1 cells transfected with the same human Slo1 cDNA. Both mAbs were validated against BK channel knock-out mice (Misonou et al., 2006). The L6 mAbs can be obtained from the University of California, Davis/National Institutes of Health NeuroMab Facility (Davis, CA).

Immunolabeling. All animal use procedures were in strict accordance with the *Guide for the Care and Use of Laboratory Animals* described by the National Institutes of Health and approved by institutional animal

use committees. Sprague Dawley rats, wild-type C57BL/6 mice, and Caspr-deficient mice (Gollan et al., 2003) were used. Animals were anesthetized with 60 mg/kg pentobarbital (intraperitoneal) and perfused briefly with a saline solution, followed by 4% paraformaldehyde in 0.1 M phosphate buffer, pH 7.4. Sagittal brain sections (40 μ m thick) were prepared as described previously (Rhodes et al., 1997; Hermanstynne et al., 2010). Brain sections were permeabilized with 0.1% Triton X-100 in Tris-buffered saline (10 mM Tris, pH 7.5, and 0.15 M NaCl). Sections were blocked with 10% goat serum and then incubated overnight at 4°C with L6/60 mAb (IgG2a) or L6/48 mAb (IgG1) (each at 10 μ g/ml) and mouse mAbs raised against Kv1.2 (K14/16, IgG2b, 1 μ g/ml), Caspr (K65/35, IgG1, 1 μ g/ml), and Nav1.6 (K87A/10, IgG1, 5 μ g/ml; all from the University of California, Davis/National Institutes of Health NeuroMab Facility), a mouse mAb cocktail neurofilament H (BioLegend), rabbit polyclonal antibodies against β IV spectrin (Yang et al., 2004), or rabbit polyclonal antibodies against parvalbumin (Merck Millipore). Sections were then incubated with species-specific or mouse IgG subclass-specific Alexa Fluor-conjugated secondary antibodies (Invitrogen). Fluorescent images were taken with a 24-bit CCD camera installed on a Carl Zeiss Axiovert 200M microscope with a 63 \times , 1.3 numerical aperture (NA) lens and Apotome, using Axiovision software. Most of the images are maximum projection images from multiple optical sections.

Preparation of brain membrane fraction. Crude brain membrane fractions and detergent-resistant fractions were prepared from rats and mice as described previously (Schafer et al., 2004; Ogawa et al., 2006). Either whole brains or isolated cerebella were homogenized in ice-cold homogenization buffer containing 0.32 M sucrose, 5 mM sodium phosphate, pH 7.4, and 1 mM sodium fluoride, containing 1 mM phenylmethylsulfonyl fluoride (PMSF), 2 μ g/ml aprotinin, 1 μ g/ml leupeptin, 2 μ g/ml antipain, and 10 μ g/ml benzamide (10 ml/g wet tissue weight). Crude homogenates were then centrifuged at 600 \times g for 10 min to remove debris and nuclei. The resulting supernatant was centrifuged at 45,000 \times g for 60 min. This pellet was then resuspended in 2.5 ml of ice-cold homogenization buffer per gram of brain used. Protein concentrations were determined using the BCA method (Pierce).

Detergent-insoluble membrane fractions were isolated by solubilizing brain membrane fractions in 1% Triton X-100 lysis buffer (20 mM Tris-HCl, pH 8.0, 10 mM EDTA, 0.15 M NaCl, 10 mM iodoacetamide, 0.5 mM PMSF, 10 mM sodium azide, and the same mixture of protease inhibitors as described above) at a concentration of 1 mg/ml protein for 1 h on a rotator at 4°C. The resulting lysate was centrifuged at 13,000 \times g for 30 min to separate the detergent-soluble and -insoluble fractions. Detergent-insoluble fractions were resuspended to 1 ml in lysis buffer (without Triton X-100). The pellet suspension was then mixed with 1 ml of 2 M sucrose. The resulting mixture was then overlaid with 2 ml of 1 M sucrose and 1.5 ml of 0.2 M sucrose. Samples were then centrifuged for 19 h at 192,000 \times g, and 0.4 ml fractions were then collected from the top of the tube. Sucrose and protein concentrations were measured for each fraction. Proteins were concentrated by overnight ethanol precipitation. The pellets were then resuspended in 100 μ l of reducing sample buffer, boiled, and analyzed by SDS-PAGE and immunoblotting.

Immunoblotting. Proteins were separated on 7.5% SDS polyacrylamide gels (SDS-PAGE), transferred to nitrocellulose membrane, and immunoblotted with L6/48 or L6/60, as described previously (Misonou et al., 2005). The blots were incubated with HRP-conjugated secondary antibodies (ICN Biomedicals), followed by enhanced chemiluminescence reagent (PerkinElmer Life and Analytical Sciences). Immunoreactive bands were visualized by exposing the blot to x-ray film.

Slice preparation. Cerebellar slices were prepared from C57BL/6 mice at postnatal day 25 (P25) to P35 of either sex as described previously (Hirono et al., 2012). The mice were treated with CO₂ and decapitated, and their cerebella were removed rapidly. Parasagittal slices (250 μ m thick) of the cerebellar vermis were cut with a vibrating microtome (VT1200S; Leica) in an ice-cold extracellular solution containing 252 mM sucrose, 3.35 mM KCl, 21 mM NaHCO₃, 0.6 mM NaH₂PO₄, 9.9 mM glucose, 0.5 mM CaCl₂, and 10 mM MgCl₂ and gassed with a mixture of 95% O₂ and 5% CO₂, pH 7.4. The slices were maintained at room temperature for at least 1 h in a holding chamber, in which they were submerged in artificial CSF (ACSF) containing the following (in mM): 138.6 NaCl, 3.35

KCl, 21 NaHCO₃, 0.6 NaH₂PO₄, 9.9 glucose, 2 CaCl₂, and 1 MgCl₂ (bubbled with 95% O₂ and 5% CO₂ to maintain the pH at 7.4).

Electrophysiology. Individual slices were transferred to a recording chamber attached to the stage of a microscope (BX51WI; Olympus) and superfused with oxygenated ACSF. Purkinje cells were identified visually under Nomarski optics with a water-immersion objective (60 \times , 0.90 NA). After establishing the whole-cell patch clamp, the membrane potential was held at approximately -65 mV under a current-clamp mode with a patch pipette (2–3 M Ω) filled with the potassium methanesulfonate-based internal solution containing the following (in mM): 120 KCH₃SO₃, 25 KCl, 0.1 CaCl₂, 1.0 K-EGTA, 10.0 Na-HEPES, 3.0 Mg-ATP, and 0.4 Na-GTP, pH 7.4. To visualize the axon, Alexa Fluor 594 (40 μ M) was added to the internal solution. Neurons with no or very short axons were not used. To block synaptic transmissions, 10 μ M NBQX, 30 μ M APV, 10 μ M SR95531 [2-(3-carboxypropyl)-3-amino-6-(4-methoxyphenyl)pyridazinium bromide], and 2 μ M strychnine were added to the ACSF throughout the recordings. To evoke antidromic APs in Purkinje cells, a bipolar tungsten stimulating electrode was placed in the white matter, and focal stimulation (30–60 V, 0.1–0.2 ms) was applied to the axon at 0.067–0.1 Hz. For recording of synaptic currents, deep cerebellar nucleus (DCN) neurons were voltage clamped at -20 to 0 mV. Recordings were made from large neurons with somatic diameter of ~ 20 μ m, most of which are thought to correspond to the glutamatergic projection neurons in the DCN (Telgkamp and Raman, 2002; Uusisaari et al., 2007). A patch pipette was filled with the cesium methanesulfonate-based internal solution containing the following (in mM): 140 CsCH₃SO₃, 5 CsCl, 0.1 CaCl₂, 1.0 K-EGTA, 10.0 Na-HEPES, 0.6 QX-314, 3.0 Mg-ATP, and 0.4 Na-GTP, pH 7.4. IPSCs were evoked by focal stimulation (30–60 V, 0.04–0.12 ms) through a bipolar tungsten stimulating electrode or a concentric bipolar electrode (FHC) placed in the white matter. Glutamate transmission was blocked by kynurenic acid (1 mM) or 10 μ M NBQX and 30 μ M APV added to the ACSF. Alexa Fluor 594 (40 μ M) was also added to the patch pipette solution to examine morphology of recorded cells. Series resistance (10–18 M Ω) was compensated by 60–70% and monitored with 2 mV hyperpolarizing voltage pulse (30–50 ms) every 15 s, and experiments were discarded if the value changed $>20\%$. Signals were recorded with a MultiClamp 700B amplifier (Molecular Devices) and pClamp 10.3 software (Molecular Devices), digitized, and stored on a computer disk for offline analysis. All signals were filtered at 4 kHz and sampled at 10–20 kHz. All experiments were performed at room temperature (23–26°C).

Drug application for electrophysiology. Drugs were applied to the axon in pressure pulses (3–6 psi, 400 ms duration) at 0.5 Hz using a micro-pressure ejection system (PV820 Pneumatic PicoPump; World Precision Instruments) with a glass pipette (5–10 μ m tip diameters). Iberiotoxin, NBQX, paxilline, penitrem A, and SR95531 were obtained from Tocris Bioscience. Alexa Fluor 594 was obtained from Invitrogen. Tetrodotoxin (TTX) was obtained from Wako. All other chemicals were from Sigma.

Statistical analyses. Data are presented as the mean \pm SEM, unless noted otherwise. In electrophysiology experiments, the number of sample (n) indicates the number of cells used for recording. However, slices from at least three different animals were used in each experiment. A t value of $p < 0.05$ was considered to be statistically significant. For multiple comparisons, two-way ANOVA was performed with *post hoc* multiple comparisons. All statistical analyses were performed using GraphPad Prism (GraphPad Software).

Results

Axonal expression of Slo1/BK channels in the cerebellum

The BK channel is highly expressed in Purkinje cells of the cerebellum, in which the majority of BK immunoreactivity is found in the soma and dendrites (Misonou et al., 2006). Here, using the specific mouse mAb L6/60 (Misonou et al., 2006), we found that Purkinje cells also express BK channels in their axons. Non-uniform BK labeling is present in a subset of axons running in the granule cell layer of the rat cerebellum (Fig. 1A). The inset images (Fig. 1A, insets) show that BK channels are concentrated into two small bands, with a clear gap between adjacent bands. The axonal

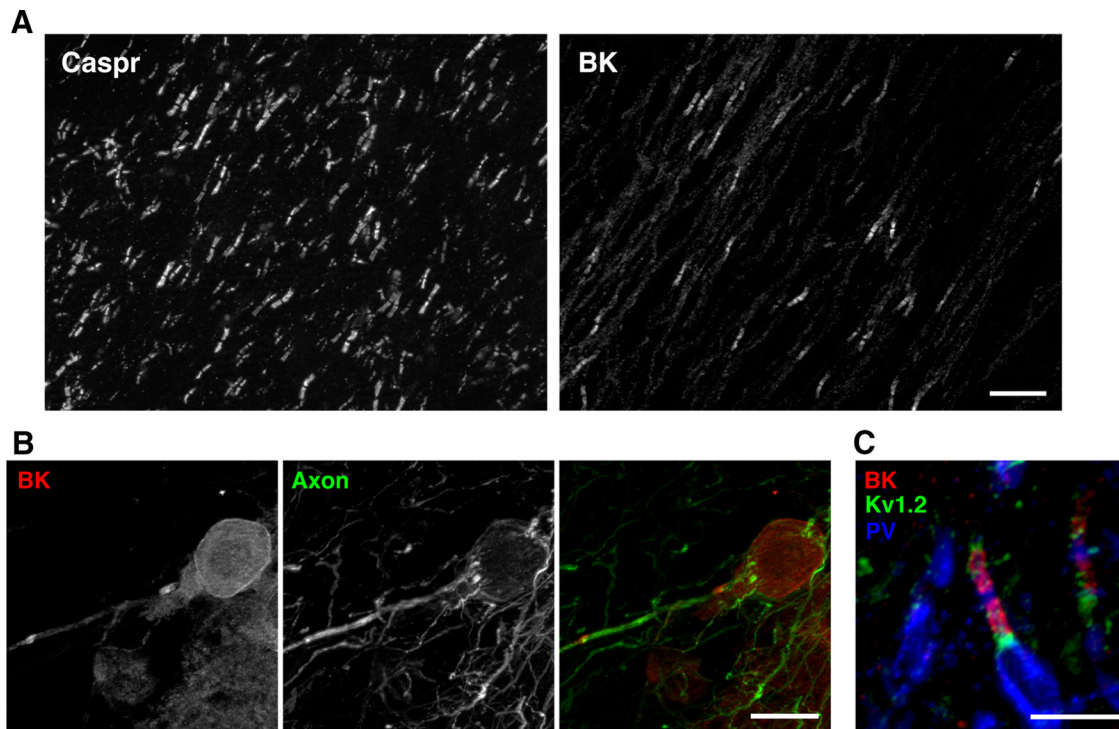


Figure 2. Paranodal BK channels in rat Purkinje cells. **A**, Paranodal BK channel immunolabeling was detected only in a subset of Caspr-positive paranodes in the cerebellar white matter. Scale bar, 20 μm . **B**, Paranodal BK channels (red) were detected near the Purkinje cell soma. The axon is labeled using an antibody against unphosphorylated neurofilament H (green). Scale bar, 20 μm . **C**, Paranodal BK channel immunolabeling (red) found on parvalbumin (PV; blue)-positive axons in the white matter. Juxtaparanodes are immunolabeled using antibodies against Kv1.2 (green). Scale bar, 10 μm .

expression of BK channels was confirmed with another anti-BK channel mAb (L6/48) that binds to a region of the BK channel distinct from the L6/60 mAb (Fig. 1*B,C*). The clear gap between the opposed segments of BK channel immunoreactivity suggested they are expressed in the paranodal region of myelinated axons. Indeed, these BK-positive structures colabeled with antibodies recognizing the axonal paranodal cell-adhesion molecule Caspr (Fig. 1*D*). Furthermore, Nav1.6, the predominant nodal Nav channel in adult rodents, was found in the nodal gap between BK-labeled paranodes (Fig. 1*E*).

In addition to these axons in the granule cell layer, we also detected the paranodal BK channel expression in the white matter of the cerebellum (Fig. 2*A*). However, BK channels were detected in fewer than 10% of Caspr-positive paranodes (Fig. 2*A*), a number consistent with the proportion of Purkinje cell axons in cerebellar white matter, in which mossy fiber and climbing fiber axons predominate (Palkovits et al., 1972). Moreover, prominent paranodal BK labeling was observed near the site of origin of Purkinje cell axons in the Purkinje layer (Fig. 2*B*). These considerations led us to suspect that BK channels are expressed specifically in the paranodes of Purkinje cell axons. To test this possibility, we triple immunolabeled cerebellar sections with anti-BK channel mAb L6/60, an antibody against the Purkinje cell marker parvalbumin, and an anti-Kv1.2 channel antibody that labels the juxtaparanodal domains of myelinated axons. As shown in Figure 2*C*, BK channels were restricted to the paranodes of parvalbumin-positive axons, indicating the specific expression of BK channels in Purkinje cell axons. Furthermore, paranodal BK channels were not detected in myelinated axons in other areas of the nervous system, including white matter tracts within the brain, optic nerve, and sciatic nerve. These results suggest that BK channels are found specifically in the paranodes of Purkinje cell axons.

Caspr-dependent localization of BK channels in the paranode

Paranodal proteins have biochemical properties similar to raft proteins (Schafer et al., 2004). To determine whether BK channels in the cerebellum also have this property, we prepared detergent-soluble and -insoluble fractions (Ogawa et al., 2006) from the whole brain and the cerebellum of rat. As expected, Caspr was recovered mainly in the detergent-insoluble fraction from both whole-brain and cerebellar samples (Fig. 3*A*). This was also observed for the glial paranodal protein Neurofascin-155 (Schafer et al., 2004) but not for axonal Neurofascin-186, which localizes at the node (Davis et al., 1996; Fig. 3*A*). Furthermore, BK channel and Caspr proteins from the cerebellum were found in the low-density detergent-insoluble fractions isolated from sucrose gradients (Fig. 3*B*). Thus, a subset of BK channels in the cerebellum share similar biochemical characteristics with those of other paranodal membrane proteins (Schafer et al., 2004; Ogawa et al., 2006). Similar to other paranodal proteins (e.g., glycosylphosphatidylinositol-anchored contactin), a fraction of the BK channels remained detergent insoluble in Caspr-deficient mice (Gollan et al., 2003; Fig. 3*C*), indicating that some BK channels remain in raft-like structures independent of paranodal junctions. Consistent with this idea, BK channels are modified with palmitate (Jeffries et al., 2010), which is a posttranslational lipid modification that promotes the partitioning of proteins into detergent-insoluble lipid rafts (Levental et al., 2010).

To more directly examine the role of paranodal junctions in regulating BK channel localization, we also performed immunolabeling to examine BK channel localization in the cerebellum of Caspr-deficient mice. First, we confirmed the paranodal localization of BK channels in the cerebellum of wild-type mice (Fig. 3*D,E*), indicating that the paranodal expression of BK channels is a common property of rodent Purkinje cells. In contrast, Caspr-

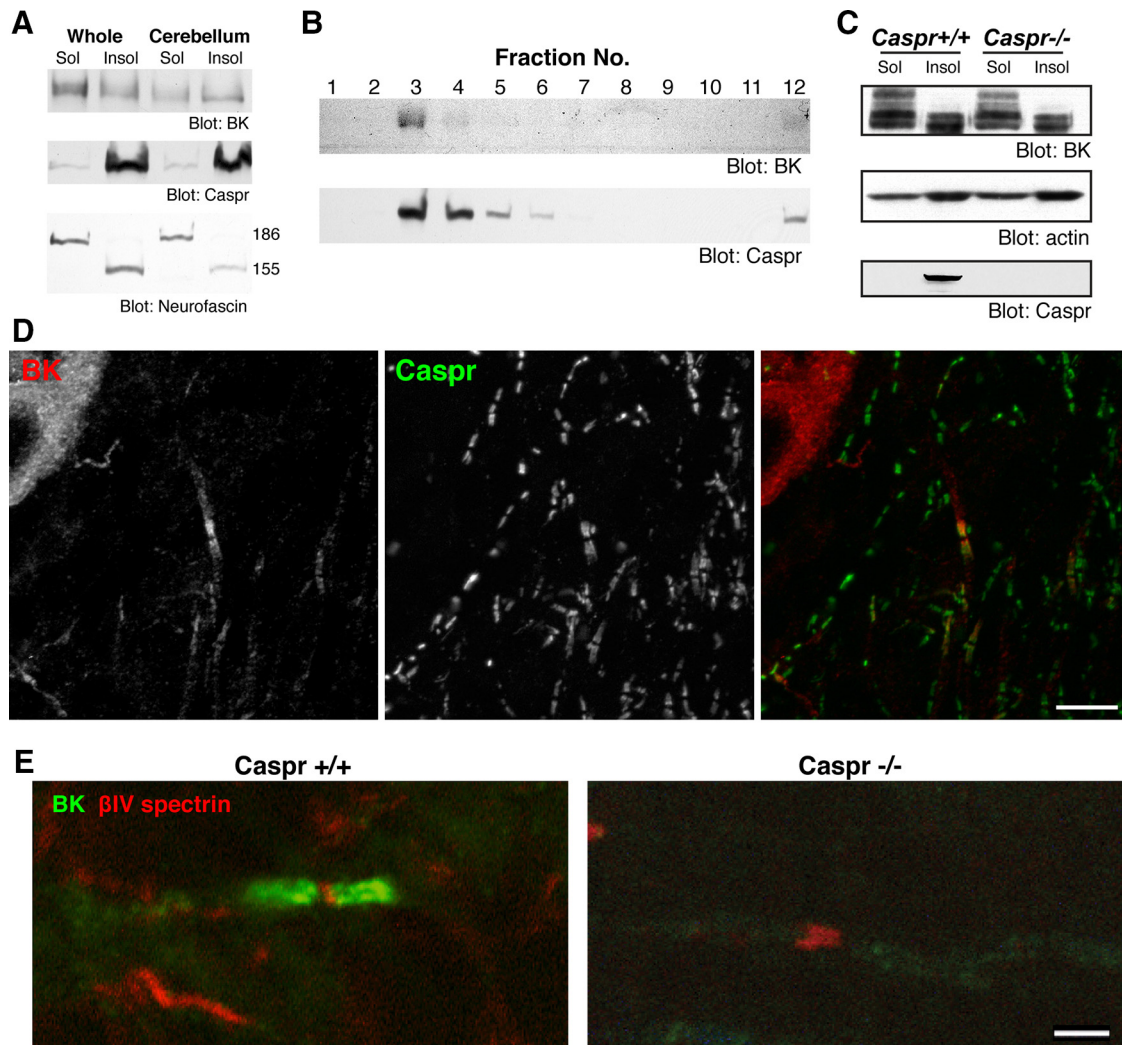


Figure 3. Paranodal localization of BK channels depends on an intact paranodal junction. **A**, Biochemical characteristics of BK channels in the cerebellum. Membrane fractions were prepared from rat whole brain (Whole) or cerebellum. Membrane preparations were incubated with 1% Triton X-100 for 30 min and separated into soluble (Sol) and insoluble (Insol) fractions by centrifugation. The samples were subjected to immunoblotting and probed for BK channels, the paranodal membrane protein Caspr, and another paranodal protein, Neurofascin. Note that only the paranodal 155 kDa isoform of Neurofascin was detected in the insoluble fraction. **B**, Cofractionation of BK channels and Caspr. Detergent-insoluble fractions from the cerebellum were fractionated using sucrose-density gradient centrifugation. Both BK channels and Caspr were detected in the low-density paranodal protein–lipid complex fraction. **C**, Detergent insolubility of BK channels in the cerebella of wild-type (*Caspr*^{+/+}) and *Caspr*-deficient (*Caspr*^{-/-}) mice. Actin was used as a loading control. **D**, Paranodal BK channels in the mouse cerebellum. Mouse cerebellar sections were immunolabeled for BK channels (red) and Caspr (green). Scale bar, 10 μ m. **E**, BK channels are not detected at paranodes in *Caspr*-deficient mice with disrupted paranodes. Cerebellar sections from wild-type (*Caspr*^{+/+}) and *Caspr*-deficient (*Caspr*^{-/-}) mice were immunolabeled for BK channels (green) and β IV-spectrin (red). Scale bar, 2 μ m.

deficient mice completely lacked BK channels at the paranodes (Fig. 3E). Furthermore, despite the strong enrichment of BK channels at the adult paranodal junction, BK channel enrichment at paranodes lagged behind paranodal junction assembly during development in mice. For example, although Caspr immunoreactivity already defines paranodes at P19, paranodal BK labeling was not apparent until P23 and fully matured between P25 and P30 (Fig. 4A). Together, these results suggest that the paranodal clustering of BK channels is developmentally regulated by a Caspr- and paranodal junction-dependent mechanism.

Axonal physiology of Purkinje cells in young adult mouse slices

To determine whether paranodal BK channels regulate APs in myelinated axons, we measured APs evoked in the axon before and after local blockade of paranodal BK channels. Although axonal patch recordings have been performed on Purkinje cell axons of juvenile rats and mice (Clark et al., 2005; Khaliq and

Raman, 2005; Monsivais et al., 2005; Yang and Wang, 2013), myelination of the Purkinje cell axons prevented similar measurements in cerebellar slices from young adult mice older than P25, when paranodal BK expression becomes prominent (Fig. 4A). Therefore, we took an alternative approach. We evoked APs in the axon and recorded the resultant antidromic APs in the soma. By applying BK channel blockers to the axon and examining their effects on antidromic APs, we tested whether paranodal BK channels have significant roles in AP generation and conduction in the myelinated axons of Purkinje cells.

Purkinje cell somata were subjected to whole-cell patch-clamp recording and infused with a fluorescent dye through the patch pipette to label the axons. After finding a cell with a long intact axon, a bipolar electrode was placed near the axon for extracellular stimulation. The position of the electrode was adjusted for maximum and stable responses. APs were evoked in distal axons with the extracellular electrode and recorded under the whole-cell patch-clamp mode at the soma of Purkinje cells

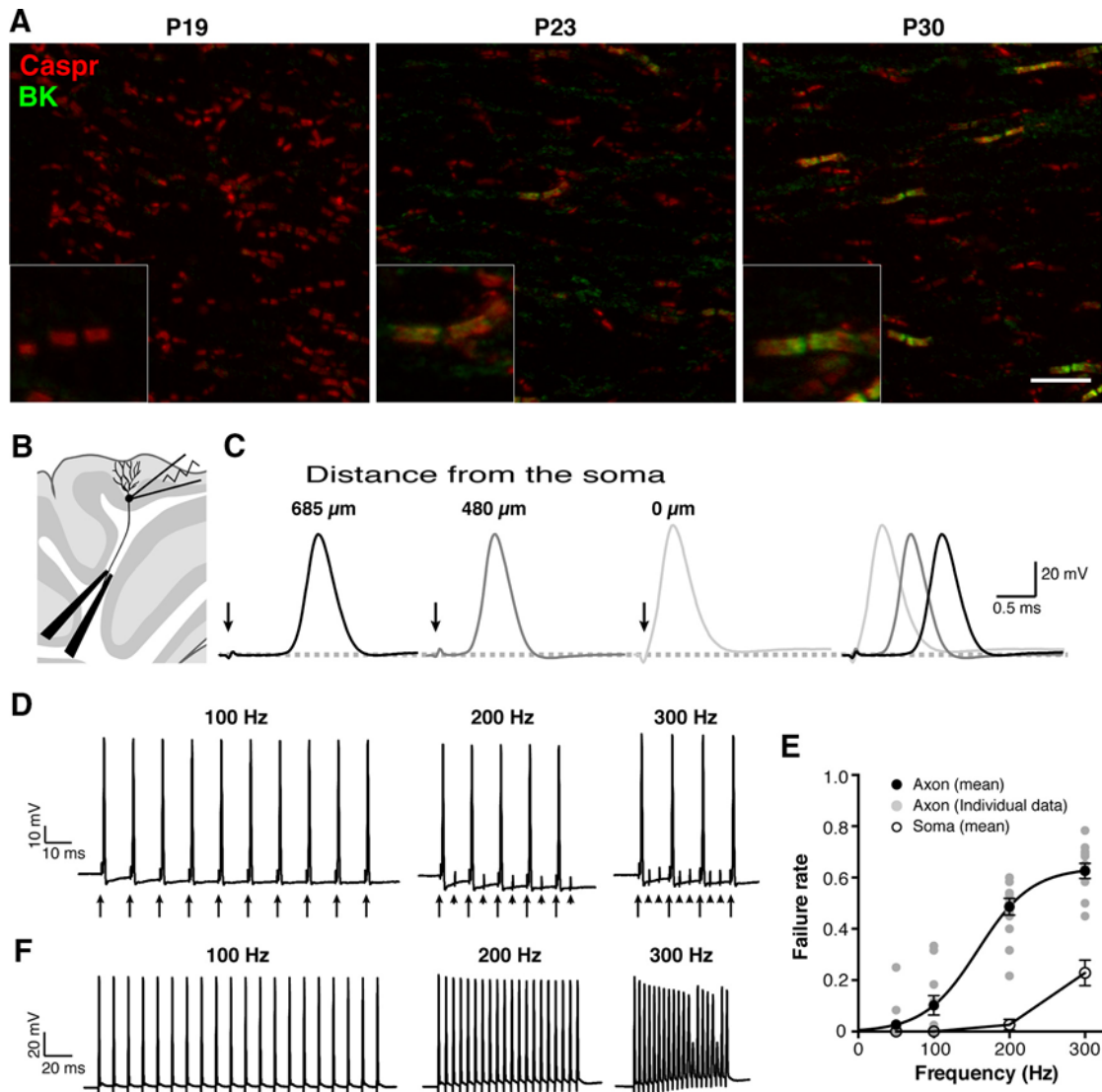


Figure 4. Recording of antidromic APs as an experimental model to investigate the role of paranodal BK channels. *A*, Immunolabeling of developing mouse cerebella from P19 to P30 with the L6/60 (green) and anti-Caspr antibody (red). Paranodal BK channel immunolabeling was absent in P19 but becomes apparent at P23. Scale bar, 10 μ m. Insets show magnified views of the paranodes. *B*, Experimental setup to evoke and record antidromic APs. *C*, Antidromic APs evoked by stimulating the white matter at different distances from the soma. The arrows indicate the stimulation artifact. The distance-dependent delay indicates the antidromic nature of the signals. *D*, Antidromic APs evoked at different stimulation frequencies. The arrows indicate the stimulation, and the arrowheads show failures. *E*, The failure rate of APs at different frequencies. APs were evoked in either the axon or the soma. Error bars indicate SEM ($n = 50$). Data from the axonal stimulation were fitted with a Boltzmann sigmoidal curve. *F*, Reliable firing of APs at the soma. Extracellular stimulation was given to the soma to evoke APs at the soma.

(Fig. 4*B*), while keeping the somatic resting membrane potential at approximately -65 mV. To verify that the recorded APs originated in the distal axon, we placed the stimulation electrode at different distances from the soma to confirm a distance-dependent delay in the onset of APs. When the stimulation was given at 685 μ m from the soma, there was a significant delay between the stimulation and the onset of the AP recorded at the soma (Fig. 4*C*). This delay was shortened, as the stimulation electrode was moved closer to the soma. The average conduction velocity computed from the latency was 0.52 ± 0.05 m/s ($n = 21$), a value consistent with that reported previously (Clark et al., 2005).

Given that we could evoke and record antidromic APs from Purkinje cells, we next investigated the properties of antidromic APs in Purkinje cell axons, particularly their fidelity during high-frequency firing. Cerebellar Purkinje cells typically fire at frequencies above 50 Hz, such that we stimulated Purkinje cell axons at 50, 100, 200, and 300 Hz. Surprisingly, we observed

substantial failures of APs at stimulation frequencies above 100 Hz (Fig. 4*D,E*). This was not attributable to reduced excitability of the soma in our preparation, because APs were evoked without failures even at 200 Hz when the extracellular stimulation was applied to the soma (Fig. 4*E,F*); we do not know whether this difference reflects a failure of stimulation or the nature of distal axons (see Discussion). Nevertheless, our data show that the maximum net frequency of antidromic AP firing was ~ 120 Hz.

Paranodal BK channels modulate high-frequency firing in Purkinje cell axons

To investigate directly the physiological role of paranodal BK channels, we examined the effects of BK channel blockers on antidromic APs. Because BK channels are also expressed in the soma and dendrites of Purkinje cells, we pursued locally inhibiting only axonal BK channels through focal application of BK channel blockers. To demonstrate the precision and specificity of

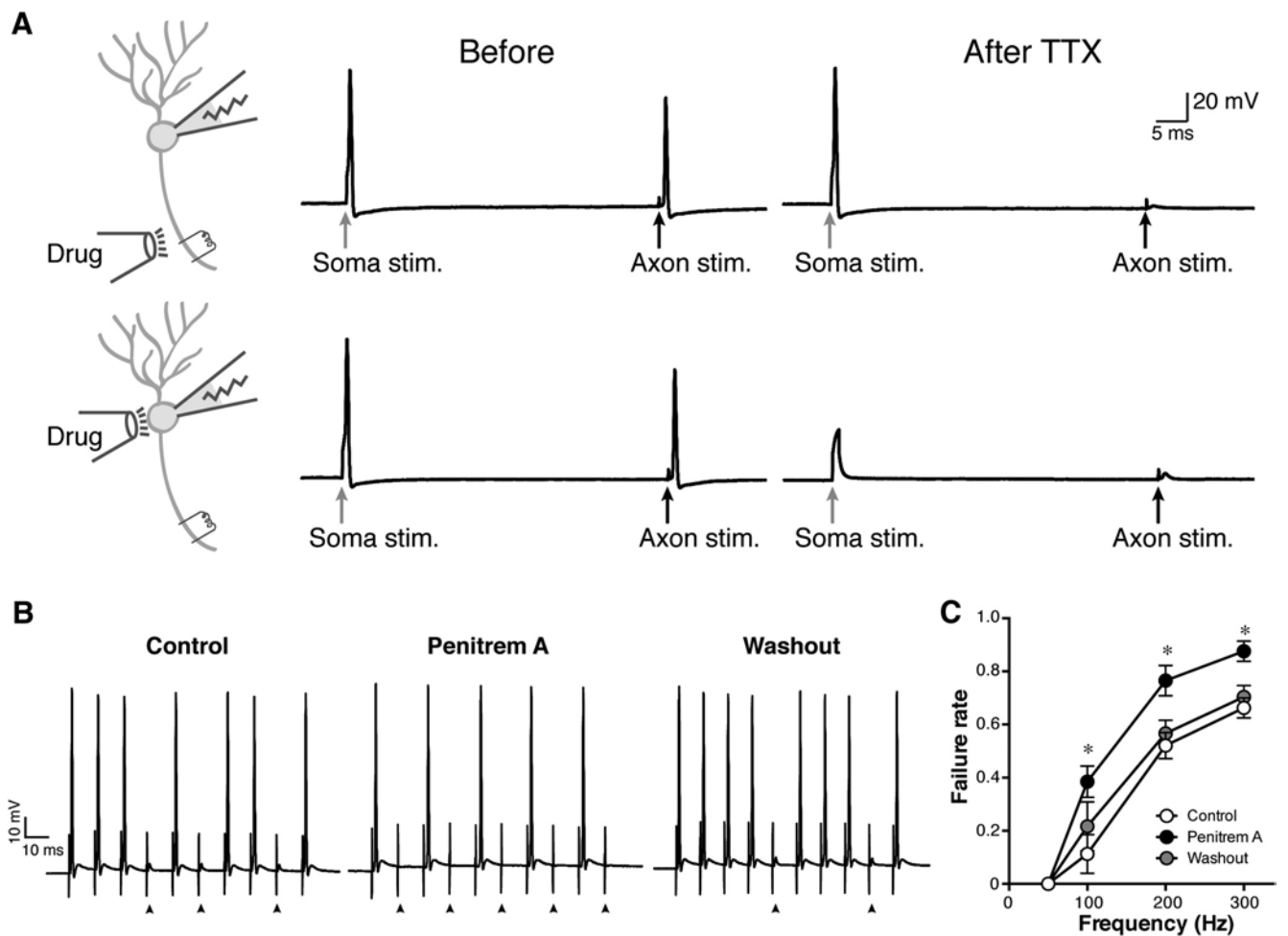


Figure 5. Increased failure of antidromic APs by BK channel inhibition. **A**, Verification of the specificity of local drug application. TTX was applied focally to either the axon or the soma as indicated in the schematic diagram. Before TTX application, both somatic current injection and extracellular axonal stimulation evoked APs. After applying TTX at $0.5 \mu\text{M}$ for 5 min to the axon, only the antidromic AP evoked by the axonal stimulation was attenuated, whereas the somatic application blocked both. Arrows show the timing of stimulation. **B**, Increased failure of antidromic APs by penitrem A at 100 Hz. The arrowheads indicate failures. Before the drug application, there were a few failures of antidromic APs observed at 100 Hz stimulation. Application of penitrem A at $10 \mu\text{M}$ to the axon for 5 min substantially increased failures. This effect was reversed by a 10 min washout of the drug. **C**, Pooled data ($n = 4$). * $p = 0.001$ (at 100 Hz), 0.002 (at 200 Hz), and 0.008 (at 300 Hz), respectively, for Control versus Penitrem A, and $p = 0.015$ (at 200 Hz) and 0.046 (at 300 Hz) for Washout versus Penitrem A.

the local drug application, we first locally applied the Na^+ channel inhibitor TTX ($0.5 \mu\text{M}$) in brief pulses to the axon using a glass pipette and then evoked APs in the soma and the axon. As shown in Figure 5A, both somatic and axonal stimulation evoked APs, but only the antidromic APs were inhibited after local axonal application of TTX. In contrast, somatic application of TTX blocked both APs (Fig. 5A).

We next focally applied BK channel blockers to the axon and examined their effects on antidromic APs. We found that the membrane-permeable BK channel blocker penitrem A ($10 \mu\text{M}$; Knaus et al., 1994) significantly increased the failure rate of antidromic APs (from 0.11 ± 0.07 to 0.39 ± 0.06 at 100 Hz, $p = 0.001$, $n = 4$; Fig. 5B,C). This effect was reversible, such that the failure rate decreased to the control level after washing out the drug for 10 min. We also tested other BK channel blockers, including iberiotoxin (Galvez et al., 1990) and paxilline (Knaus et al., 1994). Interestingly, the membrane-impermeable iberiotoxin (250 nM) did not show significant effects on failure rates (from 0.02 ± 0.02 to 0.00 ± 0.00 at 100 Hz, $p = 0.956$, $n = 4$) of antidromic APs (Fig. 6A). Consistent with the limited permeability of the paranodal junction (Mierzwa et al., 2010), we speculate that this may be attributable to the fact that paranodal BK chan-

nels are covered with glial membranes and not readily accessible to the relatively large (4.2 kDa) iberiotoxin. In contrast, membrane-permeable paxilline ($10 \mu\text{M}$) elicited an effect similar to penitrem A, such that it increased the failure rate of antidromic APs (from 0.09 ± 0.05 to 0.25 ± 0.13 at 100 Hz, $p = 0.015$, $n = 6$; Fig. 6B), particularly at 100 and 200 Hz stimulation (Fig. 6C). The increased failure was observed reliably in all cells examined (Fig. 6D). As a result, the maximum net firing rate decreased from 120.8 ± 14.1 to 87.6 ± 16.1 Hz ($p = 0.033$, $n = 6$; Fig. 6E).

Although we did not detect substantial levels of BK channels in the internodal region, it is possible that the effects of BK blockers result, at least in part, from blocking internodal BK channels expressed at levels sufficiently low to avoid detection in our immunolabeling experiments. To investigate this, we tested two predictions. First, the activation of internodal BK channels would cause shunting. Second, the activation of internodal BK channels would decrease the membrane resistance and the length constant. Therefore, inhibition of internodal BK channels would either decrease the failure rate of antidromic APs or increase the conduction velocity. Our results shown above demonstrated clearly that the former is not the case. We also did not observe any changes in the conduction velocity during axonal BK channel

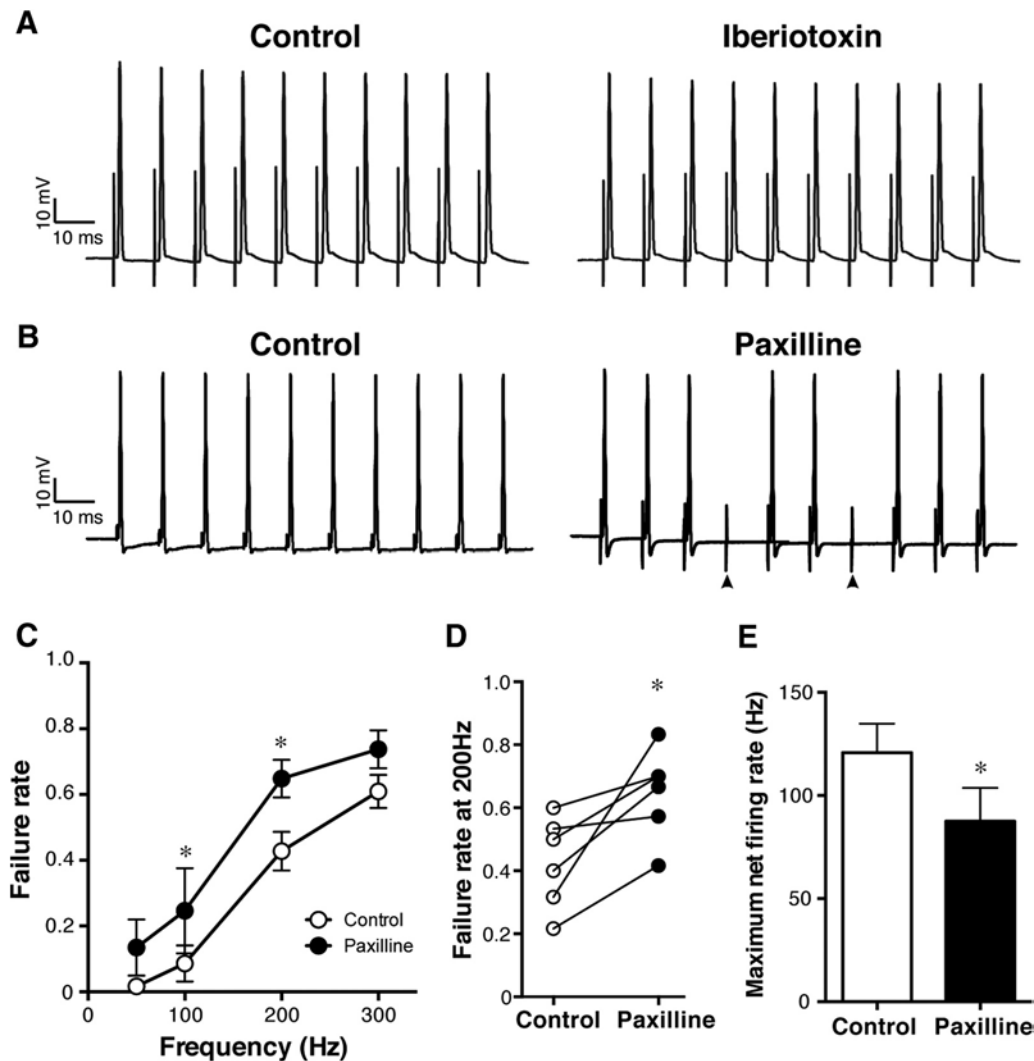


Figure 6. Increased failure of antidromic APs by membrane-permeable, but not membrane-impermeable, BK channel blockers. *A*, No significant effect of iberiotoxin (250 nM) on the antidromic APs at 100 Hz. *B*, Increased failure of antidromic APs by paxilline (10 μ M) at 100 Hz. The arrowheads indicate failures. *C*, Pooled data for paxilline ($n = 6$). * $p = 0.015$ (at 200 Hz) and 0.001 (at 300 Hz). *D*, The failure rate at 200 Hz stimulation before and after the paxilline application. $p = 0.02$. *E*, Decrease of the maximum net firing rate after the paxilline treatment. * $p = 0.03$.

inhibition ($100.0 \pm 9.8\%$ in control vs $101.0 \pm 11.2\%$ after paxilline treatment, $n = 6$), indicating that the contribution of internodal BK channels is minuscule. Together, these results show that local (i.e., axonal) inhibition of BK channels reduces the fidelity of axonal AP conduction and suggest that paranodal BK channels support the high-frequency firing of Purkinje cell axons.

Potential involvement of voltage-gated Ca^{2+} channels in the nodal region

Because BK channels generally require an increase in $[\text{Ca}^{2+}]_i$ to be activated by depolarization within the physiological range of membrane potentials (Barrett et al., 1982), they are often tightly coupled with voltage-gated Ca^{2+} (Cav) channels (Grunnet and Kaufmann, 2004; Liu et al., 2004; Berkefeld et al., 2006), which provide Ca^{2+} for their activation. Ca^{2+} transients in unmyelinated axons have been reported in several types of neurons (Lev-Ram and Ellisman, 1995; Tsantoulas et al., 2013; Sargoy et al., 2014), including immature Purkinje cells (Callewaert et al., 1996). Thus, Cav channels may be nearby in either the nodal or the paranodal membranes to participate in the activation of BK channels. To test this possibility, we first determined whether Ca^{2+} influx is necessary for reliable high-frequency firing of an-

tidromic APs. Recording was performed before and after applying ACSF without Ca^{2+} for 5 min. Importantly, the failure rate of antidromic APs at 100 Hz increased significantly after the treatment (from 0.11 ± 0.11 to 0.74 ± 0.13 , $p = 0.001$ at 100 Hz, $n = 3$; Fig. 7*A,B*). This effect was also reversible (Fig. 7*A*). These results indicate that Ca^{2+} influx influences AP firing in the axon. We next examined the effect of Ni^{2+} , which is a relatively broad inhibitor of Cav channels (Tsien et al., 1988). We chose Ni^{2+} over other more specific Cav blockers because Ni^{2+} -sensitive Cav channels have been reported in the axon of Purkinje cells (Bender and Trussell, 2009) and because Cav channels, like paranodal BK channels, might be covered by glial membranes and less accessible to those large organic inhibitors. Interestingly, Ni^{2+} (100 μ M) showed an effect similar to paxilline and penitrem A and increased the failure of antidromic APs when applied locally to the axon from 0.51 ± 0.03 to 0.67 ± 0.07 at 200 Hz ($p = 0.030$, $n = 4$; Fig. 7*C–E*). This also resulted in a significant reduction in the maximum net firing rate of antidromic APs from 125.0 ± 15.0 to 88.3 ± 4.7 Hz ($p = 0.041$, $n = 4$; Fig. 7*F*). These results suggest that Ni^{2+} -sensitive Cav channels support high-frequency firing of APs in the axon and may provide Ca^{2+} for the activation for paranodal BK channels.

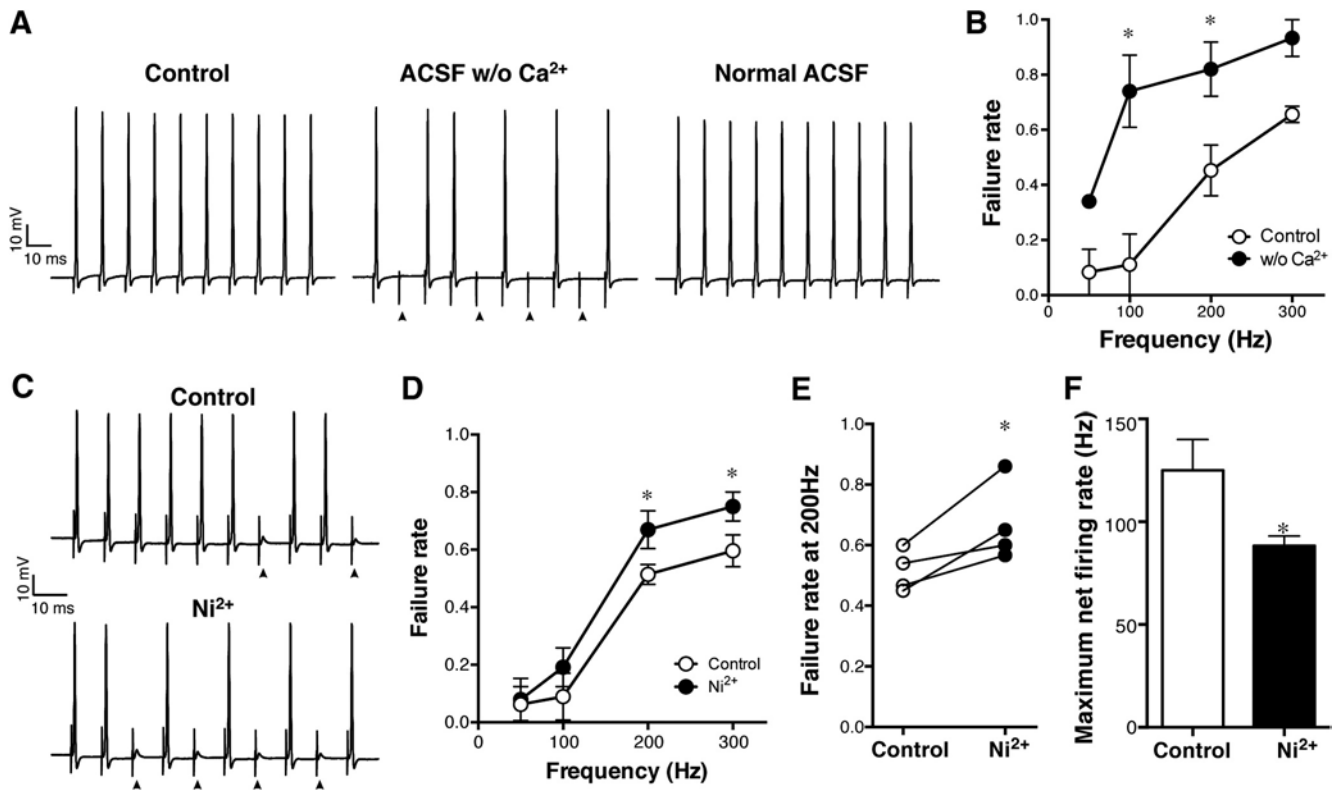


Figure 7. Increased failure of antidromic APs by inhibiting Ca²⁺ influx. **A**, The failure of antidromic APs was also increased by applying ACSF with no Ca²⁺ (ACSF w/o Ca²⁺) to the axon. This effect was reversed in normal ACSF (Normal ACSF). **B**, Pooled data ($n = 3$). * $p = 0.001$ (at 100 Hz) and 0.019 (at 200 Hz). **C**, Similar increase in the failure rate induced by Ni²⁺. Ni²⁺ at 100 μM was applied to the axon for 5 min. **D**, Pooled data ($n = 4$). * $p = 0.03$. **E**, The failure rate at 200 Hz stimulation before and after the Ni²⁺ application. $p = 0.04$. **F**, Decrease of the maximum net firing rate after the Ni²⁺ treatment. * $p = 0.04$.

Effect of the axonal BK channels on the output of the cerebellar cortex

We have shown so far that axonal BK channels localized to the paranodal region regulate axonal APs, evidenced by the effects of BK channel blockers on antidromic APs. Purkinje cell axons diverge extensively in the white matter and form multiple synapses on neurons in the DCNs. This extensive branching is thought to make axonal APs intrinsically prone to failures (Bucher and Goaillard, 2011; Debanne et al., 2011). Therefore, the regulation of axonal APs by paranodal BK channels would affect the final synaptic output of Purkinje cells to DCNs. To test this, we also examined the effect of BK channel blockers on IPSCs in DCN neurons evoked by stimulating Purkinje cell axons in the white matter (Fig. 8A). The pipette solution contained cesium instead of potassium to block K⁺ channels in the postsynaptic DCN neurons. Penitrem A was then applied locally to the cerebellar white matter away from the DCNs. We predicted that increased failures of APs in the axons by penitrem A would result in the overall reduction of IPSCs rather than occasional failures of IPSCs because these postsynaptic neurons receive inputs from multiple Purkinje cell axons (Fig. 8B). Based on the results from antidromic AP recordings, we chose to stimulate the axons at 100 Hz, at which frequency we observed a significant and consistent increase of failures of antidromic APs by penitrem A (Fig. 5B,C) and can reliably measure phasic IPSCs (Telgkamp et al., 2004). In fact, we found that the local puff application of penitrem A to the axon significantly ($p = 0.045$, two-way ANOVA, $n = 10$) decreased the amplitude of phasic IPSCs (Fig. 8C). Similar to the effect on antidromic APs, this decrease was reversed after 15 min washout of the drug (Fig. 8C). The effect of axonal BK channel

inhibition was the opposite of what was expected from the inhibition of presynaptic BK channels, which would increase the IPSC amplitude by extending Ca²⁺ influx. In contrast, the effect was somewhat similar to that of reducing presynaptic Ca²⁺ entry by baclofen (Telgkamp et al., 2004), indicating that the increased AP failures in multiple axons by BK channel inhibition resulted in the reduction of presynaptic Ca²⁺ influx in some presynaptic boutons. These results suggest that BK channels specifically localized to paranodes of Purkinje cell axons regulate axonal APs and the final output of the cerebellar cortex to the cerebellar nuclei.

Discussion

Purkinje cells are the sole output of the cerebellar cortex. To understand information processing in the cerebellar circuit, it is important to understand the mechanisms regulating APs in their myelinated axons. Here, we described a new regulatory mechanism by paranodal BK channels for high-frequency and high-fidelity axonal AP propagation. This novel paranodal localization of BK channels was confirmed by two distinct mouse mAbs, indicating that the labeling is genuine and that the specific localization at Purkinje cell paranodes is not attributable to epitope masking preventing labeling of BK channels at other sites. Because the effect of BK channel blockers was observed on axonal APs in virtually all Purkinje cells analyzed (for an example, see Fig. 6D) and on the integrated synaptic output (Fig. 8), the majority of Purkinje cell axons are likely to express BK channels. Although several different K⁺ channels have been found at the node of Ranvier and in the juxtaparanodal region (Rasband and Shrager, 2000; Devaux et al., 2003; Pan et al., 2006; Trimmer,

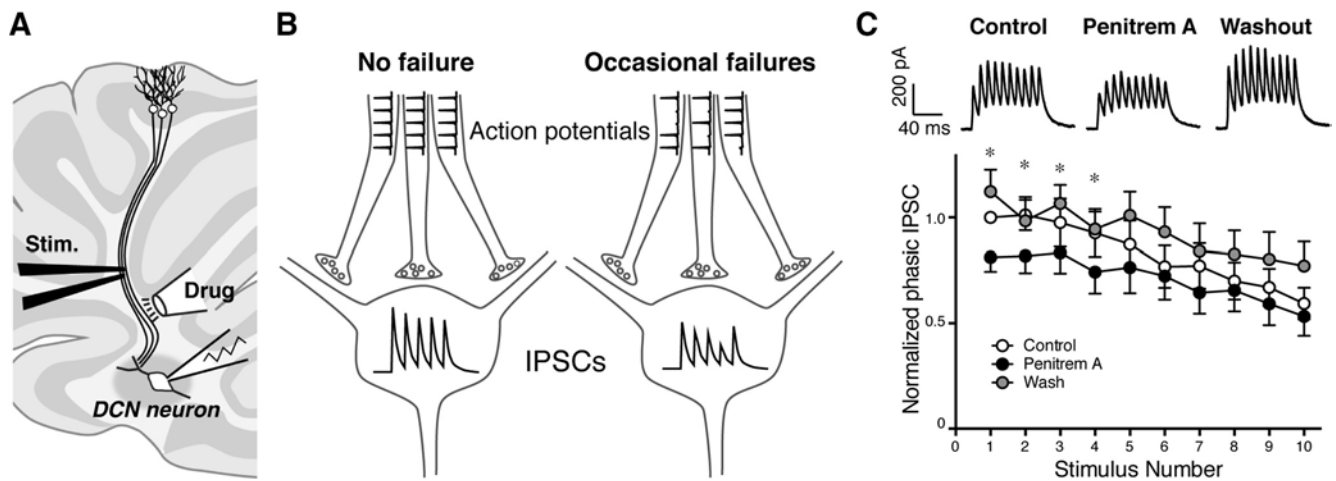


Figure 8. Reduction of IPSC amplitude in DCNs by local application of penitrem A to Purkinje cell axons. **A**, Schematic diagram showing the experimental setup. **B**, Prediction of the effect of penitrem A. Blocking axonal BK channels would augment the propensity of failures of APs in the axon. Because single DCN neurons receive inputs from multiple Purkinje cell axons, occasional failures of axonal APs would translate to a reduction of the amplitude of IPSCs rather than their failures. **C**, IPSCs recorded from DCN neurons before (Control) and after the application of penitrem A to the white matter away from DCNs. Values were normalized to the first phasic IPSC in control. The blocker significantly reduced the overall amplitude of IPSCs evoked at 100 Hz. IPSCs recovered after a 5 min washout ($p = 0.05$ with 2-way ANOVA between Control and Penitrem A, $n = 10$). $*p < 0.05$ with *post hoc* analysis between Control and Penitrem A.

2015), this is the first example of a K^+ channel in the paranode. Paranodal BK channels may have been overlooked because they appear to be present only in Purkinje cell axons.

Paranodes are organized by cell-adhesion molecules at the axon–glia junction, which functions not only to electrically isolate internodal membranes from nodal membranes but also to limit the lateral diffusion of ion channels in the axonal membrane (Chang and Rasband, 2013). Among the cell-adhesion molecules, Caspr is critical in forming these paranodal structures (Gollan et al., 2003), and loss of Caspr results in mislocalization of juxtaparanodal Kv1 channels (Bhat et al., 2001). In this study, we found that the paranodal localization of BK channels was disrupted in Caspr-deficient mice. Therefore, the paranodal localization of BK channels in Purkinje cell axons depends on a paranodal junction-dependent mechanism, although the precise molecular mechanism that clusters paranodal BK channels specifically in Purkinje cells remains to be elucidated. Interestingly, mice with disrupted paranodal junctions have preferential degeneration of Purkinje cell axons (Garcia-Fresco et al., 2006). Loss of paranodal BK channels may contribute to this Purkinje cell-specific axon degeneration through excitotoxic mechanisms.

Using specific BK channel blockers, we also provide evidence that paranodal BK channels support high-frequency axonal AP firing. To investigate the role of paranodal BK channels, we recorded antidromic APs evoked in the axon. These antidromic APs exhibited substantial failures above a 100 Hz firing rate. The fidelity of antidromic APs in our experiments is low compared with those reported in previous studies using mouse cerebellar slices, in which virtually no axonal AP failures were observed at firing rates up to 200 Hz (Khaliq and Raman, 2005, 2006; Monrivais et al., 2005). This may reflect differences in the age of animals used (juvenile in previous studies vs young adults in this study) and/or the recording temperature. Alternatively, the extracellular stimulation of the myelinated axons in our experiments might have occasionally failed to evoke APs. Nevertheless, the significant increase in the failure rate of antidromic APs observed after treatment with the BK channel blockers strongly suggests that paranodal BK channels play pivotal roles in regulating axonal APs in Purkinje cells.

We observed increased AP failures with two membrane-permeable BK channel blockers, paxilline and penitrem A, but not with membrane-impermeable iberitoxin. Although we attribute the lack of effect of iberitoxin to its limited accessibility to paranodal BK channels, it is also possible that iberitoxin-insensitive BK channels dominate the paranodal region, as is the case with BK channels in the Purkinje cell somata (Benton et al., 2013). It was also necessary to use the membrane-permeable BK channel blockers at relatively high concentrations to observe changes in the antidromic APs within several minutes. We speculate that this reflects the fact that the BK channels at paranodes are covered with glial membranes and that these lipophilic blockers may be absorbed by these membranes and restricted from effectively reaching the BK channels. The result that two different and structurally dissimilar BK channel blockers, paxilline and penitrem A, both elicited a similar increase in the failure rate suggests that the effect results from specific inhibition of axonal BK channels.

To further generalize our findings to orthodromic APs, we also investigated the effects of BK channel blockers, as applied locally to Purkinje cell axons, on the inhibitory synaptic transmission between Purkinje cells and DCN neurons. We predicted that, as BK channel blockers increase the failure of orthodromic APs, synaptic transmission would be suppressed. In fact, we observed a significant reduction of IPSC amplitude after focally blocking axonal BK channels. Together, our results suggest that axonal BK channels support high-frequency and high-fidelity firing of APs and their conduction in the myelinated axon of Purkinje cells, thereby ensuring the output of the cerebellar cortex.

How does the BK channel support high-fidelity firing in the axon? BK channels have rapid activation and deactivation kinetics (Cui et al., 1997), which allow them to contribute to AHPs in Purkinje cell somata (Womack and Khodakhah, 2002; Edgerton and Reinhart, 2003; Swensen and Bean, 2003), in which an increase of $[Ca^{2+}]_i$ in response to a single AP is sufficient to activate somatic BK channels. Inhibition of somatic BK channels in Purkinje cells reduces AHPs and yields increased AP firing (Edgerton and Reinhart, 2003; Swensen and Bean, 2003; Womack et al., 2009), presumably because of increased membrane depolarization after each AP. Therefore, if paranodal BK channels serve a

similar role in the axon, BK channel inhibition would cause increased axonal AP firing. However, the inhibition of axonal BK channels decreased the firing of antidromic APs by increasing the failure rate. In addition to nodal K^+ channels (Devaux et al., 2003; Pan et al., 2006), large-conductance paranodal BK channels might be critical to repolarize the nodal membrane to recover Nav channels during high-frequency firing. In this scenario, inhibition of axonal BK channels would cause a slightly more depolarized nodal membrane potentials after each AP, thereby slowing the recovery of Nav channels from inactivation and thus reducing the availability of nodal Nav channels, resulting in an increased failure rate (Yang and Wang, 2013). This is generally consistent with the higher firing rates seen in dentate granule cells in response to the gain of function for BK channels obtained in the BK- $\beta 4$ subunit knock-out mouse (Brenner et al., 2005). Moreover, that BK channels located at different sites in the same neuron can generate bidirectional effects on neuronal firing under distinct conditions is consistent with complex roles for BK channels in regulating excitability (Montgomery and Meredith, 2012). Future modeling studies may help clarify the ionic mechanism whereby paranodal BK channels support axonal APs in Purkinje cells.

BK channels generally require Ca^{2+} for their activation by physiological membrane potentials (Barrett et al., 1982), and a recent report argues that Ca^{2+} is the primary determinant of BK channel activation (Berkefeld and Fakler, 2013). However, there exist distinct BK channel splicing isoforms, auxiliary subunits, and interacting proteins that yield BK channels activated solely by physiological membrane depolarization (Chen et al., 2005; Yan and Aldrich, 2010). Therefore, it is possible that paranodal BK channels do not require Ca^{2+} . Although highly localized increases in Ca^{2+} have been observed at nodes of Ranvier of certain axons (Zhang et al., 2010), more uniform Ca^{2+} transients are seen in others (Zhang et al., 2006). We found that the broad-spectrum Cav channel blocker Ni^{2+} showed an effect similar to BK channel blockers in increasing the failure of antidromic APs. These results suggest that R- and T-type Ni^{2+} -sensitive Cav channels contribute to the regulation of axonal APs. This may be consistent with the finding that Ni^{2+} -sensitive Cav channels are expressed in the axon initial segment of Purkinje cells (Bender and Trussell, 2009), because the nodal region often expresses a similar repertoire of ion channels as found in the initial segment (Chang and Rasband, 2013). Although the effects of Ni^{2+} , as well as Ca^{2+} -free ACSF, might be mediated by other Ca^{2+} -sensitive K^+ channels or Ca^{2+} -dependent processes, given the similar effect to BK blockers, we speculate that Cav channels supply Ca^{2+} to paranodal BK channels and thereby contribute to the repolarization of Purkinje cell axon nodal membranes.

In summary, the results described here demonstrate that paranodal BK channels regulate the function of Purkinje cell axons. The regulation of individual axons by paranodal BK channels also affects the synaptic transmission of Purkinje cells to DCNs, the final output of the cerebellar cortex. Because we did not find paranodal BK channels outside of the cerebellum, we speculate that these paranodal BK channels may be a molecular specialization unique to the Purkinje cell axon, which confers on them unique axonal physiology. Furthermore, the implication that Cav channels are involved in regulating axonal APs suggests that other Ca^{2+} -dependent processes may operate in myelinated axons to influence plasticity of axonal AP conduction in Purkinje cells. The results presented here may contribute to a deeper understanding of the role of axonal Ca^{2+} in information processing and cerebellar dysfunction.

References

- Barrett JN, Magleby KL, Pallotta BS (1982) Properties of single calcium-activated potassium channels in cultured rat muscle. *J Physiol* 331:211–230. [CrossRef Medline](#)
- Bender KJ, Trussell LO (2009) Axon initial segment Ca^{2+} channels influence action potential generation and timing. *Neuron* 61:259–271. [CrossRef Medline](#)
- Benton MD, Lewis AH, Bant JS, Raman IM (2013) Iberitoxin-sensitive and -insensitive BK currents in Purkinje neuron somata. *J Neurophysiol* 109:2528–2541. [CrossRef Medline](#)
- Berkefeld H, Fakler B (2013) Ligand-gating by Ca^{2+} is rate limiting for physiological operation of BK(Ca) channels. *J Neurosci* 33:7358–7367. [CrossRef Medline](#)
- Berkefeld H, Sailer CA, Bildl W, Rohde V, Thumfart JO, Eble S, Klugbauer N, Reisinger E, Bischofberger J, Oliver D, Knaus HG, Schulte U, Fakler B (2006) BKCa-Cav channel complexes mediate rapid and localized Ca^{2+} -activated K^+ signaling. *Science* 314:615–620. [CrossRef Medline](#)
- Bhat MA, Rios JC, Lu Y, Garcia-Fresco GP, Ching W, St Martin M, Li J, Einheber S, Chesler M, Rosenbluth J, Salzer JL, Bellen HJ (2001) Axon-glia interactions and the domain organization of myelinated axons requires neurexin IV/Caspr/Paranodin. *Neuron* 30:369–383. [CrossRef Medline](#)
- Brenner R, Chen QH, Vilaythong A, Toney GM, Noebels JL, Aldrich RW (2005) BK channel beta4 subunit reduces dentate gyrus excitability and protects against temporal lobe seizures. *Nat Neurosci* 8:1752–1759. [CrossRef Medline](#)
- Bucher D, Goaillard JM (2011) Beyond faithful conduction: short-term dynamics, neuromodulation, and long-term regulation of spike propagation in the axon. *Prog Neurobiol* 94:307–346. [CrossRef Medline](#)
- Callewaert G, Eilers J, Konnerth A (1996) Axonal calcium entry during fast “sodium” action potentials in rat cerebellar Purkinje neurons. *J Physiol* 495:641–647. [CrossRef Medline](#)
- Chang KJ, Rasband MN (2013) Excitable domains of myelinated nerves: axon initial segments and nodes of Ranvier. *Curr Top Membr* 72:159–192. [CrossRef Medline](#)
- Chen L, Tian L, MacDonald SH, McClafferty H, Hammond MS, Huibant JM, Ruth P, Knaus HG, Shipston MJ (2005) Functionally diverse complement of large conductance calcium- and voltage-activated potassium channel (BK) alpha-subunits generated from a single site of splicing. *J Biol Chem* 280:33599–33609. [CrossRef Medline](#)
- Clark BA, Monsivais P, Branco T, London M, Häusser M (2005) The site of action potential initiation in cerebellar Purkinje neurons. *Nat Neurosci* 8:137–139. [CrossRef Medline](#)
- Cui J, Cox DH, Aldrich RW (1997) Intrinsic voltage dependence and Ca^{2+} regulation of mslo large conductance Ca -activated K^+ channels. *J Gen Physiol* 109:647–673. [CrossRef Medline](#)
- Davis JQ, Lambert S, Bennett V (1996) Molecular composition of the node of Ranvier: identification of ankyrin-binding cell adhesion molecules neurofascin (mucin+/third FNIII domain-) and NrCAM at nodal axon segments. *J Cell Biol* 135:1355–1367. [CrossRef Medline](#)
- Debanne D, Campanac E, Bialowas A, Carlier E, Alcaraz G (2011) Axon physiology. *Physiol Rev* 91:555–602. [CrossRef Medline](#)
- Devaux J, Alcaraz G, Grinspan J, Bennett V, Joho R, Crest M, Scherer SS (2003) Kv3.1b is a novel component of CNS nodes. *J Neurosci* 23:4509–4518. [Medline](#)
- Edgerton JR, Reinhart PH (2003) Distinct contributions of small and large conductance Ca^{2+} -activated K^+ channels to rat Purkinje neuron function. *J Physiol* 548:53–69. [CrossRef Medline](#)
- Einheber S, Zanazzi G, Ching W, Scherer S, Milner TA, Peles E, Salzer JL (1997) The axonal membrane protein Caspr, a homologue of neurexin IV, is a component of the septate-like paranodal junctions that assemble during myelination. *J Cell Biol* 139:1495–1506. [CrossRef Medline](#)
- Faber ES, Sah P (2003) Calcium-activated potassium channels: multiple contributions to neuronal function. *Neuroscientist* 9:181–194. [CrossRef Medline](#)
- Galvez A, Gimenez-Gallego G, Reuben JP, Roy-Contancin L, Feigenbaum P, Kaczorowski GJ, Garcia ML (1990) Purification and characterization of a unique, potent, peptidyl probe for the high conductance calcium-activated potassium channel from venom of the scorpion *Buthus tamulus*. *J Biol Chem* 265:11083–11090. [Medline](#)
- Garcia-Fresco GP, Sousa AD, Pillai AM, Moy SS, Crawley JN, Tassarollo L, Dupree JL, Bhat MA (2006) Disruption of axo-glia junctions causes

- cytoskeletal disorganization and degeneration of Purkinje neuron axons. *Proc Natl Acad Sci U S A* 103:5137–5142. [CrossRef Medline](#)
- Gollan L, Salomon D, Salzer JL, Peles E (2003) Caspr regulates the processing of contactin and inhibits its binding to neurofascin. *J Cell Biol* 163:1213–1218. [CrossRef Medline](#)
- Grunnet M, Kaufmann WA (2004) Coassembly of big conductance Ca₂⁺-activated K⁺ channels and L-type voltage-gated Ca₂⁺ channels in rat brain. *J Biol Chem* 279:36445–36453. [CrossRef Medline](#)
- Hermanstynne TO, Kihira Y, Misono K, Deitchler A, Yanagawa Y, Misonou H (2010) Immunolocalization of the voltage-gated potassium channel Kv2.2 in GABAergic neurons in the basal forebrain of rats and mice. *J Comp Neurol* 518:4298–4310. [CrossRef Medline](#)
- Hirono M, Saitow F, Kudo M, Suzuki H, Yanagawa Y, Yamada M, Nagao S, Konishi S, Obata K (2012) Cerebellar globular cells receive monoaminergic excitation and monosynaptic inhibition from Purkinje cells. *PLoS One* 7:e29663. [CrossRef Medline](#)
- Jeffries O, Geiger N, Rowe IC, Tian L, McClafferty H, Chen L, Bi D, Knaus HG, Ruth P, Shipston MJ (2010) Palmitoylation of the S0–S1 linker regulates cell surface expression of voltage- and calcium-activated potassium (BK) channels. *J Biol Chem* 285:33307–33314. [CrossRef Medline](#)
- Khalik ZM, Raman IM (2005) Axonal propagation of simple and complex spikes in cerebellar Purkinje neurons. *J Neurosci* 25:454–463. [CrossRef Medline](#)
- Khalik ZM, Raman IM (2006) Relative contributions of axonal and somatic Na channels to action potential initiation in cerebellar Purkinje neurons. *J Neurosci* 26:1935–1944. [CrossRef Medline](#)
- Knaus HG, McManus OB, Lee SH, Schmalhofer WA, Garcia-Calvo M, Helms LM, Sanchez M, Giangiacomo K, Reuben JP, Smith AB 3rd, Kaczorowski GJ, Garcia ML (1994) Tremorgenic indole alkaloids potently inhibit smooth muscle high-conductance calcium-activated potassium channels. *Biochemistry* 33:5819–5828. [CrossRef Medline](#)
- Kocsis JD, Waxman SG (1980) Absence of potassium conductance in central myelinated axons. *Nature* 287:348–349. [CrossRef Medline](#)
- Lai HC, Jan LY (2006) The distribution and targeting of neuronal voltage-gated ion channels. *Nat Rev Neurosci* 7:548–562. [CrossRef Medline](#)
- Levental I, Lingwood D, Grzybek M, Coskun U, Simons K (2010) Palmitoylation regulates raft affinity for the majority of integral raft proteins. *Proc Natl Acad Sci U S A* 107:22050–22054. [CrossRef Medline](#)
- Lev-Ram V, Ellisman MH (1995) Axonal activation-induced calcium transients in myelinating Schwann cells, sources, and mechanisms. *J Neurosci* 15:2628–2637. [Medline](#)
- Liu G, Shi J, Yang L, Cao L, Park SM, Cui J, Marx SO (2004) Assembly of a Ca₂⁺-dependent BK channel signaling complex by binding to beta2 adrenergic receptor. *EMBO J* 23:2196–2205. [CrossRef Medline](#)
- Meera P, Wallner M, Song M, Toro L (1997) Large conductance voltage- and calcium-dependent K⁺ channel, a distinct member of voltage-dependent ion channels with seven N-terminal transmembrane segments (S0–S6), an extracellular N terminus, and an intracellular (S9–S10) C terminus. *Proc Natl Acad Sci U S A* 94:14066–14071. [CrossRef Medline](#)
- Menegoz M, Gaspar P, Le Bert M, Galvez T, Burgaya F, Palfrey C, Ezan P, Arnos F, Girault JA (1997) Paranodin, a glycoprotein of neuronal paranodal membranes. *Neuron* 19:319–331. [CrossRef Medline](#)
- Mierzwa A, Shroff S, Rosenbluth J (2010) Permeability of the paranodal junction of myelinated nerve fibers. *J Neurosci* 30:15962–15968. [CrossRef Medline](#)
- Misonou H, Mohapatra DP, Menegola M, Trimmer JS (2005) Calcium- and metabolic state-dependent modulation of the voltage-dependent Kv2.1 channel regulates neuronal excitability in response to ischemia. *J Neurosci* 25:11184–11193. [CrossRef Medline](#)
- Misonou H, Menegola M, Buchwalder L, Park EW, Meredith A, Rhodes KJ, Aldrich RW, Trimmer JS (2006) Immunolocalization of the Ca(2+)-activated K(+) channel Slo1 in axons and nerve terminals of mammalian brain and cultured neurons. *J Comp Neurol* 496:289–302. [CrossRef Medline](#)
- Monsivais P, Clark BA, Roth A, Häusser M (2005) Determinants of action potential propagation in cerebellar Purkinje cell axons. *J Neurosci* 25:464–472. [CrossRef Medline](#)
- Montgomery JR, Meredith AL (2012) Genetic activation of BK currents in vivo generates bidirectional effects on neuronal excitability. *Proc Natl Acad Sci U S A* 109:18997–19002. [CrossRef Medline](#)
- Ogawa Y, Schafer DP, Horresh I, Bar V, Hales K, Yang Y, Susuki K, Peles E, Stankewich MC, Rasband MN (2006) Spectrins and ankyrinB constitute a specialized paranodal cytoskeleton. *J Neurosci* 26:5230–5239. [CrossRef Medline](#)
- Palkovits M, Magyar P, Szentágothai J (1972) Quantitative histological analysis of the cerebellar cortex in the cat. IV. Mossy fiber-Purkinje cell numerical transfer. *Brain Res* 45:15–29. [CrossRef Medline](#)
- Pan Z, Kao T, Horvath Z, Lemos J, Sul JY, Cranstoun SD, Bennett V, Scherer SS, Cooper EC (2006) A common ankyrin-G-based mechanism retains KCNQ and NaV channels at electrically active domains of the axon. *J Neurosci* 26:2599–2613. [CrossRef Medline](#)
- Poliak S, Peles E (2003) The local differentiation of myelinated axons at nodes of Ranvier. *Nat Rev Neurosci* 4:968–980. [CrossRef Medline](#)
- Rasband, MN (2004) It's "juxta" potassium channel! *J Neurosci Res* 76:749–757.
- Rasband MN, Shrager P (2000) Ion channel sequestration in central nervous system axons. *J Physiol* 525:63–73. [CrossRef Medline](#)
- Rasband MN, Trimmer JS, Schwarz TL, Levinson SR, Ellisman MH, Schachner M, Shrager P (1998) Potassium channel distribution, clustering, and function in remyelinating rat axons. *J Neurosci* 18:36–47. [Medline](#)
- Rhodes KJ, Strassle BW, Monaghan MM, Bekele-Arcuri Z, Matos MF, Trimmer JS (1997) Association and colocalization of the Kvbeta1 and Kvbeta2 beta-subunits with Kv1 alpha-subunits in mammalian brain K⁺ channel complexes. *J Neurosci* 17:8246–8258. [Medline](#)
- Salkoff L, Butler A, Ferreira G, Santi C, Wei A (2006) High-conductance potassium channels of the SLO family. *Nat Rev Neurosci* 7:921–931. [CrossRef Medline](#)
- Sargoy A, Sun X, Barnes S, Brecha NC (2014) Differential calcium signaling mediated by voltage-gated calcium channels in rat retinal ganglion cells and their unmyelinated axons. *PLoS One* 9:e84507. [CrossRef Medline](#)
- Sausbier M, Hu H, Arntz C, Feil S, Kamm S, Adelsberger H, Sausbier U, Sailer CA, Feil R, Hofmann F, Korth M, Shipston MJ, Knaus HG, Wolfer DP, Pedroarena CM, Storm JF, Ruth P (2004) Cerebellar ataxia and Purkinje cell dysfunction caused by Ca₂⁺-activated K⁺ channel deficiency. *Proc Natl Acad Sci U S A* 101:9474–9478. [CrossRef Medline](#)
- Sausbier U, Sausbier M, Sailer CA, Arntz C, Knaus HG, Neuhuber W, Ruth P (2006) Ca₂⁺-activated K⁺ channels of the BK-type in the mouse brain. *Histochem Cell Biol* 125:725–741. [CrossRef Medline](#)
- Schafer DP, Bansal R, Hedstrom KL, Pfeiffer SE, Rasband MN (2004) Does paranode formation and maintenance require partitioning of neurofascin 155 into lipid rafts? *J Neurosci* 24:3176–3185. [CrossRef Medline](#)
- Schwarz JR, Glassmeier G, Cooper EC, Kao TC, Nodera H, Tabuena D, Kaji R, Bostock H (2006) KCNQ channels mediate IKs, a slow K⁺ current regulating excitability in the rat node of Ranvier. *J Physiol* 573:17–34. [CrossRef Medline](#)
- Swensen AM, Bean BP (2003) Ionic mechanisms of burst firing in dissociated Purkinje neurons. *J Neurosci* 23:9650–9663. [Medline](#)
- Telgkamp P, Raman IM (2002) Depression of inhibitory synaptic transmission between Purkinje cells and neurons of the cerebellar nuclei. *J Neurosci* 22:8447–8457. [Medline](#)
- Telgkamp P, Padgett DE, Ledoux VA, Woolley CS, Raman IM (2004) Maintenance of high-frequency transmission at purkinje to cerebellar nuclear synapses by spillover from boutons with multiple release sites. *Neuron* 41:113–126. [CrossRef Medline](#)
- Trimmer JS (2015) Subcellular localization of K channels in mammalian brain neurons: remarkable precision in the midst of extraordinary complexity. *Neuron* 85:238–256. [CrossRef Medline](#)
- Tsantoulas C, Farmer C, Machado P, Baba K, McMahon SB, Raouf R (2013) Probing functional properties of nociceptive axons using a microfluidic culture system. *PLoS One* 8:e80722. [CrossRef Medline](#)
- Tsien RW, Lipscombe D, Madison DV, Bley KR, Fox AP (1988) Multiple types of neuronal calcium channels and their selective modulation. *Trends Neurosci* 11:431–438. [CrossRef Medline](#)
- Uusisaari M, Obata K, Knöpfel T (2007) Morphological and electrophysiological properties of GABAergic and non-GABAergic cells in the deep cerebellar nuclei. *J Neurophysiol* 97:901–911. [CrossRef Medline](#)
- Vacher H, Mohapatra DP, Trimmer JS (2008) Localization and targeting of voltage-dependent ion channels in mammalian central neurons. *Physiol Rev* 88:1407–1447. [CrossRef Medline](#)
- Wang H, Kunkel DD, Martin TM, Schwartzkroin PA, Tempel BL (1993) Heteromultimeric K⁺ channels in terminal and juxtaparanodal regions of neurons. *Nature* 365:75–79. [CrossRef Medline](#)
- Womack MD, Khodakhah K (2002) Characterization of large conductance

